

Circuit quantum electrodynamics

Alexandre Blais 

*Institut quantique and Département de Physique, Université de Sherbrooke,
Sherbrooke, Québec J1K 2R1, Canada
and Canadian Institute for Advanced Research, Toronto M5G 1M1, Ontario, Canada*

Arne L. Grimsmo

*Centre for Engineered Quantum Systems, School of Physics,
The University of Sydney, Sydney, New South Wales 2006, Australia*

S. M. Girvin

Yale Quantum Institute, P.O. Box 208 334, New Haven, Connecticut 06520-8263, USA

Andreas Wallraff 

*Department of Physics, ETH Zurich, CH-8093 Zurich, Switzerland and Quantum Center,
ETH Zurich, CH-8093 Zurich, Switzerland*

 (published 19 May 2021)

Quantum-mechanical effects at the macroscopic level were first explored in Josephson-junction-based superconducting circuits in the 1980s. In recent decades, the emergence of quantum information science has intensified research toward using these circuits as qubits in quantum information processors. The realization that superconducting qubits can be made to strongly and controllably interact with microwave photons, the quantized electromagnetic fields stored in superconducting circuits, led to the creation of the field of circuit quantum electrodynamics (QED), the topic of this review. While atomic cavity QED inspired many of the early developments of circuit QED, the latter has now become an independent and thriving field of research in its own right. Circuit QED allows the study and control of light-matter interaction at the quantum level in unprecedented detail. It also plays an essential role in all current approaches to gate-based digital quantum information processing with superconducting circuits. In addition, circuit QED provides a framework for the study of hybrid quantum systems, such as quantum dots, magnons, Rydberg atoms, surface acoustic waves, and mechanical systems interacting with microwave photons. Here the coherent coupling of superconducting qubits to microwave photons in high-quality oscillators focusing on the physics of the Jaynes-Cummings model, its dispersive limit, and the different regimes of light-matter interaction in this system are reviewed. Also discussed is coupling of superconducting circuits to their environment, which is necessary for coherent control and measurements in circuit QED, but which also invariably leads to decoherence. Dispersive qubit readout, a central ingredient in almost all circuit QED experiments, is also described. Following an introduction to these fundamental concepts that are at the heart of circuit QED, important use cases of these ideas in quantum information processing and in quantum optics are discussed. Circuit QED realizes a broad set of concepts that open up new possibilities for the study of quantum physics at the macro scale with superconducting circuits and applications to quantum information science in the widest sense.

DOI: [10.1103/RevModPhys.93.025005](https://doi.org/10.1103/RevModPhys.93.025005)

CONTENTS

| | | | |
|---|----|---|----|
| I. Introduction | 2 | A. Exchange interaction between a transmon and an oscillator | 12 |
| II. Superconducting Quantum Circuits | 3 | B. The Jaynes-Cummings spectrum | 13 |
| A. The quantum LC resonator | 3 | C. Dispersive regime | 14 |
| B. 2D resonators | 4 | 1. Schrieffer-Wolff approach | 14 |
| 1. Quantized modes of the transmission-line resonator | 6 | 2. Bogoliubov approach | 15 |
| C. 3D resonators | 7 | D. Josephson junctions embedded in multimode electromagnetic environments | 16 |
| D. The transmon artificial atom | 8 | E. Beyond the transmon: Multilevel artificial atom | 17 |
| E. Flux-tunable transmons | 11 | F. Alternative coupling schemes | 18 |
| F. Other superconducting qubits | 11 | IV. Coupling to the Environment | 18 |
| III. Light-Matter Interaction in Circuit QED | 12 | A. Wiring up quantum systems with transmission lines | 18 |
| | | B. Input-output theory in electrical networks | 19 |

| | |
|--|----|
| C. Qubit relaxation and dephasing | 20 |
| D. Dissipation in the dispersive regime | 21 |
| E. Multimode Purcell effect and Purcell filters | 22 |
| F. Controlling quantum systems with microwave drives | 23 |
| V. Measurements in Circuit QED | 23 |
| A. Microwave field detection | 23 |
| B. Phase-space representations and their relation to field detection | 26 |
| C. Dispersive qubit readout | 27 |
| 1. Steady-state intracavity field | 27 |
| 2. Signal-to-noise ratio and measurement fidelity | 29 |
| 3. Other approaches to qubit readout | 31 |
| a. Josephson bifurcation amplifier | 31 |
| b. High-power readout and qubit “punch out” | 31 |
| c. Squeezing | 31 |
| d. Longitudinal readout | 31 |
| VI. Qubit-Resonator Coupling Regimes | 32 |
| A. Resonant regime | 32 |
| 1. Bad-cavity limit | 32 |
| 2. Bad-qubit limit | 33 |
| 3. Strong-coupling regime | 33 |
| B. Dispersive regime | 35 |
| 1. Qubit spectroscopy | 36 |
| 2. ac-Stark shift and measurement-induced broadening | 36 |
| C. Beyond strong coupling: Ultrastrong-coupling regime | 38 |
| VII. Quantum Computing With Circuit QED | 39 |
| A. Single-qubit gates | 39 |
| B. Two-qubit gates | 41 |
| 1. Qubit-qubit exchange interaction | 41 |
| a. Direct capacitive coupling | 41 |
| b. Resonator mediated coupling | 42 |
| 2. Flux-tuned 11-02 phase gate | 43 |
| 3. All-microwave gates | 44 |
| a. Resonator-induced phase gate | 44 |
| b. Cross-resonance gate | 45 |
| 4. Parametric gates | 46 |
| C. Encoding a qubit in an oscillator | 47 |
| VIII. Quantum Optics on a Chip | 49 |
| A. Intracavity fields | 49 |
| B. Quantum-limited amplification | 50 |
| C. Propagating fields and their characterization | 51 |
| 1. Itinerant single and multiphoton states | 51 |
| 2. Squeezed microwave fields | 52 |
| D. Remote entanglement generation | 53 |
| E. Waveguide QED | 54 |
| F. Single-microwave photon detection | 55 |
| IX. Outlook | 56 |
| Acknowledgments | 57 |
| Appendix A: Hamiltonian of a Voltage Biased Transmon | 57 |
| 1. Classical gate voltage | 58 |
| 2. Coupling to an LC oscillator | 58 |
| Appendix B: Unitary Transformations | 59 |
| 1. Schrieffer-Wolff perturbation theory | 59 |
| 2. Schrieffer-Wolff transformation for a multilevel system coupled to an oscillator in the dispersive regime | 60 |
| a. The transmon | 60 |
| b. The Jaynes-Cummings model | 61 |
| 3. Bogoliubov approach to the dispersive regime | 61 |
| 4. Off-resonantly driven transmon | 62 |
| Appendix C: Input-Output Theory | 63 |
| References | 64 |

I. INTRODUCTION

Circuit quantum electrodynamics (QED) is the study of the interaction of nonlinear superconducting circuits, acting as artificial atoms or as qubits for quantum information processing, with quantized electromagnetic fields in the microwave-frequency domain. Inspired by cavity QED (Kimble, 1998; Haroche and Raimond, 2006), a field of research originating from atomic physics and quantum optics, circuit QED has led to advances in the fundamental study of light-matter interaction, in the development of quantum information processing technology (Clarke and Wilhelm, 2008; Wendin, 2017; Krantz *et al.*, 2019; Blais, Girvin, and Oliver, 2020; Kjaergaard, Schwartz *et al.*, 2020), and in the exploration of novel hybrid quantum systems (Xiang *et al.*, 2013; Clerk *et al.*, 2020).

First steps toward exploring the quantum physics of superconducting circuits were made in the mid 1980s. At that time, the question arose as to whether quantum phenomena, such as quantum tunneling or energy level quantization, could be observed in macroscopic systems of any kind (Leggett, 1980, 1984b). One example of such a macroscopic system is the Josephson tunnel junction (Josephson, 1962; Tinkham, 2004) formed by a thin insulating barrier at the interface between two superconductors and in which macroscopic quantities such as the current flowing through the junction or the voltage developed across it are governed by the dynamics of the gauge-invariant phase difference of the Cooper pair condensate across the junction. The first experimental evidence for quantum effects in these circuits (Clarke *et al.*, 1988) was the observation of quantum tunneling of the phase degree of freedom of a Josephson junction (Devoret, Martinis, and Clarke, 1985), rapidly followed by the measurement of quantized energy levels of the same degree of freedom (Martinis, Devoret, and Clarke, 1985).

While the possibility of observation of coherent quantum phenomena in Josephson-junction-based circuits, such as coherent oscillations between two quantum states of the junction and the preparation of quantum superpositions, was already envisaged in the 1980s (Teschke, 1987), the prospect of realizing superconducting qubits for quantum computation revived interest in the pursuit of this goal (Bocko, Herr, and Feldman, 1997; Shnirman, Schön, and Hermon, 1997; Bouchiat *et al.*, 1998; Makhlin, Schön, and Shnirman, 1999, 2001). In a groundbreaking experiment, time-resolved coherent oscillations with a superconducting qubit were observed in 1999 (Nakamura, Pashkin, and Tsai, 1999). Further progress resulted in the observation of coherent oscillations in coupled superconducting qubits (Pashkin *et al.*, 2003; Yamamoto *et al.*, 2003) and in significant improvements of the coherence times of these devices by exploiting symmetries in the Hamiltonian underlying the description of the circuits (Vion *et al.*, 2002; Clarke and Wilhelm, 2008; Kjaergaard, Schwartz *et al.*, 2020).

In parallel to these advances, in atomic physics and quantum optics cavity QED developed into an excellent setting for the study of the coherent interactions between individual atoms and quantum radiation fields (Rempe, Walther, and Klein, 1987; Haroche and Kleppner, 1989; Thompson, Rempe, and Kimble, 1992; Brune *et al.*, 1996), and its application to quantum communication (Kimble, 2008)

and quantum computation (Kimble, 1998; Haroche and Raimond, 2006). In the early 2000s, the concept of realizing the physics of cavity QED with superconducting circuits emerged with proposals to coherently couple superconducting qubits to microwave photons in open 3D cavities (Al-Saidi and Stroud, 2001; Yang, Chu, and Han, 2003; You and Nori, 2003), in discrete LC oscillators (Buisson and Hekking, 2001; Makhlin, Schön, and Shnirman, 2001), and in large Josephson junctions (Marquardt and Bruder, 2001; Blais, van den Brink, and Zagoskin, 2003; Plastina and Falci, 2003). The prospect of realizing strong coupling of superconducting qubits to photons stored in high-quality coplanar waveguide resonators, together with suggestions to use this approach to protect qubits from decoherence, to read out their state, and to couple them to each other in a quantum computer architecture advanced the study of cavity QED with superconducting circuits (Blais *et al.*, 2004). The possibility of exploring both the foundations of light-matter interaction and advancing quantum information processing technology with superconducting circuits provided motivation for the rapid advance in experimental research, culminating in the first experimental realization of a circuit QED system achieving the strong-coupling regime of light-matter interaction where the coupling overwhelms damping (Chiorescu *et al.*, 2004; Wallraff *et al.*, 2004).

Circuit QED combines the theoretical and experimental tools of atomic physics, quantum optics, and the physics of mesoscopic superconducting circuits not only to further explore the physics of cavity QED and quantum optics in novel parameter regimes but also to allow the realization of engineered quantum devices with technological applications. Indeed, after 15 years of development, circuit QED is now a leading architecture for quantum computation. Simple quantum algorithms have been implemented (DiCarlo *et al.*, 2009; Lucero *et al.*, 2012; Kandala *et al.*, 2017; Zheng *et al.*, 2017; Arute *et al.*, 2020b), cloud-based devices are accessible, demonstrations of quantum-error correction have approached or reached the so-called break-even point (Ofek *et al.*, 2016; Hu *et al.*, 2019), and devices with several tens of qubits have been operated with claims of quantum supremacy (Arute *et al.*, 2019).

More generally, circuit QED is opening new research directions. These include the development of quantum-limited amplifiers (Clerk *et al.*, 2010; Roy and Devoret, 2016) and single-microwave photon detectors (Besse *et al.*, 2018; Kono *et al.*, 2018; Lescanne, Deléglise *et al.*, 2020), with applications ranging from quantum information processing to the search for dark matter axions (Lamoreaux *et al.*, 2013; Zheng *et al.*, 2016; Dixit *et al.*, 2020; Backes *et al.*, 2021), to hybrid quantum systems (Clerk *et al.*, 2020) where different physical systems such as nitrogen-vacancy (NV) centers (Kubo *et al.*, 2010), mechanical oscillators (Aspelmeyer, Kippenberg, and Marquardt, 2014), semiconducting quantum dots (Burkard *et al.*, 2020), and collective spin excitations in ferromagnetic crystals (Lachance-Quirion *et al.*, 2019) are interfaced with superconducting quantum circuits.

In this review, we start in Sec. II by introducing the two main actors of circuit QED: high-quality superconducting oscillators and superconducting artificial atoms. The latter are also known as superconducting qubits in the context of

quantum information processing. There are many types of superconducting qubits and we choose to focus on the transmon (Koch *et al.*, 2007). This choice is made not only because the transmon is the most widely used qubit but also because this allows us to present the main ideas of circuit QED without having to delve into the rich physics of the different types of superconducting qubits. Much of the material presented in this review applies to other qubits without significant modification. Section III is devoted to light-matter coupling in circuit QED, including a discussion of the Jaynes-Cummings model and its dispersive limit. Different methods to obtain approximate effective Hamiltonians valid in the dispersive regime are presented. Section IV addresses the coupling of superconducting quantum circuits to their electromagnetic environment, considering both dissipation and coherent control. In Sec. V, we turn to measurements in circuit QED, with an emphasis on dispersive qubit readout. Building on this discussion, Sec. VI presents the different regimes of light-matter coupling that are reached in circuit QED and their experimental signatures. In the last sections, we turn to two applications of circuit QED: quantum computing in Sec. VII and quantum optics in Sec. VIII.

Our objective in this review is to give the reader a solid background on the foundations of circuit QED rather than to showcase the latest developments in the field. We hope that this introductory text will allow one to understand the recent advances of the field and to become an active participant in its development.

II. SUPERCONDUCTING QUANTUM CIRCUITS

Circuit components with spatial dimensions that are small compared to the relevant wavelength can be treated as lumped elements (Devoret, 1997), and we start this section with a particularly simple lumped-element circuit: the quantum LC oscillator. We subsequently discuss the closely related two- and three-dimensional microwave resonators that play a central role in circuit QED experiments and that can be thought of as distributed versions of the LC oscillator with a set of harmonic frequencies. Finally, we move on to nonlinear quantum circuits with Josephson junctions as the source of nonlinearity and discuss how such circuits can behave as artificial atoms with addressable energy levels. We put special emphasis on the transmon qubit (Koch *et al.*, 2007), which is the most widely used artificial atom design in current circuit QED experiments.

A. The quantum LC resonator

An LC oscillator is characterized by its inductance L and capacitance C or, equivalently, by its angular frequency $\omega_r = 1/\sqrt{LC}$ and characteristic impedance $Z_r = \sqrt{L/C}$. The total energy of this oscillator is given by the sum of its charging and inductive energy

$$H_{LC} = \frac{Q^2}{2C} + \frac{\Phi^2}{2L}, \quad (1)$$

where Q is the charge on the capacitor and Φ is the flux threading the inductor; see Fig. 1. From charge conservation, charge is related to current I by $Q(t) = \int_{t_0}^t dt' I(t')$, and from

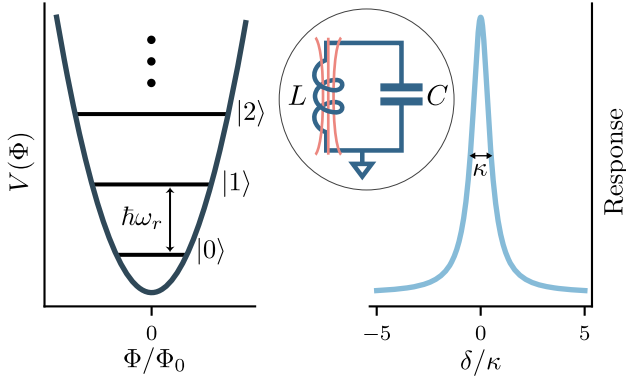


FIG. 1. Left panel: harmonic potential vs flux of the LC circuit with $\Phi_0 = h/2e$ the flux quantum. Right panel: response of the oscillator to an external perturbation as a function of the detuning δ of the perturbation from the oscillator frequency. Here $\kappa = \omega_r/Q$, with Q the oscillator's quality factor, is the full width at half maximum (FWHM) of the oscillator response. Equivalently, $1/\kappa$ is the average lifetime of the single-photon state $|1\rangle$ before it decays to $|0\rangle$. Inset: lumped-element LC oscillator of inductance L and capacitance C .

Faraday's induction law flux is related to voltage by $\Phi(t) = \int_{t_0}^t dt' V(t')$, where we have assumed that the charge and flux are zero at an initial time t_0 , often taken to be in the distant past (Vool and Devoret, 2017).

It is instructive to rewrite H_{LC} as

$$H_{LC} = \frac{Q^2}{2C} + \frac{1}{2} C \omega_r^2 \Phi^2. \quad (2)$$

This form emphasizes the analogy of the LC oscillator with a mechanical oscillator of coordinate Φ , conjugate momentum Q , and mass C . With this analogy in mind, quantization proceeds in a well-known manner: The charge and flux variables are promoted to noncommuting observables satisfying the commutation relation

$$[\hat{\Phi}, \hat{Q}] = i\hbar. \quad (3)$$

It is useful to introduce the standard annihilation \hat{a} and creation \hat{a}^\dagger operators of the harmonic oscillator. With the previously mentioned mechanical analogy in mind, we choose these operators as

$$\hat{\Phi} = \Phi_{\text{zpf}}(\hat{a}^\dagger + \hat{a}), \quad \hat{Q} = iQ_{\text{zpf}}(\hat{a}^\dagger - \hat{a}), \quad (4)$$

with $\Phi_{\text{zpf}} = \sqrt{\hbar/2\omega_r C} = \sqrt{\hbar Z_r/2}$ and $Q_{\text{zpf}} = \sqrt{\hbar\omega_r C/2} = \sqrt{\hbar/2Z_r}$ the characteristic magnitude of the zero-point fluctuations of the flux and the charge, respectively. With these definitions, the previous Hamiltonian takes the usual form

$$\hat{H}_{LC} = \hbar\omega_r(\hat{a}^\dagger \hat{a} + 1/2), \quad (5)$$

with eigenstates that satisfy $\hat{a}^\dagger \hat{a}|n\rangle = n|n\rangle$ for $n = 0, 1, 2, \dots$. In the rest of this review, we follow the convention of dropping from the Hamiltonian the factor of $1/2$ corresponding to zero-point energy. The action of $\hat{a}^\dagger = \sqrt{(1/2)\hbar Z_r}(\hat{\Phi} - iZ_r \hat{Q})$ is to create a quantized excitation of the flux and charge degrees of

freedom of the oscillator or, equivalently, of the magnetic and electric fields. In other words, \hat{a}^\dagger creates a photon of frequency ω_r stored in the circuit.

While formally correct, one can wonder if this quantization procedure is relevant in practice. Is it possible to operate LC oscillators in a regime where quantum effects are important? For this to be the case, at least two conditions must be satisfied. First, the oscillator should be sufficiently well decoupled from uncontrolled degrees of freedom such that its energy levels are considerably less broad than their separation. In short, we require the oscillator's quality factor $Q = \omega_r/\kappa$, with κ the oscillator linewidth or, equivalently, the photon-loss rate, to be large. An approach to treat the environment of a quantum system is described in Sec. IV. Because losses are at the origin of level broadening, superconductors on low-loss dielectric substrates such as sapphire or high-resistivity silicon wafers are ideal for reaching the quantum regime. Care must also be taken to minimize the effect of coupling to the external circuitry that is essential for operating the oscillator. As discussed later, large quality factors ranging from $Q \sim 10^3$ to 10^8 can be obtained in the laboratory (Frunzio *et al.*, 2005; Bruno *et al.*, 2015; Reagor *et al.*, 2016).

Given that your typical microwave oven has a quality factor approaching 10^4 (Vollmer, 2004), it is not surprising that large Q -factor oscillators can be realized in state-of-the-art laboratories. The relation to kitchen appliances, however, stops here with the second condition requiring the energy separation $\hbar\omega_r$ between adjacent eigenstates to be larger than thermal energy $k_B T$. Since $1 \text{ GHz} \times h/k_B \sim 50 \text{ mK}$, the condition $\hbar\omega_r \gg k_B T$ can be easily satisfied with microwave-frequency circuits operated at $\sim 10 \text{ mK}$ in a dilution refrigerator. These circuits are therefore operated at temperatures far below the critical temperature ($\sim 1\text{--}10 \text{ K}$) of the superconducting films from which they are made.

With these two requirements satisfied, an oscillator with a frequency in the microwave range can be operated in the quantum regime. This means that the circuit can be prepared in its quantum-mechanical ground state $|n=0\rangle$ simply by waiting for a time of the order of a few photon lifetimes $T_\kappa = 1/\kappa$. It is also crucial to note that the vacuum fluctuations of the voltage are typically relatively large. For example, taking reasonable values $L \sim 0.8 \text{ nH}$ and $C \sim 0.4 \text{ pF}$, corresponding to $\omega_r/2\pi \sim 8 \text{ GHz}$ and $Z_r \sim 50 \Omega$, the ground state is characterized by vacuum fluctuations of the voltage of variance as large as $\Delta V_0 = [\langle \hat{V}^2 \rangle - \langle \hat{V} \rangle^2]^{1/2} = \sqrt{\hbar\omega_r/2C} \sim 1 \mu\text{V}$, with $\hat{V} = \hat{Q}/C$. As we make clear later, this leads to large electric field fluctuations and therefore to large electric-dipole interactions when coupling to an artificial atom.

B. 2D resonators

Quantum harmonic oscillators come in many shapes and sizes, the LC oscillator being just one example. Other types of harmonic oscillators that feature centrally in circuit QED are microwave resonators where the electromagnetic field is confined either in a planar, essentially two-dimensional structure (2D resonators) or in a three-dimensional volume

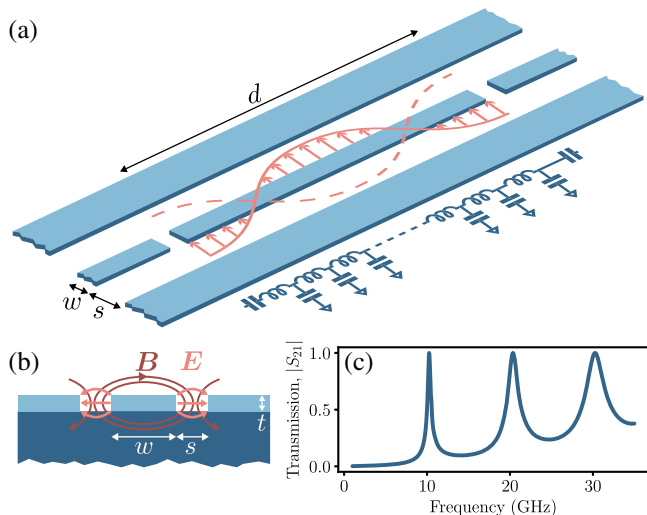


FIG. 2. (a) Schematic layout of a $\lambda/2$ coplanar waveguide resonator of length d , center conductor width w , and ground plane separation s , together with its capacitively coupled input and output ports. The cosine shape of the second mode function ($m = 1$) is illustrated with pink arrows. Also shown is the equivalent lumped-element circuit model. Adapted from Blais *et al.*, 2004. (b) Cross-section cut of the coplanar waveguide resonator showing the substrate (dark blue), the two ground planes, and the center conductor (light blue) as well as schematic representations of the E and B field distributions. (c) Transmission vs frequency for an overcoupled resonator. The first three resonances of frequencies $f_m = (m + 1)f_0$ are illustrated with $f_0 = v_0/2d \sim 10$ GHz and linewidth $\kappa_m/2\pi = f_m/Q$.

(3D resonators). The boundary conditions imposed by the geometry of these different resonators lead to a discretization of the electromagnetic field into a set of modes with distinct frequencies, where each mode can be thought of as an independent harmonic oscillator. Conversely (especially for the 2D case) one can think of these modes as nearly dissipationless plasma modes of superconductors.

Early experiments in circuit QED were motivated by the observation of large quality factors in coplanar waveguide resonators in the context of experiments for radiation detectors (Day *et al.*, 2003) and by the understanding of the importance of presenting a clean electromagnetic environment to the qubits. Early circuit QED experiments were performed with these 2D coplanar waveguide resonators (Wallraff *et al.*, 2004), which remains one of the most commonly used architectures today.

A coplanar waveguide resonator consists of a coplanar waveguide of finite length formed by a center conductor of width w and thickness t , separated on both sides by a distance s from a ground plane of the same thickness; see Fig. 2(a) (Simons, 2001; Pozar, 2011). Both conductors are typically deposited on a low-loss dielectric substrate of permittivity ϵ and thickness much larger than the dimensions w , s , t . This planar structure acts as a transmission line along which signals are transmitted in a way analogous to a conventional coaxial cable. As in a coaxial cable, the coplanar waveguide confines the electromagnetic field to a small volume between its center conductor and the ground; see Fig. 2(b). The dimensions of

the center conductor, the gaps, and the thickness of the dielectric are chosen such that the field is concentrated between the center conductor and ground, and radiation in other directions is minimized. This structure supports a quasi-TEM mode (Wen, 1969), with the electromagnetic field partly in the dielectric substrate and in the vacuum or another dielectric above the substrate, and with the largest concentration in the gaps between the center conductor and the ground planes. In practice, the coplanar waveguide can be treated as an essentially dispersion-free, linear dielectric medium. To minimize losses, superconducting metals such as aluminum, niobium, and niobium titanium nitride (NbTiN) are used in combination with dielectrics of low-loss tangent, such as sapphire and high-resistivity silicon (Nersisyan *et al.*, 2019; McRae *et al.*, 2020).

As with the lumped LC oscillator, the electromagnetic properties of a coplanar waveguide resonator are described by its characteristic impedance $Z_r = \sqrt{l_0/c_0}$ and the speed of light in the waveguide $v_0 = 1/\sqrt{l_0 c_0}$, where we have introduced the capacitance to ground c_0 and inductance l_0 per unit length (Simons, 2001). Typical values of these parameters are $Z_r \sim 50 \Omega$ and $v_0 \sim 1.3 \times 10^8$ m/s, or about a third of the speed of light in vacuum (Göppl *et al.*, 2008). For a given substrate, the characteristic impedance can be adjusted by varying the parameters w , s , and t of the waveguide (Simons, 2001). In the coplanar waveguide geometry, transmission lines of constant impedance Z_r can therefore be realized for different center conductor width w by keeping the ratio of w/s close to a constant (Simons, 2001). This allows the experimenter to fabricate a device with large w at the edges for convenient interfacing, and small w away from the edges to minimize the mode volume or simply for miniaturization.

A resonator is formed from a coplanar waveguide by imposing boundary conditions of either zero current or zero voltage at the two end points separated by a distance d . Zero current can be achieved by microfabricating a gap in the center conductor (open boundary), while zero voltage can be achieved by grounding an end point (shorted boundary). A resonator with open boundary conditions at both ends, as illustrated in Fig. 2(a), has a fundamental frequency $f_0 = v_0/2d$ with harmonics at $f_m = (m + 1)f_0$, and is known as a $\lambda/2$ resonator. On the other hand, $\lambda/4$ resonators with fundamental frequency $f_0 = v_0/4d$ are obtained with one open end and one grounded end. A typical example is a $\lambda/2$ resonator of length 1.0 cm and speed of light 1.3×10^8 m/s corresponding to a fundamental frequency of 6.5 GHz.

This coplanar waveguide geometry is flexible and a large range of frequencies can be achieved. In practice, however, the useful frequency range is restricted from above by the superconducting gap of the metal from which the resonator is made (82 GHz for aluminum). Above this energy, losses due to quasiparticles increase dramatically. Low-frequency resonators can be made by using long, meandering coplanar waveguides. Sundaresan *et al.* (2015) realized a resonator with a length of 0.68 m and a fundamental frequency of $f_0 = 92$ MHz. With this frequency corresponding to a temperature of 4.4 mK, the low-frequency modes of such long resonators are not in the vacuum state. Indeed, according to the Bose-Einstein distribution, the thermal occupation of the

fundamental mode frequency at 10 mK is $\bar{n}_\kappa = 1/(e^{\hbar f_0/k_B T} - 1) \sim 1.8$. Typical circuit QED experiments instead work with resonators in the range of 5–15 GHz, where microwave electronics is well developed.

As mentioned, entering the quantum regime for a given mode m requires more than $\hbar\omega_m \gg k_B T$. It is also important that the linewidth κ_m be small compared to the mode frequency ω_m . As for the LC oscillator, the linewidth can be expressed in terms of the quality factor Q_m of the resonator mode as $\kappa_m = \omega_m/Q_m$. An expression for the linewidth in terms of circuit parameters is given in Sec. IV. There are multiple sources of losses and it is common to distinguish between internal losses due to coupling to uncontrolled degrees of freedom (dielectric and conductor losses at the surfaces and interfaces, substrate dielectric losses, nonequilibrium quasiparticles, vortices, two-level fluctuators, etc.) and external losses due to coupling to the input and output ports used to couple signals in and out of the resonator (Göppl *et al.*, 2008). In terms of these two contributions, the total dissipation rate of mode m is $\kappa_m = \kappa_{\text{ext},m} + \kappa_{\text{int},m}$ and the total, or loaded, quality factor of the resonator is therefore $Q_{L,m} = (Q_{\text{ext},m}^{-1} + Q_{\text{int},m}^{-1})^{-1}$. It is always advantageous to maximize the internal quality factor and much effort has been invested in improving resonator fabrication such that values of $Q_{\text{int}} \sim 10^5$ are routinely achieved. A dominant source of internal losses in superconducting resonators at low power is believed to be two-level systems (TLSs) that reside in the bulk dielectric, in the metal substrate, and in the metal-vacuum and substrate-vacuum interfaces where the electric field is large (Sage *et al.*, 2011; Oliver and Welander, 2013; Wang *et al.*, 2015). Internal quality factors over 10^6 have been achieved by careful fabrication minimizing the occurrence of TLSs and by etching techniques to avoid substrate-vacuum interfaces in regions of high electric fields (Vissers *et al.*, 2010; Megrant *et al.*, 2012; Bruno *et al.*, 2015; Calusine *et al.*, 2018).

On the other hand, the external quality factor can be adjusted via the coupling at the ends of the resonator to input-output transmission lines. For the case of an open end, this is a capacitive coupling. In coplanar waveguide resonators, these input and output coupling capacitors are frequently chosen either as a simple gap of a defined width in the center conductor, as illustrated in Fig. 2(a), but they can also be formed by interdigitated capacitors (Göppl *et al.*, 2008). The choice $Q_{\text{ext}} \ll Q_{\text{int}}$ corresponding to an “overcoupled” resonator is ideal for fast qubit measurement, which is discussed in more detail in Sec. V. On the other hand, undercoupled resonators ($Q_{\text{ext}} \gg Q_{\text{int}}$), where dissipation is limited only by internal losses, which are kept as small as possible, can serve as quantum memories to store microwave photons for long times. Using different modes of the same resonator (Leek *et al.*, 2010) or combinations of resonators (Johnson *et al.*, 2010; Kirchmair *et al.*, 2013), regimes of both high and low external losses can be combined in the same circuit QED device. A general approach for describing losses in quantum systems is detailed in Sec. IV.

Finally, the magnitude of the vacuum fluctuations of the electric field in coplanar waveguide resonators is related to the mode volume. While the longitudinal dimension of the mode is limited by the length of the resonator, which also sets the

fundamental frequency $d \sim \lambda/2$, the transverse dimension can be adjusted over a broad range. Commonly chosen transverse dimensions are of the order of $w \sim 10 \mu\text{m}$ and $s \sim 5 \mu\text{m}$ (Wallraff *et al.*, 2004). If desired, the transverse dimension of the center conductor may be reduced to the submicron scale, up to a limit set by the penetration depth of the superconducting thin films, which is typically of the order of 100–200 nm. When combining the typical separation $s \sim 5 \mu\text{m}$ with the magnitude of the voltage fluctuations $\Delta V_0 \sim 1 \mu\text{V}$ already expected from the discussion of the LC circuit, we find that the zero-point electric field in a coplanar resonator can be as large as $\Delta E_0 = \Delta V_0/s \sim 0.2 \text{ V/m}$. This is at least 2 orders of magnitude larger than the typical amplitude of ΔE_0 in the 3D cavities used in cavity QED (Haroche and Raimond, 2006). As will become clear later, together with the large size of superconducting artificial atoms, this will lead to the large light-matter coupling strengths that are characteristic of circuit QED.

1. Quantized modes of the transmission-line resonator

While only a single mode of the transmission-line resonator is often considered, there are many circuit QED experiments where the multimode structure of the device plays an important role. In this section, we present the standard approach to finding the normal modes of a distributed resonator, first by using a classical description of the circuit.

For the small signals that are relevant to circuit QED, the electromagnetic properties along the x direction of a coplanar waveguide resonator of length d can be modeled using a linear, dispersion-free one-dimensional medium. Figure 3 shows the telegrapher model for such a system where the distributed inductance of the resonator’s center conductor is represented by the series of lumped-element inductances and the capacitance to ground by a parallel combination of capacitances (Pozar, 2011). Using the flux and charge variables introduced in the description of the LC oscillator, the energy associated with each capacitance is $Q_n^2/2C_0$, while the energy associated with each inductance is $(\Phi_{n+1} - \Phi_n)^2/2L_0$. In these expressions, Φ_n is the flux variable associated with the n th node and Q_n is the conjugate variable that is the charge on that node. Using the standard approach (Devoret, 1997), we can thus write the classical Hamiltonian corresponding to Fig. 3 as

$$H = \sum_{n=0}^{N-1} \left[\frac{1}{2C_0} Q_n^2 + \frac{1}{2L_0} (\Phi_{n+1} - \Phi_n)^2 \right]. \quad (6)$$

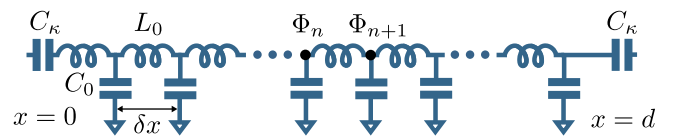


FIG. 3. Telegrapher model of an open-ended transmission-line resonator of length d . L_0 and C_0 are, respectively, the inductance and capacitance associated to each node n of flux Φ_n . The resonator is coupled to external transmission lines (not shown) at its input and output ports via the capacitors C_κ .

It is useful to consider a continuum limit of this Hamiltonian where the size of a unit cell δx is taken to be zero. For this purpose, we write $C_0 = \delta x c_0$ and $L_0 = \delta x l_0$, with c_0 and l_0 the capacitance and inductance per unit length, respectively. Moreover, we define a continuum flux field via $\Phi(x_n) = \Phi_n$ and charge density field $Q(x_n) = Q_n/\delta x$. We can subsequently take the continuum limit $\delta x \rightarrow 0$, while keeping $d = N\Delta x$ constant to find

$$H = \int_0^d dx \left\{ \frac{1}{2c_0} Q(x)^2 + \frac{1}{2l_0} [\partial_x \Phi(x)]^2 \right\}, \quad (7)$$

where we have used $\partial_x \Phi(x_n) = \lim_{\delta x \rightarrow 0} (\Phi_{n+1} - \Phi_n)/\delta x$. In Eq. (7), the charge $Q(x, t) = c_0 \partial_t \Phi(x, t)$ is the canonical momentum to the generalized flux $\Phi(x, t) = \int_{-\infty}^t dt' V(x, t')$, with $V(x, t)$ the voltage to ground on the center conductor.

Using Hamilton's equations together with Eq. (7), we find that the propagation along the transmission line is described by the wave equation

$$v_0^2 \frac{\partial^2 \Phi(x, t)}{\partial x^2} - \frac{\partial^2 \Phi(x, t)}{\partial t^2} = 0, \quad (8)$$

with $v_0 = 1/\sqrt{l_0 c_0}$ the speed of light in the medium. The solution to Eq. (8) can be expressed in terms of normal modes

$$\Phi(x, t) = \sum_{m=0}^{\infty} u_m(x) \Phi_m(t), \quad (9)$$

with $\ddot{\Phi}_m = -\omega_m^2 \Phi_m$ a function of time oscillating at the mode frequency ω_m and

$$u_m(x) = A_m \cos[k_m x + \varphi_m] \quad (10)$$

being the spatial profile of the mode with amplitude A_m . The wave vector $k_m = \omega_m/v_0$ and the phase φ_m are set by the boundary conditions. For an open-ended $\lambda/2$ resonator these are

$$I(x=0, d) = -\frac{1}{l_0} \frac{\partial \Phi(x, t)}{\partial x} \Big|_{x=0, d} = 0, \quad (11)$$

corresponding to the fact that the current vanishes at the two extremities. A $\lambda/4$ resonator is modeled by requiring that the voltage $V(x, t) = \partial_t \Phi(x, t)$ vanishes at the grounded boundary. Asking for Eq. (11) to be satisfied for every mode implies that $\varphi_m = 0$ and that the wave vector is discrete with $k_m = m\pi/d$. Finally, it is useful to choose the normalization constant A_m such that

$$\frac{1}{d} \int_0^d dx u_m(x) u_{m'}(x) = \delta_{mm'}, \quad (12)$$

resulting in $A_m = \sqrt{2}$. This normalization implies that the amplitude of the modes in a 1D resonator decreases with the square root of the length d .

Using this normal mode decomposition in Eq. (7), the Hamiltonian can now be expressed in the simpler form

$$H = \sum_{m=0}^{\infty} \left[\frac{Q_m^2}{2C_r} + \frac{1}{2} C_r \omega_m^2 \Phi_m^2 \right], \quad (13)$$

where $C_r = dc_0$ is the total capacitance of the resonator and $Q_m = C_r \dot{\Phi}_m$ is the charge conjugate to Φ_m . We immediately recognize this Hamiltonian to be a sum over independent harmonic oscillators; see Eq. (1).

Following once more the quantization procedure of Sec. II.A, the two conjugate variables Φ_m and Q_m are promoted to noncommuting operators

$$\hat{\Phi}_m = \sqrt{\frac{\hbar Z_m}{2}} (\hat{a}_m^\dagger + \hat{a}_m), \quad (14)$$

$$\hat{Q}_m = i \sqrt{\frac{\hbar}{2Z_m}} (\hat{a}_m^\dagger - \hat{a}_m), \quad (15)$$

with $Z_m = \sqrt{L_m/C_r}$ the characteristic impedance of mode m and $L_m^{-1} \equiv C_r \omega_m^2$. Using these expressions in Eq. (13) immediately leads to the final result

$$\hat{H} = \sum_{m=0}^{\infty} \hbar \omega_m \hat{a}_m^\dagger \hat{a}_m, \quad (16)$$

with $\omega_m = (m+1)\omega_0$ the mode frequency and $\omega_0/2\pi = v_0/2d$ the fundamental frequency of the $\lambda/2$ transmission-line resonator.

To simplify the discussion, we assumed here that the medium forming the resonator is homogeneous. In particular, we ignored the presence of the input and output port capacitors in the boundary condition of Eq. (11). In addition to lowering the external quality factor Q_{ext} , these capacitances modify the amplitude and phase of the mode functions and shift the mode frequencies. It is possible to render the resonator nonlinear by introducing one or several Josephson junctions directly into the center conductor of the resonator. A theoretical treatment of the resonator mode functions, frequencies, and nonlinearity in the presence of resonator inhomogeneities, including embedded junctions, was given by Bourassa *et al.* (2012) and is also discussed in Sec. III.D.

C. 3D resonators

Although their physical origin is not yet fully understood, dielectric losses at interfaces and surfaces are important limiting factors to the internal quality factor of coplanar transmission-line resonators and lumped-element LC oscillators; see Oliver and Welander (2013) for a review. An approach for mitigating the effect of these losses is to lower the ratio of the electric field energy stored at interfaces and surfaces to the energy stored in vacuum. Indeed, it has been observed that planar resonators with larger feature sizes (s and w), and hence weaker electric fields near the interfaces and surfaces, typically have larger internal quality factors (Sage *et al.*, 2011).

This approach can be pushed further by using three-dimensional microwave cavities rather than planar circuits (Paik *et al.*, 2011). In 3D resonators formed by a metallic cavity, a larger fraction of the field energy is stored in the

vacuum inside the cavity than close to the surface. As a result, the surface participation ratio—the ratio of the energy stored at surfaces versus in vacuum—can be as small as 10^{-7} in 3D cavities, in comparison to 10^{-5} for typical planar geometries (Reagor, 2015). Another potential advantage is that the harmonic mode does not require a dielectric substrate. In practice, however, this does not lead to a major gain in quality factor since, while coplanar resonators can have air-substrate participation ratios as large as 0.9, the bulk loss tangent of sapphire and silicon substrate is significantly smaller than that of the interface oxides and does not appear to be the limiting factor (Wang *et al.*, 2015).

In practice, three-dimensional resonators come in many different form factors and can reach a higher quality factor than lumped-element oscillators and 1D resonators. Quality factors as high as 4.2×10^{10} have been reported at 51 GHz and 0.8 K with Fabry-Perot cavities formed by two highly polished copper mirrors coated with niobium (Kuhr *et al.*, 2007). Corresponding to single-microwave photon lifetimes of 130 ms, these cavities have been used in landmark cavity QED experiments (Haroche and Raimond, 2006). Similar quality factors have also been achieved with niobium micro-maser cavities at 22 GHz and 0.15 K (Varcoe *et al.*, 2000). In the context of circuit QED, commonly used geometries include rectangular (Paik *et al.*, 2011; Rigetti *et al.*, 2012) and coaxial $\lambda/4$ cavities (Reagor *et al.*, 2016). The latter have important practical advantages in that no current flows near any seams created in the assembly of the device that can be responsible for contact resistance (Brecht *et al.*, 2015; Reagor, 2015).

As illustrated in Fig. 4(a) and in close analogy with the coplanar waveguide resonator, rectangular cavities are formed by a finite section of a rectangular waveguide terminated by two metal walls acting as shorts. These three-dimensional resonators are thus simply vacuum surrounded on all sides by metal, typically aluminum to maximize the internal quality factor or copper if magnetic field tuning of components placed inside the cavity is required. The metallic walls impose boundary conditions on the electromagnetic field in the cavity, leading to a discrete set of TE and TM cavity modes of frequency (Pozar, 2011)

$$\omega_{mnl} = c \sqrt{\left(\frac{m\pi}{a}\right)^2 + \left(\frac{n\pi}{b}\right)^2 + \left(\frac{l\pi}{d}\right)^2}, \quad (17)$$

labeled by the three integers (m, n, l), where c is the speed of light and a, b , and d are the cavity dimensions. Dimensions of the order of a centimeter lead to resonance frequencies in the gigahertz range for the first modes. The TE modes to which superconducting artificial atoms couple are illustrated in Figs. 4(b)–4(e). Because these modes are independent, once quantized the cavity Hamiltonian again takes the form of Eq. (16), corresponding to a sum of independent harmonic oscillators. We return to the question of quantizing the electromagnetic field in arbitrary geometries in Sec. III.D.

As mentioned, a major advantage of 3D cavities compared to their 1D or lumped-element analogs is their high quality factor or, equivalently, long photon lifetime. A typical internal Q factor for rectangular aluminum cavities is 5×10^6 , corresponding to a photon lifetime above $50 \mu\text{s}$ (Paik *et al.*,

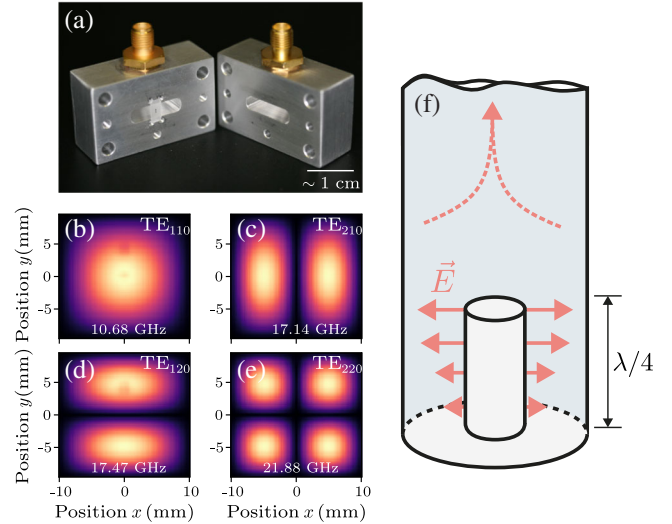


FIG. 4. (a) Photograph of a 3D rectangular superconducting cavity showing the interior volume of the waveguide enclosure housing a sapphire chip and transmon qubit, with two symmetric coaxial connectors for coupling signals in and out. (b)–(e) First four TE_{mnl} modes of a 3D rectangular superconducting cavity obtained from COMSOL. (f) Schematic representation of a coaxial $\lambda/4$ cavity with electric field (solid line) pointing from the inner conductor to the sidewalls and evanescent field (dashed line) rapidly decaying from the top of the inner conductor. Adapted from Reagor *et al.* 2016.

2011). These numbers are even higher for coaxial cavities where $Q_{\text{int}} = 7 \times 10^7$, or above a millisecond of photon storage time, has been reported (Reagor *et al.*, 2016). Moreover, the latter type of cavity is more robust against imperfections that arise when integrating 3D resonators with Josephson-junction-based circuits. Lifetimes of up to 2 s have also been reported in niobium cavities that were initially developed for accelerators (Romanenko *et al.*, 2020). At such long photon lifetimes, microwave cavities are longer-lived quantum memories than the transmon qubit that we introduce in Sec. II.D. This has led to a new paradigm for quantum information processing in which information is stored in a cavity with the role of the qubit limited to providing the essential nonlinearity (Mirrahimi *et al.*, 2014). We return to these ideas in Sec. VII.C.

D. The transmon artificial atom

Although the oscillators discussed in Sec. II.C can be prepared in their quantum-mechanical ground state, it is challenging to observe quantum behavior with such linear systems. Indeed, harmonic oscillators are always in the correspondence limit, and some degree of nonlinearity is therefore essential to encode and manipulate quantum information in these systems (Leggett, 1984a). Superconductivity allows one to introduce nonlinearity in quantum electrical circuits while avoiding losses. Indeed, the Josephson junction is a nonlinear circuit element that is compatible with the requirements for high quality factors and operation at millikelvin temperatures. The physics of these junctions was first understood in 1962 by Brian Josephson (Josephson, 1962; McDonald, 2001).

Contrary to expectations (Bardeen, 1962), Josephson showed that a dissipationless current, i.e., a supercurrent, could flow between two superconducting electrodes separated by a thin insulating barrier. More precisely, he showed that this supercurrent is given by

$$I = I_c \sin \varphi, \quad (18)$$

where I_c is the junction's critical current and φ is the phase difference between the superconducting condensates on either side of the junction (Tinkham, 2004). The critical current, whose magnitude is determined by the junction size and material parameters, is the maximum current that can be supported before Cooper pairs are broken. Once this happens, dissipation kicks in and a finite voltage develops across the junction accompanied by a resistive current. Operation in the quantum regime requires currents well below this critical current. Josephson also showed that the time dependence of the phase difference φ is related to the voltage across the junction according to

$$\frac{d\varphi}{dt} = \frac{2\pi}{\Phi_0} V, \quad (19)$$

with $\Phi_0 = h/2e$ the flux quantum. It is useful to write this expression as $\varphi(t) = 2\pi\Phi(t)/\Phi_0 = 2\pi \int dt' V(t')/\Phi_0$, with $\Phi(t)$ the flux variable introduced in Sec. II.A.

Taken together, the Josephson relations of Eqs. (18) and (19) make it clear that a Josephson junction relates current I to flux Φ . The relation (18) is analogous to the constitutive relation of a geometric inductance $\Phi = LI$, which also links these two quantities. For this reason, it is useful to define the Josephson inductance

$$L_J(\Phi) = \left(\frac{\partial I}{\partial \Phi} \right)^{-1} = \frac{\Phi_0}{2\pi I_c \cos(2\pi\Phi/\Phi_0)}. \quad (20)$$

In contrast to geometric inductances, L_J depends on Φ . As a result, when operated below the critical current the Josephson junction can be thought of as a nonlinear inductor.

Replacing the geometric inductance L of the LC oscillator discussed in Sec. II.A with a Josephson junction, as in Fig. 5(b), therefore renders the circuit nonlinear. In this situation, the energy levels of the circuit are no longer equidistant. If the nonlinearity and the quality factor of the junction are large enough, the energy spectrum resembles that of an atom, with well-resolved and nonuniformly spread spectral lines that can be addressed. We therefore often refer to this circuit as an *artificial atom* (Clarke *et al.*, 1988; Martinis, Devoret, and Clarke, 2020). In many situations, and as it is the focus of much of this review, we can furthermore restrict our attention to only two energy levels, typically the ground and first excited states, forming a qubit.

To make this discussion more precise, it is useful to see how the Hamiltonian of the circuit of Fig. 5(b) is modified by the presence of the Josephson junction taking the place of the linear inductor. While the energy stored in a linear inductor is $E = \int dt V(t)I(t) = \int dt (d\Phi/dt)I = \Phi^2/2L$, where we use $\Phi = LI$ in the last equality, the energy of the nonlinear inductance instead takes the form

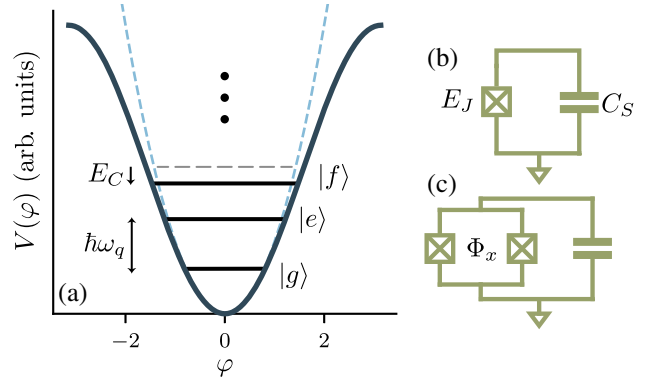


FIG. 5. (a) Cosine potential well of the transmon qubit (solid line) compared to the quadratic potential of the LC oscillator (dashed lines). The spectrum of the former has eigenstates labeled $\{|g\rangle, |e\rangle, |f\rangle, |h\rangle, \dots\}$ and is characterized by an anharmonicity $-E_C$. (b) Circuit for the fixed-frequency transmon qubit. The square with a cross represents a Josephson junction with Josephson energy E_J and junction capacitance C_J . (c) By using a SQUID rather than a single junction, the frequency of the transmon qubit becomes flux tunable.

$$E = I_c \int dt \left(\frac{d\Phi}{dt} \right) \sin \left(\frac{2\pi}{\Phi_0} \Phi \right) = -E_J \cos \left(\frac{2\pi}{\Phi_0} \Phi \right), \quad (21)$$

with $E_J = \Phi_0 I_c / 2\pi$ the Josephson energy. This quantity represents the energy associated with the coherent tunneling of Cooper pairs across the junction. Taking this contribution into account, the quantized Hamiltonian of the capacitively shunted Josephson junction therefore reads (see Appendix A)

$$\begin{aligned} \hat{H}_T &= \frac{(\hat{Q} - Q_g)^2}{2C_\Sigma} - E_J \cos \left(\frac{2\pi}{\Phi_0} \hat{\Phi} \right) \\ &= 4E_C (\hat{n} - n_g)^2 - E_J \cos \hat{\varphi}. \end{aligned} \quad (22)$$

In Eq. (22), $C_\Sigma = C_J + C_S$ is the total capacitance, including the junction's capacitance C_J and the shunt capacitance C_S . On the second line, we define the charge number operator $\hat{n} = \hat{Q}/2e$, the phase operator $\hat{\varphi} = (2\pi/\Phi_0)\hat{\Phi}$, and the charging energy $E_C = e^2/2C_\Sigma$. We also include a possible offset charge $n_g = Q_g/2e$ term representing the effect (up to a constant term in the Hamiltonian we have neglected) of an external electric field bias. The offset charge term can arise from spurious unwanted degrees of freedom in the transmon's environment or from an intentional external gate voltage $V_g = Q_g/C_g$.

The spectrum of \hat{H}_T is controlled by the ratio E_J/E_C , with $E_J/E_C \ll 1$ corresponding to charge qubits (Nakamura, Pashkin, and Tsai, 1999), $E_J/E_C \sim 1$ corresponding to the quantrium (Vion *et al.*, 2002), and $E_J/E_C \gg 1$ corresponding to the transmon; see the reviews given by Makhlin, Schön, and Shnirman (2001), Zagoskin and Blais (2007), Clarke and Wilhelm (2008), and Kjaergaard, Schwartz *et al.* (2020). Regardless of the parameter regime, one can always express the Hamiltonian in the diagonal form $\hat{H} = \sum_j \hbar\omega_j |j\rangle\langle j|$ in

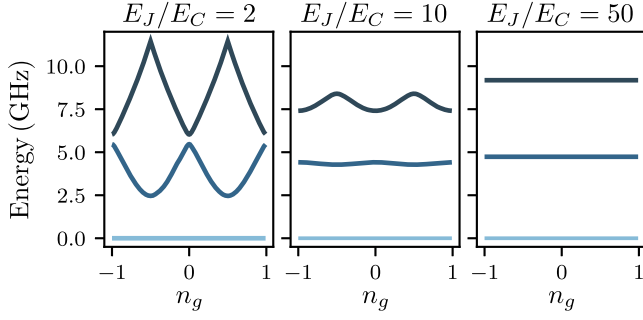


FIG. 6. Frequency difference $\omega_j - \omega_0$ of the first three energy levels of the transmon Hamiltonian obtained from numerical diagonalization of Eq. (22) expressed in the charge basis $\{|n\rangle\}$ for different E_J/E_C ratios and a fixed plasma frequency $\omega_p/2\pi = 5$ GHz. For large values of E_J/E_C the energy levels become insensitive to the offset charge n_g .

terms of its eigenfrequencies ω_j and eigenstates $|j\rangle$. In the literature, two notations are commonly used to label these eigenstates: $\{|g\rangle, |e\rangle, |f\rangle, |h\rangle, \dots\}$ and, when there is no risk of confusion with resonator Fock states, $\{|0\rangle, |1\rangle, |2\rangle, \dots\}$. Depending on the context, we use both notations in this review. Figure 6 shows the energy difference $E_{0j}/\hbar = \omega_j - \omega_0$ for the three lowest energy levels for different ratios E_J/E_C as obtained from numerical diagonalization of Eq. (22). If the charging energy dominates ($E_J/E_C < 1$), the eigenstates of the Hamiltonian are approximately given by eigenstates of the charge operator $|j\rangle \simeq |n\rangle$, with $\hat{n}|n\rangle = n|n\rangle$. In this situation, a change in gate charge n_g has a large impact on the transition frequency of the device. As a result, unavoidable charge fluctuations in the circuit's environment lead to fluctuations in the qubit transition frequency and, consequently, to dephasing.

To mitigate this problem, a solution is to work in the *transmon regime*, where, as previously alluded to, the ratio E_J/E_C is large, with typical values being $E_J/E_C \sim 20$ – 80 (Koch *et al.*, 2007; Schreier *et al.*, 2008). In this situation, the charge degree of freedom is highly delocalized due to the large Josephson energy. For this reason, as shown in Fig. 6(c), the first energy levels of the device become essentially independent of the gate charge. It can in fact be shown that the charge dispersion, which describes the variation of the energy levels with gate charge, decreases exponentially with E_J/E_C in the transmon regime (Koch *et al.*, 2007). The net result is that the coherence time of the device is much larger than at small E_J/E_C . However, as also shown in Fig. 6, the price to pay for this increased coherence is the reduced anharmonicity $\alpha = E_{12} - E_{01}$ of the transmon, anharmonicity that is required to control the qubit without causing unwanted transitions to higher excited states. While charge dispersion is exponentially small with E_J/E_C , the loss of anharmonicity has a much weaker dependence on this ratio given by $\sim (E_J/E_C)^{-1/2}$. As discussed in more detail in Sec. VII, because of the gain in coherence the reduction in anharmonicity is not an impediment to controlling the transmon state with high fidelity.

While the variance of the charge degree of freedom is large when $E_J/E_C \gg 1$, the variance of its conjugate variable $\hat{\phi}$ is

correspondingly small, with $\Delta\hat{\phi} = \sqrt{\langle\hat{\phi}^2\rangle - \langle\hat{\phi}\rangle^2} \ll 1$. In this situation, it is instructive to rewrite Eq. (22) as

$$\hat{H}_T = 4E_C\hat{n}^2 + \frac{1}{2}E_J\hat{\phi}^2 - E_J(\cos\hat{\phi} + \frac{1}{2}\hat{\phi}^2), \quad (23)$$

with the first two terms corresponding to an *LC* circuit of capacitance C_Σ and inductance $E_J^{-1}(\Phi_0/2\pi)^2$, the linear part of the Josephson inductance equation (20). We have dropped the offset charge n_g in Eq. (23) on the basis that the frequency of the relevant low-lying energy levels is insensitive to variations in n_g , it is still possible to use an external oscillating voltage source to cause a transition between the transmon states. We return to this later. The last term of Eq. (23) is the nonlinear correction to this harmonic potential, which for $E_J/E_C \gg 1$ and therefore $\Delta\hat{\phi} \ll 1$ can be truncated to its first nonlinear correction leading to the approximate transmon Hamiltonian

$$\hat{H}_q = 4E_C\hat{n}^2 + \frac{1}{2}E_J\hat{\phi}^2 - \frac{1}{4!}E_J\hat{\phi}^4. \quad (24)$$

As expected from the previous discussion, the transmon is thus a weakly anharmonic oscillator. Note that the 2π periodicity of the Hamiltonian is broken under this approximation.

Following Sec. II.A, it is then useful to introduce creation and annihilation operators chosen to diagonalize the first two terms of Eq. (24). Denoting these operators as \hat{b}^\dagger and \hat{b} , in analogy to Eq. (4) we have

$$\hat{\phi} = \left(\frac{2E_C}{E_J}\right)^{1/4} (\hat{b}^\dagger + \hat{b}), \quad (25)$$

$$\hat{n} = \frac{i}{2} \left(\frac{E_J}{2E_C}\right)^{1/4} (\hat{b}^\dagger - \hat{b}). \quad (26)$$

This form makes it clear that fluctuations of the phase $\hat{\phi}$ decrease with E_J/E_C , while the reverse is true for the conjugate charge \hat{n} . Using these expressions in Eq. (24) finally leads to¹

$$\begin{aligned} \hat{H}_q &= \sqrt{8E_CE_J}\hat{b}^\dagger\hat{b} - \frac{E_C}{12}(\hat{b}^\dagger + \hat{b})^4 \\ &\approx \hbar\omega_q\hat{b}^\dagger\hat{b} - \frac{E_C}{2}\hat{b}^\dagger\hat{b}^\dagger\hat{b}\hat{b}, \end{aligned} \quad (27)$$

where $\hbar\omega_q = \sqrt{8E_CE_J} - E_C$. On the second line, we have kept only the terms that have the same number of creation and annihilation operators. This is reasonable because, in a frame rotating at ω_q , any terms with an unequal number of \hat{b} and \hat{b}^\dagger will oscillate. If the frequency of these oscillations is larger than the prefactor of the oscillating term, then this term rapidly

¹The approximate Hamiltonian equation (27) is not bounded from below: an artifact of the truncation of the cosine operator. Care should therefore be taken when using this form, and it should strictly speaking be used only in a truncated subspace of the original Hilbert space.

averages out and can be neglected (Cohen-Tannoudji, Diu, and Laloe, 1977). This rotating-wave approximation (RWA) is valid here if $\hbar\omega_q \gg E_C/4$, an inequality that is easily satisfied in the transmon regime.

We can interpret Eq. (22) as describing an effective phase particle in a cosine potential, with the phase playing the role of position and C playing the role of mass. The plasma frequency $\omega_p = \sqrt{8E_C E_J}/\hbar$ corresponds to the frequency of small oscillations at the bottom of a well of the cosine potential. In the transmon regime, this frequency is renormalized by a ‘‘Lamb shift’’ equal to the charging energy E_C such that $\omega_q = \omega_p - E_C/\hbar$ is the transition frequency between the ground and first excited states. Finally, the last term of Eq. (27) is a Kerr nonlinearity, with E_C/\hbar playing the role of Kerr frequency shift per excitation of the nonlinear oscillator (Walls and Milburn, 2008). To see this more clearly, it can be useful to rewrite Eq. (27) as $H_q = \hbar\tilde{\omega}_q(\hat{b}^\dagger\hat{b})\hat{b}^\dagger\hat{b}$, where the frequency $\tilde{\omega}_q(\hat{b}^\dagger\hat{b}) = \omega_q - E_C(\hat{b}^\dagger\hat{b} - 1)/2\hbar$ of the oscillator is a decreasing function of the excitation number $\hat{b}^\dagger\hat{b}$. Considering only the first few levels of the transmon, this simply means that the e - f transition frequency is smaller by E_C than the g - e transition frequency; see Fig. 5(a). In other words, in the regime of validity of the approximation made to obtain Eq. (24), the anharmonicity of the transmon is $-E_C$, with typical values $E_C/\hbar \sim 100$ – 400 MHz (Koch *et al.*, 2007). Corrections to the anharmonicity from $-E_C$ can be obtained numerically or by keeping higher-order terms in the expansion of Eq. (24).

While the nonlinearity E_C/\hbar is small with respect to the oscillator frequency ω_q , it is in practice much larger than the spectral linewidth that can routinely be obtained for these artificial atoms and can therefore easily be spectrally resolved. As a result and in contrast to more traditional realizations of Kerr nonlinearities in quantum optics (Walls and Milburn, 2008), it is possible with superconducting quantum circuits to have a large Kerr nonlinearity even at the single-photon level. Some of the many implications of this observation are discussed further later in this review. For quantum information processing, the presence of this nonlinearity is necessary to address only the ground and first excited states without unwanted transition to other states. In this case, the transmon acts as a two-level system, or qubit. However, keep in mind that the transmon is a multilevel system and that it is often necessary to include higher levels in the description of the device to quantitatively explain experimental observations. These higher levels can also be used to considerable advantage in some cases (Rosenblum *et al.*, 2018; Elder *et al.*, 2020; Ma, Zhang *et al.*, 2020; Reinhold *et al.*, 2020).

E. Flux-tunable transmons

A useful variant of the transmon artificial atom is the flux-tunable transmon, where the single Josephson junction is replaced with two parallel junctions forming a superconducting quantum interference device (SQUID); see Fig. 5(c) (Koch *et al.*, 2007). The transmon Hamiltonian then reads

$$\hat{H}_T = 4E_C\hat{n}^2 - E_{J1}\cos\hat{\varphi}_1 - E_{J2}\cos\hat{\varphi}_2, \quad (28)$$

where E_{Ji} is the Josephson energy of junction i and $\hat{\varphi}_i$ is the phase difference across that junction. In the presence of an external flux Φ_x threading the SQUID loop and in the limit of small geometric inductance of the loop,² flux quantization requires that $\hat{\varphi}_1 - \hat{\varphi}_2 = 2\pi\Phi_x/\Phi_0 \pmod{2\pi}$ (Tinkham, 2004). Defining the average phase difference as $\hat{\varphi} = (\hat{\varphi}_1 + \hat{\varphi}_2)/2$, the Hamiltonian can then be rewritten as (Tinkham, 2004; Koch *et al.*, 2007)

$$\hat{H}_T = 4E_C\hat{n}^2 - E_J(\Phi_x)\cos(\hat{\varphi} - \varphi_0), \quad (29)$$

where

$$E_J(\Phi_x) = E_{J\Sigma}\cos\left(\frac{\pi\Phi_x}{\Phi_0}\right)\sqrt{1 + d^2\tan^2\left(\frac{\pi\Phi_x}{\Phi_0}\right)}, \quad (30)$$

with $E_{J\Sigma} = E_{J2} + E_{J1}$ and $d = (E_{J2} - E_{J1})/E_{J\Sigma}$ the junction asymmetry. The phase $\varphi_0 = d\tan(\pi\Phi_x/\Phi_0)$ can be ignored for a time-independent flux (Koch *et al.*, 2007). According to Eq. (29), replacing the single junction with a SQUID loop yields an effective flux-tunable Josephson energy $E_J(\Phi_x)$. In turn, this results in a flux-tunable transmon frequency $\omega_q(\Phi_x) = \sqrt{8E_C|E_J(\Phi_x)|} - E_C/\hbar$.³ In practice, the transmon frequency can be tuned by as much as 1 GHz in as little as 10–20 ns (DiCarlo *et al.*, 2009; Rol *et al.*, 2019, 2020). This possibility is exploited in several applications, including quantum logical gates, as discussed in more detail in Sec. VII.

As discussed later, this additional control knob can lead to dephasing due to noise in the flux threading the SQUID loop. With this in mind, it is worth noticing that transmon qubits with a finite asymmetry d can have a smaller range of tunability than symmetric transmons, and thus also made less susceptible to flux noise (Hutchings *et al.*, 2017). Finally, first steps toward realizing voltage tunable transmons where a semiconducting nanowire takes the place of the SQUID loop have been demonstrated (Casparis *et al.*, 2018; Luthi *et al.*, 2018).

F. Other superconducting qubits

While the transmon is currently the most extensively used and studied superconducting qubit, many other types of superconducting artificial atoms are used in the context of circuit QED. In addition to working with different ratios of E_J/E_C , these other qubits vary in the number of Josephson junctions and the topology of the circuit in which these junctions are embedded. This includes charge qubits (Shnirman, Schön, and Hermon, 1997; Bouchiat *et al.*, 1998; Nakamura, Pashkin, and Tsai, 1999), flux qubits (Mooij *et al.*, 1999; Orlando *et al.*, 1999) including variations

²If the geometric inductance is sufficiently small, we can neglect the dynamics of the high-frequency mode associated with oscillating circulating currents in the loop.

³The absolute value arises because, when expanding the Hamiltonian in powers of $\hat{\varphi}$ in Eq. (24), the potential energy term must always be expanded around a minimum. This discussion also assumes that the ratio $|E_J(\Phi_x)|/E_C$ is in the transmon range for all relevant Φ_x .

with a large shunting capacitance (You *et al.*, 2007; Yan *et al.*, 2016), phase qubits (Martinis *et al.*, 2002), the quantrium (Vion *et al.*, 2002), the fluxonium (Manucharyan *et al.*, 2009), the $0 - \pi$ qubit (Brooks, Kitaev, and Preskill, 2013; Gyenies *et al.*, 2021), the bifluxon (Kalashnikov *et al.*, 2020), and the blochonium (Pechenezhskiy *et al.*, 2020), among others. For more details about these different qubits, see reviews on the topic given by Makhlin, Schön, and Shnirman (2001), Zagoskin and Blais (2007), Clarke and Wilhelm (2008), Krantz *et al.* (2019), and Kjaergaard, Schwartz *et al.* (2020).

III. LIGHT-MATTER INTERACTION IN CIRCUIT QED

A. Exchange interaction between a transmon and an oscillator

Having introduced the two main characters of this review, the quantum harmonic oscillator and the transmon artificial atom, we are now ready to consider their interaction. Because of their large size coming from the requirement of having a low charging energy (large capacitance), transmon qubits can naturally be capacitively coupled to microwave resonators; see Fig. 7 for schematic representations. With the resonator taking the place of the classical voltage source V_g , capacitive coupling to a resonator can be introduced in the transmon Hamiltonian equation (22) with a dynamical gate voltage $n_g \rightarrow -\hat{n}_r$, representing the effective offset charge term of the transmon due to the quantum electric field operator of the resonator (the choice of sign is simply a common convention in the literature that we adopt here; see Appendix A). The Hamiltonian of the combined system is therefore (Blais *et al.*, 2004)

$$\hat{H} = 4E_C(\hat{n} + \hat{n}_r)^2 - E_J \cos \hat{\phi} + \sum_m \hbar \omega_m \hat{a}_m^\dagger \hat{a}_m, \quad (31)$$

where $\hat{n}_r = \sum_m \hat{n}_m$, with $\hat{n}_m = (C_g/C_m)\hat{Q}_m/2e$, is the contribution to the offset charge term due to the m th resonator mode. Here C_g is the gate capacitance and C_m is the associated resonator mode capacitance. To simplify these expressions, we assume here that $C_g \ll C_\Sigma, C_m$. A derivation of the Hamiltonian of Eq. (31) that goes beyond the simple replacement of n_g by $-\hat{n}_r$ and without the previous assumption is given in Appendix A for the case of a single LC oscillator coupled to the transmon.

Assuming that the transmon frequency is much closer to one of the resonator modes than all the other modes, say, $|\omega_0 - \omega_q| \ll |\omega_m - \omega_q|$ for $m \geq 1$, we truncate the sum over m in Eq. (31) to a single term. In this single-mode approximation, the Hamiltonian reduces to a single oscillator of frequency denoted ω_r coupled to a transmon. Note that, regardless of the physical nature of the oscillator (for example, a single mode of a 2D or 3D resonator), it is possible to represent this Hamiltonian with an equivalent circuit where the transmon is capacitively coupled to an LC oscillator, as illustrated in Fig. 7(b). This type of formal representation of complex geometries in terms of equivalent lumped-element circuits is generally known as “black-box quantization” (Nigg *et al.*, 2012) and is explored in more detail in Sec. III.D. As discussed in Sec. IV.E, despite the single-mode approximation being useful, there are many situations of experimental relevance where ignoring the multimode nature of the resonator leads to inaccurate predictions.

Using the creation and annihilation operators introduced in Secs. II.A and II.D, in the single-mode approximation Eq. (31) reduces to⁴

$$\begin{aligned} \hat{H} \approx & \hbar \omega_r \hat{a}^\dagger \hat{a} + \hbar \omega_q \hat{b}^\dagger \hat{b} - \frac{E_C}{2} \hat{b}^\dagger \hat{b}^\dagger \hat{b} \hat{b} \\ & - \hbar g (\hat{b}^\dagger - \hat{b}) (\hat{a}^\dagger - \hat{a}), \end{aligned} \quad (32)$$

where ω_r is the frequency of the mode of interest and

$$g = \omega_r \frac{C_g}{C_\Sigma} \left(\frac{E_J}{2E_C} \right)^{1/4} \sqrt{\frac{\pi Z_r}{R_K}}, \quad (33)$$

the oscillator-transmon, or light-matter, coupling constant. Here Z_r is the characteristic impedance of the resonator mode and $R_K = h/e^2 \sim 25.8 \text{ k}\Omega$ is the resistance quantum. The Hamiltonian (32) can be further simplified in the experimentally relevant situation where the coupling constant is much smaller than the system frequencies: $|g| \ll \omega_r, \omega_q$. Invoking the rotating-wave approximation, it simplifies to

⁴One might worry about the term \hat{n}_r^2 arising from Eq. (31). However, this term can be absorbed in the charging energy term of the resonator mode [see Eq. (1)] and therefore leads to a renormalization of the resonator frequency, which we omit here for simplicity. See Eqs. (A9) and (A10) for further details.

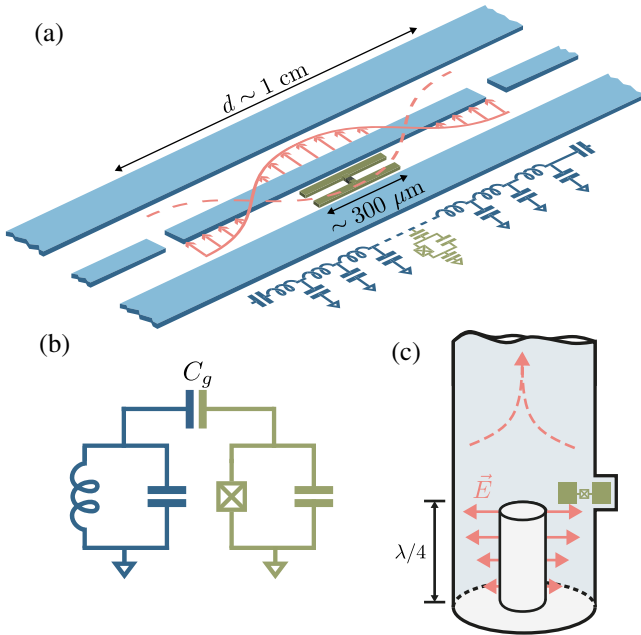


FIG. 7. Schematic representation of a transmon qubit (green) coupled to (a) a 1D transmission-line resonator, (b) a lumped-element LC circuit, and (c) a 3D coaxial cavity. (a) Adapted from Blais *et al.*, 2004. (c) Adapted from Reagor *et al.*, 2016.

$$\hat{H} \approx \hbar\omega_r \hat{a}^\dagger \hat{a} + \hbar\omega_q \hat{b}^\dagger \hat{b} - \frac{E_C}{2} \hat{b}^\dagger \hat{b}^\dagger \hat{b} \hat{b} + \hbar g (\hat{b}^\dagger \hat{a} + \hat{b} \hat{a}^\dagger). \quad (34)$$

As can be seen from Eq. (26), the prefactor $(E_J/2E_C)^{1/4}$ in Eq. (33) is linked to the size of charge fluctuations in the transmon. By introducing a length scale l corresponding to the distance a Cooper pair travels when tunneling across the transmon's junction, it is tempting to interpret Eq. (33) as $\hbar g = d_0 \mathcal{E}_0$, with $d_0 = 2el(E_J/32E_C)^{1/4}$ the dipole moment of the transmon and $\mathcal{E}_0 = (\omega_r/l)(C_g/C_\Sigma)\sqrt{\hbar Z_r/2}$ the resonator's zero-point electric field as seen by the transmon. Since these two factors can be made large, especially so in the transmon regime where $d_0 \gg 2el$, the electric-dipole interaction strength g can be made large, much more so than with natural atoms in cavity QED. It is also instructive to express Eq. (33) as

$$g = \omega_r \frac{C_g}{C_\Sigma} \left(\frac{E_J}{2E_C} \right)^{1/4} \sqrt{\frac{Z_r}{Z_{\text{vac}}}} \sqrt{2\pi\alpha}, \quad (35)$$

where $\alpha = Z_{\text{vac}}/2R_K$ is the fine-structure constant and $Z_{\text{vac}} = \sqrt{\mu_0/\epsilon_0} \sim 377 \Omega$ is the impedance of vacuum, with ϵ_0 the vacuum permittivity and μ_0 the vacuum permeability (Devoret, Girvin, and Schoelkopf, 2007). To find α here should not be surprising because this quantity characterizes the interaction between the electromagnetic field and charged particles. Here this interaction is reduced by the fact that both Z_r/Z_{vac} and C_g/C_Σ are smaller than unity. Large couplings can nevertheless be achieved by working with large values of E_J/E_C or, in other words, in the transmon regime. Large g is therefore obtained at the expense of reducing the transmon's relative anharmonicity $-E_C/\hbar\omega_q \simeq -\sqrt{E_C/8E_J}$. We note that the coupling can be increased by boosting the resonator's impedance, something that can be realized, for example, by replacing the resonator's center conductor with a junction array (Andersen and Blais, 2017; Stockklauser *et al.*, 2017).

Apart from a change in the details of the expression of the coupling g , the previous discussion holds for transmons coupled to lumped 2D or 3D resonators. By going from 2D to 3D, the resonator mode volume is made significantly larger, leading to a reduction in the vacuum fluctuations of the electric field. As first demonstrated by Paik *et al.* (2011), this can be made without change in the magnitude of g simply by making the transmon larger, thereby increasing its dipole moment. As illustrated in Fig. 7(c), the transmon then essentially becomes an antenna that is optimally placed within the 3D resonator to strongly couple to one of the resonator modes.

To strengthen the analogy with cavity QED even further, it is useful to restrict the description of the transmon to its first two levels. This corresponds to making the replacements $\hat{b}^\dagger \rightarrow \hat{\sigma}_+ = |e\rangle\langle g|$ and $\hat{b} \rightarrow \hat{\sigma}_- = |g\rangle\langle e|$ in Eq. (32) to obtain the well-known Jaynes-Cummings Hamiltonian (Blais *et al.*, 2004; Haroche and Raimond, 2006)

$$\hat{H}_{\text{JC}} = \hbar\omega_r \hat{a}^\dagger \hat{a} + \frac{\hbar\omega_q}{2} \hat{\sigma}_z + \hbar g (\hat{a}^\dagger \hat{\sigma}_- + \hat{a} \hat{\sigma}_+), \quad (36)$$

where we use the convention $\hat{\sigma}_z = |e\rangle\langle e| - |g\rangle\langle g|$. The last term of this Hamiltonian describes the coherent exchange of a single quantum between light and matter, here realized as a photon in the oscillator or an excitation of the artificial atom.

B. The Jaynes-Cummings spectrum

The Jaynes-Cummings Hamiltonian is an exactly solvable model that accurately describes many situations in which an atom, artificial or natural, can be considered a two-level system in interaction with a single mode of the electromagnetic field. This model can yield qualitative agreement with experiments in situations where only the first two levels of the transmon ($|\sigma = \{g, e\}\rangle$) play an important role. It is often the case, however, that quantitative agreement between theoretical predictions and experiments is obtained only when accounting for higher transmon energy levels and the multimode nature of the field. Nevertheless, since a great deal of insight can be gained, in this section we consider the Jaynes-Cummings model more closely.

In the absence of the coupling g , the *bare* states of the qubit-field system are labeled $|\sigma, n\rangle$ with σ as previously defined and n the photon number. The *dressed* eigenstates of the Jaynes-Cummings Hamiltonian $|\bar{\sigma}, \bar{n}\rangle = \hat{U}^\dagger |\sigma, n\rangle$ can be obtained from these bare states using the Bogoliubov-like unitary transformation (Carbonaro, Compagno, and Persico, 1979; Boissonneault, Gambetta, and Blais, 2009)

$$\hat{U} = \exp[\Lambda(\hat{N}_T)(\hat{a}^\dagger \hat{\sigma}_- - \hat{a} \hat{\sigma}_+)], \quad (37)$$

where we define

$$\Lambda(\hat{N}_T) = \frac{\arctan(2\lambda\sqrt{\hat{N}_T})}{2\sqrt{\hat{N}_T}}. \quad (38)$$

Here $\hat{N}_T = \hat{a}^\dagger \hat{a} + \hat{\sigma}_+ \hat{\sigma}_-$ is the operator associated with the total number of excitations, which commutes with \hat{H}_{JC} , and $\lambda = g/\Delta$, with $\Delta = \omega_q - \omega_r$ the qubit-resonator detuning. Under this transformation, \hat{H}_{JC} takes the diagonal form

$$\begin{aligned} \hat{H}_D &= \hat{U}^\dagger \hat{H}_{\text{JC}} \hat{U} \\ &= \hbar\omega_r \hat{a}^\dagger \hat{a} + \frac{\hbar\omega_q}{2} \hat{\sigma}_z - \frac{\hbar\Delta}{2} \left(1 - \sqrt{1 + 4\lambda^2 \hat{N}_T} \right) \hat{\sigma}_z. \end{aligned} \quad (39)$$

The dressed-state energies can be read directly from Eq. (39) and, as illustrated in Fig. 8, the Jaynes-Cummings spectrum consists of doublets $\{|\bar{g}, \bar{n}\rangle, |e, n-1\rangle\}$ of fixed excitation number⁵

⁵To arrive at these expressions, we add $\hbar\omega_r/2$ to \hat{H}_D . This global energy shift is without consequences.

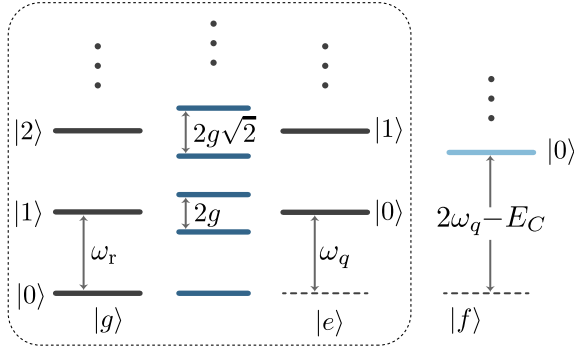


FIG. 8. Box: energy spectrum of the uncoupled (gray lines) and dressed (blue lines) states of the Jaynes-Cummings Hamiltonian at zero detuning: $\Delta = \omega_q - \omega_r = 0$. Transmon states are labeled $\{|g\rangle, |e\rangle\}$, while photon numbers in the cavity are labeled $|n = 0, 1, 2, \dots\rangle$ and plotted vertically. The degeneracy of the two-dimensional manifolds of states with n quanta is lifted by $2g\sqrt{n}$ by the electric-dipole coupling. The light blue line outside of the main box represents the third excited state of the transmon, labeled $|f\rangle$. Although it is not illustrated here, the presence of this level shifts the dressed states in the manifolds with $n \geq 2$ quanta (Fink *et al.*, 2008).

$$\begin{aligned} E_{\bar{g},n} &= \hbar n \omega_r - \frac{\hbar}{2} \sqrt{\Delta^2 + 4g^2 n}, \\ E_{\bar{e},n-1} &= \hbar n \omega_r + \frac{\hbar}{2} \sqrt{\Delta^2 + 4g^2 n}, \end{aligned} \quad (40)$$

and of the ground state $|\bar{g}, 0\rangle = |g, 0\rangle$ of energy $E_{\bar{g},0} = -\hbar\omega_q/2$. The excited dressed states are

$$\begin{aligned} |\bar{g}, n\rangle &= \cos(\theta_n/2)|g, n\rangle - \sin(\theta_n/2)|e, n-1\rangle, \\ |\bar{e}, n-1\rangle &= \sin(\theta_n/2)|g, n\rangle + \cos(\theta_n/2)|e, n-1\rangle, \end{aligned} \quad (41)$$

with $\theta_n = \arctan(2g\sqrt{n}/\Delta)$.

A crucial feature of the energy spectrum of Eq. (40) is the scaling with the photon number n . In particular, for zero detuning ($\Delta = 0$) the energy levels $E_{\bar{g},n}$ and $E_{\bar{e},n-1}$ are split by $2g\sqrt{n}$. This is in contrast to coupled harmonic oscillators where the energy splitting is independent of n . Experimentally probing this spectrum thus constitutes a way to assess the quantum nature of the coupled system (Carmichael, Kochan, and Sanders, 1996; Fink *et al.*, 2008). We return to this and related features of the spectrum in Sec. VI.A.

C. Dispersive regime

On resonance ($\Delta = 0$), the dressed states in Eq. (41) are maximally entangled qubit-resonator states, implying that the qubit is, by itself, never in a well-defined state; i.e., the reduced state of the qubit found by tracing over the resonator is not pure. For quantum information processing, it is therefore more practical to work in the dispersive regime where the qubit-resonator detuning is large with respect to the coupling strength: $|\lambda| = |g/\Delta| \ll 1$. In this case, the coherent exchange of quanta between the two systems described by the last term of \hat{H}_{JC} is not resonant, and interactions take place only via virtual photon processes. Qubit and resonator are therefore

only weakly entangled and a simplified model obtained later from second-order perturbation theory is often an excellent approximation. As the virtual processes can involve higher energy levels of the transmon, it is, however, crucial to account for its multilevel nature. For this reason, our starting point will be the Hamiltonian of Eq. (34) and not its two-level approximation in Eq. (36). For the same reason, the results obtained here are applicable only to the transmon. The energy level structure of other superconducting qubits can lead to significantly different expressions than those obtained next.

1. Schrieffer-Wolff approach

To find an approximation to Eq. (34) valid in the dispersive regime, we perform a Schrieffer-Wolff transformation to second order (Blais *et al.*, 2004; Koch *et al.*, 2007). As shown in Appendix B, as long as the interaction term in Eq. (34) is sufficiently small, the resulting effective Hamiltonian is well approximated by

$$\begin{aligned} \hat{H}_{\text{disp}} &\simeq \hbar\omega_r \hat{a}^\dagger \hat{a} + \hbar\omega_q \hat{b}^\dagger \hat{b} - \frac{E_C}{2} \hat{b}^\dagger \hat{b}^\dagger \hat{b} \hat{b} \\ &+ \sum_{j=0}^{\infty} \hbar(\Lambda_j + \chi_j \hat{a}^\dagger \hat{a}) |j\rangle \langle j|, \end{aligned} \quad (42)$$

where $|j\rangle$ label the eigenstates of the transmon that, under the approximation used to obtain Eq. (27), are just the eigenstates of the number operator $\hat{b}^\dagger \hat{b}$. Moreover, we have defined

$$\Lambda_j = \chi_{j-1,j}, \quad \chi_j = \chi_{j-1,j} - \chi_{j,j+1}, \quad (43a)$$

$$\chi_{j-1,j} = \frac{jg^2}{\Delta - (j-1)E_C/\hbar}, \quad (43b)$$

for $j > 0$ and with $\Lambda_0 = 0$, $\chi_0 = -g^2/\Delta$. Here the χ_j 's are known as dispersive shifts, while the Λ_j 's are Lamb shifts and are signatures of vacuum fluctuations (Bethe, 1947; Lamb and Retherford, 1947; Fragner *et al.*, 2008).

Truncating Eq. (42) to the first two levels of the transmon leads to the more standard form of the dispersive Hamiltonian (Blais *et al.*, 2004)

$$\hat{H}_{\text{disp}} \approx \hbar\omega'_r \hat{a}^\dagger \hat{a} + \frac{\hbar\omega'_q}{2} \hat{\sigma}_z + \hbar\chi \hat{a}^\dagger \hat{a} \hat{\sigma}_z, \quad (44)$$

where χ is the qubit-state-dependent dispersive cavity shift with (Koch *et al.*, 2007)

$$\begin{aligned} \omega'_r &= \omega_r - \frac{g^2}{\Delta - E_C/\hbar}, & \omega'_q &= \omega_q + \frac{g^2}{\Delta}, \\ \chi &= -\frac{g^2 E_C/\hbar}{\Delta(\Delta - E_C/\hbar)}. \end{aligned} \quad (45)$$

These dressed frequencies are what are measured experimentally in the dispersive regime and it is important to emphasize that the frequencies entering the right-hand sides of Eq. (45) are the bare qubit and resonator frequencies. The spectrum of this two-level dispersive Hamiltonian is illustrated in Fig. 9. Much of this review is devoted to the consequences of this

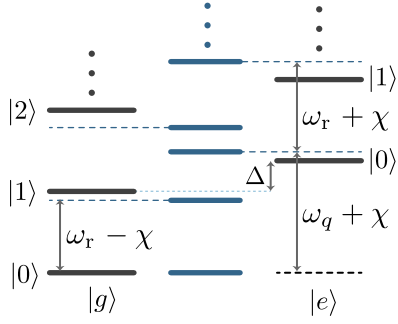


FIG. 9. Energy spectrum of the uncoupled (gray lines) and dressed states in the dispersive regime (blue lines). The two lowest transmon states are labeled $\{|g\rangle, |e\rangle\}$, while photon numbers in the cavity are labeled $|n = 0, 1, 2, \dots\rangle$ and are plotted vertically. In the dispersive regime, the g - e transition frequency of the qubit in the absence of resonator photons is Lamb shifted and takes the value $\omega_q + \chi$. Moreover, the cavity frequency is pulled by its interaction with the qubit and takes the qubit-state-dependent value $\omega_r \pm \chi$.

dispersive Hamiltonian for qubit readout and quantum information processing. We note that the Schrieffer-Wolff transformation also gives rise to resonator and qubit self-Kerr nonlinearities at fourth order (Zhu *et al.*, 2013).

As mentioned, the previous perturbative results are valid when the interaction term in Eq. (34) is sufficiently small relative to the energy splitting of the bare transmon-oscillator energy levels: $|\lambda| = |g/\Delta| \ll 1$. Because the matrix elements of the operators involved in the interaction term scale with the number of photons in the resonator and the number of qubit excitations, a more precise bound on the validity of Eq. (42) needs to take these quantities into account. As discussed in Appendix B.2.a, we find that for the previously mentioned second-order perturbative results to be a good approximation, the oscillator photon number \bar{n} should be much smaller than a critical photon number n_{crit} :

$$\bar{n} \ll n_{\text{crit}} \equiv \frac{1}{2j+1} \left(\frac{|\Delta - jE_C/\hbar|^2}{4g^2} - j \right), \quad (46)$$

where $j = 0, 1, \dots$ refers to the qubit state as before. For $j = 0$, this yields the familiar value $n_{\text{crit}} = (\Delta/2g)^2$ for the critical photon number expected from the Jaynes-Cummings model (Blais *et al.*, 2004), while setting $j = 1$ gives a more conservative bound. In either case, this gives only an approximate estimate for when to expect higher-order effects to become important.

It is worth contrasting Eq. (45) with the results expected from performing a dispersive approximation to the Jaynes-Cummings model (36), which leads to $\chi = g^2/\Delta$; see Appendix B.2.b (Blais *et al.*, 2004; Boissonneault, Gambetta, and Blais, 2010). This agrees with the previous result in the limit of large E_C , but, since E_C/\hbar is typically small compared to Δ in most transmon experiments, the two-level system Jaynes-Cummings model gives a poor prediction for the dispersive shift χ in practice. The intuition here is that E_C determines the anharmonicity of the transmon. Two coupled harmonic oscillators can shift each other's frequencies, but only

in a state-independent manner. Thus the dispersive shift must vanish in the limit of E_C going to zero.

2. Bogoliubov approach

We now present an approach to arrive at Eq. (44) that can be simpler than performing a Schrieffer-Wolff transformation and that is often used in the circuit QED literature.

To proceed, it is convenient to write Eq. (34) as the sum of a linear and a nonlinear part ($\hat{H} = \hat{H}_{\text{lin}} + \hat{H}_{\text{nl}}$), where

$$\hat{H}_{\text{lin}} = \hbar\omega_r \hat{a}^\dagger \hat{a} + \hbar\omega_q \hat{b}^\dagger \hat{b} + \hbar g(\hat{b}^\dagger \hat{a} + \hat{b} \hat{a}^\dagger), \quad (47)$$

$$\hat{H}_{\text{nl}} = -\frac{E_C}{2} \hat{b}^\dagger \hat{b}^\dagger \hat{b} \hat{b}. \quad (48)$$

The linear part \hat{H}_{lin} can be diagonalized exactly using the Bogoliubov transformation

$$\hat{U}_{\text{disp}} = \exp[\Lambda(\hat{a}^\dagger \hat{b} - \hat{a} \hat{b}^\dagger)]. \quad (49)$$

Under this unitary, the annihilation operators transform as $\hat{U}_{\text{disp}}^\dagger \hat{a} \hat{U}_{\text{disp}} = \cos(\Lambda) \hat{a} + \sin(\Lambda) \hat{b}$ and $\hat{U}_{\text{disp}}^\dagger \hat{b} \hat{U}_{\text{disp}} = \cos(\Lambda) \hat{b} - \sin(\Lambda) \hat{a}$. With the choice $\Lambda = (1/2) \arctan(2\lambda)$, this results in the diagonal form

$$\hat{U}_{\text{disp}}^\dagger \hat{H}_{\text{lin}} \hat{U}_{\text{disp}} = \hbar\tilde{\omega}_r \hat{a}^\dagger \hat{a} + \hbar\tilde{\omega}_q \hat{b}^\dagger \hat{b}, \quad (50)$$

with the dressed frequencies

$$\tilde{\omega}_r = \frac{1}{2}(\omega_r + \omega_q - \sqrt{\Delta^2 + 4g^2}), \quad (51a)$$

$$\tilde{\omega}_q = \frac{1}{2}(\omega_r + \omega_q + \sqrt{\Delta^2 + 4g^2}). \quad (51b)$$

Applying the same transformation to \hat{H}_{nl} and, in the dispersive regime, expanding the result in orders of λ lead to the dispersive Hamiltonian (see Appendix B.3)

$$\begin{aligned} \hat{H}_{\text{disp}} &= \hat{U}_{\text{disp}}^\dagger \hat{H} \hat{U}_{\text{disp}} \\ &\simeq \hbar\tilde{\omega}_r \hat{a}^\dagger \hat{a} + \hbar\tilde{\omega}_q \hat{b}^\dagger \hat{b} \\ &\quad + \frac{\hbar K_a}{2} \hat{a}^\dagger \hat{a}^\dagger \hat{a} \hat{a} + \frac{\hbar K_b}{2} \hat{b}^\dagger \hat{b}^\dagger \hat{b} \hat{b} + \hbar\chi_{ab} \hat{a}^\dagger \hat{a} \hat{b}^\dagger \hat{b}, \end{aligned} \quad (52)$$

where we introduce

$$\begin{aligned} K_a &\simeq -\frac{E_C}{\hbar} \left(\frac{g}{\Delta} \right)^4, & K_b &\simeq -E_C/\hbar, \\ \chi_{ab} &\simeq -2 \frac{g^2 E_C/\hbar}{\Delta(\Delta - E_C/\hbar)}. \end{aligned} \quad (53)$$

The first two of these quantities are self-Kerr nonlinearities, while the third is a cross-Kerr interaction. All are negative in the dispersive regime. As discussed in Appendix B.3, the expression for χ_{ab} in Eq. (53) is obtained after performing a Schrieffer-Wolff transformation to eliminate a term of the form $\hat{b}^\dagger \hat{b} \hat{a}^\dagger \hat{b} + \text{H.c.}$ that results from applying U_{disp} on H_{nl} . Higher-order terms in λ and other terms rotating at frequency

Δ or faster have been dropped to arrive at Eq. (52). These terms are given in Eq. (B33).

Truncating Eq. (52) to the first two levels of the transmon correctly leads to Eqs. (44) and (45). These expressions are not valid if the excitation number of the resonator or the transmon is too large or if $|\Delta| \sim E_C/\hbar$. Indeed, the regime $0 < \Delta < E_C$, known as the straddling regime, is qualitatively different from the usual dispersive regime. It is characterized by positive self-Kerr and cross-Kerr nonlinearities ($K_a, \chi_{ab} > 0$) and is better addressed by exact numerical diagonalization of Eq. (31) (Koch *et al.*, 2007).

An interesting feature of circuit QED is the large nonlinearities that are achievable in the dispersive regime. Dispersive shifts larger than the resonator or qubit linewidth ($\chi > \kappa, \gamma$) are readily realized in experiments, a regime referred to as strong-dispersive coupling (Gambetta *et al.*, 2006; Schuster *et al.*, 2007). Some of the consequences of this regime are discussed in Sec. VI.B. It is also possible to achieve large self-Kerr nonlinearities for the resonator: $|K_a| > \kappa$.⁶ These nonlinearities can be enhanced by embedding Josephson junctions in the center conductor of the resonator (Bourassa *et al.*, 2012; Ong *et al.*, 2013), an approach that is used in quantum-limited parametric amplifiers (Castellanos-Beltran *et al.*, 2008) and in the preparation of quantum states of the microwave electromagnetic field (Kirchmair *et al.*, 2013; Holland *et al.*, 2015; Puri, Boutin, and Blais, 2017).

D. Josephson junctions embedded in multimode electromagnetic environments

Thus far we have focused on the capacitive coupling of a transmon to a single mode of an oscillator. For many situations of experimental relevance it is, however, necessary to consider the transmon, or even multiple transmons, embedded in an electromagnetic environment with a possibly complex geometry, such as a 3D cavity.

Consider the situation depicted in Fig. 10(a), where a capacitively shunted Josephson junction is embedded in some electromagnetic environment represented by the impedance $Z(\omega)$. To keep the discussion simple, we consider here a single junction but the procedure can easily be extended to multiple junctions. As discussed in Sec. II.D, the Hamiltonian of the shunted junction [Eq. (23)] can be decomposed into the sum of a linear contribution of capacitance $C_\Sigma = C_S + C_J$ and linear inductance $L_J = E_J^{-1}(\Phi_0/2\pi)^2$, and a purely nonlinear contribution. This decomposition is illustrated in Fig. 10(b), where the spider symbol represents the nonlinear contribution (Manucharyan *et al.*, 2007; Bourassa *et al.*, 2012).

We assume that the electromagnetic environment is linear and nonmagnetic and has no free charges and currents. Since C_Σ and L_J are themselves linear elements, we consider them part of the electromagnetic environment too, which is illustrated by the box in Fig. 10(b). Combining all linear contributions, we write a Hamiltonian for the entire system—junction plus the surrounding electromagnetic environment—as $\hat{H} = \hat{H}_{\text{lin}} + \hat{H}_{\text{nl}}$ where

⁶The transmon is itself an oscillator with a large self-Kerr given by $\hbar K_b = -E_C$.

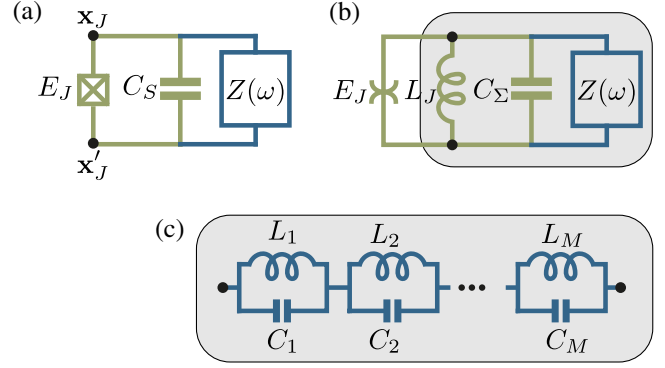


FIG. 10. (a) Transmon qubit coupled to an arbitrary impedance, such as that realized by a 3D microwave cavity. (b) The Josephson junction can be represented as a capacitive element C_J and a linear inductive element L_J in parallel with a purely nonlinear element that is indicated by the spiderlike symbol. Here $C_\Sigma = C_S + C_J$ is the parallel combination of the Josephson capacitance and the shunting capacitance of the transmon. (c) Normal mode decomposition of the parallel combination of the impedance $Z(\omega)$ together with L_J and C_Σ represented by effective LC circuits.

$$\hat{H}_{\text{nl}} = -E_J(\cos \hat{\varphi} + \frac{1}{2}\hat{\varphi}^2) \quad (54)$$

is the nonlinear part of the transmon Hamiltonian introduced in Eq. (23). A good strategy is to first diagonalize the linear part \hat{H}_{lin} , which can in principle be done much as was done in Sec. III.C. Subsequently, the phase difference $\hat{\varphi}$ across the junction can be expressed as a linear combination of the eigenmodes of \hat{H}_{lin} , a decomposition that is then used in \hat{H}_{nl} .

A convenient choice of canonical fields for the electromagnetic environment is the electric displacement field $\hat{\mathbf{D}}(\mathbf{x})$ and the magnetic field $\hat{\mathbf{B}}(\mathbf{x})$, which can be expressed in terms of bosonic creation and annihilation operators (Bhat and Sipe, 2006)

$$\hat{\mathbf{D}}(\mathbf{x}) = \sum_m [\mathbf{D}_m(\mathbf{x})\hat{a}_m + \text{H.c.}], \quad (55a)$$

$$\hat{\mathbf{B}}(\mathbf{x}) = \sum_m [\mathbf{B}_m(\mathbf{x})\hat{a}_m + \text{H.c.}], \quad (55b)$$

where $[\hat{a}_m, \hat{a}_n^\dagger] = \delta_{mn}$. The more commonly used electric field is related to the displacement field through $\hat{\mathbf{D}}(\mathbf{x}) = \epsilon_0 \hat{\mathbf{E}}(\mathbf{x}) + \hat{\mathbf{P}}(\mathbf{x})$, where $\hat{\mathbf{P}}(\mathbf{x})$ is the polarization of the medium. Moreover, the mode functions $\mathbf{D}_m(\mathbf{x})$ and $\mathbf{B}_m(\mathbf{x})$ can be chosen to satisfy orthogonality and normalization conditions such that

$$\hat{H}_{\text{lin}} = \sum_m \hbar \omega_m \hat{a}_m^\dagger \hat{a}_m. \quad (56)$$

In Eqs. (55) and (56), we implicitly assume that the eigenmodes form a discrete set. If some part of the spectrum is continuous, which is the case for infinite systems such as open waveguides, the sums must be replaced by integrals over the relevant frequency ranges. The result is general, holds for

arbitrary geometries, and can include inhomogeneities such as partially reflecting mirrors and materials with dispersion (Bhat and Sipe, 2006). We restrict ourselves, however, to discrete spectra in the following.

Diagonalizing \hat{H}_{lin} amounts to determining the mode functions $\{\hat{\mathbf{D}}_m(\mathbf{x}), \hat{\mathbf{B}}_m(\mathbf{x})\}$, which is essentially a classical electromagnetism problem that can be approached using numerical software such as finite element solvers (Minev *et al.*, 2020). Assuming that the mode functions have been found, we now turn to \hat{H}_{nl} , for which we relate $\hat{\varphi}$ to the bosonic operators \hat{a}_m . This can be done by noting again that $\hat{\varphi}(t) = 2\pi \int dt' \hat{V}(t')/\Phi_0$, where the voltage is simply the line integral of the electric field $\hat{V}(t) = \int d\mathbf{l} \cdot \hat{\mathbf{E}}(\mathbf{x}) = \int d\mathbf{l} \cdot \hat{\mathbf{D}}(\mathbf{x})/\epsilon$ across the junction (Vool *et al.*, 2016). Consequently, the phase variable can be expressed as

$$\hat{\varphi} = \sum_m [\varphi_m \hat{a}_m + \text{H.c.}], \quad (57)$$

where $\varphi_m = i(2\pi/\Phi_0) \int_{\mathbf{x}'_j}^{\mathbf{x}_j} d\mathbf{l} \cdot \mathbf{D}_m(\mathbf{x})/\omega_m \epsilon$ is the dimensionless magnitude of the zero-point fluctuations of the m th mode, as seen by the junction and the boundary conditions defined as in Fig. 10(a).

Using Eq. (57) in \hat{H}_{nl} we expand the cosine to fourth order in analogy with Eq. (24). This means that we are assuming that the capacitively shunted junction is well into the transmon regime, with a small anharmonicity relative to the Josephson energy. Focusing on the dispersive regime where all eigenfrequencies ω_m are sufficiently well separated, and neglecting fast-rotating terms in analogy with Sec. III.C leads to

$$\begin{aligned} \hat{H}_{\text{nl}} \simeq & \sum_m \hbar \Delta_m \hat{a}_m^\dagger \hat{a}_m + \frac{1}{2} \sum_m \hbar K_m (\hat{a}_m^\dagger)^2 \hat{a}_m^2, \\ & + \sum_{m>n} \hbar \chi_{m,n} \hat{a}_m^\dagger \hat{a}_m \hat{a}_n^\dagger \hat{a}_n, \end{aligned} \quad (58)$$

where $\Delta_m = (1/2) \sum_n \chi_{m,n}$, $K_m = \chi_{m,m}/2$, and

$$\hbar \chi_{m,n} = -E_J \varphi_m^2 \varphi_n^2. \quad (59)$$

It is also useful to introduce the energy participation ratio p_m , defined as the fraction of the total inductive energy of mode m that is stored in the junction $p_m = (2E_J/\hbar\omega_m)\varphi_m^2$ such that we can write (Minev *et al.*, 2020)

$$\chi_{m,n} = -\frac{\hbar\omega_m\omega_n}{4E_J} p_m p_n. \quad (60)$$

As is clear from the previous discussion, finding the nonlinear Hamiltonian can be reduced to finding the eigenmodes of the system and the zero-point fluctuations of each mode across the junction. Finding the mode frequencies ω_m and zero-point fluctuations φ_m , or alternatively the energy participation ratios p_m , can be complicated for a complex geometry. As mentioned this is, however, an entirely classical electromagnetism problem that can be handled numerically (Bhat and Sipe, 2006; Minev *et al.*, 2020).

An alternative approach is to represent the linear electromagnetic environment seen by the purely nonlinear element as an impedance $Z(\omega)$, as illustrated in Fig. 10(c). Neglecting loss, any such impedance can be represented by an equivalent circuit of possibly infinitely many LC oscillators connected in series. The eigenfrequencies $\hbar\omega_m = 1/\sqrt{L_m C_m}$, can be determined by the real parts of the zeros of the admittance $Y(\omega) = Z^{-1}(\omega)$, and the effective impedance of the m th mode as seen by the junction can be found from $Z_m^{\text{eff}} = 2/\omega_m \text{Im}Y'(\omega_m)$ (Nigg *et al.*, 2012; Solgun, Abraham, and DiVincenzo, 2014). The effective impedance is related to the previously used zero-point fluctuations as $Z_m^{\text{eff}} = 2(\Phi_0/2\pi)^2 \varphi_m^2/\hbar = R_K \varphi_m^2/(4\pi)$. From this point of view, the quantization procedure thus reduces to the task of determining the impedance $Z(\omega)$ as a function of frequency.

E. Beyond the transmon: Multilevel artificial atom

Thus far we have relied on a perturbative expansion of the cosine potential of the transmon under the assumption that $E_J/E_C \gg 1$. To go beyond this regime one can instead resort to exact diagonalization of the transmon Hamiltonian. Returning to the full transmon-resonator Hamiltonian in Eq. (31), we write (Koch *et al.*, 2007)

$$\begin{aligned} \hat{H} &= 4E_C \hat{n}^2 - E_J \cos \hat{\varphi} + \hbar\omega_r \hat{a}^\dagger \hat{a} + 8E_C \hat{n} \hat{n}_r \\ &= \sum_j \hbar\omega_j |j\rangle \langle j| + \hbar\omega_r \hat{a}^\dagger \hat{a} + i \sum_{ij} \hbar g_{ij} |i\rangle \langle j| (\hat{a}^\dagger - \hat{a}), \end{aligned} \quad (61)$$

where $|j\rangle$ are now the eigenstates of the bare transmon Hamiltonian $\hat{H}_t = 4E_C \hat{n}^2 - E_J \cos \hat{\varphi}$ obtained from numerical diagonalization and we define

$$\hbar g_{ij} = 2e \frac{C_g}{CC_\Sigma} Q_{\text{zpf}} \langle i|\hat{n}|j\rangle. \quad (62)$$

The eigenfrequencies ω_j and the matrix elements $\langle i|\hat{n}|j\rangle$ can be computed numerically in the charge basis, an approach that is applicable to other superconducting qubits. Alternatively, these expressions can be determined by taking advantage of the fact that, in the phase basis $\hat{\varphi}|\varphi\rangle = \varphi|\varphi\rangle$, Eq. (22) takes the form of a Mathieu equation whose exact solution is known (Cottet, 2002; Koch *et al.*, 2007).

The second form of Eq. (61) written in terms of energy eigenstates $|j\rangle$ is a general Hamiltonian that can describe an arbitrary multilevel artificial atom capacitively coupled to a resonator. As in the discussion in Sec. III.C, in the dispersive regime where $|g_{ij}|\sqrt{n+1} \ll |\omega_i - \omega_j - \omega_r|$ for all relevant atomic transitions $i \leftrightarrow j$ and with n the oscillator photon number, it is possible to use a Schrieffer-Wolff transformation to approximately diagonalize Eq. (61). As discussed in Appendix B.2, to second order one finds that (Zhu *et al.*, 2013)

$$\hat{H} \simeq \sum_j \hbar(\omega_j + \Lambda_j) |j\rangle \langle j| + \hbar\omega_r \hat{a}^\dagger \hat{a} + \sum_j \hbar \chi_j \hat{a}^\dagger \hat{a} |j\rangle \langle j|, \quad (63)$$

where

$$\Lambda_j = \sum_i \frac{|g_{ij}|^2}{\omega_j - \omega_i - \omega_r}, \quad (64a)$$

$$\chi_j = \sum_i \left(\frac{|g_{ij}|^2}{\omega_j - \omega_i - \omega_r} - \frac{|g_{ij}|^2}{\omega_i - \omega_j - \omega_r} \right). \quad (64b)$$

This result is, as previously stated, general, and it can be used with a variety of artificial atoms coupled to a resonator in the dispersive limit. Higher-order expressions were given by Boissonneault, Gambetta, and Blais (2010) and Zhu *et al.* (2013).

F. Alternative coupling schemes

Coupling the electric-dipole moment of a qubit to the zero-point electric field of an oscillator via a capacitor is the most common approach to light-matter coupling in a circuit, but it is not the only possibility. Another approach is to take advantage of the mutual inductance between a flux qubit and the center conductor of a resonator to couple the qubit's magnetic dipole to the resonator's magnetic field. A stronger interaction can be obtained by galvanically connecting the flux qubit to the center conductor of a transmission-line resonator (Bourassa *et al.*, 2009). In such a situation, the coupling can be engineered to approach, or even be larger, than the system frequencies allowing to reach what is known as the ultra-strong-coupling regime; see Sec. VI.C.

Yet another approach is to couple the qubit to the oscillator in such a way that the resonator field does not result in qubit transitions but instead only shifts the qubit's frequency. This is known as longitudinal coupling and is represented by the Hamiltonian (Kerman, 2013; Billangeon, Tsai, and Nakamura, 2015a, 2015b; Didier, Bourassa, and Blais, 2015; Richer and DiVincenzo, 2016; Richer *et al.*, 2017)

$$\hat{H}_z = \hbar\omega_r \hat{a}^\dagger \hat{a} + \frac{\hbar\omega_q}{2} \hat{\sigma}_z + \hbar g_z (\hat{a}^\dagger + \hat{a}) \hat{\sigma}_z. \quad (65)$$

Because the light-matter interaction in \hat{H}_z is proportional to $\hat{\sigma}_z$ rather than $\hat{\sigma}_x$, the longitudinal interaction does not lead to dressing of the qubit by a resonator field of the form discussed in Sec. III.B. Some of the consequences of this observation, particularly for qubit readout, are discussed in Sec. V.C.3.

IV. COUPLING TO THE ENVIRONMENT

Thus far we have dealt with isolated quantum systems. A complete description of quantum electrical circuits, however, must also take into account a description of how these systems couple to their environment, including any measurement apparatus and control circuitry. In fact, the environment plays a dual role in quantum technology: Not only is a description of quantum systems as perfectly isolated unrealistic, as coupling to unwanted environmental degrees of freedom is unavoidable, but a perfectly isolated system would also not be useful since we would have no means of controlling or observing it. For these reasons, in this section we consider quantum systems coupled to external transmission lines. We also

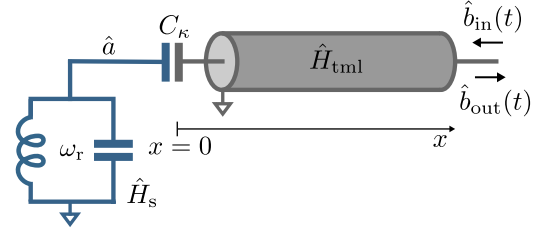


FIG. 11. LC circuit capacitively coupled to a semi-infinite transmission line used to model both damping and driving of the system. Here $\hat{b}_{\text{in}}(t)$ and $\hat{b}_{\text{out}}(t)$ are the oscillator's input and output fields, respectively.

introduce the input-output theory, which is of central importance in understanding qubit readout in circuit QED in Sec. V.

A. Wiring up quantum systems with transmission lines

We start the discussion by considering transmission lines coupled to individual quantum systems, which are a model for losses and can be used to apply and receive quantum signals for control and measurement. To be specific, we consider a semi-infinite coplanar waveguide transmission line capacitively coupled at one end to an oscillator; see Fig. 11. The semi-infinite transmission line can be considered a limit of the coplanar waveguide resonator of finite length discussed in Sec. II.B.1, where one of the boundaries is now pushed to infinity. This leads to a densely packed frequency spectrum, which in its infinite limit must be treated as a continuum. In analogy with Eq. (16), the Hamiltonian of the transmission line is consequently

$$\hat{H}_{\text{tml}} = \int_0^\infty d\omega \hbar\omega \hat{b}_\omega^\dagger \hat{b}_\omega, \quad (66)$$

where the mode operators now satisfy $[\hat{b}_\omega, \hat{b}_{\omega'}^\dagger] = \delta(\omega - \omega')$. Similarly, the position-dependent flux and charge operators of the transmission line are, in analogy with Eqs. (9), (10), (14), and (15), given in the continuum limit by (Yurke, 2004)

$$\hat{\Phi}_{\text{tml}}(x) = \int_0^\infty d\omega \sqrt{\frac{\hbar}{\pi\omega c v}} \cos\left(\frac{\omega x}{v}\right) (\hat{b}_\omega^\dagger + \hat{b}_\omega), \quad (67a)$$

$$\hat{Q}_{\text{tml}}(x) = i \int_0^\infty d\omega \sqrt{\frac{\hbar\omega c}{\pi v}} \cos\left(\frac{\omega x}{v}\right) (\hat{b}_\omega^\dagger - \hat{b}_\omega). \quad (67b)$$

These are the canonical fields of the transmission line and in the Heisenberg picture under Eq. (66) are related through $\hat{Q}_{\text{tml}}(x, t) = c \dot{\hat{\Phi}}_{\text{tml}}(x, t)$. In Eqs. (67), $v = 1/\sqrt{Lc}$ is the speed of light in the transmission line, with c and l the capacitance and inductance per unit length, respectively.

Considering capacitive coupling of the line to the oscillator at $x = 0$, the total Hamiltonian takes the form

$$\hat{H} = \hat{H}_s + \hat{H}_{\text{tml}} - \hbar \int_0^\infty d\omega \lambda(\omega) (\hat{b}_\omega^\dagger - \hat{b}_\omega) (\hat{a}^\dagger - \hat{a}), \quad (68)$$

where $\hat{H}_s = \hbar\omega_r \hat{a}^\dagger \hat{a}$ is the oscillator Hamiltonian. Moreover, $\lambda(\omega) = (C_\kappa / \sqrt{cC_r}) \sqrt{\omega_r \omega / 2\pi v}$ is the frequency-dependent

coupling strength, with C_κ the coupling capacitance and C_r the resonator capacitance. These expressions neglect small renormalizations of the capacitances due to C_κ , as discussed in Appendix A.

In the following, $\lambda(\omega)$ is assumed to be sufficiently small relative to ω_r such that the interaction can be treated as a perturbation. In this situation, the system's Q factor is large and the oscillator responds in a small bandwidth only around ω_r . It is therefore reasonable to take $\lambda(\omega) \simeq \lambda(\omega_r)$ in Eq. (68). Dropping rapidly oscillating terms finally leads to (Gardiner and Zoller, 1999)

$$\hat{H} \simeq \hat{H}_s + \hat{H}_{\text{tml}} + \hbar \int_0^\infty d\omega \lambda(\omega_r) (\hat{a} \hat{b}_\omega^\dagger + \hat{a}^\dagger \hat{b}_\omega). \quad (69)$$

Under the well-established Born-Markov approximations, Eq. (69) leads to the following Lindblad-form Markovian master equation for the system's density matrix ρ (Gardiner and Zoller, 1999; Breuer and Petruccione, 2002; Carmichael, 2002):

$$\dot{\rho} = -i[\hat{H}_s, \rho] + \kappa(\bar{n}_\kappa + 1)\mathcal{D}[\hat{a}]\rho + \kappa\bar{n}_\kappa\mathcal{D}[\hat{a}^\dagger]\rho, \quad (70)$$

where $\kappa = 2\pi\lambda(\omega_r)^2 = Z_{\text{tml}}\omega_r^2 C_\kappa^2 / C_r$ is the photon decay rate, or linewidth, of the oscillator introduced earlier and, as expected from Fermi's golden rule (Clerk *et al.*, 2010), is evaluated at the system frequency ω_r . Moreover, $\bar{n}_\kappa = \bar{n}_\kappa(\omega_r)$ is the number of thermal photons of the transmission line as given by the Bose-Einstein distribution $\langle \hat{b}_\omega^\dagger \hat{b}_{\omega'} \rangle = \bar{n}_\kappa(\omega)\delta(\omega - \omega')$ at the system frequency ω_r and environment temperature T . The symbol $\mathcal{D}[\hat{O}]\bullet$ represents the dissipator

$$\mathcal{D}[\hat{O}]\bullet = \hat{O}\bullet\hat{O}^\dagger - \frac{1}{2}\{\hat{O}^\dagger\hat{O}, \bullet\}, \quad (71)$$

with $\{\cdot, \cdot\}$ the anticommutator. Focusing on the second term of Eq. (70), the role of this superoperator can be understood intuitively by noting that the term $\hat{O}\rho\hat{O}^\dagger$ with $\hat{O} = \hat{a}$ in Eq. (71) acts on the Fock state $|n\rangle$ as $\hat{a}|n\rangle\langle n|\hat{a}^\dagger = n|n-1\rangle\langle n-1|$. The second term of Eq. (70) therefore corresponds to photon loss at rate κ . Finite temperature stimulates photon emission, boosting the loss rate to $\kappa(\bar{n}_\kappa + 1)$. On the other hand, the last term of Eq. (70) corresponds to absorption of thermal photons by the system. Because $\hbar\omega_r \gg k_B T$ at dilution refrigerator temperatures, it is often assumed that $\bar{n}_\kappa \rightarrow 0$. Deviations from this expected behavior are, however, common in practice due to residual thermal radiation propagating along control lines connecting to room-temperature equipment and to uncontrolled sources of heating. Approaches to mitigate this problem using absorptive components are being developed (Córcoles *et al.*, 2011; Wang *et al.*, 2019).

B. Input-output theory in electrical networks

While the master equation describes the system's damped dynamics, it provides no information on the fields radiated by the system. Since radiated signals are what is measured experimentally, it is of practical importance to include those in our model. This is known as the input-output theory for which two standard approaches exist. The first approach is to

work directly with Eq. (69) and consider Heisenberg picture equations of motion for the system and field annihilation operators \hat{a} and \hat{b}_ω . This is the route taken by Gardiner and Collett, one that is widely used in the quantum optics literature (Collett and Gardiner, 1984; Gardiner and Collett, 1985).

An alternative approach is to introduce a decomposition of the transmission-line modes in terms of left- and right-moving fields, linked by a boundary condition at the position of the oscillator that we take to be $x = 0$ with the transmission line at $x \geq 0$ (Yurke and Denker, 1984). The advantage of this approach is that the oscillator's input and output fields are then defined in terms of easily identifiable left-moving ($\hat{b}_{L\omega}$) and right-moving ($\hat{b}_{R\omega}$) radiation field components propagating along the transmission line. To achieve this, we replace the modes $\cos(\omega x/v)\hat{b}_\omega$ in Eqs. (67a) and (67b) by $(\hat{b}_{R\omega}e^{i\omega x/v} + \hat{b}_{L\omega}e^{-i\omega x/v})/2$. Since the number of degrees of freedom of the transmission line has seemingly doubled, the modes $\hat{b}_{L/R\omega}$ cannot be independent. Indeed, the dynamics of one set of modes is fully determined by the other set through a boundary condition linking the left and right movers at $x = 0$.

To see this, it is useful to first decompose the voltage $\hat{V}(x, t) = \hat{\Phi}_{\text{tml}}(x, t)$ at $x = 0$ into left-moving (input) and right-moving (output) contributions as $\hat{V}(t) = \hat{V}(x = 0, t) = \hat{V}_{\text{in}}(t) + \hat{V}_{\text{out}}(t)$, where

$$\hat{V}_{\text{in/out}}(t) = i \int_0^\infty d\omega \sqrt{\frac{\hbar\omega}{4\pi c v}} e^{i\omega t} \hat{b}_{L/R\omega}^\dagger + \text{H.c.} \quad (72)$$

The boundary condition at $x = 0$ follows from Kirchhoff's current law

$$\hat{I}(t) = \frac{\hat{V}_{\text{out}}(t) - \hat{V}_{\text{in}}(t)}{Z_{\text{tml}}}, \quad (73)$$

where the left-hand side $\hat{I}(t) = (C_\kappa/C_r)\dot{\hat{Q}}_r(t)$ is the current injected by the sample, with \hat{Q}_r the oscillator charge (see Appendix C for a derivation), while the right-hand side is the transmission-line voltage difference at $x = 0$.⁷ A mode expansion of the operators involved in Eq. (73) leads to the standard input-output relation (see Appendix C for details)

$$\hat{b}_{\text{out}}(t) - \hat{b}_{\text{in}}(t) = \sqrt{\kappa}\hat{a}(t), \quad (74)$$

where the input and output fields are defined as

$$\hat{b}_{\text{in}}(t) = \frac{i}{\sqrt{2\pi}} \int_{-\infty}^\infty d\omega \hat{b}_{L\omega} e^{-i(\omega - \omega_r)t}, \quad (75)$$

$$\hat{b}_{\text{out}}(t) = \frac{i}{\sqrt{2\pi}} \int_{-\infty}^\infty d\omega \hat{b}_{R\omega} e^{-i(\omega - \omega_r)t} \quad (76)$$

and satisfy the commutation relations $[\hat{b}_{\text{in}}(t), \hat{b}_{\text{in}}^\dagger(t')] = [\hat{b}_{\text{out}}(t), \hat{b}_{\text{out}}^\dagger(t')] = \delta(t - t')$. To arrive at Eq. (74), terms

⁷Note that if instead we have a boundary condition of zero current at $x = 0$, it would follow that $\hat{V}_{\text{in}}(t) = \hat{V}_{\text{out}}(t)$; i.e., the end point serves simply as a mirror reflecting the input signal.

rotating at $\omega + \omega_r$, have been dropped based on the previously mentioned assumption that the system responds only to frequencies $\omega \simeq \omega_r$ such that these terms are fast rotating (Yurke, 2004). In turn, this approximation allows one to extend the range of integration from $(0, \infty)$ to $(-\infty, \infty)$ in Eqs. (75) and (76). We have also approximated $\lambda(\omega) \simeq \lambda(\omega_r)$ over the relevant frequency range. These approximations are compatible with those used to arrive at the Lindblad-form Markovian master equation of Eq. (70).

The same expressions and approximations can be used to obtain the equation of motion for the resonator field $\hat{a}(t)$ in the Heisenberg picture, which takes the form (see Appendix C for details)

$$\dot{\hat{a}}(t) = i[\hat{H}_s, \hat{a}(t)] - \frac{\kappa}{2}\hat{a}(t) + \sqrt{\kappa}\hat{b}_{\text{in}}(t). \quad (77)$$

Equation (77) shows that the resonator dynamics is determined by the input field (in practice, noise or drive), while Eq. (74) shows how the output can, in turn, be found from the input and the system dynamics. The output field thus holds information about the system's response to the input, which can be measured to indirectly give us access to information about the dynamics of the system. As discussed in more detail in Sec. V, this can be done by measuring the voltage at some $x > 0$ away from the oscillator. Under the previously used approximations, this voltage can be expressed as

$$\hat{V}(x, t) \simeq \sqrt{\frac{\hbar\omega_r Z_{\text{tml}}}{2}} [e^{i\omega_r x/v - i\omega_r t} \hat{b}_{\text{out}}(t) + e^{-i\omega_r x/v - i\omega_r t} \hat{b}_{\text{in}}(t) + \text{H.c.}]. \quad (78)$$

Note that this approximate expression assumes that all relevant frequencies are near ω_r and, furthermore, neglects all non-Markovian time-delay effects.

In this section we have considered a particularly simple setup: a single quantum system connected to the end point of a semi-infinite transmission line. More generally, quantum systems can be made to interact by coupling them to a common transmission line, and multiple transmission lines can be used to form quantum networks. These more complex setups can be treated using the SLH formalism, which generalizes the results in this section (Gough and James, 2009; Combes, Kerckhoff, and Sarovar, 2017).

C. Qubit relaxation and dephasing

The master equation (70) was derived for an oscillator coupled to a transmission line, but this form of the master equation is quite general. In fact, Eq. (68) is itself a generic system-bath Hamiltonian that can be used to model dissipation due to a variety of different noise sources (Caldeira and Leggett, 1981). To model damping of an arbitrary quantum system, for example, a transmon qubit or a coupled resonator-transmon system, the operator \hat{a} in Eq. (68) is simply replaced with the relevant system operator that couples to the transmission line (or, more generally, the bath).

For the case of a transmon (see Fig. 12), \hat{H}_s in Eq. (70) is replaced with the Hamiltonian \hat{H}_q of Eq. (27) together with

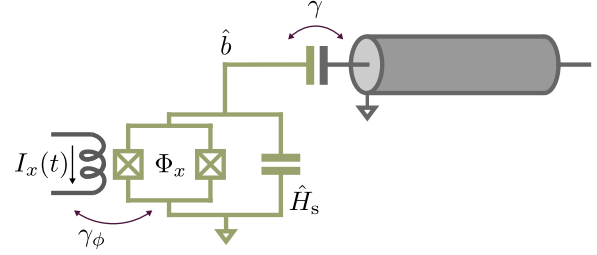


FIG. 12. Transmon qubit coupled capacitively to a semi-infinite transmission line and inductively to a flux line. These ports are used to control the qubit state and to change its transition frequency. They also lead to qubit decay into the transmission line and to dephasing due to flux noise.

the additional replacements $\mathcal{D}[\hat{a}] \bullet \rightarrow \mathcal{D}[\hat{b}] \bullet$, $\mathcal{D}[\hat{a}^\dagger] \bullet \rightarrow \mathcal{D}[\hat{b}^\dagger] \bullet$, and $\kappa \rightarrow \gamma$. Here $\gamma = 2\pi\lambda(\omega_q)^2$ is the relaxation rate of the artificial atom that is related to the qubit-environment coupling strength evaluated at the qubit frequency. This immediately leads to the master equation

$$\dot{\rho} = -i[\hat{H}_q, \rho] + \gamma(\bar{n}_\gamma + 1)\mathcal{D}[\hat{b}]\rho + \gamma\bar{n}_\gamma\mathcal{D}[\hat{b}^\dagger]\rho, \quad (79)$$

where ρ now refers to the transmon state and \bar{n}_γ is the thermal photon number of the transmon's environment. It is often assumed that $\bar{n}_\gamma \rightarrow 0$ but, as with the oscillator, a residual thermal population is often observed in practice (Córcoles *et al.*, 2011; Wang *et al.*, 2019).

Superconducting quantum circuits can also suffer from dephasing caused, for example, by fluctuations of parameters controlling their transition frequency and by dispersive coupling to other degrees of freedom in their environment. For a transmon, a phenomenological model for dephasing can be introduced by adding the following term to the master equation (Carmichael, 2002):

$$2\gamma_\phi\mathcal{D}[\hat{b}^\dagger\hat{b}]\rho, \quad (80)$$

with γ_ϕ the pure dephasing rate. Because of its insensitivity to charge noise (see Fig. 6), γ_ϕ is often small for the 0-1 transition of transmon qubits (Koch *et al.*, 2007). Given that charge dispersion increases exponentially with level number, dephasing due to charge noise can be apparent on higher transmon levels; see Egger *et al.* (2019). Another source of dephasing for the transmon is the residual thermal photon population of a resonator to which the transmon is dispersively coupled. This can be understood from the form of the interaction in the dispersive regime $\chi_{ab}\hat{a}^\dagger\hat{a}\hat{b}^\dagger\hat{b}$, where fluctuations of the photon number lead to fluctuations in the qubit frequency and therefore to dephasing (Bertet *et al.*, 2005; Schuster *et al.*, 2005; Gambetta *et al.*, 2006; Rigetti *et al.*, 2012). Other sources of relaxation and dephasing include two-level systems within the materials and interfaces of the devices (Müller, Cole, and Lisenfeld, 2019), quasiparticles (Glazman and Catelani, 2020) generated by a number of phenomena including infrared radiation (Barends *et al.*, 2011; Córcoles *et al.*, 2011), and even ionizing radiation (Vepsäläinen *et al.*, 2020). We note that a term of the form of Eq. (80) but with $\hat{b}^\dagger\hat{b}$

replaced by $\hat{a}^\dagger \hat{a}$ can also be added to the master equation of the oscillator to model dephasing of the cavity itself. Oscillator dephasing rates are, however, typically small and this contribution is often neglected (Reagor *et al.*, 2016).

Combining these results, the master equation for a transmon subject to relaxation and dephasing assuming that $\bar{n}_\gamma \rightarrow 0$ is

$$\dot{\rho} = -i[\hat{H}_q, \rho] + \gamma \mathcal{D}[\hat{b}]\rho + 2\gamma_\phi \mathcal{D}[\hat{b}^\dagger \hat{b}]\rho. \quad (81)$$

It is common to express this master equation in the two-level approximation of the transmon, which is obtained simply by taking $\hat{H}_q \rightarrow \hbar\omega_a \hat{\sigma}_z/2$, $\hat{b}^\dagger \hat{b} \rightarrow (\hat{\sigma}_z + 1)/2$, $\hat{b} \rightarrow \hat{\sigma}_-$, and $\hat{b}^\dagger \rightarrow \hat{\sigma}_+$.

Note that the rates γ and γ_ϕ appearing in the previous expressions are related to the characteristic T_1 relaxation time and T_2 coherence time of the artificial atom, which are defined as (Schoelkopf *et al.*, 2003)

$$T_1 = \frac{1}{\gamma_1} = \frac{1}{\gamma_\downarrow + \gamma_\uparrow} \simeq \frac{1}{\gamma}, \quad (82a)$$

$$T_2 = \frac{1}{\gamma_2} = \left(\frac{\gamma_1}{2} + \gamma_\phi \right)^{-1}, \quad (82b)$$

where $\gamma_\downarrow = (\bar{n}_\gamma + 1)\gamma$ and $\gamma_\uparrow = \bar{n}_\gamma\gamma$. The approximation in Eq. (82a) holds for $\bar{n}_\gamma \rightarrow 0$. At zero temperature, T_1 is the characteristic time for the artificial atom to relax from its first excited state to the ground state. On the other hand, T_2 is the dephasing time, which quantifies the characteristic lifetime of coherent superpositions, and includes a contribution from both pure dephasing (γ_ϕ) and relaxation (γ_1). Current best values for the T_1 and T_2 time of fixed-frequency transmon qubits are in the 50–120 μs range for aluminum-based transmons (Devoret and Schoelkopf, 2013; Nersisyan *et al.*, 2019; Kjaergaard, Schwartz *et al.*, 2020; Wei *et al.*, 2020). Relaxation times above 300 μs have been reported in transmon qubits where the transmon pads have been made with tantalum rather than aluminum, but the Josephson junction is still made from aluminum and aluminum oxide (Place *et al.*, 2020). Other superconducting qubits also show large relaxation and coherence times. Examples are $T_1, T_2 \sim 300 \mu\text{s}$ for heavy-fluxonium qubits (Zhang *et al.*, 2021), and $T_1 \sim 1.6 \text{ ms}$ and $T_2 \sim 25 \mu\text{s}$ for the $0-\pi$ qubit (Gyenis *et al.*, 2021).

Qubit relaxation and incoherent excitation occur due to uncontrolled exchange of gigahertz frequency photons between the qubit and its environment. These processes are observed to be well described by the Markovian master equation of Eq. (81). In contrast, the dynamics leading to dephasing are typically non-Markovian, happening at low frequencies (i.e., slow time scales set by the phase coherence time itself). As a result, it is observed that these processes cannot be accurately described by a Markovian master equation such as Eq. (81). This equation thus represents a somewhat crude approximation to dephasing in superconducting qubits. That being said, in practice the Markovian theory is still useful, particularly because it correctly predicts the results of experiments probing the steady-state response of the system.

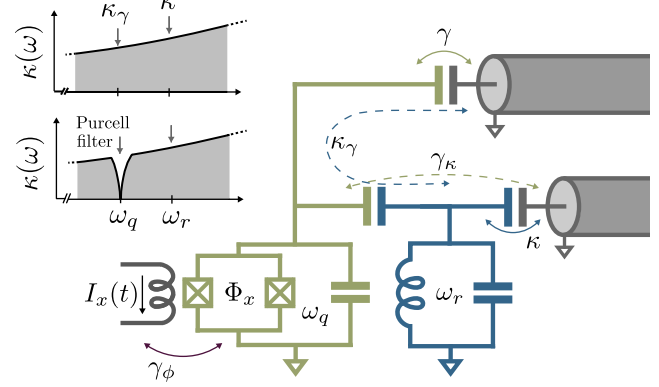


FIG. 13. Because the dressed states in the dispersive regime are entangled qubit-cavity states, cavity damping at the rate κ leads to qubit relaxation at the Purcell rate γ_κ . Conversely, qubit relaxation leads to cavity decay at the inverse Purcell rate κ_γ . Adding a Purcell filter (not shown) reduces the cavity density of states at the qubit frequency and therefore suppresses Purcell decay.

D. Dissipation in the dispersive regime

We now turn to a description of dissipation for the coupled transmon-resonator system of Sec. III. Assuming that the transmon and the resonator are coupled to independent baths as illustrated in Fig. 13, the master equation for this composite system is (taking $\bar{n}_{\kappa,\gamma} \rightarrow 0$ for simplicity)

$$\dot{\rho} = -i[\hat{H}, \rho] + \kappa \mathcal{D}[\hat{a}]\rho + \gamma \mathcal{D}[\hat{b}]\rho + 2\gamma_\phi \mathcal{D}[\hat{b}^\dagger \hat{b}]\rho, \quad (83)$$

where ρ is now a density matrix for the total system and \hat{H} describes the coupled system as in Eq. (34). Equation (83) is valid only at small values of $g/(\omega_r, \omega_q)$. This is because energy decay occurs via transitions between system eigenstates, while the previous expression describes transitions between the uncoupled bare states. A derivation of the master equation valid at arbitrary g was given by Beaudoin, Gambetta, and Blais (2011).

More important to the present discussion is the fact that, at first glance, Eq. (83) gives the impression that dissipative processes influence the transmon and the resonator in completely independent manners. However, because \hat{H} entangles the two systems, the loss of a resonator photon can lead to relaxation of the dressed qubit. Moving to the dispersive regime, a more complete picture of dissipation therefore emerges after applying the unitary transformation in Eq. (49) not only on the Hamiltonian but also on the previous master equation. Neglecting fast-rotating terms and considering corrections to second order in λ [which is consistent if $\kappa, \gamma, \gamma_\phi = \mathcal{O}(E_C g^2 / \Delta^2)$] leads to the dispersive master equation (Boissonneault, Gambetta, and Blais, 2009)

$$\begin{aligned} \dot{\rho}_{\text{disp}} = & -i[\hat{H}_{\text{disp}}, \rho_{\text{disp}}] \\ & + (\kappa + \kappa_\gamma) \mathcal{D}[\hat{a}]\rho_{\text{disp}} + (\gamma + \gamma_\kappa) \mathcal{D}[\hat{b}]\rho_{\text{disp}} \\ & + 2\gamma_\phi \mathcal{D}[\hat{b}^\dagger \hat{b}]\rho_{\text{disp}} \\ & + \gamma_\Delta \mathcal{D}[\hat{a}^\dagger \hat{b}]\rho_{\text{disp}} + \gamma_\Delta \mathcal{D}[\hat{b}^\dagger \hat{a}]\rho_{\text{disp}}, \end{aligned} \quad (84)$$

where we have introduced

$$\gamma_\kappa = \left(\frac{g}{\Delta}\right)^2 \kappa, \quad \kappa_\gamma = \left(\frac{g}{\Delta}\right)^2 \gamma, \quad \gamma_\Delta = 2\left(\frac{g}{\Delta}\right)^2 \gamma_\varphi, \quad (85)$$

and $\rho_{\text{disp}} = \hat{U}_{\text{disp}}^\dagger \rho \hat{U}_{\text{disp}}$ is the density matrix in the dispersive frame. Equation (85) has three new rates, the first of which is known as the Purcell decay rate γ_κ (Purcell, 1946). This rate captures the fact that the qubit dressed by the field can relax by emission of a resonator photon. It can be understood simply from the form Eq. (41) of the dressed eigenstate $|\bar{e}, \bar{0}\rangle \sim |e, 0\rangle + (g/\Delta)|g, 1\rangle$ that is closest to a bare qubit excitation $|e\rangle$. This state is the superposition of the qubit first excited state with no photon and, with probability $(g/\Delta)^2$, the qubit ground state with a photon in the resonator. The latter component can decay at the rate κ , taking the dressed excited qubit to the ground state $|g, 0\rangle$ with a rate γ_κ . Similar intuition is also applied to κ_γ , now associated with a resonator photon loss through a qubit decay event.

The situation is more subtle in the last line of Eq. (84). Following Boissonneault, Gambetta, and Blais (2008, 2009), an effective master equation for the transmon can be obtained from Eq. (84) by approximately eliminating the resonator degrees of freedom. This results in transmon relaxation and excitation rates given approximately by $\bar{n}\gamma_\Delta$, with \bar{n} the average photon number in the resonator. Commonly known as dressed dephasing, this leads to spurious transitions during qubit measurement and can be interpreted as originating from dephasing noise at the detuning frequency Δ that is up- or down-converted by readout photons to cause spurious qubit-state transitions.

Because we have taken the shortcut of applying the dispersive transformation on the master equation, the previous discussion neglects the frequency dependence of the various decay rates. In a more careful derivation, the dispersive transformation is applied on the system plus bath Hamiltonian, and only then is the master equation derived (Boissonneault, Gambetta, and Blais, 2009). The result has the same form as Eq. (84), but with different expressions for the rates. Indeed, it is useful to write $\kappa = \kappa(\omega_r)$ and $\gamma = \gamma(\omega_q)$ to recognize that, while photon relaxation is probing the environment at the resonator frequency ω_r , qubit relaxation is probing the environment at ω_q . With this notation, the first two rates of Eq. (85) become in the more careful derivation $\gamma_\kappa = (g/\Delta)^2 \kappa(\omega_q)$ and $\kappa_\gamma = (g/\Delta)^2 \gamma(\omega_r)$. In other words, Purcell decay occurs by emitting a photon at the qubit frequency and not at the resonator frequency suggested by the completely white noise model used to derive Eq. (85). In the same way, it is useful to write the dephasing rate as $\gamma_\varphi = \gamma_\varphi(\omega \rightarrow 0)$ to recognize the importance of low-frequency noise to dephasing. Using this notation, the rates in the last two terms of Eq. (84) become, respectively, $\gamma_\Delta = 2(g/\Delta)^2 \gamma_\varphi(\Delta)$ and $\gamma_{-\Delta} = 2(g/\Delta)^2 \gamma_\varphi(-\Delta)$ (Boissonneault, Gambetta, and Blais, 2009). In short, dressed dephasing probes the noise responsible for dephasing at the transmon-resonator detuning frequency Δ . This observation was used to probe this noise at gigahertz frequencies by Slichter *et al.*

(2012). Moreover, in the presence of qubit or resonator drives, effective master equations derived from the full system plus bath Hamiltonian without the rotating-wave or two-level approximations also obtain drive-power-dependent relaxation rates (Malekakhlagh, Petrescu, and Türeci, 2020; Müller, 2020; Petrescu, Malekakhlagh, and Türeci, 2020). In particular, these theories attribute the drive-induced enhancement of qubit relaxation to correlated qubit-cavity processes such as stimulated emission.

The observations in this section result from the qubit-oscillator dressing that occurs under the Jaynes-Cummings Hamiltonian. For this reason, the situation is substantially different if the electric-dipole interaction leading to the Jaynes-Cummings Hamiltonian is replaced by a longitudinal interaction of the form of Eq. (65). In this case, there is no light-matter dressing and, consequently, no Purcell decay or dressed dephasing (Kerman, 2013; Billangeon, Tsai, and Nakamura, 2015a). This is one of the advantages of this alternative light-matter coupling.

E. Multimode Purcell effect and Purcell filters

Thus far we have considered dissipation for a qubit dispersively coupled to a single-mode oscillator. Replacing the latter with a multimode resonator leads to dressing of the qubit by all of the resonator modes and therefore to a modification of the Purcell decay rate. Following the previous discussion, one may then expect the contributions to add up, leading to the modified rate $\sum_{m=0}^{\infty} (g_m/\Delta_m)^2 \kappa_m$, with m the mode index. However, when accounting for the frequency dependence of κ_m , g_m , and Δ_m , this expression diverges (Houck *et al.*, 2008). It is possible to cure this problem by using a more refined model (Parra-Rodriguez *et al.*, 2018). The divergence is removed when the finite size of the transmon and the frequency dependence of the impedance of the resonator's input and output capacitors is included (Bourassa, 2012) or, in the dipole approximation for the qubit, by taking into account the frequency dependence of the qubit-resonator coupling capacitance (Malekakhlagh, Petrescu, and Türeci, 2017).

Given that damping rates in quantum electrical circuits are set by classical system parameters (Leggett, 1984b), a simpler approach to compute the Purcell rate exists. It can indeed be shown that $\gamma_\kappa = \text{Re}[Y(\omega_q)]/C_\Sigma$, with $Y(\omega) = 1/Z(\omega)$ the admittance of the electromagnetic environment seen by the transmon (Esteve, Devoret, and Martinis, 1986; Houck *et al.*, 2008). This expression again makes it clear that relaxation probes the environment (here represented by the admittance) at the system frequency. It also suggests that engineering the admittance $Y(\omega)$ such that it is purely reactive at ω_q can cancel Purcell decay; see the inset of Fig. 13. This can be done by adding a transmission-line stub of appropriate length and terminated in an open circuit at the output of the resonator, something that is known as a Purcell filter (Reed, Johnson *et al.*, 2010). Because of the increased freedom in optimizing the system parameters (essentially decoupling the choice of κ from the qubit relaxation rate), Purcell filters of various types are commonly used experimentally (Jeffrey *et al.*, 2014; Bronn *et al.*, 2015; Walter *et al.*, 2017).

F. Controlling quantum systems with microwave drives

While connecting a quantum system to external transmission lines leads to losses, such connections are nevertheless necessary to control and measure the system. Consider a continuous microwave tone of frequency ω_d and phase ϕ_d applied to the input port of the resonator. A simple approach to model this drive is based on the input-output approach of Sec. IV.B. Indeed, the drive can be taken into account by replacing the input field $\hat{b}_{\text{in}}(t)$ in Eq. (77) with $\hat{b}_{\text{in}}(t) \rightarrow \hat{b}_{\text{in}}(t) + \beta(t)$, where $\beta(t) = A(t) \exp(-i\omega_d t - i\phi_d)$ is the coherent classical part of the input field of amplitude $A(t)$. The resulting term $\sqrt{\kappa}\beta(t)$ in the Langevin equation can be absorbed in the system Hamiltonian with the replacement $\hat{H}_s \rightarrow \hat{H}_s + \hat{H}_d$, where

$$\hat{H}_d = \hbar[\varepsilon(t)\hat{a}^\dagger e^{-i\omega_d t - i\phi_d} + \varepsilon^*(t)\hat{a}e^{i\omega_d t + i\phi_d}], \quad (86)$$

with $\varepsilon(t) = i\sqrt{\kappa}A(t)$ the possibly time-dependent amplitude of the drive as seen by the resonator mode. Generalizing to multiple drives on the resonator and/or drives on the transmon is straightforward.

The drive Hamiltonian \hat{H}_d is the generator of displacement in phase space of the resonator. As a result, by choosing appropriate parameters for the drive, evolution under \hat{H}_d will bring the intracavity state from vacuum to an arbitrary coherent state (Gardiner and Zoller, 1999; Carmichael, 2002)

$$|\alpha\rangle = \hat{D}(\alpha)|0\rangle = e^{-|\alpha|^2/2} \sum_{n=0}^{\infty} \frac{\alpha^n}{\sqrt{n!}} |n\rangle, \quad (87)$$

where $\hat{D}(\alpha)$ is known as the displacement operator and takes the form

$$\hat{D}(\alpha) = e^{\alpha\hat{a}^\dagger - \alpha^*\hat{a}}. \quad (88)$$

As discussed in the next section, coherent states play an important role in qubit readout in circuit QED.

It is important to note that \hat{H}_d derives from Eq. (77), which is itself the result of a rotating-wave approximation. As can be understood from Eq. (22), before this approximation the drive rather takes the form $i\hbar\varepsilon(t) \cos(\omega_d t + \phi_d)(\hat{a}^\dagger - \hat{a})$. Although \hat{H}_d is sufficient in most cases of practical interest, departures from the predictions of Eq. (86) can be seen at large drive amplitudes (Pietikäinen *et al.*, 2017; Verney *et al.*, 2019).

V. MEASUREMENTS IN CIRCUIT QED

Before the development of circuit QED, the quantum state of superconducting qubits was measured by fabricating and operating a measurement device, such as a single-electron transistor or dc SQUID, in close proximity to the qubit (Makhlin, Schön, and Shnirman, 2001; Clarke and Wilhelm, 2008). A challenge with such an approach is that the readout circuitry must be strongly coupled to the qubit during measurement so as to extract information on a time-scale much smaller than T_1 , while being well decoupled from the qubit when the measurement is turned off to avoid

unwanted backaction. Especially given that measurement necessarily involves dissipation (Landauer, 1991), simultaneously satisfying these two requirements is challenging. Circuit QED, however, has several advantages to offer over the previous approaches. Indeed, as discussed in this section, qubit readout in this architecture is realized by measuring scattering of a probe tone off an oscillator coupled to the qubit. This approach first leads to an excellent measurement on-off ratio since qubit readout occurs only in the presence of the probe tone. A second advantage is that the necessary dissipation now occurs away from the qubit, essentially at a voltage meter located at room temperature, rather than in a device fabricated at close proximity to the qubit. Unwanted energy exchange is, moreover, inhibited when working in the dispersive regime where the effective qubit-resonator interaction in Eq. (44) is such that even the probe-tone photons are not absorbed by the qubit. As a result, the backaction on the qubit is to a large extent limited to the essential dephasing that quantum measurements must impart on the measured system, leading in principle to a quantum nondemolition (QND) qubit readout.

Because of the small energy of microwave photons with respect to optical photons, single-photon detectors in the microwave-frequency regime are still being developed; see Sec. VIII.F. Therefore, measurements in circuit QED rely on amplification of weak microwave signals followed by detection of field quadratures using heterodyne detection. Before discussing qubit readout, in Sec. V.A we explain these terms and go over the main challenges related to such measurements in the quantum regime.

A. Microwave field detection

Figure 14 illustrates a typical measurement chain in circuit QED. The signal of a microwave source is directed to the input port of the resonator first going through a series of attenuators thermally anchored at different stages of the dilution refrigerator. The role of these attenuators is to absorb the room-temperature thermal noise propagating toward the sample. The field transmitted by the resonator is first amplified, then mixed with a reference signal, converted from analog to digital, and finally processed with a field-programmable gate array (FPGA) or recorded. Circulators are inserted before the amplification stage to prevent noise generated by the amplifier from reaching the resonator. Circulators are directional devices that transmit signals in the forward direction, while strongly attenuating signals propagate in the reverse direction (here coming from the amplifier) (Pozar, 2011). In practice, circulators are bulky off-chip devices relying on permanent magnets that are not compatible with the requirement for integration with superconducting quantum circuits. They also introduce additional losses due to insertion losses and off-chip cable losses. Significant effort is currently being devoted to developing compact, on-chip, superconducting circuit-based circulators (Kamal, Clarke, and Devoret, 2011; Chapman *et al.*, 2017; Lecocq *et al.*, 2017; Abdo *et al.*, 2019).

In practice, the different components and cables of the measurement chain have a finite bandwidth that we assume to be larger than the bandwidth of the signal of interest $\hat{b}_{\text{out}}(t)$ at the output of the resonator. To account for the finite bandwidth

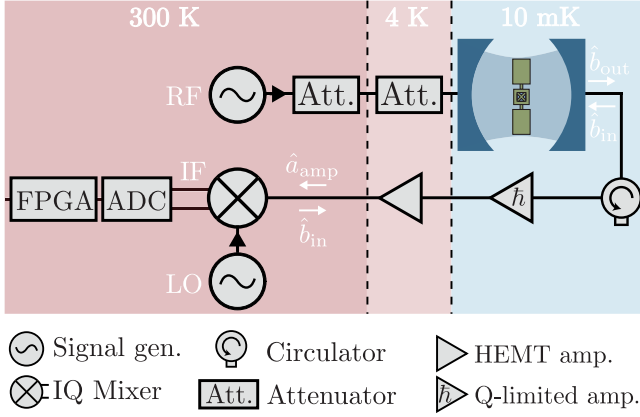


FIG. 14. Schematic representation of the microwave measurement chain for field detection in circuit QED, with the resonator depicted as a Fabry-Perot cavity. The signal (RF) from a microwave source is applied to the input port of the resonator first passing through attenuators to reduce the level of thermal radiation. After passing through a circulator, the resonator's output field is first amplified by a quantum-limited amplifier, such as a JPA or a JTWPA, and then by a HEMT amplifier. The signal is then mixed with a local oscillator (LO). The signal at the output of the mixer is digitized with an analog-to-digital converter (ADC) and can be further processed by a field-programmable gate array (FPGA). The two lines at the output of the mixer correspond to the two quadratures of the field. The temperature at which the different components are operated is indicated.

of the measurement chain and to simplify the following discussion, it is useful to consider the filtered output field

$$\begin{aligned}\hat{a}_f(t) &= (f \star \hat{b}_{\text{out}})(t) \\ &= \int_{-\infty}^{\infty} d\tau f(t - \tau) \hat{b}_{\text{out}}(\tau) \\ &= \int_{-\infty}^{\infty} d\tau f(t - \tau) [\sqrt{\kappa} \hat{a}(\tau) + \hat{b}_{\text{in}}(\tau)],\end{aligned}\quad (89)$$

which is linked to the intracavity field \hat{a} via the input-output boundary condition [Eq. (74)] that we use on the last line of Eq. (89). In this equation the filter function $f(t)$ is normalized to $\int_{-\infty}^{\infty} dt |f(t)|^2 = 1$ such that $[\hat{a}_f(t), \hat{a}_f^\dagger(t)] = 1$. As discussed later in the context of qubit readout, in addition to representing the measurement bandwidth, filter functions are used to optimize the distinguishability between the qubit states.

Ignoring the presence of the circulator and assuming that a phase-preserving amplifier (i.e., an amplifier that amplifies both signal quadratures equally) is used, in the first stage of the measurement chain the signal is transformed according to (Caves, 1982; Clerk *et al.*, 2010)

$$\hat{a}_{\text{amp}} = \sqrt{G} \hat{a}_f + \sqrt{G - 1} \hat{h}^\dagger, \quad (90)$$

where G is the power gain and \hat{h}^\dagger accounts for noise added by the amplifier. The presence of this added noise is required for the amplified signal to obey the bosonic commutation relation $[\hat{a}_{\text{amp}}, \hat{a}_{\text{amp}}^\dagger] = 1$. Equivalently, the noise must be present because the two quadratures of the signal are canonically

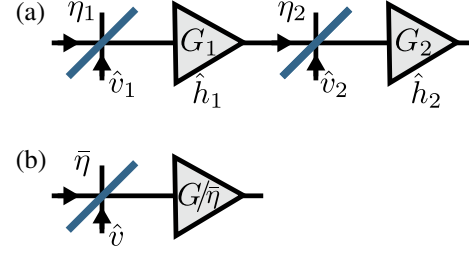


FIG. 15. (a) Amplification chain with amplifiers of gain $G_{1,2}$ and noise mode $\hat{h}_{1,2}$ with attenuation modeled by beam splitters of transmissivity $\eta_{1,2}$. The beam splitters each have a vacuum port with vacuum mode $\hat{v}_{1,2}$ such that $\langle \hat{v}_{1,2}^\dagger \hat{v}_{1,2} \rangle = 0$. The quantum efficiency derived from this model is $\eta = 1/(N_T + 1) \leq 1$, with $N_T = \langle \hat{h}_T^\dagger \hat{h}_T \rangle$ the total added noise number given in Eq. (91). (b) Alternative model where a noisy amplifier is modeled by a noiseless amplifier preceded by a beam splitter of transmissivity $\bar{\eta}$. The quantum efficiency derived from this model is $\bar{\eta} = 1/(2\mathcal{A} + 1) \leq 1/2$, with \mathcal{A} the added noise given in Eq. (94).

conjugate. Amplification of both quadratures without added noise would allow us to violate the Heisenberg uncertainty relation between the two quadratures.

In a standard parametric amplifier, \hat{a}_f in Eq. (90) represents the amplitude of the signal mode and \hat{h} represents the amplitude of a second mode called the idler. The physical interpretation of Eq. (90) is that an ideal amplifier performs a Bogoliubov transformation on the signal and idler modes. The signal mode is amplified, but the requirement that the transformation be canonical implies that the phase conjugated and amplified quantum noise from the idler port must appear in the signal output port. Ideally, the input to the idler is vacuum with $\langle \hat{h}^\dagger \hat{h} \rangle = 0$ and $\langle \hat{h} \hat{h}^\dagger \rangle = 1$, so the amplifier adds only quantum noise. Near-quantum-limited amplifiers with ~ 20 dB power gain approaching this ideal behavior are now routinely used in circuit QED experiments. These Josephson-junction-based devices, as well as the distinction between phase-preserving and phase-sensitive amplification, are discussed further in Sec. VIII.B.

To measure the weak signals that are typical in circuit QED, the output of the first near-quantum-limited amplifier is further amplified by a low-noise high-electron-mobility transistor (HEMT) amplifier. The latter acts on the signal again following Eq. (90), now with a larger power gain ~ 30 – 40 dB but also a larger added noise photon number. The best cryogenic HEMT amplifiers in the 4–8 GHz band have noise figures as low as $\langle \hat{h}^\dagger \hat{h} \rangle \sim 5$ – 10 . However, the effect of attenuation due to cabling up to the previous element of the amplification chain, i.e., a quantum-limited amplifier or the sample of interest itself, can degrade this figure significantly. A more complete understanding of the added noise in this situation can be derived from Fig. 15(a). There, beam splitters of transmissivity $\eta_{1,2}$ model the attenuation leading to the two amplifiers of gain labeled G_1 and G_2 . Taking into account vacuum noise $\hat{v}_{1,2}$ at the beam splitters, the input-output expression of this chain can be cast under the form of Eq. (90) with a total gain $G_T = \eta_1 \eta_2 G_1 G_2$ and noise mode \hat{h}_T^\dagger corresponding to the total added noise number

$$\begin{aligned}
N_T &= \frac{1}{G_T - 1} [\eta_1 (G_1 - 1) G_2 (N_1 + 1) \\
&\quad + (G_2 - 1)(N_2 + 1)] - 1 \\
&\approx \frac{1}{\eta_1} \left[1 + N_1 + \frac{N_2}{\eta_2 G_1} \right] - 1, \quad (91)
\end{aligned}$$

where $N_i = \langle \hat{h}_i^\dagger \hat{h}_i \rangle$, with $i = 1, 2, T$. The last expression corresponds to the large gain limit. According to Eq. (91), if the gain G_1 of the first amplifier is large, the noise of the chain is dominated by the noise N_1 of the first amplifier. This emphasizes the importance of using near-quantum-limited amplifiers with low noise in the first stage of the chain. In the literature, the quantum efficiency $\eta = 1/(N_T + 1)$ is often used to characterize the measurement chain, with $\eta = 1$ in the ideal case $N_T = 0$.

It is worthwhile to note that another definition of the quantum efficiency can often be found in the literature. This alternative definition is based on Fig. 15(b) where a noisy amplifier of gain G is replaced by a noiseless amplifier of gain $G/\bar{\eta}$ preceded by a fictitious beam splitter of transmittivity $\bar{\eta}$ adding vacuum noise to the amplifier's input (Leonhardt and Paul, 1993). The quantum efficiency corresponds here to the transmittivity $\bar{\eta}$ of the fictitious beam splitter. The input-output relation of the network of Fig. 15(b) with its noiseless phase-preserving amplifier reads $\hat{a}_{\text{amp}} = \sqrt{G/\bar{\eta}}(\sqrt{\bar{\eta}}\hat{a}_f + \sqrt{1-\bar{\eta}}\hat{v})$, which can be expressed as

$$\langle |\hat{a}_{\text{amp}}|^2 \rangle = \frac{G}{\bar{\eta}} \left[(1-\bar{\eta})\frac{1}{2} + \bar{\eta}\langle |\hat{a}_f|^2 \rangle \right], \quad (92)$$

with $\langle |\hat{O}|^2 \rangle = \langle \{\hat{O}^\dagger, \hat{O}\} \rangle / 2$ the symmetrized fluctuations. The first term of Eq. (92) corresponds to the noise added by the amplifier, here represented by vacuum noise added to the signal before amplification, while the second term corresponds to noise in the signal at the input of the amplifier. On the other hand, Eq. (90) for a noisy amplifier can also be cast in the form of Eq. (92) with

$$\langle |\hat{a}_{\text{amp}}|^2 \rangle = G(\mathcal{A} + \langle |\hat{a}_f|^2 \rangle), \quad (93)$$

where we introduce the added noise

$$\mathcal{A} = \frac{G-1}{G} \left(\langle \hat{h}^\dagger \hat{h} \rangle + \frac{1}{2} \right). \quad (94)$$

In the limit of low amplifier noise $\langle \hat{h}^\dagger \hat{h} \rangle \rightarrow 0$ and large gain, the added noise is found to be bounded by $\mathcal{A} \geq (1 - G^{-1})/2 \simeq 1/2$ corresponding to half a photon of noise (Caves, 1982). Using Eqs. (92) and (93), the quantum efficiency of a phase-preserving amplifier can therefore be written as $\bar{\eta} = 1/(2\mathcal{A} + 1) \leq 1/2$ and is found to be bounded by 1/2 in the ideal case. The concept of quantum efficiency is not limited to amplification and can be applied to the entire measurement chain illustrated in Fig. 14.

Using Eqs. (78) and (90), the voltage after amplification can be expressed as

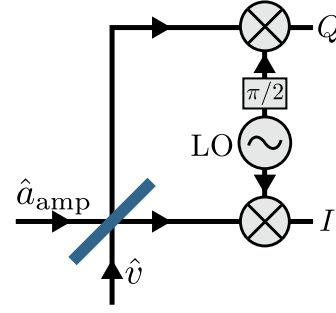


FIG. 16. Schematic representation of an IQ mixer. The rf signal \hat{a}_{amp} is split into two parts at a power divider, here illustrated as a beam splitter to account for added noise due to internal modes. Ideally, only vacuum noise \hat{v} is introduced at that stage. The two outputs are combined with a LO at mixers. By phase shifting the LO by $\pi/2$ in one of the two arms, it is possible to simultaneously measure the two quadratures of the field.

$$\hat{V}_{\text{amp}}(t) \simeq \sqrt{\frac{\hbar\omega_{\text{RF}}Z_{\text{inl}}}{2}} [e^{-i\omega_{\text{RF}}t}\hat{a}_{\text{amp}} + \text{H.c.}], \quad (95)$$

where ω_{RF} is the signal frequency. To simplify the expressions, we have dropped the phase associated with the finite cable length. We have also dropped the contribution from the input field $\hat{b}_{\text{in}}(t)$ moving toward the amplifier in the opposite direction at that point (see Fig. 14), because this field is not amplified and therefore gives a small contribution compared to the amplified output field. Recall, however, the contribution of this field to the filtered signal [Eq. (89)].

Different strategies can be used to extract information from the amplified signal, and here we take the next stage of the chain to be an in-phase and quadrature (IQ) mixer. As schematically illustrated in Fig. 16, in this microwave device the signal first encounters a power divider, illustrated here as a beam splitter accounting for added noise due to internal modes, followed in each branch by mixers with local oscillators (LOs) that are offset in phase by $\pi/2$. The LO consists of a reference signal of well-defined amplitude A_{LO} , frequency ω_{LO} , and phase ϕ_{LO} :

$$V_{\text{LO}}(t) = A_{\text{LO}} \cos(\omega_{\text{LO}}t - \phi_{\text{LO}}). \quad (96)$$

Mixers use nonlinearity to down-convert the input signal to a lower frequency referred to as the intermediate frequency (IF) signal.

First describing the signal as a classical voltage $V_{\text{RF}}(t) = A_{\text{RF}} \cos(\omega_{\text{RF}}t + \phi_{\text{RF}})$, the output at one of these mixers is (Poazar, 2011)

$$\begin{aligned}
V_{\text{mixer}}(t) &= KV_{\text{RF}}(t)V_{\text{LO}}(t) \\
&= \frac{1}{2}KA_{\text{LO}}A_{\text{RF}}\{\cos[(\omega_{\text{LO}} - \omega_{\text{RF}})t - \phi_{\text{LO}}] \\
&\quad + \cos[(\omega_{\text{LO}} + \omega_{\text{RF}})t - \phi_{\text{LO}}]\}, \quad (97)
\end{aligned}$$

where K accounts for voltage conversion losses. According to Eq. (97), mixing with the LO results in two sidebands of frequencies $\omega_{\text{LO}} \pm \omega_{\text{RF}}$. The high-frequency component is filtered out with a low-pass filter (not shown) leaving only the

lower sideband of frequency $\omega_{\text{IF}} = \omega_{\text{LO}} - \omega_{\text{RF}}$. The choice $\omega_{\text{IF}} \neq 0$ is known as heterodyne detection. Taking the LO frequency such that ω_{IF} is in the range of a few tens of megahertz to a few hundred, the signal can be digitized using an analog-to-digital converter (ADC) with a sampling rate chosen in accordance with the bandwidth requirements of the signal to be recorded. This bandwidth is set by the choice of IF frequency and the signal bandwidth. For qubit readout, this is typically a few megahertz to a few tens of megahertz and is set by the bandwidth $\kappa/2\pi$ of the readout cavity. The recorded signal can then be averaged, or processed and analyzed in more complex ways, using real-time FPGA electronics or processed off-line. A detailed discussion of digital signal processing in the context of circuit QED was given by [Salathé *et al.* \(2018\)](#).

Going back to a quantum-mechanical description of the signal by combining Eqs. (95) and (97), the IF signals at the I and Q ports of the IQ mixer read

$$\hat{V}_I(t) = V_{\text{IF}}[\hat{X}_f(t) \cos(\omega_{\text{IF}}t) - \hat{P}_f(t) \sin(\omega_{\text{IF}}t)] + \hat{V}_{\text{noise},I}(t), \quad (98a)$$

$$\hat{V}_Q(t) = -V_{\text{IF}}[\hat{P}_f(t) \cos(\omega_{\text{IF}}t) + \hat{X}_f(t) \sin(\omega_{\text{IF}}t)] + \hat{V}_{\text{noise},Q}(t), \quad (98b)$$

where we take $\phi_{\text{LO}} = 0$ in the I arm of the IQ mixer, and $\phi_{\text{LO}} = \pi/2$ in the Q arm. We have defined $V_{\text{IF}} = KA_{\text{LO}}\sqrt{\kappa GZ_{\text{cm}}}\hbar\omega_{\text{RF}}/2$, and $\hat{V}_{\text{noise},I/Q}$ as the contributions from the amplifier noise and any other added noise. We have also introduced the quadratures

$$\hat{X}_f = \frac{\hat{a}_f^\dagger + \hat{a}_f}{2}, \quad \hat{P}_f = \frac{i(\hat{a}_f^\dagger - \hat{a}_f)}{2}, \quad (99)$$

the dimensionless position and momentum operators of the simple harmonic oscillator, here defined such that $[\hat{X}_f, \hat{P}_f] = i/2$. Taken together $\hat{V}_I(t)$ and $\hat{V}_Q(t)$ trace a circle in the $x_f - p_f$ plane and contain information about the quadratures \hat{X}_f and \hat{P}_f at all times. It is therefore possible to digitally transform the signals by going to a frame where they are stationary using the rotation matrix

$$R(t) = \begin{pmatrix} \cos(\omega_{\text{IF}}t) & -\sin(\omega_{\text{IF}}t) \\ \sin(\omega_{\text{IF}}t) & \cos(\omega_{\text{IF}}t) \end{pmatrix} \quad (100)$$

to extract $\hat{X}_f(t)$ and $\hat{P}_f(t)$.

We note that the case $\omega_{\text{IF}} = 0$ is generally known as homodyne detection ([Leonhardt, 1997](#); [Gardiner and Zoller, 1999](#); [Wiseman and Milburn, 2010](#); [Pozar, 2011](#)). Leaving the LO phase arbitrary, we find in this situation that the IF signal after down-conversion by a mixer is directly proportional to time-independent quadrature

$$\begin{aligned} \hat{X}_{f,\phi_{\text{LO}}} &= \frac{\hat{a}_f^\dagger e^{i\phi_{\text{LO}}} + \hat{a}_f e^{-i\phi_{\text{LO}}}}{2} \\ &= \hat{X}_f \cos \phi_{\text{LO}} + \hat{P}_f \sin \phi_{\text{LO}}. \end{aligned} \quad (101)$$

While this is in appearance simpler than the previous approach since a quadrature is immediately obtained, this measurement is susceptible to $1/f$ noise and drift because the homodyne signal is at dc. It is also worthwhile to note that homodyne detection as realized with the approach described here differs from optical homodyne detection, which can be performed in a noiseless fashion (in the present case, noise is added at the least by the phase-preserving amplifiers and the noise port of the IQ mixer) ([Eichler, Bozyigit, and Wallraff, 2012](#)). [Schuster *et al.* \(2005\)](#) and [Krantz *et al.* \(2019\)](#) provided more detailed discussions of the different field measurement techniques in the context of circuit QED.

B. Phase-space representations and their relation to field detection

In the context of field detection, it is particularly useful to represent the quantum state of the electromagnetic field using phase-space representations. There are several such representations, and here we focus on the Wigner function and the Husimi- Q distribution ([Carmichael, 2002](#); [Haroche and Raimond, 2006](#)). This discussion applies equally well to the intracavity field \hat{a} and to the filtered output field \hat{a}_f .

The Wigner function is a quasiprobability distribution given by the Fourier transform

$$W_\rho(x, p) = \frac{1}{\pi^2} \iint_{-\infty}^{\infty} dx' dp' C_\rho(x', p') e^{2i(px' - xp')} \quad (102)$$

of the characteristic function

$$C_\rho(x, p) = \text{Tr}\{\rho e^{2i(p\hat{X} - x\hat{P})}\}. \quad (103)$$

With ρ the state of the electromagnetic field, $C_\rho(x, p)$ can be understood as the expectation value of the displacement operator

$$\hat{D}(\alpha) = e^{2i(p\hat{X} - x\hat{P})} = e^{\alpha\hat{a}^\dagger - \alpha^*\hat{a}}, \quad (104)$$

with $\alpha = x + ip$; see Eq. (88).

The coherent states introduced in Eq. (87) have particularly simple Wigner functions. Indeed, as illustrated schematically in Fig. 17, the Wigner function $W_{|\beta\rangle}(\alpha)$ of the coherent state $|\beta\rangle$ is simply a Gaussian centered at β in phase space

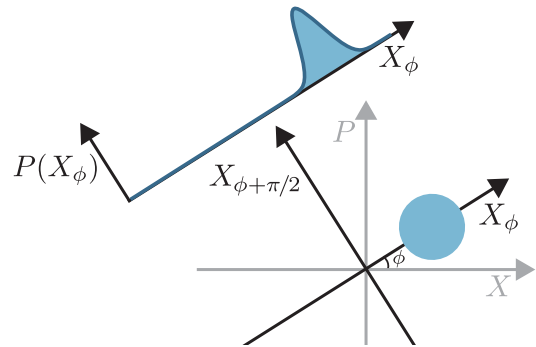


FIG. 17. Pictorial phase-space distribution of a coherent state and its marginal along an axis X_ϕ rotated by ϕ from X .

$$W_{|\beta\rangle}(\alpha) = \frac{2}{\pi} e^{-2|\alpha-\beta|^2}. \quad (105)$$

The width $1/\sqrt{2}$ of the Gaussian is a signature of quantum noise and implies that coherent states saturate the Heisenberg inequality $\Delta X \Delta P = 1/4$ with $\Delta O^2 = \langle \hat{O}^2 \rangle - \langle \hat{O} \rangle^2$. We note that, in contrast to Eq. (105), Wigner functions take negative values for nonclassical states of the field.

In the context of dispersive qubit measurements, the Wigner function is particularly useful because it is related to the probability distribution for the outcome of measurements of the quadratures \hat{X} and \hat{P} . Indeed, the marginals $P(x)$ and $P(p)$, obtained by integrating $W_\rho(x, p)$ along the orthogonal quadrature, are simply given by

$$P(x) = \int_{-\infty}^{\infty} dp W_\rho(x, p) = \langle x | \rho | x \rangle, \quad (106a)$$

$$P(p) = \int_{-\infty}^{\infty} dx W_\rho(x, p) = \langle p | \rho | p \rangle, \quad (106b)$$

where $|x\rangle$ and $|p\rangle$ are the eigenstates of \hat{X} and \hat{P} , respectively. This immediately implies that the probability distribution of the outcomes of an ideal homodyne measurement of the quadrature \hat{X}_ϕ is given by $P(x_\phi)$ obtained by integrating the Wigner function $W_\rho(\alpha)$ along the orthogonal quadrature $\hat{X}_{\phi+\pi/2}$. This is schematically illustrated for a coherent state in Fig. 17.

Another useful phase-space function is the Husimi- Q distribution, which for a state ρ takes the simple form

$$Q_\rho(\alpha) = \frac{1}{\pi} \langle \alpha | \rho | \alpha \rangle. \quad (107)$$

This function represents the probability distribution of finding ρ in the coherent state $|\alpha\rangle$ and, in contrast to $W_\rho(\alpha)$, it is therefore always positive.

Since $Q_\rho(\alpha)$ and $W_\rho(\alpha)$ are both complete descriptions of the state ρ , it is not surprising that one can be expressed in terms of the other. For example, in terms of the Wigner function, the Q function takes the form (Carmichael, 2002)

$$Q_\rho(\alpha) = \frac{2}{\pi} \int_{-\infty}^{\infty} d^2\beta W_\rho(\beta) e^{-2|\alpha-\beta|^2} = W_\rho(\alpha) * W_{|0\rangle}(\alpha). \quad (108)$$

The Husimi- Q distribution $Q_\rho(\alpha)$ is thus obtained by convolution of the Wigner function with a Gaussian and is therefore smoother than $W_\rho(\alpha)$. As made clear by the second equality, this Gaussian is in fact the Wigner function of the vacuum state $W_{|0\rangle}(\alpha)$, obtained from Eq. (105) with $\beta = 0$. In other words, the Q function for ρ is obtained from the Wigner function of the same state after adding vacuum noise. As illustrated in Fig. 16, heterodyne detection with an IQ mixer ideally adds vacuum noise to the signal before detection. This leads to the conclusion that the probability distributions for the simultaneous measurement of two orthogonal quadratures in heterodyne detection are given by the marginals of the Husimi- Q distribution rather than those of the Wigner function (Caves *et al.*, 2012).

C. Dispersive qubit readout

1. Steady-state intracavity field

As discussed in Sec. III.C, in the dispersive regime the transmon-resonator Hamiltonian is well approximated by

$$\hat{H}_{\text{disp}} \approx \hbar(\omega_r + \chi \hat{\sigma}_z) \hat{a}^\dagger \hat{a} + \frac{\hbar \omega_q}{2} \hat{\sigma}_z. \quad (109)$$

To simplify the discussion, here we truncate the transmon Hamiltonian to its first two levels, absorbed Lamb shifts in the system frequencies, and neglect a transmon-induced nonlinearity of the cavity [the term $\propto K_a$ in Eq. (52)]. As made clear by the first term of Eq. (109), in the dispersive regime, the resonator frequency becomes qubit-state dependent: If the qubit is in $|g\rangle$, then $\langle \hat{\sigma}_z \rangle = -1$ and the resonator frequency is $\omega_r - \chi$. On the other hand, if the qubit is in $|e\rangle$, $\langle \hat{\sigma}_z \rangle = 1$ and ω_r is pulled to $\omega_r + \chi$. In this situation, driving the cavity results in a qubit-state-dependent coherent state, $|\alpha_{g,e}\rangle$. Thus, if the qubit is initialized in the superposition $c_g|g\rangle + c_e|e\rangle$, the system evolves to an entangled qubit-resonator state of the form

$$c_g|g, \alpha_g\rangle + c_e|e, \alpha_e\rangle. \quad (110)$$

To interpret Eq. (110), we recall the paradigm of the Stern-Gerlach experiment. There an atom passes through a magnet and the field gradient applies a spin-dependent force to the atom that entangles the spin state of the atom with the momentum state of the atom (which in turn determines where the atom lands on the detector). The experiment is usually described as measuring the spin of the atom, but in fact it measures only the final position of that atom on the detector. However, since the spin and position are entangled, we can uniquely infer the spin from the position provided that there is no overlap in the final position distributions for the two spin states. In this case we have effectively performed a projective measurement of the spin.

By analogy, if the spin-dependent coherent states of the microwave field $\alpha_{e,g}$ can be resolved by heterodyne detection, then they act as pointer states (Zurek, 1981) in the qubit measurement. Moreover, since \hat{H}_{disp} commutes with the observable that is measured ($\hat{\sigma}_z$), this is a QND measurement⁸ (Braginsky, Vorontsov, and Thorne, 1980) (in contrast to the Stern-Gerlach measurement, which is destructive). Note that for a system initially in a superposition of eigenstates of the measurement operator, a QND measurement does in fact change the state by randomly collapsing it onto one of the

⁸Note that the original Jaynes-Cummings Hamiltonian (from which \hat{H}_{disp} is derived) does not commute with the bare qubit operator $\hat{\sigma}_z$. However, in writing the dispersive Hamiltonian we have made a unitary transformation which slightly dresses (coherently mixes) the qubit and cavity excitations and this dressed spin operator does commute with the dispersive Hamiltonian. This dressing implies a small Purcell-effect damping inherited by the qubit from the bare cavity damping, which we neglect for the moment. We return to this point later, however, when discussing the measurement fidelity and other approaches to qubit readout.

measurement eigenstates. The true test of ‘‘QND-ness’’ is that subsequent measurement results are not random but simply reproduce the first measurement result.

The objective in a qubit readout is to maximize the readout fidelity in the shortest possible measurement time. To see how this goal can be reached, it is useful to first evaluate more precisely the evolution of the intracavity field under such a measurement. The intracavity field is obtained from the Langevin equation (77) with $\hat{H}_s = \hat{H}_{\text{disp}}$ and by taking into account the cavity drive as discussed in Sec. IV.F. Doing so, we find that the complex field amplitude $\langle \hat{a} \rangle_\sigma = \alpha_\sigma$ given that the qubit is in state $\sigma = \{g, e\}$ satisfies

$$\dot{\alpha}_e(t) = -i\varepsilon(t) - i(\delta_r + \chi)\alpha_e(t) - \kappa\alpha_e(t)/2, \quad (111a)$$

$$\dot{\alpha}_g(t) = -i\varepsilon(t) - i(\delta_r - \chi)\alpha_g(t) - \kappa\alpha_g(t)/2, \quad (111b)$$

with $\delta_r = \omega_r - \omega_d$ the detuning of the measurement drive to the bare cavity frequency. The time evolutions of these two cavity fields in phase space are illustrated for three different values of $2\chi/\kappa$ by dashed gray lines in Figs. 18(a)–18(c).

Focusing on the steady-state response ($\dot{\alpha}_\sigma = 0$)

$$\alpha_{e/g}^s = \frac{-\varepsilon}{(\delta_r \pm \chi) - i\kappa/2}, \quad (112)$$

with + for e and – for g , results in the steady-state intracavity quadratures

$$\langle \hat{X} \rangle_{e/g} = \frac{\varepsilon(\delta_r \pm \chi)}{(\delta_r \pm \chi)^2 + (\kappa/2)^2}, \quad (113a)$$

$$\langle \hat{P} \rangle_{e/g} = \frac{\varepsilon\kappa/2}{(\delta_r \pm \chi)^2 + (\kappa/2)^2}. \quad (113b)$$

From Eqs. (113a) and (113b), we find that when driving the cavity at its bare frequency $\delta_r = 0$ information about the qubit state is contained only in the X quadrature; see Figs. 18(a)–18(c).

It is also useful to define the steady-state amplitude

$$A_{e/g}^s = \sqrt{\langle \hat{X} \rangle_{e/g}^2 + \langle \hat{P} \rangle_{e/g}^2} = \frac{\varepsilon}{\sqrt{(\kappa/2)^2 + (\delta_r \pm \chi)^2}} \quad (114)$$

and phase

$$\phi_{e/g}^s = \arctan\left(\frac{\langle \hat{X} \rangle_{e/g}}{\langle \hat{P} \rangle_{e/g}}\right) = \arctan\left(\frac{\delta_r \pm \chi}{\kappa/2}\right). \quad (115)$$

These two quantities are plotted in Fig. 19. As expected from the form of \hat{H}_{disp} , a coherent tone of frequency $\omega_r \pm \chi$ on the resonator leads to a large displacement of the resonator field and is largely transmitted if the qubit is in the ground (excited) state, and is mostly reflected if the qubit is in the excited (ground) state. Alternatively, driving the resonator at its bare frequency ω_r leads to a different phase accumulation for the transmitted signal depending on the state of the qubit. In particular, on resonance with the bare resonator $\delta_r = 0$ the phase shift of the signal associated with the two qubit states is

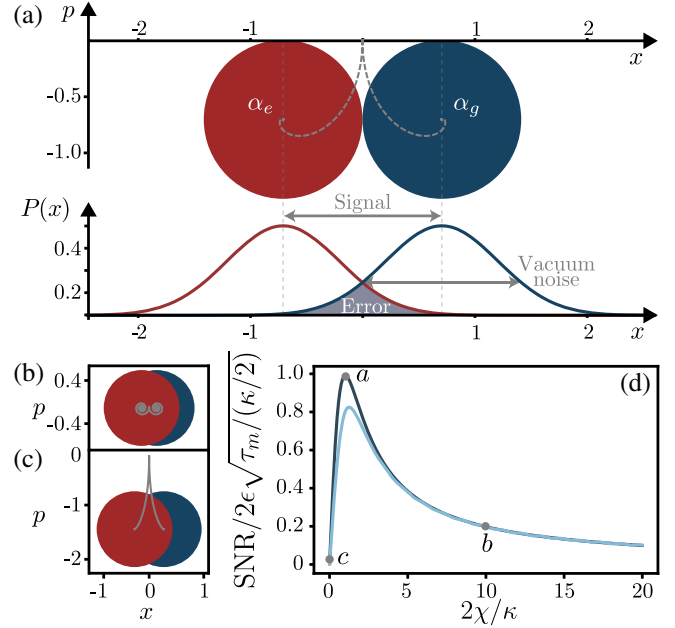


FIG. 18. (a) Path in phase space leading up to steady state of the intracavity pointer states α_g and α_e for $2\chi/\kappa = 1$, a measurement drive at the bare cavity frequency with an amplitude leading to one measurement photon at steady state, and assuming infinite qubit relaxation time (top panel). Corresponding marginals along x with the signal, noise, and error defined in the text (bottom panel). The circles of radius $1/\sqrt{2}$ represent vacuum noise. Path in phase space for (b) $2\chi/\kappa = 10$ and (c) $2\chi/\kappa = 0.2$. (d) Signal-to-noise ratio as a function of $2\chi/\kappa$ for an integration time $\tau_m/\kappa = 200$ (dark blue) and $\tau_m/\kappa = 10$ (light blue). The maximum of the SNR at short integration time is shifted away from $2\chi/\kappa = 1$. The letters correspond to the ratio $2\chi/\kappa$ of (a)–(c).

simply $\pm \arctan(2\chi/\kappa)$. As a result, in the dispersive regime measuring the amplitude and/or the phase of the transmitted or reflected signal from the resonator reveals information about the qubit state (Blais *et al.*, 2004). On the other hand, when driving the resonator at a frequency that is largely detuned from $(\omega_r, \omega_r \pm \chi)$, for example, when driving at the qubit frequency to realize a logical gate discussed in Sec. VII.A, the

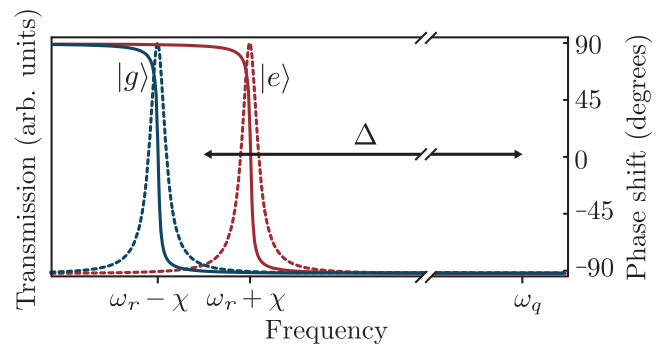


FIG. 19. Resonator transmission (dashed lines) and corresponding phase shifts (solid lines) for the two qubit states (blue, ground; red, excited). When driving the resonator close to its pulled frequencies, the resonator response strongly depends on the state of the qubit. Adapted from Blais *et al.*, 2007.

response of the resonator field only negligibly depends on the qubit state. This results in negligible entanglement in the resonator, and consequently in negligible measurement-induced dephasing on the qubit.

It is important to note that to simplify the presentation, the previous discussion was couched in terms of the amplitude and phase of the field internal to the microwave resonator. In practice, we can typically measure the field only externally in the transmission line(s) coupled to the resonator. The relation between the two is the subject of the input-output theory discussed in Sec. IV and Appendix C. The main ideas can be summarized rather simply. Consider an asymmetric cavity with one port strongly coupled to the environment and one port weakly coupled. If driven from the weak port, nearly all of the information about the state of the qubit is in the field radiated by the cavity into the strongly coupled port. The same is true if the cavity is driven from the strongly coupled side, but now the output field is a superposition of the directly reflected drive plus the field radiated by the cavity. If the drive frequency is swept across the cavity resonance, the signal undergoes a phase shift of π in the former case and 2π in the latter. This affects the sensitivity of the output field to the dispersive shift induced by the qubit. If the cavity is symmetric, then half the information about the state of the qubit appears at each output port, so this configuration is less efficient. Further details were given by Clerk *et al.* (2010).

2. Signal-to-noise ratio and measurement fidelity

Except for the last paragraph, the previous discussion concerned the steady-state intracavity field from which we can infer the steady-state heterodyne signal. It is important, however, to consider the temporal response of the resonator's output field to the measurement drive since, in the context of quantum computing, qubit readout should be as fast as possible. Moreover, the probability of assigning the correct outcome to a qubit measurement, or more simply put the measurement fidelity, must also be large. As the following discussion illustrates, simultaneously optimizing these two important quantities requires some care.

As discussed in Sec. V.A, the quadratures $\hat{X}_f(t)$ and $\hat{P}_f(t)$ are extracted from heterodyne measurement of the resonator output field. Combining these signals and integrating for a time τ_m , the operator corresponding to this measurement takes the form

$$\hat{M}(\tau_m) = \int_0^{\tau_m} dt \{ w_X(t) [V_{\text{IF}} \hat{X}_f(t) + \hat{V}_{\text{noise}, X_f}(t)] + w_P(t) [V_{\text{IF}} \hat{P}_f(t) + \hat{V}_{\text{noise}, P_f}(t)] \}, \quad (116)$$

where $\hat{V}_{\text{noise}, X_f/P_f}(t)$ is the noise in the X_f/P_f quadrature. The weighting functions $w_X(t) = \langle \hat{X}_f \rangle_e - \langle \hat{X}_f \rangle_g$ and $w_P(t) = \langle \hat{P}_f \rangle_e - \langle \hat{P}_f \rangle_g$ are multiplied by the signal and chosen to increase the discrimination of the two qubit states (Magesan *et al.*, 2015; Ryan *et al.*, 2015; Walter *et al.*, 2017; Bultink *et al.*, 2018). Intuitively, because of qubit relaxation, these functions give less weight to the cavity response at long times since it will always reveal the qubit to be in its ground state, irrespective of the prepared state (Gambetta *et al.*, 2007).

Moreover, for the situation illustrated in Fig. 18, there is no information on the qubit state in the P quadrature. Reflecting this, $w_P(t) = 0$, which prevents the noise in that quadrature from being integrated.

Following Secs. V.A and V.B, the probability distribution for the outcome of multiple shots of the measurement of $\hat{M}(\tau_m)$ is expected to be Gaussian and characterized by the marginal of the Q function of the intracavity field. Using the previous expression, the signal-to-noise ratio (SNR) of this measurement can be defined as illustrated in Fig. 18(a) for the intracavity field: it is the separation of the average combined heterodyne signals corresponding to the two qubit states divided by the standard deviation of the signal, an expression that takes the form

$$\text{SNR}^2(t) \equiv \frac{|\langle \hat{M}(t) \rangle_e - \langle \hat{M}(t) \rangle_g|^2}{\langle \hat{M}_N^2(t) \rangle_e + \langle \hat{M}_N^2(t) \rangle_g}. \quad (117)$$

Here $\langle \hat{M} \rangle_\sigma$ is the average integrated heterodyne signal, given that the qubit is in state σ and $\hat{M}_N = \hat{M} - \langle \hat{M} \rangle$ is the noise operator that takes into account the added noise and also the intrinsic vacuum noise of the quantum states of the resonator field.

In addition to the SNR, another important quantity is the measurement fidelity (Gambetta *et al.*, 2007; Walter *et al.*, 2017)⁹

$$F_m = 1 - [P(e|g) + P(g|e)] \equiv 1 - E_m, \quad (118)$$

where $P(\sigma|\sigma')$ is the probability that a qubit in state σ is measured to be in state σ' . In the second equality, we have defined the measurement error E_m , which as illustrated in Fig. 18(a) is simply the overlap of the marginals $P_\sigma(x)$ of the Q functions for the two qubit states. This can be expressed as $E_m = \int dx_{\phi_{\text{LO}} + \pi/2} \min[P_0(x_{\phi_{\text{LO}} + \pi/2}), P_1(x_{\phi_{\text{LO}} + \pi/2})]$, where the LO phase is chosen to minimize E_m . Using this expression, the measurement fidelity is found to be related to the SNR by $F_m = 1 - \text{erfc}(\text{SNR}/2)$, where erfc is the complementary error function (Gambetta *et al.*, 2007). It is important to note that this last result is valid only if the marginals are Gaussian. In practice, qubit relaxation and higher-order effects omitted in the dispersive Hamiltonian (109) can lead to distortion of the coherent states and therefore to non-Gaussian marginals (Gambetta *et al.*, 2007; Hatridge *et al.*, 2013). Kerr-type nonlinearities that are common in circuit QED tend to create a banana-shaped distortion of the coherent states in phase space, a process that is sometimes referred to as bananization (Boutin *et al.*, 2017; Malnou *et al.*, 2018; Sivak *et al.*, 2019).

Although we are interested in short measurement times, it is useful to consider a simpler expression for the longtime behavior of the SNR that suggests different strategies for

⁹An alternative definition known as the assignment fidelity is $1 - (1/2)[P(e|g) - P(g|e)]$ (Magesan *et al.*, 2015). This quantity takes values in $[0, 1]$ and formally $F_m \in [-1, 1]$. Negative values, however, are not relevant in practice. Indeed, because $F_m = -1$ corresponds to systematically reporting the incorrect value, a fidelity of 1 is recovered after flipping the measurement outcomes.

maximizing the measurement fidelity. Assuming that $\delta_r = 0$ and ignoring the prefactors related to gain and mixing, we find that (Gambetta *et al.*, 2008)

$$\text{SNR}(\tau_m \rightarrow \infty) \simeq (2\epsilon/\kappa)\sqrt{2\kappa\tau_m}|\sin 2\phi|, \quad (119)$$

where ϕ is given by Eq. (115); see Didier, Bourassa, and Blais (2015) for a detailed derivation of this expression. One can easily verify that the choice $\chi/\kappa = 1/2$ maximizes Eq. (119); see Fig. 18(d) (Gambetta *et al.*, 2008). This ratio is consequently often chosen in experiments (Walter *et al.*, 2017). While leading to a smaller steady-state SNR, other choices of the ratio χ/κ can be more advantageous at finite measurement times.

In the small χ limit, the factor $2\epsilon/\kappa$ in $\text{SNR}(\tau_m \rightarrow \infty)$ can be interpreted by using Eq. (112) as the square root of the steady-state average intracavity measurement photon number. Another approach for improving the SNR is therefore to work with the large measurement photon number \bar{n} . This idea cannot be pushed too far since increasing the measurement photon number leads to a breakdown of the approximations that have been used to derive the dispersive Hamiltonian (109). Indeed, as discussed in Sec. III.C the small parameter in the perturbation theory that leads to the dispersive approximation is not g/Δ but instead \bar{n}/n_{crit} , with n_{crit} the critical photon number introduced in Eq. (46). Well before reaching $\bar{n}/n_{\text{crit}} \sim 1$, higher-order terms in the dispersive approximation start to play a role and lead to departures from the expected behavior. For example, it is commonly experimentally observed that the dispersive measurement loses its QND character well before $\bar{n} \sim n_{\text{crit}}$ and often at measurement photon populations as small as $\bar{n} \sim 1-10$ (Johnson *et al.*, 2011; Mineev *et al.*, 2019). Because of these spurious qubit flips, measurement photon numbers are typically chosen to be well below n_{crit} (Walter *et al.*, 2017). While this non-QND-ness at $\bar{n} < n_{\text{crit}}$ is expected from the discussion of dressed dephasing found in Sec. IV.D, the predicted measurement-induced qubit flip rates are smaller than often experimentally observed. We note that qubit transitions at $\bar{n} > n_{\text{crit}}$ caused by accidental resonances within the qubit-resonator system were studied by Sank *et al.* (2016).

To reach high fidelities, it is also important for the measurement to be fast compared to the qubit relaxation time T_1 . A strategy to speed up the measurement is to use a low- Q oscillator, which leads to a faster readout rate simply because the measurement photons leak out more rapidly from the resonator to be detected. However, this should not be done at the price of increasing the Purcell rate γ_κ to the point where this mechanism dominates qubit decay (Houck *et al.*, 2008). As discussed in Sec. IV.E, it is possible to avoid this situation to a large extent by adding a Purcell filter at the output of the resonator (Reed, Johnson *et al.*, 2010; Jeffrey *et al.*, 2014; Bronn *et al.*, 2015).

Fixing κ so as to avoid Purcell decay and working at the optimal χ/κ ratio, it can be shown that the steady-state response is reached in a time $\propto 1/\chi$ (Walter *et al.*, 2017). Large dispersive shifts can therefore help to speed up the measurement. As can be seen in Eq. (45), χ can be increased by working at larger qubit anharmonicity or, in other words,

larger charging energy E_C . Once more, this cannot be pushed too far since the transmon charge dispersion, and therefore its dephasing rate, increases with E_C .

This discussion shows that QND qubit measurement in circuit QED is a highly constrained problem. When readout time is to be minimized while achieving maximum fidelity, the state of the art for such measurements recently reached $F_m \sim 98.25\%$ in $\tau_m = 48$ ns and 99.2% in 88 ns, in both cases using $\bar{n} \sim 2.5$ intracavity measurement photons (Walter *et al.*, 2017). These results were obtained by careful optimization of the system parameters, simultaneously realizing one of the largest dispersive shifts and cavity bandwidths explored in the literature and, following the previously introduced concepts, exploiting the understanding of the full-time response of the measurement signal $|\langle \hat{M}(t) \rangle_1 - \langle \hat{M}(t) \rangle_0|$. The main limitation in these reported fidelities was a relatively short qubit relaxation time of $7.6 \mu\text{s}$. With qubits of sufficiently long relaxation time, state selectively excited to higher states to increase readout performance and at the expense of longer integration time, fidelities of up to 99.96% have been achieved (Elder *et al.*, 2020). Joint simultaneous dispersive readout of two transmon qubits capacitively coupled to the same resonator has also been realized (Filipp *et al.*, 2009).

The small photon number used in some of these readout experiments underscores the importance of quantum-limited amplifiers in the first stage of the measurement chain; see Fig. 14. Before the development of these amplifiers, which created the possibility of performing strong single-shot (i.e., projective) measurements, the SNR in dispersive measurements was well below unity, forcing the results of these weak measurements to be averaged over tens of thousands of repetitions of the experiment to extract information about the qubit state (Wallraff *et al.*, 2005). The advent of near-quantum-limited amplifiers has made it possible to resolve the qubit state in a single shot, which has led to the observation of quantum jumps of a transmon qubit (Vijay, Slichter, and Siddiqi, 2011), and even to the possibility of catching and reserving quantum jumps (Mineev *et al.*, 2019).

Finally, we point out that the quantum efficiency η of the entire measurement chain can be extracted from the SNR by using (Bultink *et al.*, 2018)

$$\eta = \frac{\text{SNR}^2}{2\beta_m}, \quad (120)$$

where $\beta_m = 2\chi \int_0^{\tau_m} dt \text{Im}[\alpha_g(t)\alpha_e(t)^*]$ is related to the measurement-induced dephasing that is discussed further in Sec. VI.B.2.¹⁰ This connection between quantum efficiency, SNR, and measurement-induced dephasing results from the fundamental link between the rate at which information is gained in a quantum measurement and the unavoidable

¹⁰Note that Eq. (120) differs by a factor of 2 from the expression given by Bultink *et al.* (2018). This is because we have used the convention that the noise entering the SNR in Eq. (117) has contributions from both $\langle \hat{M}_N^2(t) \rangle_e$ and $\langle \hat{M}_N^2(t) \rangle_g$, while Bultink *et al.* (2018) took these two terms to be equal and did not add their contributions to their definition of the SNR.

backaction on the measured system (Korotkov, 2001; Clerk *et al.*, 2010).

3. Other approaches to qubit readout

a. Josephson bifurcation amplifier

While the vast majority of circuit QED experiments rely on the previously described approach, several other qubit-readout methods have been theoretically explored or experimentally implemented. One such alternative is known as the Josephson bifurcation amplifier and relies on using a transmission-line resonator that is made nonlinear by incorporating a Josephson junction into its center conductor (Boaknin *et al.*, 2007). This circuit can be seen as a distributed version of the transmon qubit and is well described by the Kerr-nonlinear Hamiltonian of Eq. (27) (Bourassa *et al.*, 2012). With a relatively weak Kerr nonlinearity (~ -500 kHz) and under a coherent drive of well-chosen amplitude and frequency, this system bifurcates from a low photon-number state to a high photon-number state (Dykman and Krivoglaz, 1980; Manucharyan *et al.*, 2007). By dispersively coupling a qubit to the nonlinear resonator, this bifurcation can be made qubit-state dependent (Vijay, Devoret, and Siddiqi, 2009). It is possible to exploit the fact that the low- and high-photon-number states can be easily distinguished to realize high-fidelity single-shot qubit readout (Mallet *et al.*, 2009).

b. High-power readout and qubit “punch out”

Returning to linear resonators, while the previously mentioned non-QND-ness at moderate measurement photon number leads to small measurement fidelity, it was observed that, in the limit of large measurement power, a fast and high-fidelity single-shot readout is recovered (Reed, DiCarlo *et al.*, 2010). Intuitive understanding of this observation can be obtained from the Jaynes-Cummings Hamiltonian (36) (Bishop, Ginossar, and Girvin, 2010; Boissonneault, Gambetta, and Blais, 2010). Indeed, for $n \gg \sqrt{n}$ the first term of this Hamiltonian dominates over the qubit-oscillator interaction $\propto g$ such that the cavity responds at its bare frequency ω_r despite the presence of the transmon. This is sometimes referred to as “punching out” the qubit and can be understood as a quantum-to-classical transition where, in the correspondence limit, the system behaves classically and therefore responds at the bare cavity frequency ω_r . With a multilevel system such as the transmon, the power at which this transition occurs depends on the state of the transmon, leading to a high-fidelity measurement. This high-power readout is obtained, however, at the expense of completely losing the QND nature of the dispersive readout (Boissonneault, Gambetta, and Blais, 2010).

c. Squeezing

Finally, the previously mentioned \sqrt{n} scaling of SNR ($\tau_m \rightarrow \infty$) can be interpreted as resulting from populating the cavity with a coherent state and is known as the standard quantum limit. It is natural to ask if replacing the coherent measurement tone with squeezed input radiation (see Sec. VIII.C.2) can lead to Heisenberg-limited scaling for which the SNR scales linearly with the measurement photon number

(Giovannetti, Lloyd, and Maccone, 2004). To achieve this, one might imagine squeezing a quadrature of the field to reduce the overlap between the two pointer states. In Fig. 18, this corresponds to squeezing along x . The situation is not so simple since the large dispersive coupling required for high-fidelity qubit readout leads to a significant rotation of the squeezing angle as the pointer states evolve from the center of phase space to their steady state. This rotation results in increased measurement noise due to contributions from the antisqueezed quadrature (Barzanjeh, DiVincenzo, and Terhal, 2014). Borrowing the idea of quantum-mechanics-free subsystems (Tsang and Caves, 2012), it has been shown that Heisenberg-limited scaling can be reached with two-mode squeezing by dispersively coupling the qubit to two rather than one resonator (Didier *et al.*, 2015).

d. Longitudinal readout

An alternative approach to qubit readout is based on the Hamiltonian \hat{H}_z of Eq. (65) with its longitudinal qubit-oscillator coupling $g_z(\hat{a}^\dagger + \hat{a})\hat{\sigma}_z$. In contrast to the dispersive Hamiltonian that leads to a rotation in phase space, longitudinal coupling generates a linear displacement of the resonator field that is conditional on the qubit state. As a result, while under the dispersive evolution there is little information gain about the qubit state at short times [see the poor pointer state separation at short times in Fig. 18(a)], \hat{H}_z instead generates the ideal dynamics for a measurement with a 180° out-of-phase displacement of the pointer states α_g and α_e . It is therefore expected that this approach can lead to much shorter measurement times than is possible with the dispersive readout (Didier, Bourassa, and Blais, 2015).

Another advantage is that \hat{H}_z commutes with the measured observable $[\hat{H}_z, \hat{\sigma}_z] = 0$ corresponding to a QND measurement. While the dispersive Hamiltonian \hat{H}_{disp} also commutes with $\hat{\sigma}_z$, it is not the case for the full Hamiltonian (34) from which \hat{H}_{disp} is perturbatively derived. As already discussed, this non-QND-ness leads to Purcell decay and to a breakdown of the dispersive approximation when the photon populations is not significantly smaller than the critical photon number n_{crit} . On the other hand, because \hat{H}_z is genuinely QND it does not suffer from these problems and the measurement photon number can, in principle, be made larger under longitudinal than under dispersive coupling. Moreover, given that \hat{H}_z leads to displacement of the pointer states rather than to rotation in phase space, single-mode squeezing can also be used to increase the measurement SNR (Didier, Bourassa, and Blais, 2015).

Because the longitudinal coupling can be thought of as a cavity drive of amplitude $\pm g_z$, with the sign conditional on the qubit state, \hat{H}_z leads in steady state to a pointer state displacement $\pm g_z/(\omega_r + i\kappa/2)$; see Eq. (112). With $\omega_r \gg g_z, \kappa$ in practice this displacement is negligible and cannot realistically be used for qubit readout. One approach to increasing the pointer state separation is to activate the longitudinal coupling by modulating g_z at the resonator frequency (Kerman, 2013; Didier, Bourassa, and Blais, 2015). Taking $g_z(t) = \tilde{g}_z \cos(\omega_r t)$ leads, in a rotating frame and after dropping rapidly oscillating terms, to the Hamiltonian

$$\tilde{H}_z = \frac{\tilde{g}_z}{2}(\hat{a}^\dagger + a)\hat{\sigma}_z. \quad (121)$$

Under this modulation, the steady-state displacement now becomes $\pm\tilde{g}_z/\kappa$ and can be significant even for moderate modulation amplitudes \tilde{g}_z .

Circuits realizing the longitudinal coupling with transmon or flux qubits have been studied (Kerman, 2013; Billangeon, Tsai, and Nakamura, 2015a, 2015b; Didier, Bourassa, and Blais, 2015; Richer and DiVincenzo, 2016; Richer *et al.*, 2017). Another approach to realizing these ideas is to strongly drive a resonator dispersively coupled to a qubit (Blais *et al.*, 2007; Dassonneville *et al.*, 2020). Indeed, the strong drive leads to a large displacement of the cavity field $\hat{a} \rightarrow \hat{a} + \alpha$, which on the dispersive Hamiltonian leads to

$$\chi\hat{a}^\dagger\hat{a}\hat{\sigma}_z \rightarrow \chi\hat{a}^\dagger\hat{a}\hat{\sigma}_z + \alpha\chi(\hat{a}^\dagger + \hat{a})\hat{\sigma}_z + \chi\alpha^2\hat{\sigma}_z, \quad (122)$$

where we have assumed α to be real for simplicity. For χ small and α large, the second term dominates, therefore realizing a synthetic longitudinal interaction of amplitude $g_z = \alpha\chi$. In other words, longitudinal readout can be realized as a limit of the dispersive readout where χ approaches zero, while α grows such that $\chi\alpha$ is constant. A simple interpretation of this observation is that for strong drives the circle on which the pointer states rotate due to the dispersive interaction has a large radius α such that, for all practical purposes, the motion appears to be linear.

A variation of this approach that allows for larger longitudinal coupling strength was experimentally realized by Ikonen *et al.* (2019) and Touzard *et al.* (2019) and relies on driving the qubit at the frequency of the resonator. This is akin to the cross-resonance gate discussed further in Sec. VII.B.3, which leads to the desired longitudinal interaction; see the last term of Eq. (146). A more subtle approach to realizing a synthetic longitudinal interaction is to drive a qubit with a Rabi frequency Ω_R while driving the resonator at the sideband frequencies $\omega_r \pm \Omega_R$. This idea was implemented by Eddins *et al.* (2018), who also showed improvement of qubit readout with single-mode squeezing. Because these realizations are based on the dispersive Hamiltonian, they suffer from Purcell decay and non-QND-ness. Circuits realizing dispersivelike interactions that are not derived from a Jaynes-Cummings interaction have been studied (Didier, Bourassa, and Blais, 2015; Dassonneville *et al.*, 2020).

VI. QUBIT-RESONATOR COUPLING REGIMES

We now turn to a discussion of the different coupling regimes that are accessible in circuit QED and of their experimental signatures. We first consider the resonant regime where the qubit is tuned in resonance with the resonator, then move on to the dispersive regime characterized by a large qubit-resonator detuning. While the situation of most experimental interest is the strong-coupling regime where the coupling strength g overwhelms the decay rates, we also touch upon the so-called bad-cavity and bad-qubit limits because of their historical importance and their current relevance to hybrid quantum systems. Finally, we consider the ultrastrong-coupling regime where g is comparable, or

even larger, than the system's frequencies. To simplify the discussion, we treat the artificial atom as a simple two-level system throughout this section.

A. Resonant regime

The low-energy physics of the Jaynes-Cummings model is well described by the ground state $|\overline{g}, \overline{0}\rangle = |g, 0\rangle$ and the first two excited states

$$\begin{aligned} |\overline{g}, \overline{1}\rangle &= (|g, 1\rangle - |e, 0\rangle)/\sqrt{2}, \\ |\overline{e}, \overline{0}\rangle &= (|g, 1\rangle + |e, 0\rangle)/\sqrt{2}, \end{aligned} \quad (123)$$

which, as illustrated in Fig. 8, are split in frequency by $2g$. As discussed in Sec. V.C in the context of the dispersive readout, the coupled qubit-resonator system can be probed by applying a coherent microwave tone to the input of the resonator and measuring the transmitted or reflected signal.

To arrive at an expression for the expected signal in such an experiment, we consider the equations of motion for the field and qubit annihilation operators in the presence of a coherent drive of amplitude ε and frequency ω_d on the resonator. In a frame rotating at the drive frequency, these equations take the form

$$\langle \dot{\hat{a}} \rangle = -\left(\frac{\kappa}{2} + i\delta_r\right)\langle \hat{a} \rangle - ig\langle \hat{\sigma}_- \rangle - i\varepsilon, \quad (124)$$

$$\langle \dot{\hat{\sigma}}_- \rangle = -(\gamma_2 + i\delta_q)\langle \hat{\sigma}_- \rangle + ig\langle \hat{a}\hat{\sigma}_z \rangle, \quad (125)$$

with $\delta_r = \omega_r - \omega_d$ and $\delta_q = \omega_q - \omega_d$, and where γ_2 is defined in Eq. (82b). Equations (124) and (125) are obtained using $\partial_t\langle \hat{O} \rangle = \text{Tr}\rho\dot{\hat{O}}$ and the master equations of Eqs. (70) and (81) at zero temperature and in the two-level approximation for the transmon. Alternatively, the expression for $\partial_t\langle \hat{a} \rangle$ is simply the average of Eq. (77), with \hat{H}_s the Jayne-Cummings Hamiltonian.

At low excitation amplitude ε , it is reasonable to truncate the Hilbert space to the previously defined first three levels. In this subspace, $\langle \hat{a}\hat{\sigma}_z \rangle = -\langle \hat{a} \rangle$ since \hat{a} acts nontrivially only if the qubit is in the ground state (Kimble, 1994). It is then simple to compute the steady-state transmitted homodyne power by solving the previous expressions with $\partial_t\langle \hat{a} \rangle = \partial_t\langle \hat{\sigma}_- \rangle = 0$ and using Eq. (114) to find

$$|A|^2 = \left(\frac{\varepsilon V_{\text{IF}}}{2}\right)^2 \left| \frac{\delta_q - i\gamma_2}{(\delta_q - i\gamma_2)(\delta_r - i\kappa/2) - g^2} \right|^2. \quad (126)$$

Taking the qubit and the oscillator to be on resonance ($\Delta = \omega_q - \omega_r = 0$), we now consider the result of cavity transmission measurements in three different regimes of qubit-cavity interaction.

1. Bad-cavity limit

We first consider the bad-cavity limit realized when the cavity decay rate overwhelms the coupling g , which is itself larger than the qubit linewidth: $\kappa > g \gg \gamma_2$. This situation corresponds to an overdamped oscillator and, at qubit-oscillator resonance, leads to rapid Purcell decay of the qubit.

A simple model for this process is obtained using the truncated Hilbert space discussed earlier, where we now drop the cavity drive for simplicity. Because of the large decay rate κ , we can assume that the oscillator will rapidly reach its steady state $\partial_t \langle \hat{a} \rangle = 0$. Using the resulting expression for $\langle \hat{a} \rangle$ in Eq. (125) immediately leads to

$$\langle \hat{\sigma}_- \rangle = - \left(\frac{\gamma_1 + \gamma'_k + \gamma_\varphi}{2} \right) \langle \hat{\sigma}_- \rangle, \quad (127)$$

where we have defined the Purcell decay rate $\gamma'_k = 4g^2/\kappa$. The expression for this rate has a different form than the Purcell rate $\gamma_k = (g/\Delta)^2\kappa$ given in Eq. (85). These two results, however, are not incompatible but have been obtained in significantly different regimes. An expression for the Purcell rate that interpolates between the two previous expressions can be obtained and takes the form of $\kappa g^2 / [(\kappa/2)^2 + \Delta^2]$ (Sete, Gambetta, and Korotkov, 2014).

The situation described here is illustrated for $\kappa/g = 10$ and $\gamma_1 = 0$ in Fig. 20(a), which shows the probability of the qubit

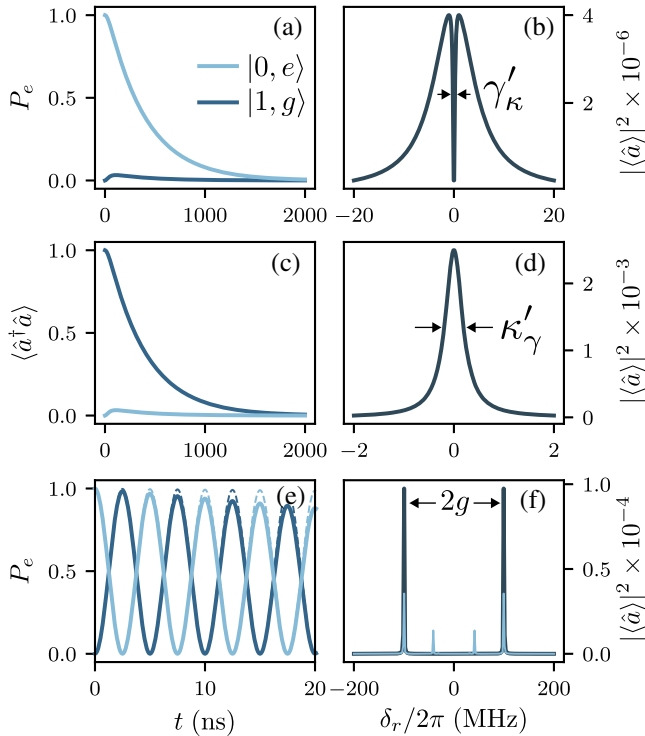


FIG. 20. Numerical simulations of the qubit-oscillator master equation for (a),(c),(e) the time evolution starting from the bare state $|0, e\rangle$ (light blue lines) or $|1, g\rangle$ (blue lines), and (b), (d),(f) steady-state response $A^2 = |\langle \hat{a} \rangle|^2$ as a function of the cavity drive frequency (dark blue lines) for the three coupling regimes. P_e : qubit excited state population. (a),(b) Bad-cavity limit: $(\kappa, \gamma_1, g)/2\pi = (10, 0, 1)$ MHz. (c),(d) Bad-qubit limit: $(\kappa, \gamma_1, g)/2\pi = (0, 10, 1)$ MHz. (e),(f) Strong coupling: $(\kappa, \gamma_1, g)/2\pi = (0.1, 0.1, 100)$ MHz [dashed lines in (e) and solid lines in (f)] and $(\kappa, \gamma_1, g)/2\pi = (1, 1, 100)$ [solid lines in (e)]. The light blue line in (f) is computed with a thermal photon number of $\bar{n}_\kappa = 0.35$, as opposed to $\bar{n}_\kappa = 0$ for all other results.

being in its excited state versus time after initializing the qubit in its excited state and the resonator in vacuum. Even in the absence of qubit T_1 , the qubit is seen to quickly relax to its ground state, which as discussed in Sec. IV.D is due to qubit-oscillator hybridization. Figure 20(b) shows the steady-state transmitted power versus drive frequency in the presence of a weak coherent tone populating the cavity with $\bar{n} \ll 1$ photons. The response shows a broad Lorentzian peak of width κ together with a narrow electromagnetically induced transparency (EIT) window of width γ'_k (Rice and Brecha, 1996; Mlynek *et al.*, 2014). This effect that is due to interference between the intracavity field and the probe tone vanishes in the presence of qubit dephasing.

Although not the main regime of interest in circuit QED, the bad-cavity limit offers an opportunity to engineer the dissipation seen by the qubit. This regime has been used to control the lifetime of long-lived donor spins in silicon in a hybrid quantum system (Bienfait *et al.*, 2016).

2. Bad-qubit limit

The bad-qubit limit corresponds to the situation where a high- Q cavity with large qubit-oscillator coupling is realized, while the qubit dephasing and/or energy relaxation rates is large: $\gamma_2 > g \gg \kappa$. Although this situation is not typical of circuit QED with transmon qubits, it is relevant for some hybrid systems that suffer from significant dephasing. This is the case in early experiments with charge qubits based on semiconductor quantum dots coupled to superconducting resonators (Frey *et al.*, 2012; Petersson *et al.*, 2012; Viennot *et al.*, 2014).

In analogy to the bad-cavity case, the strong damping of the qubit together with the qubit-resonator coupling leads to the photon decay rate $\kappa'_\gamma = 4g^2/\gamma_1$, which is sometimes known as the “inverse” Purcell rate. This is illustrated in Fig. 20(c), which shows the time evolution of the coupled system starting with a single photon in the resonator and the qubit in the ground state. In this situation, the cavity response is a simple Lorentzian broadened by the inverse Purcell rate; see Fig. 20(d). If the qubit were to be probed directly rather than indirectly via the cavity, the atomic response would show the EIT-like feature of Fig. 20(b), now with a dip of width κ'_γ (Rice and Brecha, 1996). One should also be aware that qubit-resonator detuning-dependent dispersive shifts of the cavity resonance can be observed in this bad-qubit limit. The observation of such dispersive shifts on its own should not be mistaken for an observation of strong coupling (Wallraff *et al.*, 2013).

3. Strong-coupling regime

We now turn to the case where the coupling strength overwhelms the qubit and cavity decay rates $g > \kappa, \gamma_2$. In this regime, light-matter interaction is strong enough for a single quantum to be coherently exchanged between the electromagnetic field and the qubit before it is irreversibly lost to the environment. In other words, at resonance $\Delta = 0$ the splitting $2g$ between the two dressed eigenstates $\{|g, 1\rangle, |e, 0\rangle\}$ of Eq. (123) is larger than their linewidth $\kappa/2 + \gamma_2$ and can be resolved spectroscopically. We note that with the eigenstates

being half photon and half qubit¹¹ the previous expression for the dressed-state linewidth is simply the average of the cavity and of the qubit linewidth (Haroche, 1992). Figure 20(f) shows the cavity transmission for $(\kappa, \gamma_1, \gamma_\varphi)/g = (0.1, 0.1, 0)$ and at low excitation power such that, on average, there is significantly less than one photon in the cavity. The resulting doublet of peaks located at $\omega_r \pm g$ is the direct signature of the dressed states $\{|g, \bar{1}\rangle, |e, \bar{0}\rangle\}$ and is known as the vacuum Rabi splitting. The observation of this doublet is the hallmark of the strong-coupling regime.

The first observation of this feature in cavity QED with a single atom and a single photon was reported by Thompson, Rempe, and Kimble (1992). In this experiment, the number of atoms in the cavity was not well controlled and it could be determined only that there was on average one atom in interaction with the cavity field. This distinction is important because, in the presence of N atoms, the collective interaction strength is $g\sqrt{N}$ and the observed splitting is correspondingly larger (Tavis and Cummings, 1968; Fink *et al.*, 2009). Atom number fluctuation is not a problem in circuit QED and, with the strong coupling and relatively small linewidths that can routinely be experimentally achieved, reaching the strong-coupling regime is not particularly challenging in this system. In fact, the first circuit QED experiment performed by Wallraff *et al.* (2004) reported the observation of a vacuum Rabi splitting with $2g/(\kappa/2 + \gamma_2) \sim 10$; see Fig. 21(a). This first demonstration used a charge qubit that by construction has a much smaller coupling g than typical transmon qubits. As a result, more recent experiments with transmon qubits can display ratios of peak separation to linewidth in the several hundreds; see Fig. 21(b) (Schoelkopf and Girvin, 2008).

Like Fig. 21, Fig. 22 shows the qubit-oscillator spectrum as a function of probe frequency, but now also as a function of the qubit frequency, allowing one to see the full qubit-resonator avoided crossing. The horizontal dashed line corresponds to the bare cavity frequency while the diagonal dashed line is the bare qubit frequency. The vacuum Rabi splitting of Fig. 20(f) is obtained from a linecut (dotted vertical line) at resonance between the bare qubit frequency ω_q and the bare cavity frequency ω_r . Because it is the cavity that is probed here, the response is larger when the dressed states are mostly cavitylike and disappears away from the cavity frequency, where the cavity no longer responds to the probe (Haroche, 1992).

Note that the splitting predicted by Eq. (126) for the transmitted homodyne signal is in fact smaller than $2g$ in the presence of finite relaxation and dephasing. Although not significant in circuit QED with transmon qubits, this correction can become important in systems such as charge qubits in quantum dots that are not deep in the strong-coupling regime. We also note that the observed splitting can be smaller when measured in reflection rather than in transmission.

In addition to spectroscopic measurements, strong light-matter coupling can also be displayed in time-resolved measurements (Brune *et al.*, 1996). Starting from the qubit-oscillator ground state, this can be done by first pulsing the qubit to its first excited state and then bringing it on resonance

¹¹According to some authors, these dressed states should therefore be referred to as quton and phobit (Schuster, 2007).

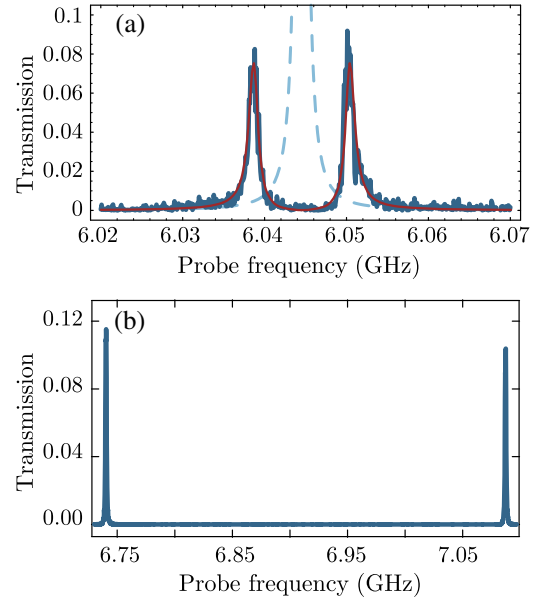


FIG. 21. (a) Transmission-line resonator transmission vs probe frequency in the first observation of vacuum Rabi splitting in circuit QED (solid blue line). The qubit is a Cooper pair box qubit with $E_J/h \approx 8$ GHz and $E_C/h \approx 5.2$ GHz. The solid red line is a calculated spectrum with $2g/2\pi \approx 11.6$ MHz, $\kappa/2\pi \approx 0.8$ MHz, and $\gamma_2/2\pi \approx 0.7$ MHz. As a reference, the dashed light blue line is the measured transmission with the qubit strongly detuned from the resonator. Adapted from Wallraff *et al.*, 2004. (b) Resonator transmission with a transmon qubit. The vacuum Rabi splitting is even more resolved with $2g/2\pi = 350$ MHz, $\kappa/2\pi \sim 800$ kHz, and $\gamma_2/2\pi \sim 200$ kHz. Notice the change in probe frequency range from (a). Adapted from Schoelkopf and Girvin, 2008.

with the cavity. As illustrated in Fig. 20(e), this results in oscillations in the qubit and cavity populations at the vacuum Rabi frequency $2g$. Time-resolved vacuum Rabi oscillations in circuit QED were first performed with a flux qubit coupled to a discrete LC oscillator realized in the bias circuitry of the device (Johansson *et al.*, 2006). This experiment was followed

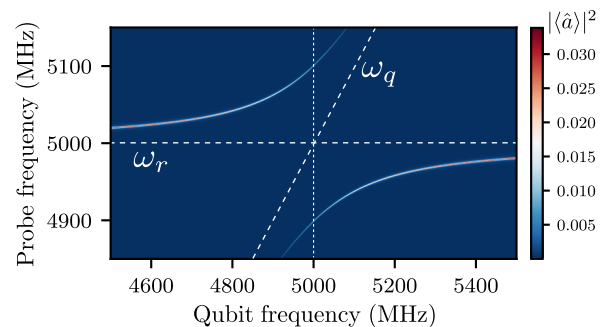


FIG. 22. Vacuum Rabi splitting revealed in numerical simulations of the cavity transmission $A^2 = |\langle \hat{a} \rangle|^2$ as a function of probe frequency and qubit transition frequency for the same parameters as in Fig. 20(f). The bare cavity and qubit frequencies are indicated by the horizontal and diagonal dashed lines, respectively. The vacuum Rabi splitting of Fig. 20(f) is obtained at resonance ($\omega_r = \omega_q$) along the vertical dotted line.

by a similar observation with a phase qubit coupled to a coplanar waveguide resonator (Hofheinz *et al.*, 2008).

In the limit of weak excitation power that we have considered thus far, the coupled qubit-oscillator system is indistinguishable from two coupled classical linear oscillators. As a result, while the dressed states that are probed in these experiments are entangled, the observation of an avoided crossing cannot be taken as a conclusive demonstration that the oscillator field is quantized or of qubit-oscillator entanglement. Indeed, the vacuum Rabi splitting can be interpreted as the familiar normal mode splitting of two coupled classical oscillators.

A signature of the quantum nature of the system can be obtained by probing the \sqrt{n} dependence of the spacing of the higher excited states of the Jaynes-Cummings ladder already discussed in Sec. III.B. This dependence results from the matrix element of the operator \hat{a} and consequently is linked to the quantum nature of the field (Carmichael, Kochan, and Sanders, 1996). Experimentally, these transitions can be accessed in several ways, including by two-tone spectroscopy (Fink *et al.*, 2008), by increasing the probe-tone power (Bishop *et al.*, 2009) or by increasing the system temperature (Fink *et al.*, 2010). The light blue line in Fig. 20(f) shows cavity transmission with a thermal photon number of $\bar{n}_\kappa = 0.35$ rather than $\bar{n}_\kappa = 0$ (dark blue line). At this more elevated temperature, additional pairs of peaks with smaller separation are now observed in addition to the original peaks separated by $2g$. As illustrated in Fig. 23, these additional structures are due to multiphoton transitions and their \sqrt{n} scaling reveal the anharmonicity of the Jaynes-Cummings ladder. The matrix elements of transitions that lie outside of the original vacuum Rabi splitting peaks are suppressed and these transitions are therefore not observed; see the red arrow in Fig. 23

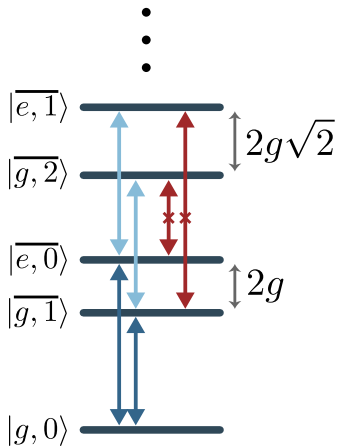


FIG. 23. Ground state and first two doublets of the Jaynes-Cummings ladder. The dark blue arrows correspond to the transitions that are probed in a vacuum Rabi experiment. The transitions illustrated with light blue arrows lead to additional peaks at transition frequencies lying inside the vacuum Rabi doublet at elevated temperature or increased probe power. On the other hand, the matrix element associated with the red transitions would lead to a response at transition frequencies outside of the vacuum Rabi doublet. Those transitions, however, are suppressed and are not observed (Rau, Johansson, and Shnirman, 2004).

(Rau, Johansson, and Shnirman, 2004). We also note that, at much larger power or at elevated temperature, the system undergoes a quantum-to-classical transition and a single peak at the resonator frequency ω_r is observed (Fink *et al.*, 2010). In short, the impact of the qubit on the system is washed away in the correspondence limit. This is to be expected from the form of the Jaynes-Cummings Hamiltonian (36), where the qubit-cavity coupling $\hbar g(\hat{a}^\dagger \hat{\sigma}_- + \hat{a} \hat{\sigma}_+)$ with its \sqrt{n} scaling is overwhelmed by the free cavity Hamiltonian $\hbar \omega_r \hat{a}^\dagger \hat{a}$, which scales as n . This is the same mechanism that leads to the high-power readout discussed in Sec. V.C.3.

Beyond this spectroscopic evidence and as further discussed in Sec. VIII.A, the \sqrt{n} dependence of the Jaynes-Cummings ladder was exploited to prepare the Fock state of the oscillator field (Hofheinz *et al.*, 2008; Wang *et al.*, 2008). The quantum nature of the field and qubit-oscillator entanglement were also demonstrated in a number of experiments directly measuring the joint density matrix of the dressed states. Eichler *et al.* (2012) achieved this by creating one of the entangled states $\{|g, 1\rangle, |e, 0\rangle\}$ in a time-resolved vacuum Rabi oscillation experiment and, subsequently, measuring the qubit state in a dispersive measurement and the photon state using a linear detection method (Eichler, Bozyigit, and Wallraff, 2012). A range of experiments used the ability to create entanglement between a qubit and a photon through the resonant interaction with a resonator in the context of quantum computation (Mariantoni *et al.*, 2011), to entangle two independent resonators (Wang *et al.*, 2011), and to transfer quantum states (Sillanpää, Park, and Simmonds, 2007).

B. Dispersive regime

For most quantum computing experiments, it is common to work in the dispersive regime where, as discussed in Sec. III.C, the qubit is strongly detuned from the oscillator with $|\Delta| \gg g$. There the dressed eigenstates are merely weakly entangled qubit-oscillator states. This is in contrast to the resonant regime, where these eigenstates are highly entangled, resulting in the qubit and the oscillator completely losing their individual character.

In the two-level system approximation, the dispersive regime is well described by the Hamiltonian \hat{H}_{disp} of Eq. (109). In the discussion surrounding that equation, we interpreted the dispersive coupling as a qubit-state-dependent shift of the oscillator frequency. This shift can be seen in Fig. 22 as the deviation of the oscillator response from the bare oscillator frequency away from resonance (horizontal dashed line). The figure also makes it clear that the qubit frequency, whose bare value is given by the diagonal dashed line, is also modified by the dispersive coupling to the oscillator. To better understand this qubit-frequency shift, it is instructive to rewrite \hat{H}_{disp} as

$$\hat{H}_{\text{disp}} \approx \hbar \omega_r \hat{a}^\dagger \hat{a} + \frac{\hbar}{2} \left[\omega_q + 2\chi \left(\hat{a}^\dagger \hat{a} + \frac{1}{2} \right) \right] \hat{\sigma}_z, \quad (128)$$

where it is now clear that the dispersive interaction of amplitude χ leads not only to a qubit-state-dependent frequency pull of the oscillator but also to a photon-number-dependent frequency shift of the qubit given by $2\chi \hat{a}^\dagger \hat{a}$. This is known as the ac-Stark

shift (or the quantized light shift) and is accompanied here by a Lamb shift corresponding to the factor of 1/2 in the last term of Eq. (128), which we dropped in Eq. (109). In this section, we explore some consequences of this new point of view on the dispersive interaction, starting by first reviewing some of the basic aspects of qubit spectroscopic measurements.

1. Qubit spectroscopy

To simplify the discussion, we first consider spectroscopically probing the qubit while assuming that the oscillator remains in its vacuum state. This is done by applying a coherent field of amplitude α_d and frequency ω_d to the qubit, either via a dedicated voltage gate on the qubit or to the input port of the resonator. Ignoring the resonator for the moment, this situation is described by the Hamiltonian $\delta_q \hat{\sigma}_z/2 + \Omega_R \hat{\sigma}_x/2$, where $\delta_q = (\omega_q + \chi) - \omega_d$ is the detuning between the Lamb-shifted qubit transition frequency and the drive frequency and $\Omega_R \propto \alpha_d$ is the Rabi frequency. Under this Hamiltonian and using the master equation (81) projected on the two qubit levels, the steady-state probability $P_e = (\langle \hat{\sigma}_z \rangle_s + 1)/2$ of the qubit being in its excited state (or, equivalently, the probability of it being in the ground state P_g) is found to be (Abragam, 1961)

$$P_e = 1 - P_g = \frac{1}{2} \frac{\Omega_R^2}{\gamma_1 \gamma_2 + \delta_q^2 \gamma_1 / \gamma_2 + \Omega_R^2}. \quad (129)$$

The Lorentzian line shape of P_e as a function of the drive frequency is illustrated in Fig. 24(a). In the limit of strong qubit drive, i.e., large Rabi frequency Ω_R , the steady-state qubit population reaches saturation with $P_e = P_g = 1/2$; see Fig. 24(b). Moreover, as the power increases, the FWHM of

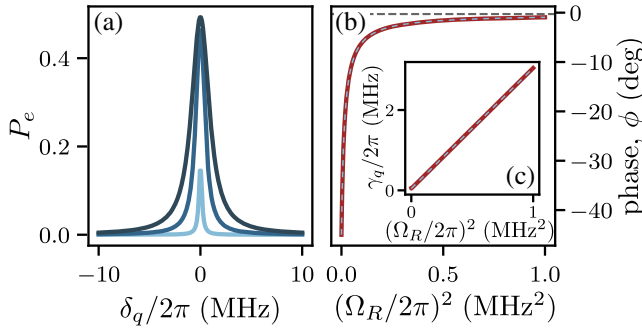


FIG. 24. Power broadening of the qubit line. (a) Excited qubit population (left vertical axis) and phase (right vertical axis) as a function of the drive detuning δ_q for the Rabi amplitudes $\Omega_R/2\pi = 0.1$ (light blue line), 0.5 (blue line), and 1 MHz (dark blue line). The phase is obtained from $\phi = \arctan(2\chi\langle\hat{\sigma}_z\rangle_s/2)$, with $2\chi/\kappa = 1$. (b) Excited qubit population and phase at $\delta_q = 0$ and as a function of Ω_R^2 . The horizontal dashed gray line corresponds to qubit saturation $P_e = 1/2$. (c) Qubit linewidth as a function of Ω_R^2 . All three panels have been obtained from numerical simulations of the dispersive qubit master equation with $\gamma_1/2\pi = 0.1$ MHz and $\gamma_q/2\pi = 0.1$ MHz, with the exception of the dashed blue lines in (b) and (c) that correspond to the analytical expressions found in the text.

the qubit line shape evolves from the bare qubit linewidth given by $\gamma_q = 2\gamma_2$ to $2\sqrt{1/T_2^2 + \Omega_R^2 T_1/T_2}$, an effect known as power broadening and illustrated in Fig. 24(c). In practice, the unbroadened dephasing rate γ_2 can be determined from spectroscopic measurements by extrapolating to zero spectroscopy tone power the linear dependence of ν_{HWHM}^2 . This quantity can also be determined in the time domain from a Ramsey fringe experiment (Vion *et al.*, 2002).¹²

In typical optical spectroscopy of atoms in a gas, one directly measures the absorption of photons by the gas as a function of the frequency of the photons. In circuit QED, one typically performs quantum jump spectroscopy by measuring the probability that an applied microwave drive will place the qubit into its excited state. The variation in qubit population with qubit drive can be measured by monitoring the change in response of the cavity to the spectroscopy drive. This is realized by measuring the cavity transmission, or reflection, of an additional drive of frequency close to ω_r . In the literature this approach is referred to as two-tone spectroscopy, with the second drive often called the probe or measurement tone, while the spectroscopy drive is also known as the pump tone. As shown in Eq. (115), the phase of the transmitted probe tone is related to the qubit population. In particular, with the probe tone at the bare cavity frequency and in the weak dispersive limit $\chi \ll \kappa$, this phase is simply proportional to the qubit population $\phi^s = \arctan(2\chi\langle\hat{\sigma}_z\rangle_s/2) \approx 2\chi\langle\hat{\sigma}_z\rangle_s/\kappa$. Monitoring ϕ^s as a function of the spectroscopy tone frequency therefore directly reveals the Lorentzian qubit line shape (Schuster *et al.*, 2005).

2. ac-Stark shift and measurement-induced broadening

In our discussion, we have implicitly assumed that the amplitude of the measure tone is such that the intracavity photon population is vanishingly small ($\langle \hat{a}^\dagger \hat{a} \rangle \rightarrow 0$). As is made clear by Eq. (128), an increase in photon population leads to a qubit-frequency shift by an average value of $2\chi\langle \hat{a}^\dagger \hat{a} \rangle$. Figure 25(a) shows this ac-Stark shift in the steady-state qubit population as a function of spectroscopy frequency for three different probe drive powers populating the cavity with different $\langle \hat{n} \rangle$. Taking advantage of the dependence of the qubit frequency on measurement power, prior knowledge of the value of χ allows one to infer the intracavity photon number as a function of input pump power

¹²Different quantities associated with the dephasing time are used in the literature, with the most common being T_2 , T_2^* , and T_2^{echo} . While T_2 corresponds to the intrinsic or “natural” dephasing time of the qubit, $T_2^* \leq T_2$ accounts for inhomogeneous broadening. For a flux-tunable transmon this broadening can be due to random fluctuations of the flux threading the qubit’s SQUID loop. A change of the flux over the time of the experiment needed to extract T_2 results in qubit-frequency shifts, which is measured as a broadening of the qubit’s intrinsic linewidth. The slow frequency fluctuations can be canceled out by applying a π pulse midway through a Ramsey fringe experiment. The measured dephasing time is then known as T_2^{echo} and is usually longer than T_2^* , with its exact value depending on the spectrum of the low-frequency noise affecting the qubit (Martinis *et al.*, 2003). The method of dynamical decoupling that relies on more complex pulse sequences can be used to cancel out higher-frequency components of the noise (Bylander *et al.*, 2011).

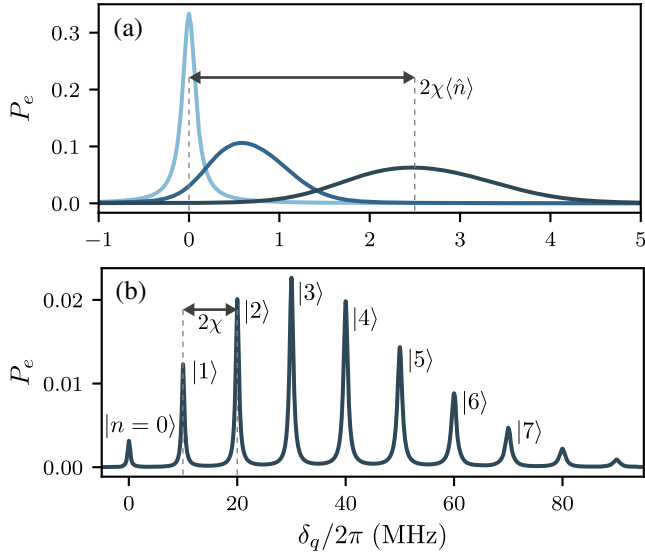


FIG. 25. Excited state population as a function of the qubit drive frequency. (a) Dispersive regime with $\chi/2\pi = 0.1$ MHz and (b) strong dispersive limit with $\chi/2\pi = 5$ MHz. The resolved peaks correspond to different cavity photon numbers $|n\rangle$. The spectroscopy drive amplitude is fixed to $\Omega_R/2\pi = 0.1$ MHz and the damping rates to $\gamma_1/2\pi = \kappa/2\pi = 0.1$ MHz. In (a) the measurement drive is on resonance with the bare cavity frequency, with amplitude $\epsilon/2\pi = 0, 0.2$, and 0.4 MHz for the light blue, blue, and dark blue lines, respectively. In (b) the measurement drive is at the pulled cavity frequency $\omega_r - \chi$ with amplitude $\epsilon/2\pi = 0.1$ MHz.

from such measurements (Schuster *et al.*, 2005). However, care must be taken since the linear dependence of the qubit frequency on power predicted in Eq. (109) is valid only well inside the dispersive regime or, more precisely, at small \bar{n}/n_{crit} . We return to this shortly.

As is apparent from Fig. 25(a), in addition to causing a frequency shift of the qubit the cavity photon population also causes a broadening of the qubit linewidth. This can be understood simply by again considering the form of \hat{H}_{disp} in Eq. (128). Indeed, while in the previous discussion we considered only the average qubit-frequency shift $2\chi\langle\hat{a}^\dagger\hat{a}\rangle$, the actual shift is instead given by $2\chi\hat{a}^\dagger\hat{a}$ such that the full photon-number distribution is important. As a result, when the cavity is prepared in a coherent state by the measurement tone, each Fock state $|n\rangle$ of the coherent field leads to its own qubit-frequency shift $2\chi n$. In the weak dispersive limit corresponding to small χ/κ , the observed qubit line shape is thus the result of the inhomogeneous broadening due to the Poisson statistics of the coherent state populating the cavity. This effect becomes more apparent as the average measurement photon number \bar{n} increases and results in a crossover from a broadened Lorentzian qubit line shape whose linewidth scales with \bar{n} to a broadened Gaussian line shape whose linewidth instead scales as $\sqrt{\bar{n}}$ (Schuster *et al.*, 2005; Gambetta *et al.*, 2006). This square-root dependence can be traced to the coherent nature of the cavity field. For a thermal cavity field, a $\bar{n}(\bar{n} + 1)$ dependence is instead expected and observed (Bertet *et al.*, 2005; Kono *et al.*, 2017).

This change in qubit linewidth due to photon shot noise in the coherent measurement tone populating the cavity can be interpreted as the unavoidable dephasing that a quantum system undergoes during measurement. Using a polaron-type transformation familiar from condensed-matter theory, the cavity can be integrated out of the qubit-cavity master equation, and in this way the associated measurement-induced dephasing rate can be expressed in the dispersive regime as $\gamma_m(t) = 2\chi\text{Im}[\alpha_g(t)\alpha_e^*(t)]$, where $\alpha_{g/e}(t)$ are the time-dependent coherent state amplitudes associated with the two qubit states obtained from Eq. (111) (Gambetta *et al.*, 2008). In the longtime limit, the previous rate can be expressed in the more intuitive form $\gamma_m = \kappa|\alpha_e^s - \alpha_g^s|^2/2$, where $|\alpha_e^s - \alpha_g^s|$ is the distance between the two steady-state pointer states (Gambetta *et al.*, 2008). Measurement-induced dephasing is faster when the pointer states are more easily distinguishable and the measurement is thus more efficient. This last expression can also be directly obtained from the dynamics of the entangled qubit-pointer state [Eq. (110)] whose coherence decays, at short times, at the rate γ_m under photon loss (Haroche and Raimond, 2006).

Using Eqs. (111a) and (111b) for the steady-state pointer state amplitude, γ_m can be expressed as

$$\gamma_m = \frac{\kappa\chi^2(\bar{n}_g + \bar{n}_e)}{\delta_r^2 + \chi^2 + (\kappa/2)^2}, \quad (130)$$

with $\bar{n}_\sigma = |\alpha_\sigma|^2$ the average cavity photon number given that the qubit is state σ . The distinction between \bar{n}_g and \bar{n}_e is important if the measurement drive is not symmetrically placed between the two pulled cavity frequencies corresponding to the two qubit states. Taking $\delta_r = \omega_r - \omega_d = 0$ and thus $\bar{n}_g = \bar{n}_e \equiv \bar{n}$ for a two-level system, the measurement-induced dephasing rate takes in the small χ/κ limit the simple form $\gamma_m \sim 8\chi^2\bar{n}/\kappa$. Thus, as mentioned, the qubit linewidth scales with \bar{n} . Keeping the cautionary remarks found at the end of this subsection in mind, measuring this linewidth versus the drive power is thus another way to infer \bar{n} experimentally.

Thus far we have been concerned with the small χ/κ limit. However, given the strong coupling and high quality factor that can be experimentally realized in circuit QED, it is also interesting to consider the opposite limit where χ/κ is large. A first consequence of this strong-dispersive regime, illustrated in Fig. 25(b), is that the qubit-frequency shift per photon can then be large enough to be resolved spectroscopically (Gambetta *et al.*, 2006; Schuster *et al.*, 2007). More precisely, this occurs if 2χ is larger than $\gamma_2 + (\bar{n} + n)\kappa/2$, the width of the n th photon peak (Gambetta *et al.*, 2006). Moreover, the amplitude of each spectroscopic line is a measure of the probability of finding the corresponding photon number in the cavity. Using this idea, it is possible to experimentally distinguish between coherent and thermal population of the cavity (Schuster *et al.*, 2007). This strong dependence of the qubit frequency on the exact photon number also allows for conditional qubit-cavity logical operations where a microwave pulse is applied such that the qubit state is flipped if and only if there are n photons in the cavity (Johnson *et al.*, 2010). Although challenging, this strong dispersive limit has also been achieved in some cavity QED experiments

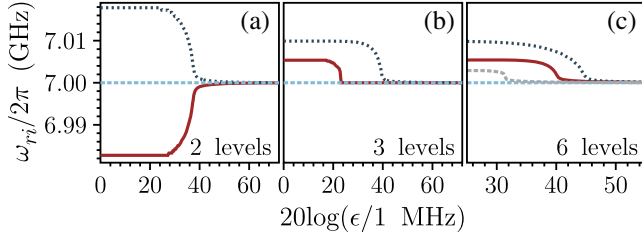


FIG. 26. Change of effective resonator frequency $\omega_{r\sigma}$ with increasing measurement drive power for the different states σ of the transmon qubit (dotted blue line, ground state; solid red line, first excited state; dashed gray line, second excited state). The horizontal green dashed line is the bare resonator frequency. (a) Two-level artificial atom taking into account (b) three levels of the transmon and (c) six levels of the transmon. The system parameters are chosen such that $(\omega_{01}, \omega_{12}, g)/2\pi = (6, 5.75, 0.1)$ GHz. Adapted from Boissonneault, Gambetta, and Blais, 2010.

(Gleyzes *et al.*, 2007; Guerlin *et al.*, 2007). This regime has also been achieved in hybrid quantum systems, such as in phonon-number-resolving measurements of nanomechanical oscillators (Arrangoiz-Arriola *et al.*, 2019; Sletten *et al.*, 2019) and magnon-number-resolving measurements (Lachance-Quirion *et al.*, 2017).

We now return to the issue of inferring the intracavity photon number from ac-Stark shift or qubit linewidth broadening measurements. As mentioned, the linear dependence of the ac-Stark shift on the measurement drive power predicted from the dispersive Hamiltonian (109) is valid only at small \bar{n}/n_{crit} . Indeed, because of higher-order corrections, the cavity pull itself is not constant with \bar{n} but instead decreases with increasing \bar{n} (Gambetta *et al.*, 2006). This change in cavity pull is illustrated in Fig. 26(a), which shows the effective resonator frequency given that the qubit is in state σ as a function of drive amplitude $\omega_{r\sigma}(n) = E_{\sigma, n+1}^- - E_{\sigma, n}^-$, with $E_{\sigma, n+1}^-$ the dressed-state energies defined in Eq. (40) (Boissonneault, Gambetta, and Blais, 2010). At low drive amplitude, the cavity frequency is pulled to the expected value $\omega_r \pm \chi$ depending on the state of the qubit. As the drive amplitude increases, and with it the intracavity photon number, the pulled cavity frequency goes back to its bare value ω_r . Figures 26(b) and 26(c) show the pulled frequencies accounting for three and six transmon levels, respectively. In contrast to the two-level approximation and as expected from Eq. (42), in this many-level situation the symmetry that was present in the two-level case is broken and the pulled frequencies are not symmetrically placed around ω_r . We note that this change in effective cavity frequency is at the heart of the high-power readout discussed in Sec. V.C.2.

Because of this change in cavity pull, which can be interpreted as χ itself changing with photon numbers, the ac-Stark shift and the measurement-induced dephasing do not necessarily follow the simple linear dependence expected from \hat{H}_{disp} . For this reason, it is possible to safely infer the intracavity photon number only from measurement of the ac-Stark shift or qubit linewidth broadening at small photon number. It is worth noting that in some cases the reduction in cavity pull can move the cavity frequency closer to the drive

frequency, thereby leading to a nonlinear increase in cavity population with power. For some system parameters, these two nonlinear effects (reduction in cavity pull and increase in cavity population) can partly compensate for each other, leading to an apparent linear dependence of the qubit ac-Stark with power (Gambetta *et al.*, 2006). We repeat that care must be taken when extracting the intracavity photon number in the dispersive regime.

C. Beyond strong coupling: Ultrastrong-coupling regime

We have discussed consequences of the strong-coupling ($g > \kappa, \gamma_2$) and strong-dispersive ($\chi > \kappa, \gamma_2$) regimes, which both can be easily realized in circuit QED. Although the effect of light-matter interaction has important consequences, in both regimes g is small with respect to the system frequencies $\omega_r, \omega_q \gg g$, a fact that allowed us to safely drop counter-rotating terms from Eq. (32). In the case of a two-level system this allowed us to work with the Jaynes-Cummings Hamiltonian (36). The situation where these terms can no longer be neglected is known as the ultrastrong-coupling regime.

As discussed in Sec. III.A, the relative smallness of g with respect to the system frequencies can be traced to Eq. (35), where we see that $g/\omega_r \propto \sqrt{\alpha}$, with $\alpha \sim 1/137$ the fine-structure constant. This is, however, not a fundamental limit and it is possible to take advantage of the flexibility of superconducting quantum circuits to engineer situations where light-matter coupling instead scales as $\propto 1/\sqrt{\alpha}$. In this case, the smallness of α now helps boost the coupling rather than constraining it. A circuit realizing this idea was first proposed by Devoret, Girvin, and Schoelkopf (2007) and is commonly known as the in-line transmon. It consists simply of a transmission-line resonator whose center conductor is interrupted by a Josephson junction. Coupling strengths as large as $g/\omega_r \sim 0.15$ can in principle be obtained in this way, but increasing this ratio further can be challenging because it is done at the expense of reducing the transmon anharmonicity (Bourassa *et al.*, 2012).

An alternative approach relies on galvanically coupling a flux qubit to the center conductor of a transmission-line resonator. In this configuration, light-matter coupling can be made large by increasing the impedance of the center conductor of the resonator in the vicinity of the qubit, which can be realized by interrupting the center conductor of the resonator with a Josephson junction or a junction array (Bourassa *et al.*, 2009). In this way, coupling strengths of $g/\omega_q \sim 1$ or larger can be achieved. These ideas were first realized by Forn-Díaz *et al.* (2010) and Niemczyk *et al.* (2010) with $g/\omega_q \sim 0.1$, and more recently with coupling strengths as large as $g/\omega_q \sim 1.34$ by Yoshihara *et al.* (2017). Similar results have also been obtained in the context of waveguide QED, where the qubit is coupled to an open transmission line rather than a localized cavity mode (Forn-Díaz, Garcia-Ripoll *et al.*, 2017).

A first consequence of reaching this ultrastrong-coupling regime is that, in addition to a Lamb shift g^2/Δ , the qubit transition frequency is further modified by the so-called Bloch-Siegert shift of magnitude $g^2/(\omega_q + \omega_r)$ (Bloch and

Siegert, 1940). Another consequence is that the ground state of the combined system is no longer the factorizable state $|g0\rangle$ but instead an entangled qubit-resonator state. An immediate implication of this observation is that the master equation (83), whose steady state is $|g0\rangle$, is not an appropriate description of damping in the ultrastrong-coupling regime (Beaudoin, Gambetta, and Blais, 2011). It is also worth mentioning that the two-level approximation for the artificial atom and the single-mode approximation for the oscillator that we use in this section may no longer be valid in this regime. Additional details about this regime of light-matter interaction were given by Forn-Díaz *et al.* (2019) and Frisk Kockum *et al.* (2019).

VII. QUANTUM COMPUTING WITH CIRCUIT QED

One of the reasons for the rapid growth of circuit QED as a field of research is its prominent role in gate-based quantum computing. The transmon is today the most widely used superconducting qubit, and the dispersive measurement described in Sec. V is the standard approach to qubit readout. Moreover, the capacitive coupling between transmons that are fabricated in proximity can be used to implement two-qubit gates. Alternatively, the transmon-resonator interaction can also be used to implement gates between qubits that are separated by distances as large as a centimeter, with the resonator acting as a quantum bus to mediate qubit-qubit interactions. As illustrated in Fig. 27, realizing a quantum computer architecture, even of modest size, requires bringing together in a single working package essentially all of the elements discussed in this review.

In this section, we describe the basic principles behind one- and two-qubit gates in circuit QED. Our objective is not to give a complete overview of the many different gates and gate-optimization techniques that have been developed. We instead focus on the key aspects of how a light-matter interaction

facilitates coherent quantum operations for superconducting qubits, and we describe some of the more commonly used gates to illustrate the basic principles. Unless otherwise noted, in this section we assume the qubits to be dispersively coupled to the resonator.

A. Single-qubit gates

Arbitrary single-qubit rotations can be realized in a NMR-like fashion with voltage drives at the qubit frequency (Blais *et al.*, 2004, 2007). One approach is to drive the qubit via one of the resonator ports (Wallraff *et al.*, 2005). Because of the large qubit-resonator detuning, a large fraction of the input power is reflected at the resonator, a situation that can be compensated for by increasing the power emitted by the source. This approach is similar to a qubit measurement but with a large detuning $\delta_r \gg \chi$ such that $|\alpha_e - \alpha_g| \sim 0$ according to Eq. (112). As illustrated in Fig. 19, this far off-resonance drive therefore causes negligible measurement-induced dephasing (Blais *et al.*, 2007). We also note that, in the presence of multiple qubits coupled to the same resonator, it is important that the qubits be sufficiently detuned in frequency from each other to avoid the control drive intended for one qubit to inadvertently affect the other qubits.

Given the last constraint, an often more convenient approach, illustrated in Figs. 13 and 27, is to capacitively couple the qubit to an additional transmission line, from which the control drives are applied. The coupling to this additional control port must be small enough to avoid any impact on the qubit relaxation time. Following Sec. IV.F, the amplitude of the drive as seen by the qubit is given by $\varepsilon = -i\sqrt{\gamma}\beta$, where β is the amplitude of the drive at the input port and γ is set by the capacitance between the qubit and the transmission line. A small γ , corresponding to a long relaxation time, can be compensated for by increasing the drive amplitude $|\beta|$ while

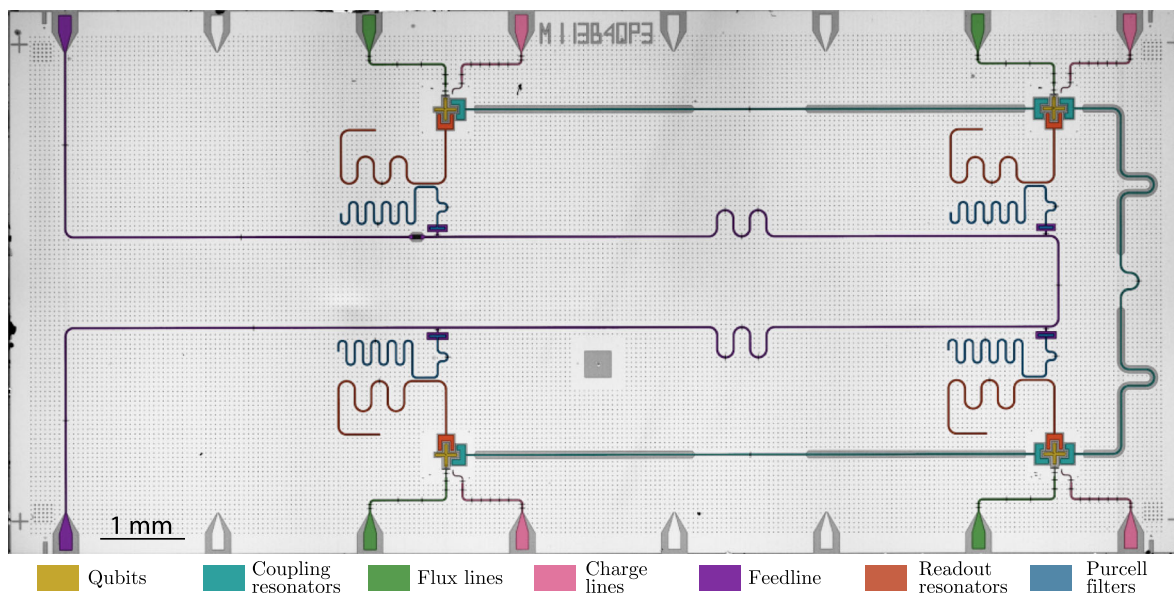


FIG. 27. False colored optical microscope image of a four-transmon device. The transmon qubits are shown in yellow, the coupling resonators are shown in cyan, the flux lines for single-qubit tuning are shown in green, the charge lines for single-qubit manipulation are shown in pink, and a common feedline for multiplexed readout is shown in purple, with transmission-line resonators for dispersive readout (red) employing Purcell filters (blue). Adapted from Andersen *et al.*, 2019.

making sure that any heating due to power dissipation close to the qubit does not affect qubit coherence. Design guidelines for wiring, an overview of the power dissipation induced by drive fields in qubit drive lines, and their effect on qubit coherence were discussed by [Krinner *et al.* \(2019\)](#).

As in Eq. (86), a coherent drive of time-dependent amplitude $\varepsilon(t)$, frequency ω_d , and phase ϕ_d on a transmon is then modeled by

$$\hat{H}(t) = \hat{H}_q + \hbar\varepsilon(t)(\hat{b}^\dagger e^{-i\omega_d t - i\phi_d} + \hat{b} e^{i\omega_d t + i\phi_d}), \quad (131)$$

where $\hat{H}_q = \hbar\omega_q \hat{b}^\dagger \hat{b} - (E_C/2)(\hat{b}^\dagger)^2 \hat{b}^2$ is the transmon Hamiltonian. Going to a frame rotating at ω_d , $\hat{H}(t)$ takes the simpler form

$$\hat{H}' = \hat{H}'_q + \hbar\varepsilon(t)(\hat{b}^\dagger e^{-i\phi_d} + \hat{b} e^{i\phi_d}), \quad (132)$$

where $\hat{H}'_q = \hbar\delta_q \hat{b}^\dagger \hat{b} - (E_C/2)(\hat{b}^\dagger)^2 \hat{b}^2$, with $\delta_q = \omega_q - \omega_d$ the detuning between the qubit and the drive frequencies.

When we truncate to two levels of the transmon as in Eq. (36), \hat{H}' takes the form

$$\hat{H}' = \frac{\hbar\delta_q}{2} \hat{\sigma}_z + \frac{\hbar\Omega_R(t)}{2} [\cos(\phi_d) \hat{\sigma}_x + \sin(\phi_d) \hat{\sigma}_y], \quad (133)$$

where we introduce the standard notation $\Omega_R = 2\varepsilon$ for the Rabi frequency. This form of \hat{H}' makes it clear how the phase of the drive ϕ_d controls the axis of rotation on the qubit Bloch sphere. Indeed, for $\delta_q = 0$ the choice $\phi_d = 0$ leads to rotations around the X axis, while $\phi_d = \pi/2$ leads to rotations around the Y axis. Since any rotation on the Bloch sphere can be decomposed into X and Y rotations, arbitrary single-qubit control is therefore possible using sequences of on-resonant drives with appropriate phases.

Implementing a desired gate requires turning on and off the drive amplitude. To realize as many logical operations as possible within the qubit coherence time, the gate time should be as short as possible and square pulses are optimal from that point of view. In practice, however, such pulses suffer from deformation as they propagate down the finite-bandwidth transmission line from the source to the qubit. Moreover, for a weakly anharmonic multilevel system such as a transmon, high-frequency components of the square pulse can cause unwanted transitions to levels outside the two-level computational subspace. This leakage can be avoided by using smooth (e.g., Gaussian) pulses, but this leads to longer gate times. Another solution is to shape the pulse so as to remove the unwanted frequency components. A widely used approach that achieves this is known as derivative removal by adiabatic gate (DRAG). It is based on driving the two quadratures of the qubit with the envelope of the second quadrature chosen to be the time derivative of the envelope of the first quadrature ([Motzoi *et al.*, 2009](#); [Gambetta *et al.*, 2011](#)). More generally, one can cast the problem of finding an optimal drive as a numerical optimization problem, which can be tackled with optimal control approaches such as the gradient ascent pulse engineering algorithm ([Khaneja *et al.*, 2005](#)).

Experimental results from [Chow *et al.* \(2010\)](#) comparing the error in single-qubit gates with and without DRAG are

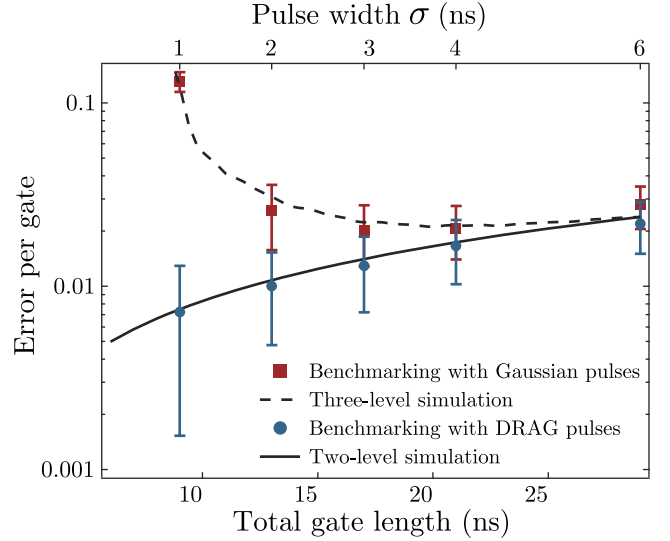


FIG. 28. Single-qubit gate errors extracted from randomized benchmarking for Gaussian and DRAG pulses as a function of total gate time and pulse width σ for Gaussian pulses. The experimental results (symbols) are compared to numerical simulations (lines) with two or three transmon levels. Adapted from [Chow *et al.*, 2010](#).

shown in Fig. 28. At long gate times, decoherence is the dominant source of error such that both Gaussian and DRAG pulses initially improve as the gate time is reduced. However, as the pulses get shorter and their frequency bandwidths become comparable to the transmon anharmonicity, leakage leads to large errors for the Gaussian pulses (red squares). In contrast, the DRAG results (blue circles) continue to improve as gates are made shorter and the results are consistent with a two-level system model of the transmon ([Chow *et al.*, 2010](#); [Lucero *et al.*, 2010](#)). These observations show that small anharmonicity is not a fundamental obstacle to fast and high-fidelity single-qubit gates. Indeed, thanks to pulse shaping techniques and long coherence times, state-of-the-art single-qubit gate errors are below 10^{-3} , well under the predicted threshold for topological error-correcting codes ([Fowler *et al.*, 2012](#); [Barends *et al.*, 2014](#); [Chen *et al.*, 2016](#)).

While rotations about the Z axis can be realized by concatenating the X and Y rotations described earlier, several other approaches are used experimentally. Working in a rotating frame as in Eq. (133) with $\delta_q = 0$, one alternative method relies on changing the qubit transition frequency such that $\delta_q \neq 0$ for a determined duration. In the absence of drive ($\Omega_R = 0$), this leads to phase accumulation by the qubit state and therefore to a rotation about the Z axis. As discussed in Sec. II.E, fast changes of the qubit transition frequency are possible by applying a magnetic field to a flux-tunable transmon. However, working with flux-tunable transmons is done at the cost of making the qubit susceptible to dephasing due to flux noise. To avoid this, the qubit transition frequency can also be tuned without relying on a flux-tunable device by applying a strongly detuned microwave tone on the qubit. For $\Omega_R/\delta_q \ll 1$, this drive does not lead to Rabi oscillations but induces an ac-Stark shift of the qubit frequency due to virtual transition caused by the drive ([Blais *et al.*, 2007](#)). Indeed, as

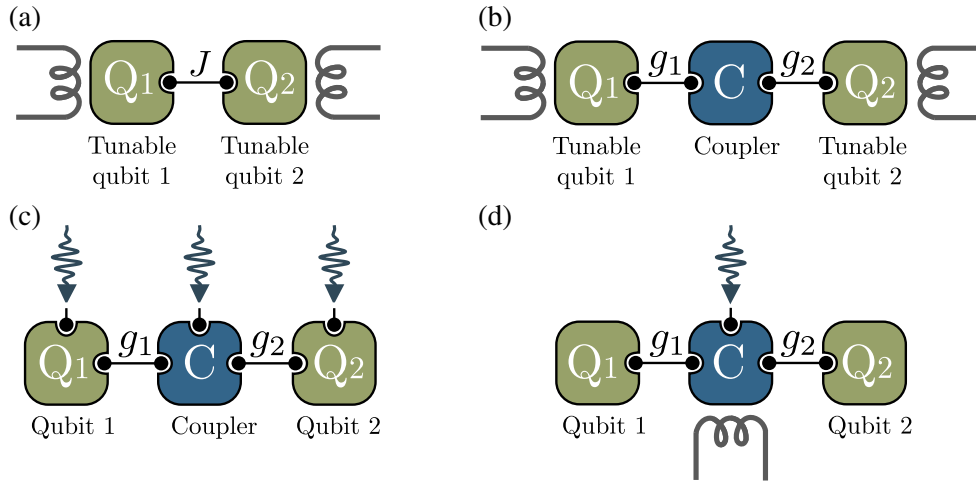


FIG. 29. Schematic illustration of some of the two-qubit gate schemes discussed in the text. Exchange interaction between two qubits (a) from direct capacitive coupling and (b) mediated by a coupler such as a bus resonator. The qubits are tuned in and out of resonance with each other to activate and deactivate the interaction, respectively. (c) All-microwave gates activated by microwave drives on the qubits and/or a coupler such as a bus resonator. In this scheme, the qubits can have a fixed frequency. (d) Parametric gates involving modulation of a system parameter, such as a tunable coupler. Adapted from Yan *et al.*, 2018.

shown in Appendix B.4, to second order in Ω_R/δ_q and assuming for simplicity a constant drive amplitude, this situation is described by the effective Hamiltonian

$$\hat{H}'' \simeq \frac{1}{2} \left(\hbar\omega_q - \frac{E_C \Omega_R^2}{2 \delta_q^2} \right) \hat{\sigma}_z. \quad (134)$$

The last term can be turned on and off with the amplitude of the detuned microwave drive and can therefore be used to realize Z rotations. Care must, however, be taken to avoid unwanted transitions due to the potentially strong drive.

Finally, since the X and Y axis in Eq. (133) are defined by the phase ϕ_d of the drive, a particularly simple approach to realizing a Z gate is to add the desired phase offset to the drive fields of all subsequent X and Y rotations and two-qubit gates. This so-called virtual Z gate can be especially useful if the computation is optimized to use a large number of Z rotations (McKay *et al.*, 2017).

B. Two-qubit gates

Two-qubit gates are generally more challenging to realize than single-qubit gates. Error rates for current two-qubit gates are often around 1% to a few percent, which is an order of magnitude higher than those of single-qubit gates. Recent experiments are, however, closing this gap (Foxen *et al.*, 2020; Negırneac *et al.*, 2020). Improving two-qubit gate fidelities at short gate times is an active area of research, and a variety of approaches have been developed. A key challenge in realizing two-qubit gates is the ability to rapidly turn interactions on and off. While for single-qubit gates this is done by simply turning on and off a microwave drive, two-qubit gates require turning on a coherent qubit-qubit interaction for a fixed time. Achieving large on-off ratios is far more challenging in this situation.

Broadly speaking, one can divide two-qubit gates into different categories depending on how the qubit-qubit

interaction is activated. The main approaches discussed in the following are illustrated schematically in Fig. 29. An important distinction between these different schemes is whether or not they rely on frequency-tunable qubits. Frequency tunability is convenient because it can be used to controllably tune qubits into resonance with one other qubit or with a resonator. Using flux-tunable transmons has led to some of the fastest and highest fidelity two-qubit gates to date; see Figs. 29(a) and 29(b) (Barends *et al.*, 2014; Chen *et al.*, 2014; Arute *et al.*, 2019). However, as mentioned this leads to additional qubit dephasing due to flux noise. An alternative involves all-microwave gates that use only microwave drives, either on the qubits or on a coupler bus such as a resonator to activate an effective qubit-qubit interaction; see Fig. 29(c). Finally, yet another category of gates is parametric gates where a system parameter is modulated in time at a frequency that bridges an energy gap between the states of two qubits. Parametric gates can be all microwave but in some instances involve modulating system frequencies using external magnetic flux; see Fig. 29(d).

1. Qubit-qubit exchange interaction

a. Direct capacitive coupling

One of the conceptually simplest ways to realize two-qubit gates is through direct capacitive coupling between the qubits; see Fig. 29(a). In analogy with Eq. (34), the Hamiltonian describing this situation reads

$$\hat{H} = \hat{H}_{q1} + \hat{H}_{q2} + \hbar J (\hat{b}_1^\dagger \hat{b}_2 + \hat{b}_1 \hat{b}_2^\dagger), \quad (135)$$

where $\hat{H}_{q_i} = \hbar\omega_{q_i} \hat{b}_i^\dagger \hat{b}_i - E_{C_i} (\hat{b}_i^\dagger)^2 \hat{b}_i^2 / 2$ is the Hamiltonian of the i th transmon and \hat{b}_i is the corresponding annihilation operator. The interaction amplitude J takes the form

$$\hbar J = \frac{2E_{C1}E_{C2}}{E_c} \left(\frac{E_{J1}}{2E_{C1}} \times \frac{E_{J2}}{2E_{C2}} \right)^{1/4}, \quad (136)$$

with E_{J_i} and E_{C_i} the transmon Josephson and charging energies and $E_{C_c} = e^2/2C_c$ the charging energy of the coupling capacitance labeled C_c . This beam-splitter Hamiltonian describes the coherent exchange of an excitation between the two qubits. In the two-level approximation, assuming the qubits to be tuned in resonance with each other, $\omega_{q_1} = \omega_{q_2}$, and moving to a frame rotating at the qubit frequency, Eq. (135) takes the familiar form

$$\hat{H}' = \hbar J(\hat{\sigma}_{+1}\hat{\sigma}_{-2} + \hat{\sigma}_{-1}\hat{\sigma}_{+2}). \quad (137)$$

Evolution under this Hamiltonian for a time $\pi/(4J)$ leads to the two-qubit \sqrt{i} SWAP gate, which is an entangling gate (Burkard *et al.*, 1999; Zhang *et al.*, 2003).

As mentioned, to precisely control the evolution under \hat{H}' , it is essential to be able to vary the qubit-qubit interaction with a large on-off ratio. There are essentially two approaches to realizing this. The most straightforward way is to tune the qubits in resonance to perform a two-qubit gate, and to strongly detune them to stop the coherent exchange induced by \hat{H}' (Blais, van den Brink, and Zagoskin, 2003; Bialczak *et al.*, 2010; Dewes *et al.*, 2012). Indeed, for $J/\Delta_{12} \ll 1$, where $\Delta_{12} = \omega_{q_1} - \omega_{q_2}$ is the detuning between the two qubits, the coherent exchange J is suppressed and can be dropped from Eq. (135) under the RWA. A more careful analysis following the same arguments and approach used to describe the dispersive regime (see Sec. III.C) shows that, to second order in J/Δ_{12} , a residual qubit-qubit interaction of the form $(J^2/\Delta_{12})\hat{\sigma}_{z_1}\hat{\sigma}_{z_2}$ remains. This unwanted interaction in the off state of the gate leads to a conditional phase accumulation on the qubits. As a result, the on-off ratio of this direct coupling gate is estimated to be $\sim \Delta_{12}/J$. This direct coupling approach was implemented by Barends *et al.* (2014) using frequency-tunable transmons with a coupling $J/2\pi = 30$ MHz and an on-off ratio of 100. In practice, the on-off ratio cannot be made arbitrarily small because increasing the detuning of one pair of qubits in a multiqubit architecture might lead to accidental resonance with a third qubit. The unwanted phase accumulation due to the residual $\hat{\sigma}_{z_1}\hat{\sigma}_{z_2}$ can, in principle, be eliminated using refocusing techniques borrowed from nuclear magnetic resonance (Slichter, 1990).

Another approach to turn the swap interaction on and off is to make the J coupling itself tunable in time. This is conceptually simple but requires more complex coupling circuitry typically involving flux-tunable elements that can open additional decoherence channels for the qubits. One advantage is that tuning a coupler rather than qubit transition frequencies helps in reducing the frequency crowding problem. This approach was used by Chen *et al.* (2014), who coupled two transmon qubits via a flux-tunable inductive coupler. In this way, it was possible to realize an on-off ratio of 1000, with a maximum coupling of 100 MHz corresponding to an \sqrt{i} SWAP gate in 2.5 ns. A simpler approach based on a frequency-tunable transmon qubit acting as coupler, suggested by Yan *et al.* (2018), was also used to tune qubit-qubit coupling from 5 to -40 MHz, going through zero coupling with a gate time of ~ 12 ns and a gate infidelity of $\sim 0.5\%$ (Arute *et al.*, 2019).

b. Resonator mediated coupling

An alternative to the previous approach is to use a resonator as a quantum bus mediating interactions between two qubits; see Fig. 29(b) (Blais *et al.*, 2004, 2007; Majer *et al.*, 2007). An advantage compared to direct coupling is that the qubits do not have to be fabricated in proximity to each other. With the qubits coupled to the same resonator, and in the absence of any direct coupling between the qubits, the Hamiltonian describing this situation is

$$\hat{H} = \hat{H}_{q_1} + \hat{H}_{q_2} + \hbar\omega_r\hat{a}^\dagger\hat{a} + \sum_{i=1}^2 \hbar g_i(\hat{a}^\dagger\hat{b}_i + \hat{a}\hat{b}_i^\dagger). \quad (138)$$

One way to make use of this pairwise interaction (assuming the resonator to be in the vacuum state) is to first tune one of the two qubits in resonance with the resonator for half a vacuum Rabi oscillation cycle, swapping an excitation from the qubit to the resonator before tuning it back out of resonance. The second qubit is then tuned in resonance, mapping the excitation from the resonator to the second qubit (Sillanpää, Park, and Simmonds, 2007). While this sequence of operations can swap the quantum state of the first qubit to the second, thereby demonstrating the role of the resonator as a quantum bus, it does not correspond to an entangling two-qubit gate.

Alternatively, a two-qubit gate can be performed by only virtually populating the resonator mode by working in the dispersive regime where both qubits are far detuned from the resonator (Blais *et al.*, 2004, 2007; Majer *et al.*, 2007). Building on the results of Sec. III.C, we find that in this situation the effective qubit-qubit interaction is revealed by applying the approximate dispersive transformation $\hat{U} = \exp[\sum_i (g_i/\Delta_i)(\hat{a}^\dagger\hat{b}_i - \hat{a}\hat{b}_i^\dagger)]$ on Eq. (138). Making use of the Baker-Campbell-Hausdorff expansion (B2) to second order in g_i/Δ_i , we find that

$$\begin{aligned} \hat{H}' &= \hat{H}'_{q_1} + \hat{H}'_{q_2} + \hbar J(\hat{b}_1^\dagger\hat{b}_2 + \hat{b}_1\hat{b}_2^\dagger) \\ &+ \hbar\tilde{\omega}_r\hat{a}^\dagger\hat{a} + \sum_{i=1}^2 \hbar\chi_{ab_i}\hat{a}^\dagger\hat{a}\hat{b}_i^\dagger\hat{b}_i \\ &+ \sum_{i \neq j} \hbar\Xi_{ij}\hat{b}_i^\dagger\hat{b}_i(\hat{b}_j^\dagger\hat{b}_i + \hat{b}_i^\dagger\hat{b}_j), \end{aligned} \quad (139)$$

with $H'_{q_i} \simeq \hbar\tilde{\omega}_{q_i}\hat{b}_i^\dagger\hat{b}_i - (E_{C_i}/2)(\hat{b}_i^\dagger)^2\hat{b}_i^2$ the transmon Hamiltonians and $\chi_{ab_i} \simeq -2E_{C_i}g_i^2/\Delta_i^2$ a cross-Kerr coupling between the resonator and the i th qubit. The frequencies $\tilde{\omega}_{q_i}$ and $\tilde{\omega}_r$ include Lamb shifts. The last line can be understood as an excitation-number-dependent exchange interaction with $\Xi_{ij} = E_{C_i}g_i g_j / (2\Delta_i\Delta_j)$. Since this term is much smaller than the J coupling, it can typically be neglected. Note that we have dropped a self-Kerr term of magnitude close to χ_{ab_i} on the resonator. This term is of no practical consequence in the dispersive regime, where the resonator is only virtually populated. The resonator-induced J coupling in \hat{H}' takes the form

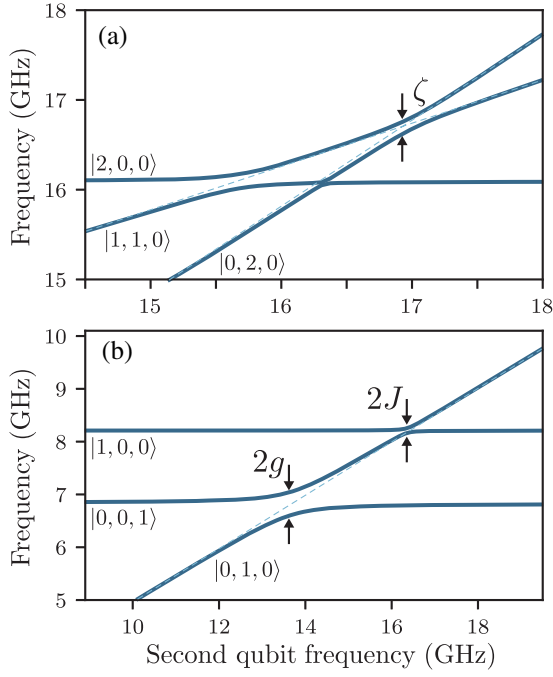


FIG. 30. Spectrum of two transmon qubits coupled to a common resonator as a function of the frequency of the second qubit in the (a) two-excitation and (b) one-excitation manifolds. The solid lines are obtained by numerical diagonalization of Eq. (138) in the charge basis with five transmon levels and five resonator levels, and with parameters adapted from DiCarlo *et al.* (2009): $E_{J_{1(2)}}/\hbar = 28.48(42.34)$ GHz, $E_{C_{1(2)}}/\hbar = 317(297)$ MHz, and $g_{1(2)}/2\pi = 199(190)$ MHz. In the one-excitation manifold, both the $2g$ anticrossing of the first qubit with the resonator and the $2J$ anticrossing of the two qubits are visible. In the two-excitation manifold, the 11-02 anticrossing of magnitude ζ can be seen. Notice the change in horizontal scale between the two panels. The states are labeled as |1st qubit, 2nd qubit, resonator>. The dashed light blue lines are guides for the eye following the bare frequency of the first qubit.

$$J = \frac{g_1 g_2}{2} \left(\frac{1}{\Delta_1} + \frac{1}{\Delta_2} \right) \quad (140)$$

and reveals itself in the frequency domain by an anticrossing of size $2J$ between the qubit states $|01\rangle$ and $|10\rangle$. This is illustrated in Fig. 30(b), which shows the eigenenergies of the Hamiltonian (138) in the one-excitation manifold. In this figure, the frequency of qubit 1 is swept, while that of qubit 2 is kept constant at ~ 8 GHz with the resonator at ~ 7 GHz. Moving from left to right, we first see the vacuum Rabi splitting of size $2g$ at $\omega_{q1} = \omega_r$, followed by a smaller anticrossing of size $2J$ at the qubit-qubit resonance. Equation (140) is valid only for single-mode oscillators and is renormalized in the presence of multiple modes (Filipp *et al.*, 2011; Solgun, DiVincenzo, and Gambetta, 2019).

To understand the consequence of the J coupling in the time domain, it is useful to note that if the resonator is initially in the vacuum state, it will remain in that state under the influence of \hat{H}' . In other words, the resonator is only virtually populated by its dispersive interaction with the qubits. For this reason, with the resonator initialized in the vacuum state, the

second line of Eq. (139) can for all practical purposes be ignored and we are back to the form of the direct coupling Hamiltonian of Eq. (135). Consequently, when both qubits are tuned in resonance with each other but still dispersive with respect to the resonator, the latter acts as a quantum bus mediating interactions between the qubits. An entangling gate can thus be performed in the same way as with direct capacitive coupling, either by tuning the qubits in and out of resonance with each other (Majer *et al.*, 2007) or by making the couplings g_i themselves tunable (Gambetta, Houck, and Blais, 2011; Srinivasan *et al.*, 2011).

2. Flux-tuned 11-02 phase gate

The 11-02 phase gate is a controlled-phase gate that is well suited to weakly anharmonic qubits such as transmons (DiCarlo *et al.*, 2009, 2010; Barends *et al.*, 2014; Martinis and Geller, 2014; Rol *et al.*, 2019; Foxen *et al.*, 2020; Kjaergaard *et al.*, 2020). It is obtained from the exchange interaction of Eq. (135) and can thus be realized through direct static or tunable qubit-qubit coupling or indirect coupling via a resonator bus.

In contrast to the \sqrt{i} SWAP gate, the 11-02 phase gate is not based on tuning the qubit transition frequencies between the computational states into resonance with each other, but instead exploits the third energy level of the transmon. The 11-02 gate thus relies on tuning the qubits to a point where the states $|11\rangle$ and $|02\rangle$ are degenerate in the absence of J coupling. As illustrated in Fig. 30(a), the qubit-qubit coupling lifts this degeneracy by an energy ζ whose value can be found perturbatively (DiCarlo *et al.*, 2009). Because of this repulsion caused by coupling to the state $|02\rangle$, the energy E_{11} of the state $|11\rangle$ is smaller than $E_{01} + E_{10}$ by ζ . Adiabatically flux tuning the qubits in and out of the 11-02 anticrossing therefore leads to a conditional phase accumulation that is equivalent to a controlled-phase gate.

To show this more clearly, we write the unitary corresponding to this adiabatic time evolution as

$$\hat{C}_Z(\phi_{01}, \phi_{10}, \phi_{11}) = \begin{pmatrix} 1 & 0 & 0 & 0 \\ 0 & e^{i\phi_{01}} & 0 & 0 \\ 0 & 0 & e^{i\phi_{10}} & 0 \\ 0 & 0 & 0 & e^{i\phi_{11}} \end{pmatrix}, \quad (141)$$

where $\phi_{ab} = \int dt E_{ab}(t)/\hbar$ is the dynamical phase accumulated over the total flux excursion. Up to single-qubit rotations, this is equivalent to a standard controlled-phase gate since

$$\begin{aligned} \hat{C}_Z(\phi) &= \text{diag}(1, 1, 1, e^{i\phi}) \\ &= \hat{R}_Z^1(-\phi_{10}) \hat{R}_Z^2(-\phi_{01}) \hat{C}_Z(\phi_{01}, \phi_{10}, \phi_{11}), \end{aligned} \quad (142)$$

with $\phi = \phi_{11} - \phi_{01} - \phi_{10} = \int dt \zeta(t)$ and where $\hat{R}_Z^i(\theta) = \text{diag}(1, e^{i\theta})$ is a single-qubit phase gate acting on qubit i . For $\phi \neq 0$ this is an entangling two-qubit gate and, in particular, for $\phi = \pi$ it is a controlled-Z gate (CPHASE).

An alternative to adiabatically tuning the flux in and out of the 11-02 resonance is to nonadiabatically pulse to this

anticrossing (Strauch *et al.*, 2003; DiCarlo *et al.*, 2010; Yamamoto *et al.*, 2010). In this sudden approximation, leaving the system there for a time t , the state $|11\rangle$ evolves into $\cos(\zeta t/2\hbar)|11\rangle + \sin(\zeta t/2\hbar)|02\rangle$. For $t = \hbar/\zeta$, $|11\rangle$ is mapped back onto itself but acquires a minus sign in the process. On the other hand, since they are far from any resonance, the other logical states evolve trivially. This therefore again results in a CPHASE gate. In this way, fast controlled-Z gates are possible. Some of the fastest and highest fidelity two-qubit gates have been achieved this way with error rates below the percent level and gate times of a few tens of nanoseconds (Barends *et al.*, 2014; Chen *et al.*, 2014). A fidelity of 99.93% with a 50 ns gate time was reported by Negirneac *et al.* (2020).

Despite its advantages, a challenge associated with this gate is the distortions in the flux pulses due to the finite bandwidth of the control electronics and line. In addition to modifying the waveform experienced by the qubit, this can lead to long timescale distortions where the flux at the qubit at a given time depends on the previous flux excursions. This situation can be partially solved by predistorting the pulses while taking into account the known distortion, but also by adapting the applied flux pulses to take advantage of the symmetry around the transmon sweet spot to cancel out unwanted contributions (Gustavsson *et al.*, 2013; Rol *et al.*, 2019).

3. All-microwave gates

Because the on-off ratio of the previously discussed gates is controlled by the detuning between the qubits, it is necessary to tune the qubit frequencies over relatively large frequency ranges or, alternatively, to have tunable coupling elements. In both cases, having a handle on the qubit frequency or qubit-qubit coupling opens the system to additional dephasing. Moreover, changing the qubit frequency over large ranges can lead to accidental resonance with other qubits or uncontrolled environmental modes, resulting in energy loss. For these reasons, it can be advantageous to control two-qubit gates in much the same way as single-qubit gates: by simply turning a microwave drive on and off. In this section, we describe two so-called all-microwave gates: the resonator-induced phase (RIP) gate and the cross-resonance (CR) gate. Both are based on fixed-frequency far off-resonance qubits with an always-on qubit-resonator coupling. The RIP gate is activated by driving a common resonator and the CR gate by driving one of the qubits. Other all-microwave gates which are not discussed further here include the sideband-based *i*SWAP (Leek *et al.*, 2009), the *b*SWAP (Poletto *et al.*, 2012), the microwave-activated CPHASE (Chow *et al.*, 2013), and the fg-ge gate (Zeytinoglu *et al.*, 2015; Egger *et al.*, 2019).

a. Resonator-induced phase gate

The RIP gate relies on two strongly detuned qubits that are dispersively coupled to a common resonator mode. The starting point is thus Eq. (139), where we now neglect the J coupling by taking $|\omega_{q1} - \omega_{q2}| \gg J$. In the two-level approximation and accounting for a drive on the resonator, this situation is described by the Hamiltonian

$$\hat{H}' = \frac{\hbar\tilde{\omega}_{q1}}{2}\hat{\sigma}_{z1} + \frac{\hbar\tilde{\omega}_{q2}}{2}\hat{\sigma}_{z2} + \hbar\tilde{\omega}_r\hat{a}^\dagger\hat{a} + \sum_{i=1}^2 \hbar\chi_i\hat{a}^\dagger\hat{a}\hat{\sigma}_{zi} + \hbar\varepsilon(t)(\hat{a}^\dagger e^{-i\omega_d t} + \hat{a} e^{i\omega_d t}), \quad (143)$$

where $\varepsilon(t)$ is the time-dependent amplitude of the resonator drive and ω_d is its frequency. Note that we also neglect the resonator self-Kerr nonlinearity.

The gate is realized by adiabatically ramping the drive $\varepsilon(t)$ on and off, such that the resonator starts and ends in the vacuum state. This means that the resonator is unentangled from the qubits at the start and end of the gate. Moreover, to avoid measurement-induced dephasing, the drive frequency is chosen to be far from the cavity mode: $|\tilde{\delta}_r| = |\tilde{\omega}_r - \omega_d| \gg \kappa$. Despite this strong detuning, the dispersive shift causes the resonator frequency to depend on the state of the two qubits, and as a result the resonator field evolves in a closed path in phase space that is qubit-state dependent. This leads to different phase accumulations for the various qubit states, and therefore to a controlled-phase gate of the form of Eq. (141).

This conditional phase accumulation can be made more apparent by moving Eq. (143) to a frame rotating at the drive frequency and by applying the polaron transformation $\hat{U} = \exp[\hat{\alpha}'(t)\hat{a}^\dagger - \hat{\alpha}'^*(t)\hat{a}]$ with $\hat{\alpha}'(t) = \alpha(t) - \sum_i \chi_i \hat{\sigma}_{zi} / \tilde{\delta}_r$ on the resulting Hamiltonian. This leads to the approximate effective Hamiltonian (Puri and Blais, 2016)

$$\hat{H}'' \simeq \sum_i \hbar \left[\frac{\tilde{\delta}_{qi}}{2} + \chi|\alpha(t)|^2 \right] \hat{\sigma}_{zi} + \hbar\delta_r\hat{a}^\dagger\hat{a} + \sum_{i=1}^2 \hbar\chi_i\hat{a}^\dagger\hat{a}\hat{\sigma}_{zi} - \hbar \frac{2\chi_1\chi_2|\alpha(t)|^2}{\delta_r} \hat{\sigma}_{z1}\hat{\sigma}_{z2}, \quad (144)$$

with $\tilde{\delta}_x = \tilde{\omega}_x - \omega_d$ and where the field amplitude $\alpha(t)$ satisfies $\dot{\alpha} = -i\tilde{\delta}_r\alpha - i\varepsilon(t)$. In this frame, it is clear how the resonator mediates a $\hat{\sigma}_{z1}\hat{\sigma}_{z2}$ interaction between the two qubits and therefore leads to a conditional phase gate. Equation (144) also makes it clear that the need to avoid measurement-induced dephasing with $|\tilde{\delta}_r| \gg \kappa$ limits the effective interaction strength and therefore leads to relatively long gate times. This can be mitigated, however, by taking advantage of pulse shaping techniques (Cross and Gambetta, 2015) or by using squeezed radiation to erase the “which-qubit” information in the output field of the resonator (Puri and Blais, 2016). As with the longitudinal readout protocol discussed in Sec. V.C.3, longitudinal coupling also offers a way to overcome many of the limitations of the conventional RIP gate (Kerman, 2013; Royer *et al.*, 2017).

Some of the advantages of this two-qubit gate are that it can couple qubits that are far detuned from each other and that it does not introduce significant leakage errors (Paik *et al.*, 2016). This gate was demonstrated by Paik *et al.* (2016) with multiple transmons coupled to a 3D resonator, achieving error rates of a few percent and gate times of several hundred nanoseconds.

b. Cross-resonance gate

The cross-resonance gate is based on qubits that are detuned from each other and coupled by an exchange term J of the form of Eq. (135) or (139) (Rigetti and Devoret, 2010; Chow *et al.*, 2011). While the RIP gate relies on off-resonant driving of a common oscillator mode, this gate is based on directly driving one of the qubits at the frequency of the other. Moreover, since the resonator is not directly used and, in fact, ideally remains in its vacuum throughout the gate, the J coupling can be mediated by a resonator or by direct capacitive coupling.

In the two-level approximation and in the absence of the drive, this interaction takes the form

$$\hat{H} = \frac{\hbar\omega_{q1}}{2}\hat{\sigma}_{z1} + \frac{\hbar\omega_{q2}}{2}\hat{\sigma}_{z2} + \hbar J(\hat{\sigma}_{+1}\hat{\sigma}_{-2} + \hat{\sigma}_{-1}\hat{\sigma}_{+2}). \quad (145)$$

To see how this gate operates, it is useful to diagonalize \hat{H} using the two-level system version of the transformation (49). The result takes the same general form as Eqs. (50) and (51) after projecting to two levels. In this frame, the presence of the J coupling leads to a renormalization of the qubit frequencies, which for strongly detuned qubits $|\Delta_{12}| = |\omega_{q1} - \omega_{q2}| \gg |J|$ take the values $\tilde{\omega}_{q1} \approx \omega_{q1} + J^2/\Delta_{12}$ and $\tilde{\omega}_{q2} \approx \omega_{q2} - J^2/\Delta_{12}$ to second order in J/Δ_{12} . In the same frame, a drive on the first qubit $\hbar\Omega_R(t)\cos(\omega_d t)\hat{\sigma}_{x1}$ takes the form (Chow *et al.*, 2011)

$$\begin{aligned} & \hbar\Omega_R(t)\cos(\omega_d t)(\cos\theta\hat{\sigma}_{x1} + \sin\theta\hat{\sigma}_{z1}\hat{\sigma}_{x2}) \\ & \approx \hbar\Omega_R(t)\cos(\omega_d t)\left(\hat{\sigma}_{x1} + \frac{J}{\Delta_{12}}\hat{\sigma}_{z1}\hat{\sigma}_{x2}\right), \end{aligned} \quad (146)$$

with $\theta = \arctan(2J/\Delta_{12})/2$ and where the second line is valid to first order in J/Δ_{12} . As a result, driving the first qubit at the frequency of the second qubit ($\omega_d = \tilde{\omega}_{q2}$) activates the term $\hat{\sigma}_{z1}\hat{\sigma}_{x2}$, which can be used to realize a CNOT gate.

More accurate expressions for the amplitude of the CR term $\hat{\sigma}_{z1}\hat{\sigma}_{x2}$ can be obtained by taking into account more levels of the transmons. In this case, the starting point is the Hamiltonian (135) with a drive term on the first qubit

$$\begin{aligned} \hat{H} &= \hat{H}_{q1} + \hat{H}_{q2} + \hbar J(\hat{b}_1^\dagger\hat{b}_2 + \hat{b}_1\hat{b}_2^\dagger) \\ &+ \hbar\varepsilon(t)(\hat{b}_1^\dagger e^{-i\omega_d t} + \hat{b}_1 e^{i\omega_d t}), \end{aligned} \quad (147)$$

where $\omega_d \sim \omega_{q2}$. As in the previous two-level system example, it is useful to eliminate the J coupling. We do this by moving to a rotating frame at the drive frequency for both qubits, followed by a Schrieffer-Wolff transformation to diagonalize the first line of Eq. (147) to second order in J ; see Appendix B.1. The drive term is modified under the same transformation by using the explicit expression for the Schrieffer-Wolff generator $\hat{S} = \hat{S}^{(1)} + \dots$ given in Eq. (B5), and the Baker-Campbell-Hausdorff formula (B2) to first order: $e^{\hat{S}}\hat{b}_1 e^{-\hat{S}} \approx \hat{b}_1 + [\hat{S}^{(1)}, \hat{b}_1]$. The full calculation is fairly involved and here we quote only the final result after truncating it to the two lowest levels of the transmon qubits (Tripathi, Khezri, and Korotkov, 2019; Magesan and Gambetta, 2020)

$$\begin{aligned} \hat{H}' &\approx \frac{\hbar\tilde{\delta}_{q1}}{2}\hat{\sigma}_{z1} + \frac{\hbar\tilde{\delta}_{q2}}{2}\hat{\sigma}_{z2} + \frac{\hbar\chi_{12}}{2}\hat{\sigma}_{z1}\hat{\sigma}_{z2} \\ &+ \hbar\varepsilon(t)\left(\hat{\sigma}_{x1} - J'\hat{\sigma}_{x2} - \frac{E_{C1}}{\hbar}\frac{J'}{\Delta_{12}}\hat{\sigma}_{z1}\hat{\sigma}_{x2}\right). \end{aligned} \quad (148)$$

In Eq. (148), the detunings include frequency shifts due to the J coupling with $\tilde{\delta}_{q1} = \omega_{q1} + J^2/\Delta_{12} + \chi_{12} - \omega_d$ and $\tilde{\delta}_{q2} = \omega_{q2} - J^2/\Delta_{12} + \chi_{12} - \omega_d$. The parameters χ_{12} and J' are given by

$$\chi_{12} = \frac{J^2}{\Delta_{12} + E_{C2}/\hbar} - \frac{J^2}{\Delta_{12} - E_{C1}/\hbar}, \quad (149a)$$

$$J' = \frac{J}{\Delta_{12} - E_{C1}/\hbar}. \quad (149b)$$

Equations (146) and (148) agree in the limit of large anharmonicity $E_{C1,2}$, and we again find that a drive on the first qubit at the frequency of the second qubit activates the CR term $\hat{\sigma}_{z1}\hat{\sigma}_{x2}$. However, there are important differences at finite $E_{C1,2}$, which highlights the importance of taking into account the multilevel nature of the transmon. Indeed, the amplitude of the CR term is smaller here than in Eq. (146) with a two-level system. Moreover, in contrast to the latter case, when taking multiple levels of the transmon qubits into account we find a spurious interaction $\hat{\sigma}_{z1}\hat{\sigma}_{z2}$ of amplitude χ_{12} between the two qubits, as well as a drive on the second qubit of amplitude $J'\varepsilon(t)$. This unwanted drive can be echoed away with additional single-qubit gates (Córcoles *et al.*, 2013; Sheldon *et al.*, 2016). The $\hat{\sigma}_{z1}\hat{\sigma}_{z2}$ interaction is detrimental to the gate fidelity as it effectively makes the frequency of the second qubit dependent on the logical state of the first qubit. Because of this, it is not possible to choose the drive frequency ω_d to always be exactly on resonance with the second qubit, irrespective of the state of the first. As a consequence, the CR term $\hat{\sigma}_{z1}\hat{\sigma}_{x2}$ in Eq. (148) rotates at an unknown qubit-state-dependent frequency, leading to a gate error. The $\hat{\sigma}_{z1}\hat{\sigma}_{z2}$ term should therefore be made small, ultimately limiting the gate speed. For a pair of qubits with equal and opposite anharmonicities, $\chi_{12} = 0$ and this unwanted effect is absent. This cannot be realized with a pair of conventional transmons but is possible with other types of qubits (Ku *et al.*, 2020).

Since J' is small, another caveat of the CR gate is that large microwave amplitudes ε are required for fast gates. For the typical low anharmonicity of transmon qubits, this can lead to leakages and to effects that are not captured by the second-order perturbative results of Eqs. (146) and (148). More detailed modeling based on the Hamiltonian of Eq. (147) suggests that classical cross talk induced on the second qubit from driving the first qubit can be important and is a source of discrepancy between the simple two-level system model and experiments (Tripathi, Khezri, and Korotkov, 2019; Ware *et al.*, 2019; Magesan and Gambetta, 2020). Because of these spurious effects, CR gate times have typically been relatively long, of the order of 300 to 400 ns with gate fidelities $\sim 94\%$ – 96% (Córcoles *et al.*, 2013). However, with careful calibration and modeling beyond Eq. (148), it has been

possible to push gate times down to the 100–200 ns range with errors per gate at the percent level (Sheldon *et al.*, 2016).

Advantages of the CR gate, which are similar to those of the RIP gate, include the fact that realizing this gate can be realized using the same drive lines that are used for single-qubit gates. Moreover, it works with fixed-frequency qubits that often have longer phase coherence times than their flux-tunable counterparts. However, both the RIP and CR gates are slower than what can now be achieved with additional flux control of the qubit frequency or the coupler. We also note that, due to the factor $E_{C1}/\hbar\Delta_{12}$ in the amplitude of the $\hat{\sigma}_{z1}\hat{\sigma}_{x2}$ term, the detuning of the two qubits cannot be too large relative to the anharmonicity, putting further constraints on the choice of the qubit frequencies. This may lead to frequency crowding issues when working with large numbers of qubits.

4. Parametric gates

Another approach to enacting a two-qubit gate with a large on-off ratio is to activate an off-resonant interaction by modulating a parameter of the system at an appropriate frequency. This parametric modulation provides the energy necessary to bridge the energy gap between the far detuned qubit states. Several such schemes, known as parametric gates, have been theoretically developed and experimentally realized; see Bertet, Harmans, and Mooij (2006), Niskanen, Nakamura, and Tsai (2006), Liu *et al.* (2007), Niskanen *et al.* (2007), Beaudoin *et al.* (2012), Strand *et al.* (2013), Kapit (2015), Sirois *et al.* (2015), McKay *et al.* (2016), Naik *et al.* (2017), Caldwell *et al.* (2018), Didier *et al.* (2018), and Reagor *et al.* (2018).

The key idea behind parametric gates is that modulation of a system parameter can induce transitions between energy levels that would otherwise be too far off resonance to give appreciable coupling. We illustrate the idea first with two directly coupled qubits described by the Hamiltonian

$$\hat{H} = \frac{\hbar\omega_{q1}}{2}\hat{\sigma}_{z1} + \frac{\hbar\omega_{q2}}{2}\hat{\sigma}_{z2} + J(t)\hat{\sigma}_{x1}\hat{\sigma}_{x2}, \quad (150)$$

where we assume that the coupling is periodically modulated at the frequency ω_m , $J(t) = J_0 + \tilde{J}\cos(\omega_m t)$. Moving to a rotating frame at the qubit frequencies, Eq. (150) takes the form

$$\begin{aligned} \hat{H}' = & J(t)(e^{i(\omega_{q1}-\omega_{q2})t}\hat{\sigma}_{+1}\hat{\sigma}_{-2} \\ & + e^{i(\omega_{q1}+\omega_{q2})t}\hat{\sigma}_{+1}\hat{\sigma}_{+2} + \text{H.c.}). \end{aligned} \quad (151)$$

As in Sec. VII.B.1.a, if the coupling is constant [$J(t) = J_0$] and $|J_0/(\omega_{q1} - \omega_{q2})|$, $|J_0/(\omega_{q1} + \omega_{q2})| \ll 1$, then \hat{H}' is fast rotating and can be neglected. In this situation, the gate is in the off state. On the other hand, by appropriately choosing the modulation frequency ω_m , it is possible to selectively activate some of these terms. Indeed, for $\omega_m = \omega_{q1} - \omega_{q2}$ the terms $\hat{\sigma}_{+1}\hat{\sigma}_{-2} + \text{H.c.}$ are no longer rotating and are effectively resonant. Dropping the rapidly rotating terms leads to

$$\hat{H}' \simeq \frac{\tilde{J}}{2}(\hat{\sigma}_{+1}\hat{\sigma}_{-2} + \hat{\sigma}_{-1}\hat{\sigma}_{+2}). \quad (152)$$

As discussed, this interaction can be used to generate entangling gates such as the $\sqrt{i\text{SWAP}}$. If instead $\omega_m = \omega_1 + \omega_2$, then $\hat{\sigma}_{+1}\hat{\sigma}_{+2} + \text{H.c.}$ is selected.

In practice, it can sometimes be easier to modulate a qubit or resonator frequency than a coupling strength. To see how this leads to a similar result, consider the Hamiltonian

$$\hat{H} = \frac{\hbar\omega_{q1}(t)}{2}\hat{\sigma}_{z1} + \frac{\hbar\omega_{q2}}{2}\hat{\sigma}_{z2} + J\hat{\sigma}_{x1}\hat{\sigma}_{x2}. \quad (153)$$

Taking $\omega_{q1}(t) = \omega_{q1} + \varepsilon \sin(\omega_m t)$, the transition frequency of the first qubit develops frequency modulation (FM) sidebands. The two qubits can then be effectively brought into resonance by choosing the modulation to align one of the FM sidebands with ω_{q2} , thereby rendering the J effectively coupling resonant. This can be seen by moving to a rotating frame defined by the unitary

$$\hat{U} = e^{-(i/2)\int_0^t dt' \omega_{q1}(t')\hat{\sigma}_{z1}} e^{-i\omega_{q2}t\hat{\sigma}_{z2}/2}, \quad (154)$$

where the Hamiltonian takes the form (Beaudoin *et al.*, 2012; Strand *et al.*, 2013)

$$\begin{aligned} \hat{H}' = & J \sum_{n=-\infty}^{\infty} J_n\left(\frac{\varepsilon}{\omega_m}\right) (i^n e^{i(\Delta_{12}-n\omega_m)t}\hat{\sigma}_{+1}\hat{\sigma}_{-2} \\ & + i^n e^{i(\omega_{q1}+\omega_{q2}-n\omega_m)t}\hat{\sigma}_{+1}\hat{\sigma}_{+2} + \text{H.c.}). \end{aligned} \quad (155)$$

To arrive at Eq. (155), we use the Jacobi-Anger expansion $e^{iz\cos\theta} = \sum_{n=-\infty}^{\infty} i^n J_n(z) e^{in\theta}$, with $J_n(z)$ Bessel functions of the first kind. Choosing the modulation frequency such that $n\omega_m = \Delta_{12}$ aligns the n th sideband with the resonator frequency such that a resonant qubit-resonator interaction is recovered. The largest contribution comes from the first sideband with J_1 , which has a maximum around $J_1(1.84) \simeq 0.58$, thus corresponding to an effective coupling that is a large fraction of the bare J coupling. Note that the assumption of having a simple sinusoidal modulation of the frequency neglects the fact that the qubit frequency has a nonlinear dependence on external flux for tunable transmons. This behavior can still be approximated by appropriately varying $\Phi_x(t)$ (Beaudoin *et al.*, 2012).

Parametric gates can also be mediated by modulating the frequency of a resonator bus to which qubits are dispersively coupled (McKay *et al.*, 2016). Much as with flux-tunable transmons, the resonator is made tunable by inserting a SQUID loop in the center conductor of the resonator (Castellanos-Beltran and Lehnert, 2007; Sandberg *et al.*, 2008). Changing the flux threading the SQUID loop changes the SQUID's inductance and therefore the effective length of the resonator. As in a trombone, this leads to a change of the resonator frequency. An advantage of modulating the resonator bus over modulating the qubit frequency is that the latter can have a fixed frequency, thus reducing its susceptibility to flux noise.

Finally, it is worth pointing out that while the speed of the cross-resonance gate is reduced when the qubit-qubit detuning is larger than the transmon anharmonicity, parametric gates do not suffer from this problem. As a result, there is more

freedom in the choice of the qubit frequencies with parametric gates, which is advantageous to avoid frequency crowding related issues such as addressability errors and cross talk. We also note that the modulation frequencies required to activate parametric gates can be a few hundred megahertz, in contrast to the RIP and CR gates, which require microwave drives. Removing the need for additional microwave generators simplifies the control electronics and may help make the process more scalable. A counterpoint is that fast parametric gates often require large modulation amplitudes, which can be challenging.

C. Encoding a qubit in an oscillator

Thus far we have discussed encoding quantum information into the first two energy levels of an artificial atom, the cavity being used for readout and two-qubit gates. However, cavity modes often have superior coherence properties to superconducting artificial atoms, something that is especially true for the 3D cavities discussed in Sec. II.C (Reagor *et al.*, 2016). This suggests that encoding quantum information in the oscillator mode can be advantageous. Using oscillator modes to store and manipulate quantum information can also be favorable for quantum-error correction, which is an essential aspect of scalable quantum computer architectures (Nielsen and Chuang, 2000).

Indeed, in addition to their long coherence time, oscillators have a simple and relatively well-understood error model: to a large extent, the dominant error is single-photon loss. Taking advantage of this, it is possible to design quantum-error correction codes that specifically correct for this most likely error. This is to be contrasted to more standard codes, such as the surface code, which aim at detecting and correcting both amplitude and phase errors (Fowler *et al.*, 2012). Moreover, as we discuss later, the infinite-dimensional Hilbert space of a single oscillator can be exploited to provide the redundancy that is necessary for error correction, thereby in principle allowing one to use fewer physical resources to protect quantum information than when using two-level systems. Finally, qubits encoded in oscillators can be concatenated with conventional error-correcting codes, where the latter should be optimized to exploit the noise resilience provided by the oscillator encoding (Tuckett, Bartlett, and Flammia, 2018; Guillaud and Mirrahimi, 2019; Tuckett *et al.*, 2019; Grimsmo, Combes, and Baragiola, 2020; Puri *et al.*, 2020; Tuckett *et al.*, 2020).

As we have already argued, nonlinearity is essential to prepare and manipulate quantum states of the oscillator. When encoding quantum information in a cavity mode, a dispersively coupled artificial atom (or other Josephson-junction-based circuit element) remains present, but only to provide nonlinearity to the oscillator, ideally without playing much of an active role.

Oscillator encodings of qubits investigated in the context of quantum optics and circuit QED include cat codes (Cochrane, Milburn, and Munro, 1999; Gilchrist *et al.*, 2004; Mirrahimi *et al.*, 2014; Ofek *et al.*, 2016; Puri, Boutin, and Blais, 2017; Grimm *et al.*, 2020; Lescanne, Villiers *et al.*, 2020), the related binomial codes (Michael *et al.*, 2016; Hu *et al.*, 2019), and Gottesman-Kitaev-Preskill (GKP) codes (Gottesman, Kitaev,

and Preskill, 2001; Flühmann *et al.*, 2019; Campagne-Ibarcq *et al.*, 2020), as well as the two-mode amplitude-damping code described by Chuang, Leung, and Yamamoto (1997).

To understand the basic idea behind this approach, we first consider the simplest instance of the binomial code in which a qubit is encoded in the following two states of a resonator mode (Michael *et al.*, 2016):

$$|0_L\rangle = \frac{1}{\sqrt{2}}(|0\rangle + |4\rangle), \quad |1_L\rangle = |2\rangle, \quad (156)$$

with Fock states $|n\rangle$. The first aspect to notice is that for both logical states the average photon number is $\bar{n} = 2$ and, as a result, the likelihood of a photon-loss event is the same for both states. An observer detecting a loss event will therefore not gain any information allowing her to distinguish whether the loss came from $|0_L\rangle$ or from $|1_L\rangle$. This is a necessary condition for a quantum state encoded using the logical states in Eq. (156) not to be “deformed” by a photon-loss event. Moreover, under the action of \hat{a} the arbitrary superposition $c_0|0_L\rangle + c_1|1_L\rangle$ becomes $c_0|3\rangle + c_1|1\rangle$ after normalization. The coefficients c_0 and c_1 encoding the quantum information are intact and the original state can in principle be recovered with a unitary transformation. By noting that, while the original state has support only on even photon numbers, the state after a photon loss only has support on odd photon numbers. We see that the photon-loss event can be detected by measuring photon-number parity $\hat{P} = (-1)^{\hat{n}}$. The parity operator thus plays the role of a stabilizer for this code (Nielsen and Chuang, 2000; Michael *et al.*, 2016).

This simple encoding should be compared to directly using the Fock states $\{|0\rangle, |1\rangle\}$ to store quantum information. In this case, a single-photon loss on $c_0|0\rangle + c_1|1\rangle$ leads to $|0\rangle$ and the quantum information has been irreversibly lost. This disadvantage is in contrast to the fact that the rate at which photons are lost, which scales with \bar{n} , is (averaged over the code words) 4 times as large when using the encoding in Eq. (156) as when using the Fock states $\{|0\rangle, |1\rangle\}$. This observation reflects the usual conundrum of quantum-error correction: using more resources (here more photons) to protect quantum information actually increases the natural error rate. The protocol for detecting and correcting errors must be fast enough and accurate enough to counteract this increase. The challenge for experimental implementations of quantum-error correction is thus to reach and go beyond the break-even point where the encoded qubit [here Eq. (156)] has a coherence time exceeding the coherence time of the unencoded constituent physical components (here the Fock states $\{|0\rangle, |1\rangle\}$). Near break-even performance with the previously mentioned binomial code was experimentally reported by Hu *et al.* (2019).

The simple instance of the previously introduced binomial code is able to correct a single amplitude-damping error (photon loss). Thus if the correction protocol is applied after a time interval δt , the probability of an uncorrectable error is reduced from $\mathcal{O}(\kappa\delta t)$ to $\mathcal{O}((\kappa\delta t)^2)$, where κ is the cavity energy decay rate.

To better understand the simplicity and efficiency advantages of bosonic quantum-error correction (QEC) codes, it is instructive to do a head-to-head comparison of the simplest binomial code with the simplest qubit code for amplitude

TABLE I. Comparison of qubit and bosonic codes for amplitude damping. γ and κ are, respectively, the qubit and oscillator energy relaxation rates.

| | Four-qubit code | Simplest binomial code |
|----------------------------------|--|---------------------------------------|
| Code word $ 0_L\rangle$ | $(1/\sqrt{2})(0000\rangle + 1111\rangle)$ | $(1/\sqrt{2})(0\rangle + 4\rangle)$ |
| Code word $ 1_L\rangle$ | $(1/\sqrt{2})(1100\rangle + 0011\rangle)$ | $ 2\rangle$ |
| Mean excitation number \bar{n} | 2 | 2 |
| Hilbert space dimension | $2^4 = 16$ | $\{0, 1, 2, 3, 4\} = 5$ |
| Number of correctable errors | $\{\hat{I}, \sigma_1^-, \sigma_2^-, \sigma_3^-, \sigma_4^-\} = 5$ | $\{\hat{I}, a\} = 2$ |
| Stabilizers | $\hat{S}_1 = \hat{Z}_1 \hat{Z}_2, \hat{S}_2 = \hat{Z}_3 \hat{Z}_4,$ $\hat{S}_3 = \hat{X}_1 \hat{X}_2 \hat{X}_3 \hat{X}_4$ | $\hat{P} = (-1)^{\hat{n}}$ |
| Number of stabilizers | 3 | 1 |
| Approximate QEC? | Yes, first order in γt | Yes, first order in κt |

damping. The smallest qubit code able to protect logical information against a general single-qubit error requires five qubits (Bennett *et al.*, 1996; Laflamme *et al.*, 1996; Knill, Laflamme, and Milburn, 2001). However, the specific case of the qubit amplitude-damping channel can be corrected to first order against single-qubit errors using a four-qubit code (Leung *et al.*, 1997) that, like the binomial code, satisfies the Knill-Laflamme conditions (Knill and Laflamme, 1997) to lowest order and whose two logical code words are

$$|0_L\rangle = \frac{1}{\sqrt{2}}(|0000\rangle + |1111\rangle), \quad (157a)$$

$$|1_L\rangle = \frac{1}{\sqrt{2}}(|1100\rangle + |0011\rangle). \quad (157b)$$

This four-qubit amplitude-damping code and the single-mode binomial bosonic code for amplitude damping are compared in Table I. Note that, just as in the binomial code, both code words have mean excitation numbers equal to 2 and thus are equally likely to suffer an excitation loss. The logical qubit of Eq. (157) lives in a Hilbert space of dimension $2^4 = 16$ and has four different physical sites at which the damping error can occur. Counting the case of no errors, there are therefore a total of five different error states that require measurement of three distinct error syndromes $\hat{Z}_1 \hat{Z}_2, \hat{Z}_3 \hat{Z}_4,$ and $\hat{X}_1 \hat{X}_2 \hat{X}_3 \hat{X}_4$ to diagnose (where \hat{P}_i refers to Pauli operator \hat{P} acting on qubit i). The required weight-2 and weight-4 operators have not been easy to measure to date in a highly QND manner and with high fidelity, but some progress has been made toward this goal (Chow *et al.*, 2014, 2015; Córcoles *et al.*, 2015; Ristè *et al.*, 2015; Takita *et al.*, 2016). In contrast, the simple bosonic code in Eq. (156) requires only the lowest five states out of the formally infinite oscillator Hilbert space. Moreover, since there is only a single mode, there is only a single error, namely, photon loss (or no loss), and it can be detected by measuring a single stabilizer, the photon-number parity. It turns out that, unlike in ordinary quantum optics, photon-number parity is relatively easy to

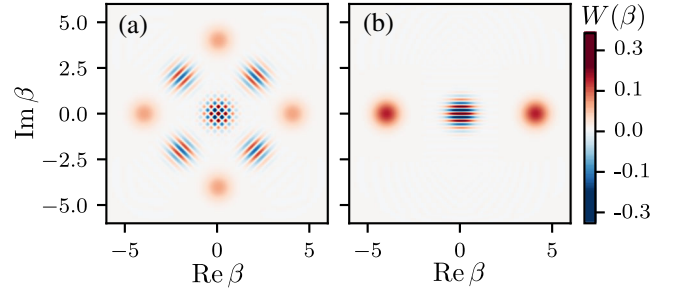


FIG. 31. Wigner function $W(\beta)$ obtained numerically for (a) four-component and (b) two-component cat states with $\alpha = 4$. Red is positive and blue is negative.

measure in circuit QED with high fidelity and minimal state demolition (Sun *et al.*, 2014; Ofek *et al.*, 2016). It is for all these reasons that, unlike the four-qubit code, the bosonic code in Eq. (156) has already been demonstrated experimentally to nearly reach the break-even point for QEC (Hu *et al.*, 2019; Ma *et al.*, 2020). Generalizations of this code to protect against more than a single-photon loss event, as well as photon gain and dephasing, were described by Michael *et al.* (2016a).

Operation slightly exceeding break even was reported by Ofek *et al.* (2016) with cat-state bosonic encoding, which we describe now. In the encoding used in that experiment, each logical code word is a superposition of four coherent states referred to as a four-component cat code (Mirrahimi *et al.*, 2014)

$$|0_L\rangle = \mathcal{N}_0(|\alpha\rangle + |i\alpha\rangle + |-\alpha\rangle + |-i\alpha\rangle), \quad (158a)$$

$$|1_L\rangle = \mathcal{N}_1(|\alpha\rangle - |i\alpha\rangle + |-\alpha\rangle - |-i\alpha\rangle), \quad (158b)$$

where \mathcal{N}_i are normalization constants, with $\mathcal{N}_0 \simeq \mathcal{N}_1$ for large $|\alpha|$. The Wigner function for the $|0_L\rangle$ code word is shown in Fig. 31(a) for $\alpha = 4$. The relationship between this encoding and the simple code in Eq. (156) can be seen by writing Eq. (158) using Eq. (87) for $|\alpha\rangle$ in terms of Fock states. One immediately finds that $|0_L\rangle$ has support on Fock states $|4n\rangle$ only with $n = 0, 1, \dots$, while $|1_L\rangle$ has support on Fock states $|4n + 2\rangle$, and again for $n = 0, 1, \dots$. It follows that the two code words are mapped onto orthogonal states under the action of \hat{a} , similar to the binomial code of Eq. (156). Moreover, the average photon number \bar{n} is approximately equal for the two logical states in the limit of large $|\alpha|$. The protection offered by this encoding is thus similar to that of the binomial code in Eq. (156). In fact, these two encodings belong to a larger class of codes characterized by rotation symmetries in phase space (Grimsmo, Combes, and Baragiola, 2020).

We end this section by discussing an encoding that is even simpler than Eq. (158), sometimes referred to as a two-component cat code. In this case, the code words are defined as $|+L\rangle = \mathcal{N}_0(|\alpha\rangle + |-\alpha\rangle)$ and $|-L\rangle = \mathcal{N}_1(|\alpha\rangle - |-\alpha\rangle)$ (Cochrane, Milburn, and Munro, 1999; Ralph *et al.*, 2003; Gilchrist *et al.*, 2004; Mirrahimi *et al.*, 2014; Puri, Boutin, and Blais, 2017). The Wigner function for $|+L\rangle$ is shown in Fig. 31(b). The choice to define these code words in the logical \hat{X}_L basis instead of the \hat{Z}_L basis is simply a convention

but turns out to be convenient for this cat code. In contrast to Eqs. (156) and (158), these two states are not mapped to two orthogonal states under the action of \hat{a} . To understand this encoding, it is useful to consider the logical \hat{Z}_L basis states in the limit of large $|\alpha|$:

$$|0_L\rangle = \frac{1}{\sqrt{2}}(|+L\rangle + |-L\rangle) = |\alpha\rangle + \mathcal{O}(e^{-2|\alpha|^2}), \quad (159a)$$

$$|1_L\rangle = \frac{1}{\sqrt{2}}(|+L\rangle - |-L\rangle) = |-\alpha\rangle + \mathcal{O}(e^{-2|\alpha|^2}). \quad (159b)$$

As is made clear by the second equality, for large enough $|\alpha|$ these logical states are close to coherent states of the same amplitude but opposite phase. The action of \hat{a} is thus, to a good approximation, a phase flip since $\hat{a}|0_L/1_L\rangle \sim \pm|0_L/1_L\rangle$.

The advantage of this encoding is that, while photon loss leads to phase flips, the bit-flip rate is exponentially small with $|\alpha|$. This can be immediately understood from the golden rule, whose relevant matrix element for bit flips is $\langle 1_L|\hat{a}|0_L\rangle \sim \langle -\alpha|\hat{a}|\alpha\rangle = \alpha e^{-2|\alpha|^2}$. In other words, if the qubit is encoded in a coherent state with many photons, losing one simply does not do much. This is akin to the redundancy required for quantum-error correction. As a result, the bit-flip rate ($1/T_1$) decreases exponentially with $|\alpha|^2$, while the phase-flip rate increases only linearly with $|\alpha|^2$. The crucial point is that the bias between bit- and phase-flip error rates increases exponentially with α , which has been verified experimentally (Grimm *et al.*, 2020; Lescanne, Villiers *et al.*, 2020). While the logical states in Eq. (159) do not allow for recovery from photon-loss errors, the strong asymmetry between different types of errors can be exploited to significantly reduce the qubit overhead necessary for fault-tolerant quantum computation (Guillaud and Mirrahimi, 2019; Puri *et al.*, 2020). The basic intuition behind this statement is that the qubit defined by Eq. (159) can be used in an error-correcting code tailored to predominantly correct the most likely error (here phase flips) rather than devoting resources to correcting both amplitude and phase errors (Tuckett, Bartlett, and Flammia, 2018; Tuckett *et al.*, 2019, 2020).

Another bosonic encoding that was recently demonstrated in circuit QED is the GKP code (Campagne-Ibarcq *et al.*, 2020). This demonstration is the first QEC experiment able to correct all logical errors, and it came close to reaching the break-even point. While all the previously described bosonic codes are based on code words that obey rotation symmetry in phase space, the GKP code is instead based on translation symmetry. We will not describe the GKP encoding in more detail here but refer the interested reader to the review given by Terhal, Conrad, and Vuillot (2020).

VIII. QUANTUM OPTICS ON A CHIP

The strong light-matter interaction realized in circuit QED together with the flexibility allowed in designing and operating superconducting quantum circuits has created the possibility of exploring the rich physics of quantum optics at microwave frequencies in circuits. As previously discussed it has made possible the observation of vacuum Rabi splitting,

photon-number splitting in the strong-dispersive regime, and signatures of ultrastrong light-matter coupling. The new parameter regimes that can be achieved in circuit QED have also made it possible to test some of the theoretical predictions from the early days of quantum optics and to explore new research avenues. A first indication that circuit QED is an ideal playground for these ideas is the strong Kerr nonlinearity relative to the decay rate K/κ that can readily be achieved in circuits. Indeed, from the point of view of quantum optics, a transmon is a Kerr-nonlinear oscillator that is so nonlinear that it exhibits photon blockade. Given the high Q factors that can be achieved in 3D superconducting cavities, such levels of nonlinearity can also be readily obtained in microwave resonators by using transmons or other Josephson-junction-based circuits to induce nonlinearity in electromagnetic modes.

Many of the links between circuit QED and quantum optics have already been highlighted in this review. In this section, we continue this discussion by presenting further examples. More information about quantum optics at microwave frequencies was given in the review by Gu *et al.* (2017).

A. Intracavity fields

Because superconducting qubits can rapidly be tuned over a wide frequency range, it is possible to bring them in and out of resonance with a cavity mode on a timescale that is fast with respect to $1/g$, the inverse of the qubit-cavity coupling strength. For all practical purposes, this is equivalent to the thought experiment of moving an atom in and out of the cavity in cavity QED. An experiment by Hofheinz *et al.* (2008) took advantage of this possibility to prepare the cavity in Fock states up to $|n = 6\rangle$. With the qubit and the cavity in their respective ground states and the two systems largely detuned, their approach is to first π pulse the qubit to its excited state. The qubit frequency is then suddenly brought into resonance with the cavity for a time $1/2g$ such as to swap the qubit excitation to a cavity photon as the system evolves under the Jaynes-Cummings Hamiltonian (36). The interaction is then effectively stopped by moving the qubits to its original frequency, after which the cycle is repeated until n excitations have been swapped in this way. Because the swap frequency between the states $|e, n - 1\rangle$ and $|g, n\rangle$ is proportional to \sqrt{n} , the time during which the qubit and cavity are kept in resonance must be adjusted accordingly at each cycle. The same \sqrt{n} dependence is then used to probe the cavity state using the qubit as a probe (Brune *et al.*, 1996; Hofheinz *et al.*, 2008).

Building on this technique and using a protocol proposed by Law and Eberly (1996) for cavity QED, the preparation of arbitrary states of the cavity field and the characterization of these states by measuring the cavity Wigner function was demonstrated (Hofheinz *et al.*, 2009). Figure 32 shows the result of this Wigner tomography for superpositions involving up to six cavity photons (top row, theory; bottom row, data). As noted by Hofheinz *et al.* (2008), a downside of this sequential method is that the preparation time rapidly becomes comparable to the Fock state lifetime, limiting the Fock states that can be reached and the fidelity of the resulting states.

Taking advantage of the large χ/κ that can be reached in 3D cavities, an alternative to create such states is to exploit qubit

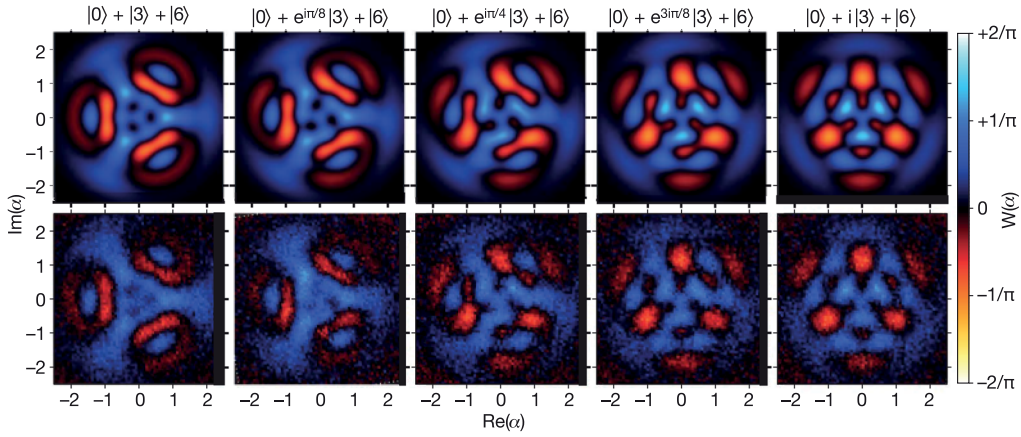


FIG. 32. Wigner function of the intracavity field for Fock state superpositions $|0\rangle + e^{i\varphi}|3\rangle + |6\rangle$ for five values of the phase φ ; see the panel titles. Top row: theory. Bottom row: experimental data. Adapted from Hofheinz *et al.*, 2009.

transitions conditioned on the Fock state of the cavity. Together with cavity displacements, these photon-number-dependent qubit transitions can be used to prepare arbitrary cavity states (Heeres *et al.*, 2015; Krastanov *et al.*, 2015). Combining these ideas with numerical optimal control allowed Heeres *et al.* (2017) to synthesize cavity states with high fidelity such as Fock states up to $|n = 6\rangle$ and four-legged cat states.

The long photon lifetime that is possible in 3D superconducting cavities together with the possibility to realize a single-photon Kerr nonlinearity that overwhelms the cavity decay ($K/\kappa > 1$) has enabled a number of similar experiments, such as the observation of collapse and revival of a coherent state in a Kerr medium (Kirchmair *et al.*, 2013) and the preparation of cat states with nearly 30 photons (Vlastakis *et al.*, 2013). Another example is the experimental encoding of qubits in oscillator states discussed in Sec. VII.C.

B. Quantum-limited amplification

Driven by the need for fast, high-fidelity single-shot readout of superconducting qubits, superconducting low-noise linear microwave amplifiers are a subject of intense research. There are two broad classes of linear amplifiers. First, phase-preserving amplifiers that equivalently amplify both quadratures of the signal. Quantum mechanics imposes the condition that these amplifiers add a minimum of half a photon of noise to the input signal (Caves, 1982, 2012; Clerk *et al.*, 2010). Second, phase-sensitive amplifiers that amplify one quadrature of the signal while squeezing the orthogonal quadrature. This type of amplifier can in principle operate without adding noise (Caves, 1982; Clerk *et al.*, 2010). Amplifiers adding the minimum amount of noise allowed by quantum mechanics, phase preserving or not, are referred to as quantum-limited amplifiers. We note that, in practice, phase-sensitive amplifiers are useful if the quadrature containing the relevant information is known in advance, a condition that is realized when trying to distinguish between two coherent states in the dispersive qubit readout discussed in Sec. V.C.

While much of the development of near-quantum-limited amplifiers has been motivated by the need to improve qubit

readout, Josephson-junction-based amplifiers have been theoretically investigated (Yurke, 1987) and experimentally demonstrated as early as the late 1980s (Yurke *et al.*, 1988, 1989). These amplifiers have now found applications in a broad range of contexts. In their simplest form, such an amplifier is realized as a driven oscillator mode rendered weakly nonlinear by incorporating a Josephson junction and are generically known as a Josephson parametric amplifier (JPA).

For weak nonlinearity, the Hamiltonian of a driven nonlinear oscillator is well approximated by

$$H = \hbar\omega_0\hat{a}^\dagger\hat{a} + \hbar\frac{K}{2}\hat{a}^{\dagger 2}\hat{a}^2 + \hbar\epsilon_p(\hat{a}^\dagger e^{-i\omega_p t} + \hat{a}e^{i\omega_p t}), \quad (160)$$

where ω_0 is the system frequency, K is the negative Kerr nonlinearity, and ϵ_p and ω_p are the pump amplitude and frequency, respectively. The physics of the JPA is best revealed by applying a displacement transformation $\hat{D}^\dagger(\alpha)\hat{a}\hat{D}(\alpha) = a + \alpha$ to H , with α chosen to cancel the pump term. Doing so leads to the transformed Hamiltonian

$$H_{\text{JPA}} = \hbar\delta\hat{a}^\dagger\hat{a} + \frac{\hbar}{2}(\epsilon_2\hat{a}^{\dagger 2} + \epsilon_2^*\hat{a}^2) + H_{\text{corr}}, \quad (161)$$

where $\delta = \omega_0 + 2|\alpha|^2K - \omega_p$ is the effective detuning, $\epsilon_2 = \alpha^2K$, and there are H_{corr} correction terms that can be dropped for weak enough pump amplitude and Kerr nonlinearity, i.e., when the single-photon loss rate κ is large relative to K and thus the drive does not populate the mode enough for higher-order nonlinearity to become important (Boutin *et al.*, 2017). The second term, of amplitude ϵ_2 , is a two-photon pump that is the generator of quadrature squeezing. Amplification is obtained when operating the device close to but under the parametric threshold $\epsilon_2 < \sqrt{\delta^2 + (\kappa/2)^2}$ (Wustmann and Shumeiko, 2013). Rather than driving the nonlinear oscillator as in Eq. (160), an alternative approach to arriving at H_{JPA} is to replace the junction with a SQUID and to apply a flux modulation at $2\omega_0$ (Yamamoto *et al.*, 2008).

Equation (161) is the Hamiltonian for a parametric amplifier working with a single physical oscillator mode. Using appropriate filtering in the frequency domain, single-mode

parametric amplifiers can be operated in a phase-sensitive mode when detecting the emitted radiation over the full bandwidth of the physical mode; see [Eichler, Bozyigit, Lang, Baur *et al.* \(2011\)](#). This is also called the degenerate mode of operation. Alternatively, the same single-oscillator-mode amplifier can be operated in the phase-preserving mode when separating frequency components above and below the pump in the experiment by using appropriately chosen narrow-band filters; see [Eichler, Bozyigit, Lang, Baur *et al.* \(2011\)](#). Parametric amplifiers with two or multiple physical modes are also frequently put to use ([Roy and Devoret, 2016](#)) and can be operated in both the phase-sensitive and phase-preserving modes, in degenerate and nondegenerate modes of operation, as demonstrated by [Eichler *et al.* \(2014\)](#).

Important parameters that different approaches to implementing JPAs aim at optimizing include amplifier gain, bandwidth, and dynamic range. The last item refers to the range of power over which the amplifier acts linearly, i.e., powers at which the amplifier output is linearly related to its input. Above a certain input power level, the correction terms in Eq. (161) resulting from the junction nonlinearity can no longer be ignored and lead to saturation of the gain ([Abdo, Kamal, and Devoret, 2013](#); [Kochetov and Fedorov, 2015](#); [Boutin *et al.*, 2017](#); [Liu *et al.*, 2017](#); [Planat *et al.*, 2019](#)). For this reason, while transmon qubits are operated in a regime where the single-photon Kerr nonlinearity is large and overwhelms the decay rate, JPAs are operated in a different regime with $|K|/\kappa \sim 10^{-2}$ or smaller.

An approach to increasing the dynamic range of JPAs is to replace the Josephson junction of energy E_J with an array of M junctions, each of energy ME_J ([Castellanos-Beltran and Lehnert, 2007](#); [Castellanos-Beltran *et al.*, 2008](#); [Eichler and Wallraff, 2014](#)). Because the voltage drop is now distributed over the array, the bias on any single junction is M times smaller, and therefore the effective Kerr nonlinearity of the device is reduced from K to K/M^2 . As a result, nonlinear effects take effect only at increased input signal powers leading to an increased dynamic range. This can be done without degrading the amplifier's bandwidth ([Eichler and Wallraff, 2014](#)). Typical values are ~ 50 MHz bandwidth with ~ -117 dBm saturation power for ~ 20 dB gain ([Planat *et al.*, 2019](#)). Variations of this idea based on modified SQUID loops known as a superconducting nonlinear asymmetric inductive element (SNAIL) have been realized with a larger saturation power of ~ -100 dBm and otherwise similar characteristics ([Fratini *et al.*, 2018](#); [Sivak *et al.*, 2019, 2020](#)). A reason for this increased dynamic range is that the SNAIL allows for more flexibility in its design and operation to reduce the amplitude of the unwanted nonlinear effects ([Fratini *et al.*, 2017](#)). It is also useful to point out that impedance engineering can be used to improve these numbers further ([Roy *et al.*, 2015](#)).

Because the JPA is based on a localized oscillator mode, the product of its gain and bandwidth is approximately constant. Therefore, increase in one must be done at the expense of the other ([Clerk *et al.*, 2010](#); [Eichler and Wallraff, 2014](#)). As a result, it has proven to be difficult to design JPAs with enough bandwidth and dynamic range to simultaneously measure more than a few transmons ([Jeffrey *et al.*, 2014](#)).

To avoid the constant gain-bandwidth product that results from relying on a resonant mode, a drastically different strategy, known as the Josephson traveling-wave parametric amplifier (JTWPA), is to use an open nonlinear medium in which the signal copropagates with the pump tone. While in a JPA the signal interacts with the nonlinearity for a long time due to the finite Q of the circuit, in the JTWPA the long interaction time is instead a result of the long propagation length of the signal through the nonlinear medium ([O'Brien *et al.*, 2014](#)). In practice, JTWPAs are realized with a metamaterial transmission line whose center conductor is made from thousands of Josephson junctions in series ([Macklin *et al.*, 2015](#)). This device does not have a fixed gain-bandwidth product and has been demonstrated to have 20 dB over as much as 3 GHz bandwidth while operating close to the quantum limit ([Macklin *et al.*, 2015](#); [White *et al.*, 2015](#); [Planat *et al.*, 2020](#)). Because every junction in the array can be made only weakly nonlinear, the JTWPA also offers a large enough dynamic range for rapidly multiplexed simultaneous readout of multiple qubits ([Heinsoo *et al.*, 2018](#)).

C. Propagating fields and their characterization

1. Itinerant single and multiphoton states

In addition to using qubits to prepare and characterize quantum states of intracavity fields, it is also possible to take advantage of the strong nonlinearity provided by a qubit to prepare states of propagating fields at the output of a cavity. This can be done in a cavity with a relatively large decay rate κ by tuning a qubit into and out of resonance with the cavity ([Bozyigit *et al.*, 2011](#)) or by applying appropriately chosen drive fields ([Houck *et al.*, 2007](#)). Alternatively, it is also possible to change the cavity decay rate in time to create single-photon states ([Sete *et al.*, 2013](#); [Yin *et al.*, 2013](#)).

The first on-chip single-photon source in the microwave regime was realized with a dispersively coupled qubit engineered such that the Purcell decay rate γ_κ dominates the qubit's intrinsic nonradiative decay rate γ_1 ([Houck *et al.*, 2007](#)). In this situation, exciting the qubit leads to rapid qubit decay by photon emission. In the absence of single-photon detectors working at microwave frequencies, the presence of a photon was observed by using a nonlinear circuit element (a diode) whose output signal was proportional to the square of the electric field [$\propto (\hat{a}^\dagger + \hat{a})^2$], and therefore indicative of the average photon number $\langle \hat{a}^\dagger \hat{a} \rangle$, in repeated measurements.

Rather than relying on direct power measurements, researchers have developed techniques to reconstruct arbitrary correlation functions of the cavity output field from the measurement records of the field quadratures ([da Silva *et al.*, 2010](#); [Menzel *et al.*, 2010](#)). These approaches rely on multiple detection channels with uncorrelated noise to quantify and subtract from the data the noise introduced by the measurement chain. In this way, it is possible to extract first- and second-order coherence functions of the microwave field. With enough averaging, this approach does not require quantum-limited amplifiers, although the number of required measurement runs is drastically reduced when such amplifiers are used in place of HEMT amplifiers.

This approach was used to measure second-order coherence functions $G^2(t, t + \tau) = \langle \hat{a}^\dagger(t) \hat{a}^\dagger(t + \tau) \hat{a}(t + \tau) \hat{a}(t) \rangle$ in the

first demonstration of antibunching of a pulsed single-microwave-frequency photon source (Bozyigit *et al.*, 2011). The same technique also enabled the observation of a resonant photon blockade at microwave frequencies (Lang *et al.*, 2011), and, using two single-photon sources at the input of a microwave beam splitter, the indistinguishability of microwave photons was demonstrated in a Hong-Ou-Mandel correlation function measurement (Lang *et al.*, 2013). A similar approach was used to characterize the blackbody radiation emitted by a $50\ \Omega$ load resistor (Mariantoni *et al.*, 2010).

Building on these results, it is also possible to reconstruct the quantum state of itinerant microwave fields from measurement of the fields moments. This technique relies on interleaving two types of measurements: measurements on the state of interest and ones in which the field is left in the vacuum as a reference to subtract the measurement chain noise (Eichler, Bozyigit, Lang, Steffen *et al.*, 2011). In this way, the Wigner function of arbitrary superpositions of vacuum and one-photon Fock states has been reconstructed (Eichler, Bozyigit, Lang, Steffen *et al.*, 2011; Kono *et al.*, 2018). This technique was extended to propagating modes containing multiple photons (Eichler, Bozyigit, and Wallraff, 2012). Similarly, entanglement between a stationary qubit and a propagating mode was quantified in this approach with joint state tomography (Eichler, Bozyigit, and Wallraff, 2012; Eichler *et al.*, 2012). Quadrature-histogram analysis also enabled the measurement of correlations between radiation fields (Flurin *et al.*, 2015) and the observation of entanglement of itinerant photon pairs in waveguide QED (Kannan *et al.*, 2020).

2. Squeezed microwave fields

Operated in the phase-sensitive mode, quantum-limited amplifiers are sources of squeezed radiation. Indeed, for $\delta = 0$ and ignoring the correction terms, the JPA Hamiltonian of Eq. (161) is the generator of the squeezing transformation

$$S(\zeta) = e^{(1/2)\zeta^* \hat{a}^2 - (1/2)\zeta \hat{a}^{\dagger 2}}, \quad (162)$$

which takes the vacuum to the squeezed vacuum $|\zeta\rangle = S(\zeta)|0\rangle$. In Eq. (162), $\zeta = r e^{i\theta}$, with r the squeezing parameter and θ the squeezing angle. As illustrated in Fig. 33(a), the action of $S(\zeta)$ on vacuum is to “squeeze” one quadrature of the field at the expense of “antisqueezing” the orthogonal quadrature while leaving the total area in phase space unchanged. As a result, squeezed states, like coherent states, saturate the Heisenberg inequality.

This can be seen more clearly in the variance of the quadrature operator \hat{X}_ϕ , which takes the form

$$\Delta X_\phi^2 = \frac{1}{4}(e^{2r} \sin^2 \tilde{\phi} + e^{-2r} \cos^2 \tilde{\phi}), \quad (163)$$

where we define $\tilde{\phi} = \phi - \theta/2$. In experiments, the squeezing level is often reported in decibels computed using

$$S = 10 \log_{10} \frac{\Delta X_\phi^2}{\Delta X_{\text{vac}}^2}. \quad (164)$$

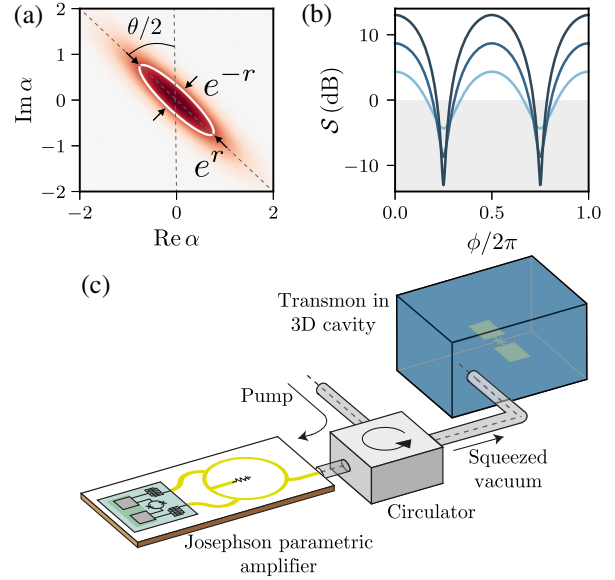


FIG. 33. (a) Wigner function of a squeezed vacuum state $S(\zeta)|0\rangle$ with $r = 0.75$ and $\theta = \pi/2$. The white contour line is an ellipse of semiminor axis $e^{-r}/2$ and semimajor axis $e^r/2$. (b) Squeezing level vs ϕ for $r = 0.5, 1.0, 1.5$ and $\theta = \pi$. The horizontal line corresponds to vacuum noise $\Delta X_{\text{vac}}^2 = 1/4$. (c) Experimental setup used by Murch, Weber, Macklin, and Siddiqi (2013) to prepare a squeezed vacuum state using a Josephson parametric amplifier and to send, via a circulator (gray box), this state to a transmon qubit in a 3D cavity (blue box). Adapted from Murch, Weber, Macklin, and Siddiqi, 2013.

Figure 33(b) shows this quantity as a function of ϕ . The variance ΔX_ϕ^2 reaches its minimal value $e^{-2r}/4$ at $\phi = [\theta + (2n + 1)\pi]/2$, where it dips below the vacuum noise level $\Delta X_{\text{vac}}^2 = 1/4$ (horizontal line).

Squeezing in Josephson devices was already observed in the late 1980s (Yurke *et al.*, 1988, 1989; Movshovich *et al.*, 1990), experiments that have been revisited with the development of near-quantum-limited amplifiers (Castellanos-Beltran *et al.*, 2008; Zhong *et al.*, 2013). Quantum-state tomography of an itinerant squeezed state at the output of a JPA was reported by Mallet *et al.* (2011). There homodyne detection with different LO phases on multiple preparations of the same squeezed state, together with maximum likelihood techniques, was used to reconstruct the Wigner function of the propagating microwave field. Moreover, the photon-number distribution of a squeezed field was measured using a qubit in the strong-dispersive regime (Kono *et al.*, 2017). As is clear from the form of the squeezing transformation $S(\zeta)$, a squeezed vacuum is composed of a superposition of only even photon numbers (Schleich and Wheeler, 1987), something that Kono *et al.* (2017) confirmed in experiments.

Thanks to the new parameter regimes that can be achieved in circuit QED, it is possible to experimentally test some long-standing theoretical predictions of quantum optics involving squeezed radiation. For example, in the mid 1980s theorists predicted how dephasing and resonance fluorescence of an atom would be modified in the presence of squeezed radiation (Gardiner, 1986; Carmichael, Lane, and Walls, 1987). Experimentally testing these ideas in the context of traditional

quantum optics with atomic systems, however, represents a formidable challenge (Turchette *et al.*, 1998; Carmichael, 2016). The situation is different in circuits where squeezed radiation can easily be guided from the source of squeezing to the qubit playing the role of artificial atom. Moreover, the reduced dimensionality in circuits compared to free-space atomic experiments limits the number of modes that are involved, such that the artificial atom can be engineered so as to preferentially interact with a squeezed radiation field.

Taking advantage of the possibilities offered by circuit QED, Murch, Weber, Beck *et al.* (2013) confirmed the prediction that squeezed radiation can inhibit phase decay of an artificial atom (Gardiner, 1986). In this experiment, the role of the two-level atom was played by the hybridized cavity-qubit state $\{|\bar{g}, 0\rangle, |\bar{e}, 0\rangle\}$. Moreover, squeezing was produced by a JPA over a bandwidth much larger than the natural linewidth of the two-level system; see Fig. 33(c). According to theory, quantum noise below the vacuum level along the squeezed quadrature leads to a reduction of dephasing. Conversely, along the antisqueezed quadrature, the enhanced fluctuations lead to increased dephasing. For the artificial atom, this results in different timescales for dephasing along the orthogonal axis of the Bloch sphere. In the experiment, phase decay inhibition along the squeezed quadrature was such that the associated dephasing time increased beyond the usual vacuum limit of $2T_1$. By measuring the dynamics of the two-level atom, it was, moreover, possible to reconstruct the Wigner distribution of the itinerant squeezed state produced by the JPA. Using a similar setup, Toyli *et al.* (2016) studied resonance fluorescence in the presence of squeezed vacuum and found excellent agreement with theoretical predictions (Carmichael, Lane, and Walls, 1987). In this way, it was possible to infer the level of squeezing (3.1 dB below vacuum) at the input of the cavity.

The discussion thus far has been limited to squeezing of a single mode. It is also possible to squeeze a pair of modes, which is often referred to as two-mode squeezing. If we label the modes as \hat{a}_1 and \hat{a}_2 , the corresponding squeezing transformation reads

$$S_{12}(\zeta) = e^{(1/2)\zeta^* \hat{a}_1 \hat{a}_2 - (1/2)\zeta \hat{a}_1^\dagger \hat{a}_2^\dagger}. \quad (165)$$

Acting on vacuum, S_{12} generates a two-mode squeezed state that is an entangled state of modes \hat{a}_1 and \hat{a}_2 . As a result, in isolation the state of one of the two entangled modes appears to be in a thermal state where the role of the Boltzmann factor $\exp(-\beta\hbar\omega_i)$, with $\omega_{i=1,2}$ the mode frequency, is played by $\tanh^2 r$ (Barnett and Radmore, 2002). In this case, correlations, and therefore squeezing, is revealed when considering joint quadratures of the form $\hat{X}_1 \pm \hat{X}_2$ and $\hat{P}_1 \pm \hat{P}_2$, rather than the quadratures of a single mode as in Fig. 33(a). In Josephson-based devices, two-mode squeezing can be produced using nondegenerate parametric amplifiers of different types (Roy and Devoret, 2016). Over 12 dB of squeezing below vacuum level between modes of different frequencies, often referred to as the signal and idler in this context, has been reported (Eichler *et al.*, 2014). Other experiments have demonstrated two-mode squeezing in two different spatial

modes, i.e., entangled signals propagating along different transmission lines (Bergeal *et al.*, 2012; Flurin *et al.*, 2012).

D. Remote entanglement generation

Several approaches to entangling nearby qubits were discussed in Sec. VII. In some instances it can be useful, however, to prepare entangled states of qubits separated by larger distances. Together with protocols such as quantum teleportation, entanglement between distant quantum nodes can be the basis of a quantum Internet (Kimble, 2008; Wehner, Elkouss, and Hanson, 2018). Because optical photons can travel for relatively long distances in room-temperature optical fiber while preserving their quantum coherence, this vision appears to be easier to realize at optical rather than microwave frequencies. Nevertheless, given that superconducting cables at millikelvin temperatures have similar losses per meter to optical fibers (Kurpiers *et al.*, 2017), there is no reason to believe that complex networks of superconductor-based quantum nodes cannot be realized. One application of this type of network is a modular quantum computer architecture where the nodes are relatively small-scale error-corrected quantum computers connected by quantum links (Monroe *et al.*, 2014; Chou *et al.*, 2018).

One approach to entangling qubits fabricated in distant cavities relies on entanglement by measurement, which is easy to understand in the case of two qubits coupled to the same cavity. Assuming the qubits to have the same dispersive shift χ due to their coupling to the cavity, the dispersive Hamiltonian in a doubly rotating frame takes the form

$$H = \chi(\hat{\sigma}_{z1} + \hat{\sigma}_{z2})\hat{a}^\dagger\hat{a}. \quad (166)$$

The cavity pull associated with odd-parity states $\{|01\rangle, |10\rangle\}$ is 0, while it is $\pm 2\chi$ for the even-parity states $\{|00\rangle, |11\rangle\}$. As a result, for $\chi \gg \kappa$ a tone at the bare cavity frequency leads to a large cavity field displacement for the even-parity subspace. On the other hand, the displacement is small or negligible for the odd-parity subspace. Starting with a uniform unentangled superposition of the states of the qubits, homodyne detection therefore stochastically collapses the system to one of these subspaces, thereby preparing an entangled state of the two qubits (Lalumière, Gambetta, and Blais, 2010), an idea that was realized experimentally (Ristè *et al.*, 2013).

The same concept was used by Roch *et al.* (2014) to entangle two transmon qubits coupled to two 3D cavities separated by more than a meter of coaxial cable. There the measurement tone transmitted through the first cavity was sent to the second cavity, only after which it was measured by homodyne detection. In the experiment, losses between the two cavities (mainly due to the presence of a circulator preventing any reflection from the second cavity back to the first cavity) as well as finite detection efficiency were the main limit to the achievable concurrence, a measure of entanglement, to 0.35. Alternatively, a protocol where losses reduce the success probability but not the fidelity of the resulting entangled state was implemented by Narla *et al.* (2016). Although the concurrence was only 0.1 in this realization, an advantage of the approach is that it results in a larger on-off ratio between the nodes of the network.

While these entanglement-by-measurement protocols probabilistically entangle a pair of qubits, a more powerful but also more experimentally challenging approach allows one, in principle, to realize this in a fully deterministic fashion (Cirac *et al.*, 1997). Developed in the context of cavity QED, this scheme relies on mapping the state of an atom strongly coupled to a cavity to a propagating photon. By choosing its wave packet to be time symmetric, one finds that the photon is absorbed with unit probability by a second cavity also containing an atom. In this way, it is possible to exchange a quantum state between the two cavities. This protocol relies on the presence of a unidirectional channel between the cavities such that no signal can propagate from the second to the first cavity. At microwave frequencies, this is achieved by inserting a circulator between the cavities. By first entangling the emitter qubit to a partner qubit located in the same cavity, this quantum-state transfer protocol can be used to entangle the two nodes.

Variations on this more direct approach to entangling remote nodes have been implemented in circuit QED (Axline *et al.*, 2018; Campagne-Ibarcq *et al.*, 2018; Kurpiers *et al.*, 2018). All three experiments rely on producing time-symmetric propagating photons by using the interaction between a transmon qubit and a cavity mode. Multiple approaches to shape and catch propagating photons have been developed in circuit QED. For example, Wenner *et al.* (2014) used a transmission-line resonator with a tunable input port to catch a shaped microwave pulse with over 99% probability. Time-reversal-symmetric photons were created by Srinivasan *et al.* (2014) using three-island transmon qubits (Gambetta, Houck, and Blais, 2011; Srinivasan *et al.*, 2011) in which the coupling to a microwave resonator is controlled in time so as to shape the mode function of spontaneously emitted photons. In a similar fashion, shaped single photons can be generated by modulating the boundary condition of a semi-infinite transmission line using a SQUID (Forn-Díaz, Warren *et al.*, 2017), which effectively controls the spontaneous emission rate of a qubit coupled to the line and emitting the photon.

Alternatively, the remote entanglement generation experiment of Kurpiers *et al.* (2018) instead relied on a microwave-induced amplitude- and phase-tunable coupling between the qubit-resonator $|f_0\rangle$ and $|g_1\rangle$ states akin to the fg-ge gate mentioned in Sec. VII.B.3 (Zeytinoglu *et al.*, 2015). Exciting the qubit to its $|f\rangle$ state followed by a π pulse on the f_0 - g_1 transition transfers the qubit excitation to a single resonator photon that is emitted as a propagating photon. This single-photon wave packet can be shaped to be time symmetric by tailoring the envelope of the f_0 - g_1 pulse (Pechal *et al.*, 2014). By inducing the reverse process with a time-reversed pulse on a second resonator also containing a transmon, the itinerant photon is absorbed by this second transmon. In this way, an arbitrary quantum state can be transferred with a probability of 98.1% between two cavities separated by 0.9 m of coaxial line bisected by a circulator (Kurpiers *et al.*, 2018). By instead preparing the emitter qubit in a $(|e\rangle + |f\rangle)/\sqrt{2}$ superposition, one finds that the same protocol deterministically prepares an entangled state of the two transmons with a fidelity of 78.9% at a rate of 50 kHz (Kurpiers *et al.*, 2018). The experiments of Axline *et al.* (2018) and Campagne-Ibarcq *et al.* (2018) reported similar Bell-state fidelities using different approaches

to prepare time-symmetric propagating photons (Pfaff *et al.*, 2017). The fidelity reported by the three experiments suffered from the presence of a circulator bisecting the nearly 1-m-long coaxial cable separating the two nodes. Replacing the lossy commercial circulator by an on-chip quantum-limited version could improve the fidelity (Kamal, Clarke, and Devoret, 2011; Metelmann and Clerk, 2015; Chapman *et al.*, 2017). By taking advantage of the multimode nature of a meter-long transmission line, it is also possible to deterministically entangle remote qubits without the need of a circulator. In this way, a bidirectional communication channel between the nodes is established and deterministic Bell pair production with 79.3% fidelity has been reported (Leung *et al.*, 2019). Finally, the same protocol as in Kurpiers *et al.* (2018) was extended to two transmon qubits located in separate dilution refrigerators connected by a 5-m-long cryogenic link (Magnard *et al.*, 2020).

E. Waveguide QED

The bulk of this review is concerned with the strong coupling of artificial atoms to the confined electromagnetic field of a cavity. Strong light-matter coupling is also possible in free space with an atom or large dipole-moment molecule by tightly confining an optical field in the vicinity of the atom or molecule (Schuller *et al.*, 2010). A signature of strong coupling in this setting is the extinction of the transmitted light by the single atom or molecule acting as a scatterer. This extinction results from destructive interference of the light beam with the collinearly emitted radiation from the scatterer. Ideally, this results in 100% reflection. In practice, because the scatterer emits in all directions, there is poor mode matching with the focused beam and reflection of $\sim 10\%$ is observed with a single atom (Tey *et al.*, 2008) and $\sim 30\%$ with a single molecule (Maser *et al.*, 2016).

Mode matching can, however, be made to be close to ideal with electromagnetic fields in 1D superconducting transmission lines and superconducting artificial atoms, where the artificial atoms can be engineered to essentially emit only in the forward and backward directions along the line (Shen and Fan, 2005). In the first realization of this idea in superconducting quantum circuits, Astafiev *et al.* (2010) observed extinction of the transmitted signal by as much as 94% by coupling a single flux qubit to a superconducting transmission line. Experiments with a transmon qubit have seen extinction as large as 99.6% (Hoi *et al.*, 2011). Pure dephasing and nonradiative decay into modes other than the transmission line are the cause of the small departure from ideal behavior in these experiments. Nevertheless, the large observed extinction is a sign that radiative decay in the transmission line γ_r (i.e., Purcell decay) overwhelms nonradiative decay γ_{nr} . In short, in this cavity-free system, referred to as waveguide QED, $\gamma_r/\gamma_{nr} \gg 1$ is the appropriate definition of strong coupling and is associated with an experimental signature: the extinction of transmission by a single scatterer.

Despite its apparent simplicity, waveguide QED is a rich toolbox with which a number of physical phenomena have been investigated (Roy, Wilson, and Firstenberg, 2017). This includes Autler-Townes splitting (Abdumalikov *et al.*, 2010), single-photon routing (Hoi *et al.*, 2011), the generation of propagating nonclassical microwave states (Hoi *et al.*, 2012),

and large cross-Kerr phase shifts at the single-photon level (Hoi *et al.*, 2013).

In another experiment, Hoi *et al.* (2015) studied the radiative decay of an artificial atom placed in front of a mirror, here formed by a short to the ground of the waveguide's center conductor. In the presence of a weak drive field applied to the waveguide, the atom relaxes by emitting a photon in both directions of the waveguide. The radiation emitted toward the mirror, assumed here to be on the left side of the atom, is reflected back to interact again with the atom after having acquired a phase shift $\theta = 2 \times 2\pi l/\lambda + \pi$, where l is the atom-mirror distance and λ is the wavelength of the emitted radiation. The additional phase factor of π accounts for the hard reflection at the mirror. When one takes into account the resulting multiple round trips, this modifies the atomic radiative decay rate that takes the form $\gamma(\theta) = 2\gamma_r \cos^2(\theta/2)$ (Glaetzle *et al.*, 2010; Koshino and Nakamura, 2012; Hoi *et al.*, 2015).

For $l/\lambda = 1/2$, the radiative decay rate vanishes corresponding to destructive interference of the right-moving field and the left-moving field after multiple reflections on the mirror. In contrast, for $l/\lambda = 1/4$, these fields interfere constructively, leading to enhanced radiative relaxation with $\gamma(\theta) = 2\gamma_r$. The ratio l/λ can be modified by shorting the waveguide's center conductor with a SQUID. In this case, the flux threading the SQUID can be used to change the boundary condition seen by the qubit, effectively changing the distance l (Sandberg *et al.*, 2008). The experiment conducted by Hoi *et al.* (2015) instead relied on flux tuning of the qubit transition frequency, thereby changing λ . In this way, a modulation of the qubit decay rate by a factor of close to 10 was observed. A similar experiment has been reported with a trapped ion in front of a movable mirror (Eschner *et al.*, 2001).

Engineering vacuum fluctuations in this system has been pushed even further by creating microwave photonic band gaps in waveguides to which transmon qubits are coupled (Liu and Houck, 2017; Mirhosseini *et al.*, 2018). For example, Mirhosseini *et al.* (2018) coupled a transmon qubit to a metamaterial formed by periodically loading the waveguide with lumped-element microwave resonators. By tuning the transmon frequency in the band gap where there is zero or only a limited density of states to accept photons emitted by the qubit, they observed an increase by a factor of 24 in the qubit lifetime.

An interpretation of the ‘‘atom in front of a mirror’’ experiments is that the atom interacts with its mirror image. Rather than using a boundary condition (i.e., a mirror) to study the resulting constructive and destructing interferences and change in the radiative decay rate, it is also possible to couple a second atom to the same waveguide (Lalumière *et al.*, 2013; van Loo *et al.*, 2013). In this case, photons (real or virtual) emitted by one atom can be absorbed by the second atom, leading to interactions between the atoms separated by a distance $2l$. As in the case of a single atom in front of a mirror, when the separation between the atoms is such that $2l/\lambda = 1/2$, correlated decay of the pair of atoms at the enhanced rate $2\gamma_1$ is expected (Chang *et al.*, 2012; Lalumière *et al.*, 2013) and experimentally observed (van Loo *et al.*, 2013). On the other hand, at a separation of $2l/\lambda = 3/4$

correlated decay is replaced by coherent energy exchange between the two atoms mediated by virtual photons (Chang *et al.*, 2012; Lalumière *et al.*, 2013; van Loo *et al.*, 2013). Moreover, adding a boundary condition acting as a mirror to a device holding two artificial atoms allowed Wen *et al.* (2019) to measure a collective Lamb shift as large as 0.8% of the qubit transition frequency. We note that these experiments with transmon qubits agree with a Markovian model of the interaction of the qubits with the waveguide (Lehmberg, 1970; Chang *et al.*, 2012; Lalumière *et al.*, 2013). Deviations from these predictions are expected as the distance between the atoms increases (Zheng and Baranger, 2013).

Finally, following a proposal by Chang *et al.* (2012), an experiment by Mirhosseini *et al.* (2019) used a pair of transmon qubits to act as an effective cavity for a third transmon qubit, with all qubits coupled to the same waveguide. In this way, vacuum Rabi oscillations between the dark state of the effective cavity and the qubit playing the role of atom were observed, confirming that the strong-coupling regime of cavity QED was achieved.

F. Single-microwave photon detection

The development of single-photon detectors at infrared, optical, and ultraviolet frequencies has been crucial to the field of quantum optics and in fundamental tests of quantum physics (Hadfield, 2009; Eisaman *et al.*, 2011). High-efficiency photon detectors are one of the elements that has allowed a loophole-free violation of Bell's inequality (Giustina *et al.*, 2015; Hensen *et al.*, 2015; Shalm *et al.*, 2015). Because microwave photons have orders of magnitude less energy than infrared, optical, and ultraviolet photons, the realization of a photon detector at microwave frequencies is more challenging. Yet photon detectors in that frequency range would find a number of applications, including those in quantum information processing (Kimble, 2008; Narla *et al.*, 2016), for quantum radars (Barzanjeh *et al.*, 2015, 2020; Chang *et al.*, 2019), and for the detection of dark matter axions (Lamoreaux *et al.*, 2013; Zheng *et al.*, 2016; Dixit *et al.*, 2020).

Nondestructive counting of microwave photons localized in a cavity has already been demonstrated experimentally by using an atom (artificial or not) as a probe in the strong-dispersive regime (Gleyzes *et al.*, 2007; Schuster *et al.*, 2007). Similar measurements have also been done using a transmon qubit mediating interactions between two cavities, one containing the photons to be measured and a second acting as a probe (Johnson *et al.*, 2010). The detection of itinerant microwave photons remains, however, more challenging. A number of theoretical proposals have appeared (Helmer *et al.*, 2009; Romero, García-Ripoll, and Solano, 2009; Koshino *et al.*, 2013, 2016; Fan *et al.*, 2014; Sathyamoorthy *et al.*, 2014; Kyriienko and Sorensen, 2016; Leppäkangas *et al.*, 2018). One common challenge for these approaches based on absorbing itinerant photons in a localized mode before detecting them can be linked to the quantum Zeno effect. Indeed, continuous monitoring of the probe mode prevents the photon from being absorbed in the first place. Approaches to mitigating this problem have been introduced, including use of an engineered, impedance matched Λ system to deterministically capture the incoming photon (Koshino *et al.*, 2016)

and use of the bright and dark states of an ensemble of absorbers (Royer *et al.*, 2018).

Despite these challenges, the first itinerant microwave photon detectors have been achieved in the laboratory (Chen *et al.*, 2011; Inomata *et al.*, 2016; Oelsner *et al.*, 2017), in some cases achieving photon detection without destroying the photon in the process (Narla *et al.*, 2016; Besse *et al.*, 2018; Kono *et al.*, 2018; Lescanne, Deléglise *et al.*, 2020). A microwave photon counter was used to measure a superconducting qubit with a fidelity of 92% without using a linear amplifier between the source and the detector (Opremcak *et al.*, 2018). Despite these advances, the realization of a high-efficiency, large-bandwidth, QND single-microwave photon detector remains a challenge for the field.

IX. OUTLOOK

Fifteen years after its introduction (Blais *et al.*, 2004; Wallraff *et al.*, 2004), circuit QED is a leading architecture for quantum computing and an exceptional platform to explore the rich physics of quantum optics in new parameter regimes. Circuit QED has, moreover, found applications in numerous other fields of research. In closing this review, we turn to some of these recent developments.

Because they are a versatile platform to interface quantum devices with transition frequencies in the microwave domain to photons stored in superconducting resonators at similar frequencies, the ideas of circuit QED are now used to couple to a variety of physical systems. An example of such hybrid quantum systems is semiconductor-based double quantum dots coupled to superconducting microwave resonators. Here the position of an electron in a double dot leads to a dipole moment to which the resonator electric field couples. First experiments with gate-defined double quantum dots in nanotubes (Delbecq *et al.*, 2011), GaAs (Frey *et al.*, 2012; Toida, Nakajima, and Komiyama, 2013; Wallraff *et al.*, 2013), and InAs nanowires (Petersson *et al.*, 2012) have demonstrated dispersive coupling and its use for characterizing charge states of quantum dots (Burkard *et al.*, 2020). These first experiments were, however, limited by the large dephasing rate of the quantum dot's charge states, but subsequent experiments have been able to reach the strong-coupling regime (Mi *et al.*, 2017; Stockklauser *et al.*, 2017; Bruhat *et al.*, 2018). Building on these results and by engineering an effective spin-orbit interaction (Pioro-Ladrière *et al.*, 2008; Beaudoin *et al.*, 2016), it has been possible to reach the strong-coupling regime with single spins (Landig *et al.*, 2018; Mi *et al.*, 2018; Samkharadze *et al.*, 2018).

When the coupling to a single spin cannot be made large enough to reach the strong-coupling regime, it is possible to rely on an ensemble of spins to boost the effective coupling. Indeed, in the presence of an ensemble of N emitters, the coupling strength to the ensemble is enhanced by \sqrt{N} (Fink *et al.*, 2009; İmamoğlu, 2009), such that for large enough $g\sqrt{N}$ the strong-coupling regime can be reached. First realizations of these ideas used ensembles of $\sim 10^{12}$ spins to bring the coupling from a few hertz to ~ 10 MHz with NV centers in diamond (Kubo *et al.*, 2010) and Cr^{3+} spins in ruby (Schuster *et al.*, 2010). One objective of these explorations is

to increase the sensitivity of electron paramagnetic resonance or electron spin resonance spectroscopy for spin detection with the ultimate goal of reaching the single-spin limit. A challenge in reaching this goal is the long lifetime of single spins in these systems, which limits the repetition rate of the experiment. By engineering the coupling between the spins and an LC oscillator fabricated in proximity, it has been possible to take advantage of the Purcell effect to reduce the relaxation time from 10^3 to 1 s (Bienfait *et al.*, 2016). This faster timescale allows for faster repetition rates, thereby boosting the sensitivity, which could lead to spin sensitivities of the order of $0.1 \text{ spin}/\sqrt{\text{Hz}}$ (Haikka *et al.*, 2017).

Mechanical systems operated in the quantum regime have also benefited from the ideas of circuit QED (Aspelmeyer, Kippenberg, and Marquardt, 2014). An example is a suspended aluminum membrane that plays the role of a vacuum gap capacitor in a microwave LC oscillator. The frequency of this oscillator depends on the separation between the plates of the capacitor, leading to a coupling between the oscillator and the flexural mode of the membrane. Strong coupling between the mechanical motion and the LC oscillator has been demonstrated (Teufel, Li *et al.*, 2011), allowing one to sideband cool the motion of the mechanical oscillator to a phonon occupation number as small as $n_{\text{phonon}} \sim 0.34$ (Teufel, Donner *et al.*, 2011). Squeezed radiation generated by a Josephson parametric amplifier was also used to cool beyond the quantum backaction limit to $n_{\text{phonon}} \sim 0.19$ (Clark *et al.*, 2017). Building on these ideas, Palomaki, Teufel *et al.* (2013) demonstrated entanglement of the mechanical motion and the microwave fields, and Palomaki, Harlow *et al.* (2013) demonstrated coherent state transfer between itinerant microwave fields and a mechanical oscillator.

Hybrid systems are also important in the context of microwave to optical frequency transduction in the quantum regime. This is a desirable primitive for quantum networks, as it would allow quantum processors based on circuit QED to be linked optically over large distances. A variety of hybrid systems are currently being investigated for this purpose, including electro-optomechanical, electro-optic, and magneto-optic ones (Higginbotham *et al.*, 2018; Lambert *et al.*, 2020; Lauk *et al.*, 2020; Zhu *et al.*, 2020). Two other hybrid quantum systems that have recently emerged are quantum surface acoustic waves interacting with superconducting qubits (Gustafsson *et al.*, 2014; Manenti *et al.*, 2017) and quantum magnonics where quanta of excitation of spin-wave modes known as magnon are strongly coupled to the field of a 3D microwave cavity (Lachance-Quirion *et al.*, 2019).

In addition to these emerging directions, the prospect of realizing circuit-QED-based fault-tolerant quantum computers is one of the main reasons for the enthusiasm toward this field of research. Although formidable challenges remain before large-scale quantum computation becomes a reality, the increasing number of qubits that can be wired up, as well as the improvements in coherence time, gate fidelity, and readout fidelity, suggests that it will eventually be possible to perform computations on circuit-QED-based quantum processors that are out of the reach of current classical computers. As a testament to these advances, quantum supremacy on a 53-qubit device has already been claimed

(Arute *et al.*, 2019), albeit on a problem of no immediate practical interest, and 65-qubit devices are now available online.

Before fault-tolerant quantum computation becomes a reality, there is much effort being devoted to finding useful computational tasks that can be performed on current and near-term noisy intermediate-scale quantum devices (Preskill, 2018). The first experimental steps in this direction have included the determination of molecular energies with variational quantum eigensolvers (O'Malley *et al.*, 2016; Kandala *et al.*, 2017; Colless *et al.*, 2018; Arute *et al.*, 2020b) or boson sampling approaches (Wang *et al.*, 2020), and machine learning with quantum-enhanced features (Havlíček *et al.*, 2019).

Engineered circuit-QED-based devices also present an exciting avenue for performing analog quantum simulations. In contrast to gate-based quantum computing architectures, quantum simulators can be tailored to explore a single specific problem. An example is arrays of resonators capacitively coupled to allow photons to hop from resonator to resonator creating photonic materials (Carusotto *et al.*, 2020). Taking advantage of the flexibility of superconducting quantum circuits, it is possible to create exotic networks of resonators such as lattices in an effective hyperbolic space with constant negative curvature (Kollár, Fitzpatrick, and Houck, 2019). Coupling a qubit to each resonator realizes a Jaynes-Cummings lattice exhibiting a quantum phase transition similar to the superfluid-Mott insulator transition in Bose-Hubbard lattices (Houck, Türeci, and Koch, 2012). Moreover, the nonlinearity provided by capacitively coupled qubits, or of Josephson junctions embedded in the center conductor of the resonators, creates photon-photon interactions. This leads to effects such as photon blockade bearing some similarities to Coulomb blockade in mesoscopic systems (Schmidt and Koch, 2013). Few resonator and qubit devices are also promising for analog quantum simulations: examples include the exploration of a simple model of the light-harvesting process in photosynthetic complexes in a circuit QED device under the influence of both coherent and incoherent drives (Potočník *et al.*, 2018) and the simulation of dissipatively stabilized strongly correlated quantum matter in a small photon Bose-Hubbard lattice (Ma *et al.*, 2019). Superconducting quantum circuits with few qubits have also been used in the context of digital quantum simulations including fermionic models (Barends *et al.*, 2015; Arute *et al.*, 2020a), many-body localization (Roushan *et al.*, 2017; Xu *et al.*, 2018), and spin models (Salathé *et al.*, 2015).

To go beyond these proof-of-principle experiments, an important goal for the field is to scale to larger number of qubits. The strategies to do so broadly fall into two categories: (i) qubits coupled by oscillator buses, parametric couplers, or the direct linear capacitive or inductive couplers discussed in most of Sec. VII, and (ii) the bosonic approach, where oscillators are coupled and controlled by the qubits specifically discussed in Sec. VII.C. While each has its own set of challenges, some are shared by the two approaches (Blais, Girvin, and Oliver, 2020). One such challenge lies in engineering architectures with high qubit connectivity, which can facilitate the execution of complex quantum algorithms. A price to pay for increased connectivity can, however, be frequency collisions between the qubits, couplers, and readout oscillators, leading to unwanted interactions, a process that is

generally referred to as frequency crowding. Related nuisances are cross talk, where a drive intended for a given qubit or oscillator affects neighboring circuits, and coherent errors, where residual qubit-qubit dispersive interactions lead to the accumulation of unwanted dynamical phases (Krinner *et al.*, 2020). In practice, these considerations limit the number of qubits that can be coupled to the same oscillator mode. One approach to minimize unwanted interactions is to rely on modular architectures where small quantum computers with limited numbers of qubits, the modules, are interconnected by quantum links; see Sec. VIII.D.

Another challenge is that increasing the qubit count also comes with an increase in the number of required control lines. In current architectures, individual input-output lines (IOs) may be associated with every qubit for single-qubit gates, two-qubit gates, and readout. This contrasts with classical computer architectures which, even with billions of transistors, have only of the order of 10^3 IOs (Vandersypen *et al.*, 2017). Frequency multiplexing where a single IO is used to control or read out multiple qubits can be used to reduce the total number of IOs; see Fig. 27, where a common feedline (purple) is used to dispersively measure several qubits. Even with frequency multiplexing, routing control and readout signals to all the qubits and resonators is already challenging in current processors comprising only a few tens of qubits. Three-dimensional integration in which signals are routed using through-silicon vias appears to be a promising path forward for both 2D planar circuits (Rosenberg *et al.*, 2017) and the 3D cavities often associated with the bosonic qubit approach (Brecht *et al.*, 2016, 2017).

Looking ahead, for fault-tolerant quantum computation to become a reality, then in addition to addressing these challenges it remains crucial to continue to improve qubit coherence times as well as gate and readout fidelities. This may require the development of more robust qubits, and of new mechanisms to control and measure these qubits. In short, progress will likely require new ideas beyond those discussed in this review, and this is one of the many reasons why the field of circuit QED will continue to be exciting for years to come.

ACKNOWLEDGMENTS

We thank Alexandre Choquette-Poitevin, Agustin Di Paolo, Christopher Eichler, Jens Koch, Dany Lachance-Quirion, Yasunobu Nakamura, William Oliver, Alexandru Petrescu, Baptiste Royer, Gerd Schön, and Irfan Siddiqi for discussions and comments on the manuscript. This work was undertaken thanks to funding from NSERC, the Canada First Research Excellence Fund, U.S. Army Research Office Grants No. W911NF-18-1-0411 and No. W911NF-18-1-0212, and the Australian Research Council (ARC) via Discovery Early Career Research Award (DECRA) Project No. DE190100380 and Centre of Excellence for Engineered Quantum Systems (EQUS) Project No. CE170100009.

APPENDIX A: HAMILTONIAN OF A VOLTAGE BIASED TRANSMON

An excellent introduction to the quantization of electromagnetic circuits was given by Vool and Devoret (2017).

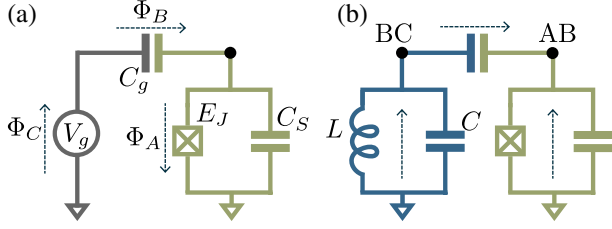


FIG. 34. (a) Voltage-biased transmon qubit with the three relevant flux branches. (b) Replacement of the classical voltage source with an LC oscillator. The dashed arrows indicate the sign convention.

Here we give only an introduction to this topic by means of two examples that are used throughout this review: a transmon qubit biased by an external voltage source and a transmon coupled to an LC oscillator.

1. Classical gate voltage

Consider first the circuit shown in Fig. 34(a), which illustrates a transmon biased by an external voltage V_g . Following [Vool and Devoret \(2017\)](#), we start by associating a branch flux $\Phi_i(t) = \int_{-\infty}^t dt' V_i(t')$ to each branch of the circuit, with V_i the voltage across branch $i = A, B, C$ indicated in Fig. 34(a). Because Kirchoff's laws impose constraints between the branch fluxes, these fluxes are not independent variables and are therefore not independent degrees of freedom of the circuit. Indeed, Kirchoff's voltage law dictates that $V_C + V_B + V_A = V_g + \dot{\Phi}_B + \dot{\Phi}_A = 0$, where we use the sign convention dictated by the arbitrarily chosen orientation of the arrows in Fig. 34(a). This constraint allows us to eliminate Φ_B in favor of Φ_A . Moreover, following Kirchoff's current law, the currents I_A and I_B flowing into and out of the node indicated by the black dot in Fig. 34(a) obey $I_A = I_B$. This constraint can be expressed in terms of the branch fluxes using the constitutive relations for the capacitances C_g and $C_\Sigma = C_S + C_J$:

$$Q_A = C_\Sigma \dot{\Phi}_A, \quad Q_B = C_g \dot{\Phi}_B, \quad (\text{A1})$$

as well as the Josephson current relation

$$I_J = I_c \sin \varphi_A, \quad (\text{A2})$$

where $\varphi_A = (2\pi/\Phi_0)\Phi_A$ and I_c is the critical current. We can thus write $I_A = \dot{Q}_A + I_J = C_\Sigma \ddot{\Phi}_A + I_c \sin \varphi_A$ and $I_B = \dot{Q}_B = C_g \ddot{\Phi}_B$. Combining the previous expressions, we arrive at

$$C_\Sigma \ddot{\Phi}_A + I_c \sin \varphi_A = -C_g (\ddot{\Phi}_A + \ddot{\Phi}_C). \quad (\text{A3})$$

Here $\dot{\Phi}_C = V_g$ is the applied bias voltage and the only dynamical variable in the equation is thus Φ_A . As can be easily verified, this equation of motion for Φ_A can equivalently be derived from the Euler-Lagrange equation for Φ_A with the Lagrangian

$$\mathcal{L}_T = \frac{C_\Sigma}{2} \dot{\Phi}_A^2 + \frac{C_g}{2} (\dot{\Phi}_A + \dot{\Phi}_C)^2 + E_J \cos \varphi_A, \quad (\text{A4})$$

where $E_J = (\Phi_0/2\pi)I_c$.

The corresponding Hamiltonian can be found by first identifying the canonical momentum associated with the coordinate Φ_A , $Q_A = \partial \mathcal{L}_T / \partial \dot{\Phi}_A = (C_\Sigma + C_g) \dot{\Phi}_A + C_g \dot{\Phi}_C$, and performing a Legendre transform to obtain ([Goldstein, Poole, and Safko, 2001](#))

$$H_T = Q_A \dot{\Phi}_A - \mathcal{L}_T = \frac{(Q_A - C_g V_g)^2}{2(C_\Sigma + C_g)} - E_J \cos \varphi_A, \quad (\text{A5})$$

where we make the replacement $\dot{\Phi}_C = V_g$ and drop the term $C_g V_g^2/2$, which leads to an overall shift of the energies. Promoting the conjugate variables to noncommuting operators $[\hat{\Phi}_A, \hat{Q}_A] = i\hbar$, we arrive at Eq. (22), where we assume that $C_g \ll C_\Sigma$ to simplify the notation.

2. Coupling to an LC oscillator

As a model for the simplest realization of circuit QED, we now replace the voltage source with an LC oscillator; see Fig. 34(b). The derivation follows the same steps as before, now with $V_g + \dot{\Phi}_B - \dot{\Phi}_A = 0$ and $I_A + I_B = 0$ because of the different choice of orientation for branch A. Moreover, at the node labeled BC we have $I_B = I_C$. Eliminating Φ_B as before and using the constitutive relations for the capacitance C and inductance L of the LC oscillator to express the current through the oscillator branch as $I_C = C \ddot{\Phi}_C + \Phi_C/L$, we find that

$$C \ddot{\Phi}_C + \frac{\Phi_C}{L} = C_g (\ddot{\Phi}_A - \ddot{\Phi}_C). \quad (\text{A6})$$

In contrast to the previous example, Φ_C is now a dynamical variable in its own right rather than being simply set by a voltage source. Together with Eq. (A3), which still holds, Eq. (A6) can equivalently be derived using the Euler-Lagrange equations with the Lagrangian

$$\mathcal{L} = \mathcal{L}_T + \mathcal{L}_{LC}, \quad (\text{A7})$$

where \mathcal{L}_T is given in Eq. (A4) and $\mathcal{L}_{LC} = (C/2) \dot{\Phi}_C^2 - (1/2L) \Phi_C^2$.

It is convenient to write Eq. (A7) as $\mathcal{L} = T - V$ with $T = (1/2) \dot{\Phi}^T \mathbf{C} \dot{\Phi}$ and $V = \Phi_C/2L - E_J \cos \varphi_A$, where we define the vector $\Phi = (\Phi_A, \Phi_C)^T$ and the capacitance matrix

$$\mathbf{C} = \begin{pmatrix} C_\Sigma + C_g & -C_g \\ -C_g & C + C_g \end{pmatrix}. \quad (\text{A8})$$

Defining the vector of conjugate momenta $\mathbf{Q} = (Q_A, Q_C)^T$, the Hamiltonian is then ([Goldstein, Poole, and Safko, 2001](#))

$$\begin{aligned}
H &= \frac{1}{2}\mathbf{Q}^T\mathbf{C}^{-1}\mathbf{Q} + V \\
&= \frac{C + C_g}{2\bar{C}^2}Q_A^2 + \frac{C_g}{\bar{C}^2}Q_A Q_C - E_J \cos \varphi_A \\
&\quad + \frac{C_\Sigma + C_g}{2\bar{C}^2}Q_C^2 + \frac{\Phi_C}{2L}, \tag{A9}
\end{aligned}$$

where we define $\bar{C}^2 = C_g C_\Sigma + C_g C + C_\Sigma C$. The limit $C_g \ll C_\Sigma, C$ results in the simplified expression

$$H \simeq \frac{[Q_A + (C_g/C)Q_C]^2}{2C_\Sigma} - E_J \cos \varphi_A + H_{LC}, \tag{A10}$$

with $H_{LC} = Q_C^2/2C + \Phi_C/2L$ the Hamiltonian of the LC circuit. By promoting the flux and charge variables to operators and defining $\hat{n} = \hat{Q}_A/2e$, $\hat{n}_r = (C_g/C)\hat{Q}_C/2e$ and diagonalizing \hat{H}_{LC} as in Sec. II.A, we arrive at Eq. (31) for a single mode $m = r$.

Equation (A10) can easily be generalized to capacitive coupling between other types of circuits, such as resonator-resonator, transmon-transmon, and transmon-transmission line coupling, by simply replacing the potential energy terms $-E_J \cos \varphi_A$ and $\Phi_C^2/2L$ to describe the type of circuits in question. This leads to Eq. (135) for two capacitively coupled transmons after introducing ladder operators as in Eqs. (25) and (26).

APPENDIX B: UNITARY TRANSFORMATIONS

We introduce a number of unitary transformations often employed in the field of circuit QED. The starting point is the usual transformation

$$\hat{H}_U = \hat{U}^\dagger \hat{H} \hat{U} - i\hbar \hat{U}^\dagger \dot{\hat{U}} \tag{B1}$$

of a Hamiltonian under a time-dependent unitary \hat{U} with the corresponding transformation for the states $|\psi_U\rangle = \hat{U}^\dagger |\psi\rangle$. Since the unitary can be written as $\hat{U} = \exp(-\hat{S})$, with \hat{S} an anti-Hermitian operator, a useful result in this context is the Baker-Campbell-Hausdorff formula, which holds for any two operators \hat{S} and \hat{H} :

$$\begin{aligned}
e^{\hat{S}} \hat{H} e^{-\hat{S}} &= \hat{H} + [\hat{S}, \hat{H}] + \frac{1}{2!} [\hat{S}, [\hat{S}, \hat{H}]] + \dots \\
&= \sum_{n=0}^{\infty} \frac{1}{n!} C_S^n[\hat{H}], \tag{B2}
\end{aligned}$$

where on the last line we introduce the shorthand notation

$$C_S^n[\hat{H}] = [\hat{S}, [\hat{S}, [\hat{S}, \dots, \hat{H}]]] \tag{B3}$$

and $C_S^0[\hat{H}] = \hat{H}$ (Boissonneault, Gambetta, and Blais, 2009).

1. Schrieffer-Wolff perturbation theory

We often seek unitary transformations that diagonalize the Hamiltonian of an interacting system. Exact diagonalization,

however, can be impractical, and we must resort to finding an effective Hamiltonian that describes the physics at low energies using perturbation theory. A general approach to perturbation theory that we follow here is known as a Schrieffer-Wolff transformation (Schrieffer and Wolff, 1966; Bravyi, DiVincenzo, and Loss, 2011). The starting point is a generic Hamiltonian of the form

$$\hat{H} = \hat{H}_0 + \hat{V}, \tag{B4}$$

with \hat{H}_0 typically a free Hamiltonian and \hat{V} a perturbation. We divide the total Hilbert space of our system into different subspaces such that \hat{H}_0 does not couple states in different subspaces while \hat{V} does. The goal of the Schrieffer-Wolff transformation is to arrive at an effective Hamiltonian for which the different subspaces are completely decoupled.

The different subspaces, which we label with a subscript μ , can conveniently be defined by a set of projection operators (Cohen-Tannoudji, Dupont-Roc, and Grynberg, 1998; Zhu *et al.*, 2013)

$$\hat{P}_\mu = \sum_n |\mu, n\rangle \langle \mu, n|, \tag{B5}$$

where $|\mu, n\rangle, n = 0, 1, \dots$, is an orthonormal basis for the subspace labeled μ . For the Schrieffer-Wolff transformation to be valid, we must assume that \hat{V} is a small perturbation. Formally, the operator norm $\|\hat{V}\| = \max_{|\psi\rangle} \|\hat{V}|\psi\rangle\|$ should be smaller than half the energy gap between the subspaces we intend to decouple; see Bravyi, DiVincenzo, and Loss (2011), Eq. (3.1). While \hat{V} is often formally unbounded in circuit QED applications, the operator is always bounded when restricting the problem to physically relevant states.

The Schrieffer-Wolff transformation is based on finding a unitary transformation $\hat{U} = e^{-\hat{S}}$ that approximately decouples the different subspaces μ by truncating the Baker-Campbell-Hausdorff formula (B2) at a desired order. We first expand both \hat{H} and \hat{S} in formal power series

$$\hat{H} = \hat{H}^{(0)} + \varepsilon \hat{H}^{(1)} + \varepsilon^2 \hat{H}^{(2)} + \dots, \tag{B6a}$$

$$\hat{S} = \varepsilon \hat{S}^{(1)} + \varepsilon^2 \hat{S}^{(2)} + \dots, \tag{B6b}$$

where ε is a fiducial parameter introduced to simplify order counting that we can ultimately set to $\varepsilon \rightarrow 1$. The Schrieffer-Wolff transformation is found by inserting Eq. (B5) back into Eq. (B2) and collecting terms at each order ε^k . We can then iteratively solve for $S^{(k)}$ and $\hat{H}^{(k)}$ by requiring that the resulting Hamiltonian \hat{H}_U is block diagonal (i.e., it does not couple different subspaces μ) at each order, and the additional requirement that \hat{S} is itself block off diagonal (Bravyi, DiVincenzo, and Loss, 2011).

For the generator, the explicit results up to $k = 2$ are (with $\varepsilon = 1$)

$$\langle \mu, n | \hat{S}^{(1)} | \nu, l \rangle = \frac{\langle \mu, n | \hat{V} | \nu, l \rangle}{E_{\mu, n} - E_{\nu, l}}, \tag{B7a}$$

$$\begin{aligned} \langle \mu, n | \hat{S}^{(2)} | \nu, l \rangle &= \sum_k \left(\frac{\langle \mu, n | \hat{V} | \nu, k \rangle \langle \nu, k | \hat{V} | \nu, l \rangle}{E_{\mu,n} - E_{\nu,l}} \frac{\langle \nu, k | \hat{V} | \nu, l \rangle}{E_{\mu,n} - E_{\nu,k}} \right. \\ &\quad \left. - \frac{\langle \mu, n | \hat{V} | \mu, k \rangle \langle \mu, k | \hat{V} | \nu, l \rangle}{E_{\mu,n} - E_{\nu,l}} \frac{\langle \mu, k | \hat{V} | \nu, l \rangle}{E_{\mu,k} - E_{\nu,l}} \right) \end{aligned} \quad (\text{B7b})$$

for $\nu \neq \mu$, while the block-diagonal matrix element vanish for $\mu = \nu$ and

$$\hat{H}^{(0)} = \hat{H}_0, \quad (\text{B8a})$$

$$\hat{H}^{(1)} = \sum_{\mu} \hat{P}_{\mu} \hat{V} \hat{P}_{\mu}, \quad (\text{B8b})$$

$$\begin{aligned} \langle \mu, n | \hat{H}^{(2)} | \mu, m \rangle &= \sum_{\nu \neq \mu, l} \langle \mu, n | \hat{V} | \nu, l \rangle \langle \nu, l | \hat{V} | \mu, m \rangle \\ &\quad \times \frac{1}{2} \left(\frac{1}{E_{\mu,n} - E_{\nu,l}} + \frac{1}{E_{\mu,m} - E_{\nu,l}} \right) \end{aligned} \quad (\text{B8c})$$

for the transformed Hamiltonian (block-off-diagonal matrix elements vanish, i.e., $\langle \mu, n | \hat{H}^{(2)} | \nu, m \rangle = 0$ for $\mu \neq \nu$). In these expressions, $E_{\mu,n}$ refers to the bare energy of $|\mu, n\rangle$ under the unperturbed Hamiltonian \hat{H}_0 . An explicit formula for $\hat{H}^{(k)}$ up to $k = 4$ was given by Winkler (2003).

2. Schrieffer-Wolff transformation for a multilevel system coupled to an oscillator in the dispersive regime

As an application of the general result of Eq. (B6) here we consider a situation that is commonly encountered in circuit QED: an arbitrary artificial atom coupled to a single-mode oscillator in the dispersive regime. Both the transmon artificial atom and the two-level system discussed in Sec. III.C are special cases of this more general example. The artificial atom, taken here to be a generic multilevel system, is described in its eigenbasis with the Hamiltonian $\hat{H}_{\text{atom}} = \sum_j \hbar \omega_j |j\rangle \langle j|$. The full Hamiltonian is therefore given by

$$\hat{H} = \hbar \omega_r \hat{a}^\dagger \hat{a} + \sum_j \hbar \omega_j |j\rangle \langle j| + (\hat{B} \hat{a}^\dagger + \hat{B}^\dagger \hat{a}), \quad (\text{B9})$$

where \hat{B} is an arbitrary operator of the artificial atom that couples to the oscillator. For example, in the case of capacitive coupling, it is proportional to the charge operator with $\hat{B} \sim \hat{n}$; see Eq. (31).

By inserting resolutions of the identity $\hat{I} = \sum_j |j\rangle \langle j|$, the interaction term can be reexpressed in the atomic eigenbasis as (Koch *et al.*, 2007)

$$\begin{aligned} \hat{H} &= \hbar \omega_r \hat{a}^\dagger \hat{a} + \sum_j \hbar \omega_j |j\rangle \langle j| \\ &\quad + \sum_{ij} \hbar (g_{ij} |i\rangle \langle j| \hat{a}^\dagger + g_{ij}^* |j\rangle \langle i| \hat{a}), \end{aligned} \quad (\text{B10})$$

where $\hbar g_{ij} = \langle i | \hat{B} | j \rangle$, with $g_{ij} = g_{ji}$ if $\hat{B} = \hat{B}^\dagger$.

To use Eq. (B6), we identify the first line of Eq. (B10) as \hat{H}_0 and the second line as the perturbation \hat{V} . The subspaces

labeled by μ are in this situation one dimensional ($\hat{P}_{\mu} = |\mu\rangle \langle \mu|$), with $|\mu\rangle = |n, j\rangle = |n\rangle \otimes |j\rangle$, $|n\rangle$ an oscillator number state and $|j\rangle$ an artificial atom eigenstate. A straightforward calculation yields the second-order result (Zhu *et al.*, 2013)

$$\begin{aligned} \hat{H}_{\text{disp}} &= e^{\hat{S}} \hat{H} e^{-\hat{S}} \simeq \hbar \omega_r \hat{a}^\dagger \hat{a} + \sum_j \hbar (\omega_j + \Lambda_j) |j\rangle \langle j| \\ &\quad + \sum_j \hbar \chi_j \hat{a}^\dagger \hat{a} |j\rangle \langle j|, \end{aligned} \quad (\text{B11})$$

where

$$\Lambda_j = \sum_i \chi_{ij}, \quad \chi_j = \sum_i (\chi_{ij} - \chi_{ji}), \quad (\text{B12})$$

with

$$\chi_{ij} = \frac{|g_{ji}|^2}{\omega_j - \omega_i - \omega_r}. \quad (\text{B13})$$

Note that we are following here the convention given by Koch *et al.* (2007) rather than that given by Zhu *et al.* (2013) for the definition of χ_{ij} .

Projecting Eq. (B11) onto the first two-atomic levels $j = 0, 1$ with the convention $\hat{\sigma}_z = |1\rangle \langle 1| - |0\rangle \langle 0|$, we obtain

$$\hat{H}_{\text{disp}} \simeq \hbar \omega'_r \hat{a}^\dagger \hat{a} + \frac{\hbar \omega'_q}{2} \hat{\sigma}_z + \hbar \chi \hat{a}^\dagger \hat{a} \hat{\sigma}_z, \quad (\text{B14})$$

where we have dropped a constant term and define $\omega'_r = \omega_r + (\chi_0 + \chi_1)/2$, $\omega'_q = \omega_1 - \omega_0 + \Lambda_1 - \Lambda_0$, and $\chi = (\chi_1 - \chi_0)/2$.

a. The transmon

The transmon capacitively coupled to an oscillator is one example of the previous result. From Eq. (34), we identify the free Hamiltonian as

$$\hat{H}_0 = \hbar \omega_r \hat{a}^\dagger \hat{a} + \hbar \omega_q \hat{b}^\dagger \hat{b} - \frac{E_C}{2} \hat{b}^\dagger \hat{b}^\dagger \hat{b} \hat{b} \quad (\text{B15})$$

and the perturbation as

$$\hat{V} = \hbar g (\hat{b}^\dagger \hat{a} + \hat{b} \hat{a}^\dagger). \quad (\text{B16})$$

In this nonlinear oscillator approximation for the transmon, the transmon eigenstates are number states $\hat{b}^\dagger \hat{b} |j\rangle = j |j\rangle$, with $j = 0, 1, \dots, \infty$. Moreover, the coupling operator is $\hat{B} = \hbar g \hat{b}$, and thus

$$g_{j,j+1} = g \langle j | \hat{b} | j+1 \rangle = g \sqrt{j+1} = g_{j,j+1}^*, \quad (\text{B17})$$

while all other matrix elements g_{ij} are 0. We consequently find

$$\Lambda_j = \chi_{j-1,j} = \frac{j g^2}{\omega_q - E_C/\hbar(j-1) - \omega_r}, \quad (\text{B18a})$$

$$\begin{aligned}\chi_j &= \chi_{j-1,j} - \chi_{j,j+1} \\ &= g^2 \left(\frac{j}{\omega_j - \omega_{j-1} - \omega_r} - \frac{j+1}{\omega_{j+1} - \omega_j - \omega_r} \right)\end{aligned}\quad (\text{B18b})$$

for $j > 0$, while for $j = 0$ we have $\Lambda_0 = 0$ and $\chi_0 = -\chi_{01} = -g^2/\Delta$, where $\Delta \equiv \omega_q - \omega_r$. In the two-level approximation of Eq. (B14), this becomes (Koch *et al.*, 2007)

$$\omega'_r = \omega_r - \frac{\chi_{12}}{2} = \omega_r - \frac{g^2}{\Delta - E_C/\hbar}, \quad (\text{B19a})$$

$$\omega'_q = \omega_1 - \omega_0 + \chi_{01} = \omega_q + \frac{g^2}{\Delta}, \quad (\text{B19b})$$

$$\chi = \chi_{01} - \frac{\chi_{12}}{2} = -\frac{g^2 E_C/\hbar}{\Delta(\Delta - E_C/\hbar)}, \quad (\text{B19c})$$

which are the results quoted in Eq. (45).

Recall that this Schrieffer-Wolff perturbation theory is valid only if the perturbation \hat{V} is sufficiently small. Following Bravyi, DiVincenzo, and Loss (2011), a more precise statement is that we require $2\|\hat{V}\| < \Delta_{\min}$, where Δ_{\min} is the smallest energy gap between any of the bare energy eigenstates $|n\rangle \otimes |j\rangle$, where $|n\rangle$ is a number state for the oscillator. Here $\hat{V} = g(\hat{b}^\dagger \hat{a} + \hat{b} \hat{a}^\dagger)$ is formally unbounded but physical states have finite excitation numbers. Therefore, replacing the operator norm with $\langle n, j | \hat{V}^\dagger \hat{V} | n, j \rangle^{1/2}$ and using $\Delta_{\min} = |\Delta - jE_C/\hbar|$ corresponding to the minimum energy gap between neighboring states $|n, j\rangle$ and $|n \pm 1, j \mp 1\rangle$, we find that a more precise criterion for the validity of the previously mentioned perturbative results is

$$n \ll n_{\text{crit}} \equiv \frac{1}{2j+1} \left(\frac{|\Delta - jE_C/\hbar|^2}{4g^2} - j \right). \quad (\text{B20})$$

Setting $j = 0$ gives the familiar expression $n_{\text{crit}} = (\Delta/2g)^2$, while setting $j = 1$ gives a more conservative estimate. As quoted in the main text, the appropriate small parameter is therefore \bar{n}/n_{crit} , with \bar{n} the average oscillator photon number. For the second-order effective Hamiltonian \hat{H}_{disp} to be an accurate description of the system requires \bar{n}/n_{crit} to be significantly smaller than unity (it is difficult to make a precise statement, but the criterion $\bar{n}/n_{\text{crit}} \lesssim 0.1$ is often used).

b. The Jaynes-Cummings model

We now contrast the previous result in which the transmon is treated as a multilevel system with the result obtained if the artificial atom is truncated to a two-level system before performing the Schrieffer-Wolff transformation. That is, we start with the Jaynes-Cummings Hamiltonian

$$\hat{H}_{\text{JC}} = \hbar\omega_r \hat{a}^\dagger \hat{a} + \frac{\hbar\omega_q}{2} \hat{\sigma}_z + \hbar g (\hat{a}^\dagger \hat{\sigma}_- + \hat{a} \hat{\sigma}_+). \quad (\text{B21})$$

Identifying the first two terms as the unperturbed Hamiltonian \hat{H}_0 and the last term as the interaction \hat{V} , we can again apply Eq. (7). Alternatively, the result can be found more directly

from Eq. (B14) by taking $g_{01} = g_{01}^* = g$ and all other $g_{ij} = 0$. The result is

$$\omega'_r = \omega_r, \quad \omega'_q = \omega_q + \frac{g^2}{\Delta}, \quad \chi = \frac{g^2}{\Delta}, \quad (\text{B22})$$

with $\Delta = \omega_q - \omega_r$ as before. We see that the results agree with Eq. (B17) only in the limit $E_C/\hbar \gg \Delta, g$. Since E_C is relatively small compared to the detuning Δ in most transmon experiments, the value for χ predicted from the Jaynes-Cummings model is far from the multilevel case. Moreover, following the same argument as before, we find that the Schrieffer-Wolff transformation is valid for photon numbers $\bar{n} < n_{\text{crit}}$, with $n_{\text{crit}} = (\Delta/2g)^2 - j$, where $j = 0, 1$ for the ground and excited qubit states, respectively.

Note that the transformation used here to approximately diagonalize the Jaynes-Cummings Hamiltonian can be obtained by Taylor expanding the generator $\Lambda(\hat{N}_T)$ of the unitary transformation (37), which exactly diagonalizes \hat{H}_{JC} . This exercise also leads to the conclusion that \bar{n}/n_{crit} , with $n_{\text{crit}} = (\Delta/2g)^2$, is the appropriate small parameter. Alternatively, \hat{H}_{disp} can also be obtained simply by Taylor expanding the diagonal form equation (39) of \hat{H}_{JC} (Boissonneault, Gambetta, and Blais, 2010).

3. Bogoliubov approach to the dispersive regime

We derive the results presented in Sec. III.C.2. Our starting point is thus the transmon-resonator Hamiltonian (34), and our final result is the dispersive Hamiltonian in Eq. (52).

It is first useful to express Eq. (34) as a sum of a linear and a nonlinear part $\hat{H} = \hat{H}_{\text{lin}} + \hat{H}_{\text{nl}}$, where

$$\hat{H}_{\text{lin}} = \hbar\omega_r \hat{a}^\dagger \hat{a} + \hbar\omega_q \hat{b}^\dagger \hat{b} + \hbar g (\hat{b}^\dagger \hat{a} + \hat{b} \hat{a}^\dagger), \quad (\text{B23})$$

$$\hat{H}_{\text{nl}} = -\frac{E_C}{2} \hat{b}^\dagger \hat{b}^\dagger \hat{b} \hat{b}. \quad (\text{B24})$$

The linear Hamiltonian \hat{H}_{lin} can be diagonalized exactly with the Bogoliubov transformation

$$\hat{U} = \exp[\Lambda(\hat{a}^\dagger \hat{b} - \hat{a} \hat{b}^\dagger)]. \quad (\text{B25})$$

Under this unitary transformation, the annihilation operators transform as $\hat{U}^\dagger \hat{a} \hat{U} = \cos(\Lambda) \hat{a} + \sin(\Lambda) \hat{b}$, $\hat{U}^\dagger \hat{b} \hat{U} = \cos(\Lambda) \hat{b} - \sin(\Lambda) \hat{a}$, leading to

$$\begin{aligned}\hat{H}'_{\text{lin}} &= \hat{U}^\dagger \hat{H}_{\text{lin}} \hat{U} = \tilde{\omega}_r \hat{a}^\dagger \hat{a} + \tilde{\omega}_q \hat{b}^\dagger \hat{b} \\ &+ \left[g \cos(2\Lambda) - \frac{\Delta}{2} \sin(2\Lambda) \right] (\hat{a}^\dagger \hat{b} + \hat{a} \hat{b}^\dagger),\end{aligned}\quad (\text{B26})$$

where

$$\tilde{\omega}_r = \cos^2(\Lambda) \omega_r + \sin^2(\Lambda) \omega_q - g \sin(2\Lambda), \quad (\text{B27})$$

$$\tilde{\omega}_q = \cos^2(\Lambda) \omega_q + \sin^2(\Lambda) \omega_r + g \sin(2\Lambda). \quad (\text{B28})$$

To cancel the last term of \hat{H}'_{lin} , we take $\Lambda = (1/2) \arctan(2\lambda)$, with $\lambda = g/\Delta$ and $\Delta = \omega_q - \omega_r$, to obtain the diagonal form

$$\hat{H}'_{\text{lin}} = \hbar\tilde{\omega}_r \hat{a}^\dagger \hat{a} + \hbar\tilde{\omega}_q \hat{b}^\dagger \hat{b}, \quad (\text{B29})$$

with the mode frequencies

$$\tilde{\omega}_r = \frac{1}{2}(\omega_r + \omega_q - \sqrt{\Delta^2 + 4g^2}), \quad (\text{B30})$$

$$\tilde{\omega}_q = \frac{1}{2}(\omega_r + \omega_q + \sqrt{\Delta^2 + 4g^2}). \quad (\text{B31})$$

The same transformation on \hat{H}_{nl} gives

$$\begin{aligned} \hat{H}'_{\text{nl}} &= \hat{U}^\dagger \hat{H}_{\text{nl}} \hat{U} \\ &= -\frac{E_C}{2} \cos^4(\Lambda) (\hat{b}^\dagger)^2 \hat{b}^2 - \frac{E_C}{2} \sin^4(\Lambda) (\hat{a}^\dagger)^2 \hat{a}^2 \\ &\quad - 2E_C \cos^2(\Lambda) \sin^2(\Lambda) \hat{a}^\dagger \hat{a} \hat{b}^\dagger \hat{b} \\ &\quad + E_C \cos^3(\Lambda) \sin(\Lambda) (\hat{b}^\dagger \hat{b} \hat{a}^\dagger \hat{a} + \text{H.c.}) \\ &\quad + E_C \cos(\Lambda) \sin^3(\Lambda) (\hat{a}^\dagger \hat{a} \hat{b}^\dagger \hat{b} + \text{H.c.}) \\ &\quad - \frac{E_C}{2} \cos(\Lambda)^2 \sin(\Lambda)^2 [(\hat{a}^\dagger)^2 \hat{b}^2 + \text{H.c.}]. \end{aligned} \quad (\text{B32})$$

Note that at this stage the transformation is exact. In the dispersive regime, we expand the mode frequencies and \hat{H}'_{nl} in powers of λ . For the nonlinear part of the Hamiltonian, this yields

$$\begin{aligned} \hat{H}'_{\text{nl}} &= -\frac{E_C}{2} (\hat{b}^\dagger)^2 \hat{b}^2 - \lambda^4 \frac{E_C}{2} (\hat{a}^\dagger)^2 \hat{a}^2 \\ &\quad - 2\lambda^2 E_C \hat{a}^\dagger \hat{a} \hat{b}^\dagger \hat{b} \\ &\quad + \lambda E_C (\hat{b}^\dagger \hat{b} \hat{a}^\dagger \hat{a} + \text{H.c.}) \\ &\quad + \lambda^3 E_C (\hat{a}^\dagger \hat{a} \hat{b}^\dagger \hat{b} + \text{H.c.}) \\ &\quad - \lambda^2 \frac{E_C}{2} [(\hat{a}^\dagger)^2 \hat{b}^2 + \text{H.c.}] + \mathcal{O}(\lambda^5). \end{aligned} \quad (\text{B33})$$

The magnitude $\lambda^2 E_C$ of the cross-Kerr term $\hat{a}^\dagger \hat{a} \hat{b}^\dagger \hat{b}$ in Eq. (B33) does not coincide with Eq. (3.12) given by Koch *et al.* (2007). To correct this situation, we apply an additional transformation to eliminate the third line of Eq. (B33). This term is important because it approximately corresponds to an exchange interaction $\hat{a}^\dagger \hat{b} + \hat{b}^\dagger \hat{a}$ with an additional number operator $\hat{b}^\dagger \hat{b}$ that distinguishes the different transmon levels. To eliminate this term, we apply a Schrieffer-Wolff transformation to second order with the generator $S = \lambda' (\hat{b}^\dagger \hat{b} \hat{a}^\dagger \hat{a} - \text{H.c.})$, where $\lambda' = \lambda E_C / [\Delta + E_C(1 - 2\lambda^2)]$. Neglecting the last two lines of Eq. (B33) and omitting a correction of order λ^2 , we arrive at Eq. (52), which agrees with Koch *et al.* (2007).

4. Off-resonantly driven transmon

We derive Eq. (134), which describes the ac-Stark shift resulting from an off-resonant drive on a transmon qubit. Our starting point is Eq. (131), which takes the form

$$\hat{H}(t) = \hbar\omega_q \hat{b}^\dagger \hat{b} - \frac{E_C}{2} (\hat{b}^\dagger)^2 \hat{b}^2 + \hbar\epsilon(t) \hat{b}^\dagger + \hbar\epsilon^*(t) \hat{b}, \quad (\text{B34})$$

where we define $\epsilon(t) = \epsilon(t) e^{-i\omega_d t - i\phi_d}$. To account for a possible time dependence of the drive envelope $\epsilon(t)$, it is useful to apply the time-dependent displacement transformation

$$\hat{U}(t) = e^{\alpha^*(t) \hat{b} - \alpha(t) \hat{b}^\dagger}. \quad (\text{B35})$$

Under $\hat{U}(t)$, \hat{b} transforms to $\hat{U}^\dagger \hat{b} \hat{U} = \hat{b} - \alpha(t)$, while

$$\hat{U}^\dagger \dot{\hat{U}} = \dot{\alpha}^* \hat{b} - \dot{\alpha} \hat{b}^\dagger + \frac{1}{2}(\dot{\alpha} \alpha^* - \dot{\alpha}^* \alpha). \quad (\text{B36})$$

Using these expressions, the transformed Hamiltonian becomes

$$\begin{aligned} \hat{H}' &= \hat{U}^\dagger \hat{H} \hat{U} - i \hat{U}^\dagger \dot{\hat{U}} \\ &\simeq \hbar\omega_q (\hat{b}^\dagger \hat{b} - \alpha^* \hat{b} - \alpha \hat{b}^\dagger) \\ &\quad - \frac{E_C}{2} [(\hat{b}^\dagger)^2 \hat{b}^2 + 4|\alpha|^2 \hat{b}^\dagger \hat{b}] \\ &\quad + \hbar\epsilon \hat{b}^\dagger + \hbar\epsilon^* \hat{b} - i\hbar(\dot{\alpha}^* \hat{b} - \dot{\alpha} \hat{b}^\dagger), \end{aligned} \quad (\text{B37})$$

where we have dropped fast-rotating terms and a scalar. The choice

$$\dot{\alpha}(t) = -i\omega_q \alpha(t) + i\epsilon(t) \quad (\text{B38})$$

cancels the linear drive term leaving

$$\hat{H}'(t) \simeq [\hbar\omega_q - 2E_C |\alpha(t)|^2] \hat{b}^\dagger \hat{b} - \frac{E_C}{2} (\hat{b}^\dagger)^2 \hat{b}^2. \quad (\text{B39})$$

Taking a constant envelope $\epsilon(t) = \epsilon$ for simplicity such that $|\alpha(t)|^2 = (\epsilon/\delta_q)^2$, Eq. (B39) takes the compact form

$$\hat{H}''(t) \simeq \frac{1}{2} \left(\hbar\omega_q - E_C \frac{\Omega_R^2}{2\delta_q^2} \right) \hat{\sigma}_z \quad (\text{B40})$$

in the two-level approximation, which is Eq. (134) of the main text.

It is instructive to obtain the same result now using the Schrieffer-Wolff approach. Assuming a constant envelope $\epsilon(t) = \epsilon$ and with $\phi_d = 0$ for simplicity, our starting point is

$$\hat{H} = \hbar\delta_q \hat{b}^\dagger \hat{b} - \frac{E_C}{2} (\hat{b}^\dagger)^2 \hat{b}^2 + \hbar\epsilon(\hat{b}^\dagger + \hat{b}) \quad (\text{B41})$$

in a frame rotating at ω_d and where $\delta_q = \omega_q - \omega_d$. We treat the drive as a perturbation and apply the second-order formula (B6) to obtain

$$\begin{aligned} \hat{H}_U &\simeq \hbar\delta_q \hat{b}^\dagger \hat{b} - \frac{E_C}{2} (\hat{b}^\dagger)^2 \hat{b}^2 \\ &+ |\varepsilon|^2 \sum_j \left(\frac{j}{\delta_q - [E_C(j-1)/\hbar]} - \frac{j+1}{\delta_q - (E_C j/\hbar)} \right) |j\rangle \langle j| \\ &\simeq \hbar\delta_q \hat{b}^\dagger \hat{b} - \frac{E_C}{2} (\hat{b}^\dagger)^2 \hat{b}^2 - 2E_C \frac{|\varepsilon|^2}{\delta_q^2} \hat{b}^\dagger \hat{b} - \frac{|\varepsilon|^2}{\delta_q}, \end{aligned} \quad (\text{B42})$$

where $|j\rangle$ is used to label transmon states as before. In the last approximation we kept only terms to $\mathcal{O}(jE_C/\delta_q)$. This agrees with Eq. (B39) for $|\alpha|^2 = |\varepsilon/\delta_q|^2$. More accurate expressions can be obtained by going to higher order in perturbation theory (Schneider *et al.*, 2018).

APPENDIX C: INPUT-OUTPUT THEORY

Closely following Yurke and Denker (1984) and Yurke (2004), we derive the input-output equations of Sec. IV.B. As illustrated in Fig. 11, we consider an LC oscillator located at $x = 0$ that is capacitively coupled to a semi-infinite transmission line extending from $x = 0$ to ∞ . In analogy with Eq. (7), the Hamiltonian for the transmission line is

$$\hat{H}_{\text{tml}} = \int_{-\infty}^{\infty} dx \theta(x) \left\{ \frac{\hat{Q}_{\text{tml}}(x)^2}{2c} + \frac{[\partial_x \hat{\Phi}_{\text{tml}}(x)]^2}{2l} \right\}, \quad (\text{C1})$$

where c and l are, respectively, the capacitance and inductance per unit length, and $\theta(x)$ is the Heaviside step function. The flux and charge operators satisfy the canonical commutation relation $[\hat{\Phi}_{\text{tml}}(x), \hat{Q}_{\text{tml}}(x')] = i\hbar\delta(x-x')$.

On the other hand, the Hamiltonian of the LC oscillator of frequency $\omega_r = 1/\sqrt{L_r C_r}$ is $\hat{H}_s = \hat{Q}_r^2/(2C_r) + \hat{\Phi}_r^2/(2L_r)$ and the interaction Hamiltonian takes the form

$$\hat{H}_{\text{int}} = \int_{-\infty}^{\infty} dx \delta(x) \frac{C_\kappa}{cC_r} \hat{Q}_r \hat{Q}_{\text{tml}}(x), \quad (\text{C2})$$

where C_κ is the coupling capacitance between the oscillator and the line. In deriving Eq. (C2), we neglect renormalizations of c and C_r due to C_κ ; cf. Appendix A. The total Hamiltonian is thus $\hat{H} = \hat{H}_s + \hat{H}_{\text{tml}} + \hat{H}_{\text{int}} = \int_{-\infty}^{\infty} dx \mathcal{H}$, where we introduce the Hamiltonian density \mathcal{H} in the obvious way.

Using these results, Hamilton's equations for the field in the transmission line take the form

$$\dot{\hat{\Phi}}_{\text{tml}}(x) = \theta(x) \frac{\hat{Q}_{\text{tml}}(x)}{c} + \delta(x) \frac{C_\kappa}{C_r c} \hat{Q}_r, \quad (\text{C3})$$

$$\dot{\hat{Q}}_{\text{tml}}(x) = \partial_x \left[\theta(x) \frac{\partial_x \hat{\Phi}_{\text{tml}}(x)}{l} \right]. \quad (\text{C4})$$

Equations (C3) and (C4) can be combined into a wave equation for $\hat{\Phi}_{\text{tml}}$, which for $x > 0$ reads

$$\ddot{\hat{\Phi}}_{\text{tml}}(x) = v^2 \partial_x^2 \hat{\Phi}_{\text{tml}}(x) \quad (\text{C5})$$

and where $v = 1/\sqrt{lc}$ is the speed of light in the line. At the location $x = 0$ of the oscillator, we instead find

$$\begin{aligned} \ddot{\hat{\Phi}}_{\text{tml}}(x) &= \theta(x) v^2 [\delta(x) \partial_x \hat{\Phi}_{\text{tml}}(x) + \partial_x^2 \hat{\Phi}_{\text{tml}}(x)] \\ &+ \delta(x) \frac{C_\kappa}{C_r c} \dot{\hat{Q}}_r, \end{aligned} \quad (\text{C6})$$

where we use $\partial_x \theta(x) = \delta(x)$. We integrate the last equation over $-\varepsilon < x < \varepsilon$ and subsequently take $\varepsilon \rightarrow 0$ to find the boundary condition

$$v^2 \partial_x \hat{\Phi}_{\text{tml}}(x=0) = -\frac{C_\kappa}{C_r c} \dot{\hat{Q}}_r. \quad (\text{C7})$$

From Eq. (C5), we find that the general solution for the flux and charge fields, defined as $\hat{Q}_{\text{tml}}(x, t) = c \partial_t \hat{\Phi}_{\text{tml}}(x, t)$, can be written for $x > 0$ as $\hat{\Phi}_{\text{tml}}(x, t) = \hat{\Phi}_L(x, t) + \hat{\Phi}_R(x, t)$ and $\hat{Q}_{\text{tml}}(x, t) = \hat{Q}_L(x, t) + \hat{Q}_R(x, t)$, with the subscripts L and R denoting left- and right-moving fields

$$\hat{\Phi}_{L/R}(x, t) = \int_0^\infty d\omega \sqrt{\frac{\hbar}{4\pi\omega c v}} e^{\pm i\omega x/v + i\omega t} \hat{b}_{L/R\omega}^\dagger + \text{H.c.}, \quad (\text{C8a})$$

$$\hat{Q}_{L/R}(x, t) = i \int_0^\infty d\omega \sqrt{\frac{\hbar\omega c}{4\pi v}} e^{\pm i\omega x/v + i\omega t} \hat{b}_{L/R\omega}^\dagger - \text{H.c.} \quad (\text{C8b})$$

In Eq. (C8), we introduce the operators $\hat{b}_{\nu\omega}$ satisfying $[\hat{b}_{\nu\omega}, \hat{b}_{\mu\omega'}] = \delta_{\nu\mu} \delta(\omega - \omega')$ for $\nu = L, R$.

Because of the boundary condition at $x = 0$, the left- and right-moving fields are not independent. To see this, we first note that, following from the form of $\hat{\Phi}_{\text{tml}}(x, t)$,

$$Z_{\text{tml}} \frac{\partial_x \hat{\Phi}_{\text{tml}}(x, t)}{l} = \dot{\hat{\Phi}}_L(x, t) - \dot{\hat{\Phi}}_R(x, t), \quad (\text{C9})$$

with $Z_{\text{tml}} = \sqrt{l/c}$ the characteristic impedance of the transmission line. Noting that $\hat{I}(x) = \partial_x \hat{\Phi}_{\text{tml}}(x)$ is the current and defining voltages $\hat{V}_{L/R}(x) = \hat{\Phi}_{L/R}(x)$, we can recognize Eq. (C9) as Ohm's law. Using Eq. (C7), we finally arrive at the boundary condition of Eq. (73) at $x = 0$:

$$\hat{V}_{\text{out}}(t) - \hat{V}_{\text{in}}(t) = Z_{\text{tml}} \frac{C_\kappa}{C_r} \dot{\hat{Q}}_r, \quad (\text{C10})$$

where we introduce the standard notation $\hat{V}_{\text{in/out}}(t) = \hat{V}_{L/R}(x=0, t)$.

Using the mode expansion of the fields in Eq. (C8) together with Eq. (4) for the LC oscillator charge operator in terms of the ladder operator \hat{a} , Eq. (C10) can be expressed as

$$\begin{aligned} &-i \int_0^\infty d\omega \sqrt{\frac{\omega}{4\pi c v}} e^{-i(\omega-\omega_r)t} (\hat{b}_{R\omega} - \hat{b}_{L\omega}) \\ &= -\omega_r Z_{\text{tml}} \frac{C_\kappa}{C_r} \sqrt{\frac{\omega_r C_r}{2}} \hat{a}, \end{aligned} \quad (\text{C11})$$

where we neglect terms rotating at $\omega + \omega_r$. After some rearrangement, this can be written in the form of the standard

input-output boundary condition (Collett and Gardiner, 1984; Gardiner and Collett, 1985)

$$\hat{b}_{\text{out}}(t) - \hat{b}_{\text{in}}(t) = \sqrt{\kappa} \hat{a}(t), \quad (\text{C12})$$

with input and output fields defined as

$$\hat{b}_{\text{in}}(t) = \frac{i}{\sqrt{2\pi}} \int_{-\infty}^{\infty} d\omega \hat{b}_{L\omega} e^{-i(\omega-\omega_r)t}, \quad (\text{C13a})$$

$$\hat{b}_{\text{out}}(t) = \frac{i}{\sqrt{2\pi}} \int_{-\infty}^{\infty} d\omega \hat{b}_{R\omega} e^{-i(\omega-\omega_r)t}. \quad (\text{C13b})$$

The photon-loss rate κ is given by

$$\kappa = \frac{Z_{\text{tml}} C_{\kappa}^2 \omega_r^2}{C_r}. \quad (\text{C14})$$

There are two further approximations that are made when we go from Eq. (C11) to Eq. (C12): We extend the range of integration over frequency from $[0, \infty)$ to $(-\infty, \infty)$ and replace the factor $\sqrt{\omega}$ with $\sqrt{\omega_r}$ inside the integrand. Both approximations are made based on the assumptions that only terms with $\omega \simeq \omega_r$ contribute significantly to the integral in Eq. (C11).

Moreover, we rewrite Eq. (C9) as

$$\begin{aligned} \partial_x \hat{\Phi}_{\text{tml}}(x, t) &= Z_{\text{tml}} [\hat{Q}_L(x, t) - \hat{Q}_R(x, t)] \\ &= Z_{\text{tml}} [2\hat{Q}_L(x, t) - \hat{Q}_{\text{tml}}(x, t)], \end{aligned} \quad (\text{C15})$$

where in the last equality we use $\hat{Q}_{\text{tml}}(x, t) = \hat{Q}_L(x, t) + \hat{Q}_R(x, t)$. At $x = 0$, this gives

$$\hat{Q}_{\text{tml}}(x = 0, t) = 2\hat{Q}_L(x = 0, t) + \frac{1}{v} \frac{C_{\kappa}}{C_r} \hat{Q}_r(t). \quad (\text{C16})$$

Using this result in the Heisenberg representation equations of motion for the LC oscillator

$$\dot{\hat{\Phi}}_r = \frac{i}{\hbar} [\hat{H}, \hat{\Phi}_r] = \frac{\hat{Q}_r}{C_r} + \frac{C_{\kappa}}{C_r c} \hat{Q}_{\text{tml}}(x = 0), \quad (\text{C17})$$

$$\dot{\hat{Q}}_r = \frac{i}{\hbar} [\hat{H}, \hat{Q}_r] = -\frac{\hat{\Phi}}{L_r}, \quad (\text{C18})$$

we arrive at a single equation of motion for the oscillator charge

$$\ddot{\hat{Q}}_r = -\omega_r^2 \left[\hat{Q}_r + \frac{C_{\kappa}}{c} \left(\frac{1}{v} \frac{C_{\kappa}}{C_r} \hat{Q}_r + 2\hat{Q}_{\text{in}} \right) \right]. \quad (\text{C19})$$

Again writing \hat{Q}_r in terms of bosonic creation and annihilation operators, it is possible to express Eq. (C19) in the form of the familiar Langevin equation (77) for the mode operator $\hat{a}(t)$. This standard expression is obtained after neglecting fast-rotating terms and making the following ‘‘slowly varying envelope’’ approximations (Yurke, 2004)

$$\frac{d^2}{dt^2} \hat{a} e^{-i\omega_r t} \simeq -\omega_r^2 \hat{a} e^{-i\omega_r t} - 2i\omega_r \dot{\hat{a}} e^{-i\omega_r t}, \quad (\text{C20a})$$

$$\frac{d}{dt} \hat{a} e^{-i\omega_r t} \simeq -i\omega_r \hat{a} e^{-i\omega_r t}, \quad (\text{C20b})$$

$$\frac{d}{dt} \hat{b}_{-\omega} e^{-i\omega t} \simeq -i\omega_r \hat{b}_{-\omega} e^{-i\omega t}. \quad (\text{C20c})$$

Equation (77) can be viewed as a Heisenberg picture analog to the Markovian master equation (70).

REFERENCES

- Abdo, B., A. Kamal, and M. Devoret, 2013, *Phys. Rev. B* **87**, 014508.
- Abdo, B., *et al.*, 2019, *Nat. Commun.* **10**, 3154.
- Abdumalikov, A. A., O. Astafiev, A. M. Zagoskin, Y. A. Pashkin, Y. Nakamura, and J. S. Tsai, 2010, *Phys. Rev. Lett.* **104**, 193601.
- Abragam, A., 1961, *Principles of Nuclear Magnetism* (Oxford University Press, New York).
- Al-Saidi, W. A., and D. Stroud, 2001, *Phys. Rev. B* **65**, 014512.
- Andersen, C. K., and A. Blais, 2017, *New J. Phys.* **19**, 023022.
- Andersen, C. K., A. Remm, S. Lazar, S. Krinner, J. Heinsoo, J.-C. Besse, M. Gabureac, A. Wallraff, and C. Eichler, 2019, *npj Quantum Inf.* **5**, 69.
- Arrangoiz-Arriola, P., E. A. Wollack, Z. Wang, M. Pechal, W. Jiang, T. P. McKenna, J. D. Witmer, R. Van Laer, and A. H. Safavi-Naeini, 2019, *Nature (London)* **571**7766, 537.
- Arute, F., *et al.*, 2019, *Nature (London)* **574**7779, 505.
- Arute, F., *et al.*, 2020a, arXiv:2010.07965.
- Arute, F., *et al.*, 2020b, *Science* **369**6507, 1084.
- Aspelmeyer, M., T. J. Kippenberg, and F. Marquardt, 2014, *Rev. Mod. Phys.* **86**, 1391.
- Astafiev, O., A. M. Zagoskin, A. A. Abdumalikov Jr., Y. A. Pashkin, T. Yamamoto, K. Inomata, Y. Nakamura, and J. S. Tsai, 2010, *Science* **327**, 840.
- Axline, C. J., *et al.*, 2018, *Nat. Phys.* **14**, 705.
- Backes, K. M., *et al.*, 2021, *Nature (London)* **590**, 238.
- Bardeen, J., 1962, *Phys. Rev. Lett.* **9**, 147.
- Barends, R., *et al.*, 2011, *Appl. Phys. Lett.* **99**, 113507.
- Barends, R., *et al.*, 2014, *Nature (London)* **508**, 500.
- Barends, R., *et al.*, 2015, *Nat. Commun.* **6**, 7654.
- Barnett, S., and P. Radmore, 2002, *Methods in Theoretical Quantum Optics*, 2nd ed. (Oxford University Press, New York).
- Barzanjeh, S., D. P. DiVincenzo, and B. M. Terhal, 2014, *Phys. Rev. B* **90**, 134515.
- Barzanjeh, S., S. Guha, C. Weedbrook, D. Vitali, J. H. Shapiro, and S. Pirandola, 2015, *Phys. Rev. Lett.* **114**, 080503.
- Barzanjeh, S., S. Pirandola, D. Vitali, and J. M. Fink, 2020, *Sci. Adv.* **6**, eabb0451.
- Beaudoin, F., M. P. da Silva, Z. Dutton, and A. Blais, 2012, *Phys. Rev. A* **86**, 022305.
- Beaudoin, F., J. M. Gambetta, and A. Blais, 2011, *Phys. Rev. A* **84**, 043832.
- Beaudoin, F., D. Lachance-Quirion, W. A. Coish, and M. Pioro-Ladrière, 2016, *Nanotechnology* **27**, 464003.
- Bennett, C. H., D. P. DiVincenzo, J. A. Smolin, and W. K. Wootters, 1996, *Phys. Rev. A* **54**, 3824.
- Bergeal, N., F. Schackert, L. Frunzio, and M. H. Devoret, 2012, *Phys. Rev. Lett.* **108**, 123902.

- Bertet, P., I. Chiorescu, G. Burkard, K. Semba, C. J. P. M. Harmans, D. P. DiVincenzo, and J. E. Mooij, 2005, *Phys. Rev. Lett.* **95**, 257002.
- Bertet, P., C. Harmans, and J. Mooij, 2006, *Phys. Rev. B* **73**, 064512.
- Besse, J.-C., S. Gasparinetti, M. C. Collodo, T. Walter, P. Kurpiers, M. Pechal, C. Eichler, and A. Wallraff, 2018, *Phys. Rev. X* **8**, 021003.
- Bethe, H. A., 1947, *Phys. Rev.* **72**, 339.
- Bhat, N. A. R., and J. E. Sipe, 2006, *Phys. Rev. A* **73**, 063808.
- Bialczak, R. C., *et al.*, 2010, *Nat. Phys.* **6**, 409.
- Bienfait, A., *et al.*, 2016, *Nature (London)* **531**7592, 74.
- Billangeon, P.-M., J. S. Tsai, and Y. Nakamura, 2015a, *Phys. Rev. B* **91**, 094517.
- Billangeon, P.-M., J. S. Tsai, and Y. Nakamura, 2015b, *Phys. Rev. B* **92**, 020509.
- Bishop, L. S., J. M. Chow, J. Koch, A. A. Houck, M. H. Devoret, E. Thuneberg, S. M. Girvin, and R. J. Schoelkopf, 2009, *Nat. Phys.* **5**, 105.
- Bishop, L. S., E. Ginossar, and S. M. Girvin, 2010, *Phys. Rev. Lett.* **105**, 100505.
- Blais, A., J. Gambetta, A. Wallraff, D. I. Schuster, S. M. Girvin, M. H. Devoret, and R. J. Schoelkopf, 2007, *Phys. Rev. A* **75**, 032329.
- Blais, A., S. M. Girvin, and W. D. Oliver, 2020, *Nat. Phys.* **16**, 247.
- Blais, A., R.-S. Huang, A. Wallraff, S. M. Girvin, and R. J. Schoelkopf, 2004, *Phys. Rev. A* **69**, 062320.
- Blais, A., A. M. van den Brink, and A. M. Zagoskin, 2003, *Phys. Rev. Lett.* **90**, 127901.
- Bloch, F., and A. Siegert, 1940, *Phys. Rev.* **57**, 522.
- Boaknin, E., V. E. Manucharyan, S. Fissette, M. Metcalfe, L. Frunzio, R. Vijay, I. Siddiqi, A. Wallraff, R. J. Schoelkopf, and M. Devoret, 2007, [arXiv:cond-mat/0702445](https://arxiv.org/abs/cond-mat/0702445).
- Bocko, M., A. Herr, and M. Feldman, 1997, *IEEE Trans. Appl. Supercond.* **7**, 3638.
- Boissonneault, M., J. M. Gambetta, and A. Blais, 2008, *Phys. Rev. A* **77**, 060305.
- Boissonneault, M., J. M. Gambetta, and A. Blais, 2009, *Phys. Rev. A* **79**, 013819.
- Boissonneault, M., J. M. Gambetta, and A. Blais, 2010, *Phys. Rev. Lett.* **105**, 100504.
- Bouchiat, V., D. Vion, P. Joyez, D. Esteve, and M. H. Devoret, 1998, *Phys. Scr.* **T76**, 165.
- Bourassa, J., 2012, Ph.D. thesis (Université de Sherbrooke).
- Bourassa, J., F. Beaudoin, J. M. Gambetta, and A. Blais, 2012, *Phys. Rev. A* **86**, 013814.
- Bourassa, J., J. M. Gambetta, J. A. A. Abdumalikov, O. Astafiev, Y. Nakamura, and A. Blais, 2009, *Phys. Rev. A* **80**, 032109.
- Boutin, S., D. M. Toyli, A. V. Venkatramani, A. W. Eddins, I. Siddiqi, and A. Blais, 2017, *Phys. Rev. Applied* **8**, 054030.
- Bozyigit, D., *et al.*, 2011, *Nat. Phys.* **7**, 154.
- Braginsky, V. B., Y. I. Vorontsov, and K. S. Thorne, 1980, *Science* **209**4456, 547.
- Bravyi, S., D. P. DiVincenzo, and D. Loss, 2011, *Ann. Phys. (Amsterdam)* **326**, 2793.
- Brecht, T., Y. Chu, C. Axline, W. Pfaff, J. Z. Blumoff, K. Chou, L. Krayzman, L. Frunzio, and R. J. Schoelkopf, 2017, *Phys. Rev. Applied* **7**, 044018.
- Brecht, T., W. Pfaff, C. Wang, Y. Chu, L. Frunzio, M. H. Devoret, and R. J. Schoelkopf, 2016, *npj Quantum Inf.* **2**, 16002.
- Brecht, T., M. Reagor, Y. Chu, W. Pfaff, C. Wang, L. Frunzio, M. H. Devoret, and R. J. Schoelkopf, 2015, *Appl. Phys. Lett.* **107**, 192603.
- Breuer, H. P., and F. Petruccione, 2002, *The Theory of Open Quantum Systems* (Oxford University Press, New York).
- Bronn, N. T., Y. Liu, J. B. Hertzberg, A. D. Córcoles, A. A. Houck, J. M. Gambetta, and J. M. Chow, 2015, *Appl. Phys. Lett.* **107**, 172601.
- Brooks, P., A. Kitaev, and J. Preskill, 2013, *Phys. Rev. A* **87**, 052306.
- Bruhata, L. E., T. Cubaynes, J. J. Viennot, M. C. Dartailh, M. M. Desjardins, A. Cottet, and T. Kontos, 2018, *Phys. Rev. B* **98**, 155313.
- Brune, M., F. Schmidt-Kaler, A. Maali, J. Dreyer, E. Hagley, J. M. Raimond, and S. Haroche, 1996, *Phys. Rev. Lett.* **76**, 1800.
- Bruno, A., G. de Lange, S. Asaad, K. L. van der Enden, N. K. Langford, and L. DiCarlo, 2015, *Appl. Phys. Lett.* **106**, 182601.
- Buisson, O., and F. Hekking, 2001, in *Macroscopic Quantum Coherence and Quantum Computing*, edited by D. V. Averin, B. Ruggiero, and P. Silvestrini (Kluwer, New York).
- Bultink, C. C., B. Tarasinski, N. Haandbæk, S. Poletto, N. Haider, D. J. Michalak, A. Bruno, and L. DiCarlo, 2018, *Appl. Phys. Lett.* **112**, 092601.
- Burkard, G., M. J. Gullans, X. Mi, and J. R. Petta, 2020, *Nat. Rev. Phys.* **2**, 129.
- Burkard, G., D. Loss, D. P. DiVincenzo, and J. A. Smolin, 1999, *Phys. Rev. B* **60**, 11404.
- Bylander, J., S. Gustavsson, F. Yan, F. Yoshihara, K. Harrabi, G. Fitch, D. G. Cory, Y. Nakamura, J.-S. Tsai, and W. D. Oliver, 2011, *Nat. Phys.* **7**, 565.
- Caldeira, A. O., and A. J. Leggett, 1981, *Phys. Rev. Lett.* **46**, 211.
- Caldwell, S. A., *et al.*, 2018, *Phys. Rev. Applied* **10**, 034050.
- Calusine, G., *et al.*, 2018, *Appl. Phys. Lett.* **112**, 062601.
- Campagne-Ibarcq, P., *et al.*, 2018, *Phys. Rev. Lett.* **120**, 200501.
- Campagne-Ibarcq, P., *et al.*, 2020, *Nature (London)* **584**7821, 368.
- Carbonaro, P., G. Compagno, and F. Persico, 1979, *Phys. Lett.* **73A**, 97.
- Carmichael, H. J., 2002, *Statistical Methods in Quantum Optics I: Master Equations and Fokker-Planck Equations*, 2nd ed. (Springer, Berlin).
- Carmichael, H. J., 2016, *Physics* **9**, 77.
- Carmichael, H. J., P. Kochan, and B. C. Sanders, 1996, *Phys. Rev. Lett.* **77**, 631.
- Carmichael, H. J., A. S. Lane, and D. F. Walls, 1987, *Phys. Rev. Lett.* **58**, 2539.
- Carusotto, I., A. A. Houck, A. J. Kollár, P. Roushan, D. I. Schuster, and J. Simon, 2020, *Nat. Phys.* **16**, 268.
- Casparis, L., *et al.*, 2018, *Nat. Nanotechnol.* **13**, 915.
- Castellanos-Beltran, M. A., K. D. Irwin, G. C. Hilton, L. R. Vale, and K. W. Lehnert, 2008, *Nat. Phys.* **4**, 929.
- Castellanos-Beltran, M. A., and K. W. Lehnert, 2007, *Appl. Phys. Lett.* **91**, 083509.
- Caves, C. M., 1982, *Phys. Rev. D* **26**, 1817.
- Caves, C. M., J. Combes, Z. Jiang, and S. Pandey, 2012, *Phys. Rev. A* **86**, 063802.
- Chang, C. W. S., A. M. Vadiraj, J. Bourassa, B. Balaji, and C. M. Wilson, 2019, *Appl. Phys. Lett.* **114**, 112601.
- Chang, D. E., L. Jiang, A. V. Gorshkov, and H. J. Kimble, 2012, *New J. Phys.* **14**, 063003.
- Chapman, B. J., E. I. Rosenthal, J. Kerckhoff, B. A. Moores, L. R. Vale, J. A. B. Mates, G. C. Hilton, K. Lalumière, A. Blais, and K. W. Lehnert, 2017, *Phys. Rev. X* **7**, 041043.
- Chen, Y., *et al.*, 2014, *Phys. Rev. Lett.* **113**, 220502.
- Chen, Y.-F., D. Hover, S. Sendelbach, L. Maurer, S. T. Merkel, E. J. Pritchett, F. K. Wilhelm, and R. McDermott, 2011, *Phys. Rev. Lett.* **107**, 217401.
- Chen, Z., *et al.*, 2016, *Phys. Rev. Lett.* **116**, 020501.
- Chiorescu, I., P. Bertet, K. Semba, Y. Nakamura, C. J. P. M. Harmans, and J. E. Mooij, 2004, *Nature (London)* **431**7005, 159.

- Chou, K. S., J. Z. Blumoff, C. S. Wang, P. C. Reinhold, C. J. Axline, Y. Y. Gao, L. Frunzio, M. H. Devoret, L. Jiang, and R. J. Schoelkopf, 2018, *Nature (London)* **561**7723, 368.
- Chow, J. M., L. DiCarlo, J. M. Gambetta, F. Motzoi, L. Frunzio, S. M. Girvin, and R. J. Schoelkopf, 2010, *Phys. Rev. A* **82**, 040305.
- Chow, J. M., J. M. Gambetta, A. W. Cross, S. T. Merkel, C. Rigetti, and M. Steffen, 2013, *New J. Phys.* **15**, 115012.
- Chow, J. M., S. J. Srinivasan, E. Magesan, A. D. Córcoles, D. W. Abraham, J. M. Gambetta, and M. Steffen, 2015, *Proc. SPIE Int. Soc. Opt. Eng.* **9500**, 95001G.
- Chow, J. M., *et al.*, 2011, *Phys. Rev. Lett.* **107**, 080502.
- Chow, J. M., *et al.*, 2014, *Nat. Commun.* **5**, 4015.
- Chuang, I. L., D. W. Leung, and Y. Yamamoto, 1997, *Phys. Rev. A* **56**, 1114.
- Cirac, J. I., P. Zoller, H. J. Kimble, and H. Mabuchi, 1997, *Phys. Rev. Lett.* **78**, 3221.
- Clark, J. B., F. Lecocq, R. W. Simmonds, J. Aumentado, and J. D. Teufel, 2017, *Nature (London)* **541**7636, 191.
- Clarke, J., A. N. Cleland, M. H. Devoret, D. Esteve, and J. M. Martinis, 1988, *Science* **239**, 992.
- Clarke, J., and F. K. Wilhelm, 2008, *Nature (London)* **453**7198, 1031.
- Clerk, A. A., M. H. Devoret, S. M. Girvin, F. Marquardt, and R. J. Schoelkopf, 2010, *Rev. Mod. Phys.* **82**, 1155.
- Clerk, A. A., K. W. Lehnert, P. Bertet, J. R. Petta, and Y. Nakamura, 2020, *Nat. Phys.* **16**, 257.
- Cochrane, P. T., G. J. Milburn, and W. J. Munro, 1999, *Phys. Rev. A* **59**, 2631.
- Cohen-Tannoudji, C., B. Diu, and F. Laloe, 1977, *Quantum Mechanics*, Vol. 2 (John Wiley & Sons, New York).
- Cohen-Tannoudji, C., J. Dupont-Roc, and G. Grynberg, 1998, *Atom-Photon Interactions: Basic Processes and Applications*, Wiley Science Paperback Series (Wiley, New York).
- Colless, J. I., V. V. Ramasesh, D. Dahlen, M. S. Blok, M. E. Kimchi-Schwartz, J. R. McClean, J. Carter, W. A. de Jong, and I. Siddiqi, 2018, *Phys. Rev. X* **8**, 011021.
- Collett, M. J., and C. W. Gardiner, 1984, *Phys. Rev. A* **30**, 1386.
- Combes, J., J. Kerckhoff, and M. Sarovar, 2017, *Adv. Phys. X* **2**, 784.
- Córcoles, A. D., J. M. Chow, J. M. Gambetta, C. Rigetti, J. R. Rozen, G. A. Keefe, M. B. Rothwell, M. B. Ketchen, and M. Steffen, 2011, *Appl. Phys. Lett.* **99**, 181906.
- Córcoles, A. D., J. M. Gambetta, J. M. Chow, J. A. Smolin, M. Ware, J. Strand, B. L. T. Plourde, and M. Steffen, 2013, *Phys. Rev. A* **87**, 030301.
- Córcoles, A. D., E. Magesan, S. J. Srinivasan, A. W. Cross, M. Steffen, J. M. Gambetta, and J. M. Chow, 2015, *Nat. Commun.* **6**, 6979.
- Cottet, A., 2002, Ph.D. thesis (Université Paris 6).
- Cross, A. W., and J. M. Gambetta, 2015, *Phys. Rev. A* **91**, 032325.
- da Silva, M. P., D. Bozyigit, A. Wallraff, and A. Blais, 2010, *Phys. Rev. A* **82**, 043804.
- Dassonneville, R., *et al.*, 2020, *Phys. Rev. X* **10**, 011045.
- Day, P. K., H. G. LeDuc, B. A. Mazin, A. Vayonakis, and J. Zmuidzinas, 2003, *Nature (London)* **425**6960, 817.
- Delbecq, M. R., V. Schmitt, F. D. Parmentier, N. Roch, J. J. Viennot, G. Fève, B. Huard, C. Mora, A. Cottet, and T. Kontos, 2011, *Phys. Rev. Lett.* **107**, 256804.
- Devoret, M., and R. J. Schoelkopf, 2013, *Science* **339**, 1169.
- Devoret, M. H., 1997, in *Quantum Fluctuations*, Proceedings of the Les Houches Summer School, Session LXIII, edited by S. Reynaud, E. Giacobino, and J. Zinn-Justin (Elsevier, New York), pp. 351–386.
- Devoret, M. H., S. Girvin, and R. Schoelkopf, 2007, *Ann. Phys. (Berlin)* **16**, 767.
- Devoret, M. H., J. M. Martinis, and J. Clarke, 1985, *Phys. Rev. Lett.* **55**, 1908.
- Dewes, A., F. R. Ong, V. Schmitt, R. Lauro, N. Boulant, P. Bertet, D. Vion, and D. Esteve, 2012, *Phys. Rev. Lett.* **108**, 057002.
- DiCarlo, L., M. D. Reed, L. Sun, B. R. Johnson, J. M. Chow, J. M. Gambetta, L. Frunzio, S. M. Girvin, M. H. Devoret, and R. J. Schoelkopf, 2010, *Nature (London)* **467**, 574.
- DiCarlo, L., *et al.*, 2009, *Nature (London)* **460**, 240.
- Didier, N., J. Bourassa, and A. Blais, 2015, *Phys. Rev. Lett.* **115**, 203601.
- Didier, N., A. Kamal, W. D. Oliver, A. Blais, and A. A. Clerk, 2015, *Phys. Rev. Lett.* **115**, 093604.
- Didier, N., E. A. Sete, M. P. da Silva, and C. Rigetti, 2018, *Phys. Rev. A* **97**, 022330.
- Dixit, A. V., S. Chakram, K. He, A. Agrawal, R. K. Naik, D. I. Schuster, and A. Chou, 2020, arXiv:2008.12231.
- Dykman, M., and M. Krivoglaz, 1980, *Physica (Amsterdam)* **104A**, 480.
- Eddins, A., S. Schreppler, D. M. Toyli, L. S. Martin, S. Hacohen-Gourgy, L. C. G. Govia, H. Ribeiro, A. A. Clerk, and I. Siddiqi, 2018, *Phys. Rev. Lett.* **120**, 040505.
- Egger, D., M. Ganzhorn, G. Salis, A. Fuhrer, P. Müller, P. Barkoutsos, N. Moll, I. Tavernelli, and S. Filipp, 2019, *Phys. Rev. Applied* **11**, 014017.
- Eichler, C., D. Bozyigit, C. Lang, M. Baur, L. Steffen, J. M. Fink, S. Filipp, and A. Wallraff, 2011, *Phys. Rev. Lett.* **107**, 113601.
- Eichler, C., D. Bozyigit, C. Lang, L. Steffen, J. Fink, and A. Wallraff, 2011, *Phys. Rev. Lett.* **106**, 220503.
- Eichler, C., D. Bozyigit, and A. Wallraff, 2012, *Phys. Rev. A* **86**, 032106.
- Eichler, C., C. Lang, J. M. Fink, J. Govenius, S. Filipp, and A. Wallraff, 2012, *Phys. Rev. Lett.* **109**, 240501.
- Eichler, C., Y. Salathe, J. Mlynek, S. Schmidt, and A. Wallraff, 2014, *Phys. Rev. Lett.* **113**, 110502.
- Eichler, C., and A. Wallraff, 2014, *EPJ Quantum Technol.* **1**, 2.
- Eisaman, M. D., J. Fan, A. Migdall, and S. V. Polyakov, 2011, *Rev. Sci. Instrum.* **82**, 071101.
- Elder, S. S., C. S. Wang, P. Reinhold, C. T. Hann, K. S. Chou, B. J. Lester, S. Rosenblum, L. Frunzio, L. Jiang, and R. J. Schoelkopf, 2020, *Phys. Rev. X* **10**, 011001.
- Eschner, J., C. Raab, F. Schmidt-Kaler, and R. Blatt, 2001, *Nature (London)* **413**, 495.
- Esteve, D., M. H. Devoret, and J. M. Martinis, 1986, *Phys. Rev. B* **34**, 158.
- Fan, B., G. Johansson, J. Combes, G. J. Milburn, and T. M. Stace, 2014, *Phys. Rev. B* **90**, 035132.
- Filipp, S., M. Göppl, J. M. Fink, M. Baur, R. Bianchetti, L. Steffen, and A. Wallraff, 2011, *Phys. Rev. A* **83**, 063827.
- Filipp, S., *et al.*, 2009, *Phys. Rev. Lett.* **102**, 200402.
- Fink, J. M., R. Bianchetti, M. Baur, M. Göppl, L. Steffen, S. Filipp, P. J. Leek, A. Blais, and A. Wallraff, 2009, *Phys. Rev. Lett.* **103**, 083601.
- Fink, J. M., M. Göppl, M. Baur, R. Bianchetti, P. J. Leek, A. Blais, and A. Wallraff, 2008, *Nature (London)* **454**7202, 315.
- Fink, J. M., *et al.*, 2010, *Phys. Rev. Lett.* **105**, 163601.
- Flühmann, C., T. L. Nguyen, M. Marinelli, V. Negnevitsky, K. Mehta, and J. P. Home, 2019, *Nature (London)* **566**, 513.
- Flurin, E., N. Roch, F. Mallet, M. H. Devoret, and B. Huard, 2012, *Phys. Rev. Lett.* **109**, 183901.
- Flurin, E., N. Roch, J. Pillet, F. Mallet, and B. Huard, 2015, *Phys. Rev. Lett.* **114**, 090503.

- Forn-Díaz, P., J. J. Garcia-Ripoll, B. Peropadre, J.-L. Orgiazzi, M. A. Yurtalan, R. Belyansky, C. M. Wilson, and A. Lupascu, 2017, *Nat. Phys.* **13**, 39.
- Forn-Díaz, P., L. Lamata, E. Rico, J. Kono, and E. Solano, 2019, *Rev. Mod. Phys.* **91**, 025005.
- Forn-Díaz, P., J. Lisenfeld, D. Marcos, J. J. García-Ripoll, E. Solano, C. J. P. M. Harmans, and J. E. Mooij, 2010, *Phys. Rev. Lett.* **105**, 237001.
- Forn-Díaz, P., C. W. Warren, C. W. S. Chang, A. M. Vadiraj, and C. M. Wilson, 2017, *Phys. Rev. Applied* **8**, 054015.
- Fowler, A. G., M. Mariantoni, J. M. Martinis, and A. N. Cleland, 2012, *Phys. Rev. A* **86**, 032324.
- Foxen, B., *et al.* (Google AI Quantum Collaboration), 2020, *Phys. Rev. Lett.* **125**, 120504.
- Fragner, A., M. Göppl, J. M. Fink, M. Baur, R. Bianchetti, P. J. Leek, A. Blais, and A. Wallraff, 2008, *Science* **322**5906, 1357.
- Frattini, N. E., V. V. Sivak, A. Lingenfelter, S. Shankar, and M. H. Devoret, 2018, *Phys. Rev. Applied* **10**, 054020.
- Frattini, N. E., U. Vool, S. Shankar, A. Narla, K. M. Sliwa, and M. H. Devoret, 2017, *Appl. Phys. Lett.* **110**, 222603.
- Frey, T., P. J. Leek, M. Beck, A. Blais, T. Ihn, K. Ensslin, and A. Wallraff, 2012, *Phys. Rev. Lett.* **108**, 046807.
- Frisk Kockum, A., A. Miranowicz, S. De Liberato, S. Savasta, and F. Nori, 2019, *Nat. Rev. Phys.* **1**, 19.
- Frunzio, L., A. Wallraff, D. Schuster, J. Majer, and R. Schoelkopf, 2005, *IEEE Trans. Appl. Supercond.* **15**, 860.
- Gambetta, J., A. Blais, M. Boissonneault, A. A. Houck, D. I. Schuster, and S. M. Girvin, 2008, *Phys. Rev. A* **77**, 012112.
- Gambetta, J., A. Blais, D. I. Schuster, A. Wallraff, L. Frunzio, J. Majer, M. H. Devoret, S. M. Girvin, and R. J. Schoelkopf, 2006, *Phys. Rev. A* **74**, 042318.
- Gambetta, J., W. A. Braff, A. Wallraff, S. M. Girvin, and R. J. Schoelkopf, 2007, *Phys. Rev. A* **76**, 012325.
- Gambetta, J. M., A. A. Houck, and A. Blais, 2011, *Phys. Rev. Lett.* **106**, 030502.
- Gambetta, J. M., F. Motzoi, S. T. Merkel, and F. K. Wilhelm, 2011, *Phys. Rev. A* **83**, 012308.
- Gardiner, C. W., 1986, *Phys. Rev. Lett.* **56**, 1917.
- Gardiner, C. W., and M. J. Collett, 1985, *Phys. Rev. A* **31**, 3761.
- Gardiner, C. W., and P. Zoller, 1999, *Quantum Noise*, 2nd ed. (Springer, Berlin).
- Gilchrist, A., K. Nemoto, W. J. Munro, T. Ralph, S. Glancy, S. L. Braunstein, and G. Milburn, 2004, *J. Opt. B* **6**, S828.
- Giovannetti, V., S. Lloyd, and L. Maccone, 2004, *Science* **306**, 1330.
- Giustina, M., *et al.*, 2015, *Phys. Rev. Lett.* **115**, 250401.
- Glaetzle, A., K. Hammerer, A. Daley, R. Blatt, and P. Zoller, 2010, *Opt. Commun.* **283**, 758.
- Glazman, L. I., and G. Catelani, 2020, [arXiv:2003.04366](https://arxiv.org/abs/2003.04366).
- Gleyzes, S., S. Kuhr, C. Guerlin, J. Bernu, S. Deleglise, U. Busk Hoff, M. Brune, J.-M. Raimond, and S. Haroche, 2007, *Nature (London)* **446**7133, 297.
- Goldstein, H., C. P. Poole, and J. L. Safko, 2001, *Classical Mechanics*, 3rd ed. (Addison-Wesley, Reading, MA).
- Göppl, M., A. Fragner, M. Baur, R. Bianchetti, S. Filipp, J. M. Fink, P. J. Leek, G. Puebla, L. Steffen, and A. Wallraff, 2008, *J. Appl. Phys.* **104**, 113904.
- Gottesman, D., A. Kitaev, and J. Preskill, 2001, *Phys. Rev. A* **64**, 012310.
- Gough, J., and M. R. James, 2009, *IEEE Trans. Autom. Control* **54**, 2530.
- Grimm, A., N. E. Frattini, S. Puri, S. O. Mundhada, S. Touzard, M. Mirrahimi, S. M. Girvin, S. Shankar, and M. H. Devoret, 2020, *Nature (London)* **584**7820, 205.
- Grimsmo, A. L., J. Combes, and B. Q. Baragiola, 2020, *Phys. Rev. X* **10**, 011058.
- Gu, X., A. F. Kockum, A. Miranowicz, Y. x. Liu, and F. Nori, 2017, *Phys. Rep.* **718-719**, 1.
- Guerlin, C., J. Bernu, S. Deleglise, C. Sayrin, S. Gleyzes, S. Kuhr, M. Brune, J.-M. Raimond, and S. Haroche, 2007, *Nature (London)* **448**, 889.
- Guillaud, J., and M. Mirrahimi, 2019, *Phys. Rev. X* **9**, 041053.
- Gustafsson, M. V., T. Aref, A. F. Kockum, M. K. Ekstram, G. Johansson, and P. Delsing, 2014, *Science* **346**6206, 207.
- Gustavsson, S., O. Zwiher, J. Bylander, F. Yan, F. Yoshihara, Y. Nakamura, T. P. Orlando, and W. D. Oliver, 2013, *Phys. Rev. Lett.* **110**, 040502.
- Gyenis, A., P. S. Mundada, A. Di Paolo, T. M. Hazard, X. You, D. I. Schuster, J. Koch, A. Blais, and A. A. Houck, 2021, *PRX Quantum* **2**, 010339.
- Hadfield, R. H., 2009, *Nat. Photonics* **3**, 696.
- Haikka, P., Y. Kubo, A. Bienfait, P. Bertet, and K. Mølmer, 2017, *Phys. Rev. A* **95**, 022306.
- Haroche, S., 1992, in *Fundamental Systems in Quantum Optics*, Proceedings of the Les Houches Summer School, Session XXXIII, edited by J. Dalibard, J. M. Raimond, and J. Zinn-Justin (North-Holland, Amsterdam), p. 767.
- Haroche, S., and D. Kleppner, 1989, *Phys. Today* **42**, No. 1, 24.
- Haroche, S., and J.-M. Raimond, 2006, *Exploring the Quantum: Atoms, Cavities, and Photons* (Oxford University Press, New York).
- Hatridge, M., *et al.*, 2013, *Science* **339**6116, 178.
- Havlíček, V., A. D. Córcoles, K. Temme, A. W. Harrow, A. Kandala, J. M. Chow, and J. M. Gambetta, 2019, *Nature (London)* **567**7747, 209.
- Heeres, R. W., P. Reinhold, N. Ofek, L. Frunzio, L. Jiang, M. H. Devoret, and R. J. Schoelkopf, 2017, *Nat. Commun.* **8**, 94.
- Heeres, R. W., B. Vlastakis, E. Holland, S. Krastanov, V. V. Albert, L. Frunzio, L. Jiang, and R. J. Schoelkopf, 2015, *Phys. Rev. Lett.* **115**, 137002.
- Heinsoo, J., *et al.*, 2018, *Phys. Rev. Applied* **10**, 034040.
- Helmer, F., M. Mariantoni, E. Solano, and F. Marquardt, 2009, *Phys. Rev. A* **79**, 052115.
- Hensen, B., *et al.*, 2015, *Nature (London)* **526**, 682.
- Higginbotham, A. P., P. S. Burns, M. D. Urmey, R. W. Peterson, N. S. Kampel, B. M. Brubaker, G. Smith, K. W. Lehnert, and C. A. Regal, 2018, *Nat. Phys.* **14**, 1038.
- Hofheinz, M., E. M. Weig, M. Ansmann, R. C. Bialczak, E. Lucero, M. Neeley, A. D. O'Connell, H. Wang, J. M. Martinis, and A. N. Cleland, 2008, *Nature (London)* **454**7202, 310.
- Hofheinz, M., *et al.*, 2009, *Nature (London)* **459**, 546.
- Hoi, I.-C., A. F. Kockum, T. Palomaki, T. M. Stace, B. Fan, L. Tornberg, S. R. Sathyamoorthy, G. Johansson, P. Delsing, and C. M. Wilson, 2013, *Phys. Rev. Lett.* **111**, 053601.
- Hoi, I.-C., A. F. Kockum, L. Tornberg, A. Pourkabirian, G. Johansson, P. Delsing, and C. M. Wilson, 2015, *Nat. Phys.* **11**, 1045.
- Hoi, I.-C., T. Palomaki, J. Lindkvist, G. Johansson, P. Delsing, and C. M. Wilson, 2012, *Phys. Rev. Lett.* **108**, 263601.
- Hoi, I.-C., C. M. Wilson, G. Johansson, T. Palomaki, B. Peropadre, and P. Delsing, 2011, *Phys. Rev. Lett.* **107**, 073601.
- Holland, E. T., *et al.*, 2015, *Phys. Rev. Lett.* **115**, 180501.
- Houck, A. A., H. E. Türeci, and J. Koch, 2012, *Nat. Phys.* **8**, 292.
- Houck, A. A., *et al.*, 2007, *Nature (London)* **449**, 328.
- Houck, A. A., *et al.*, 2008, *Phys. Rev. Lett.* **101**, 080502.
- Hu, L., *et al.*, 2019, *Nat. Phys.* **15**, 503.
- Hutchings, M., J. Hertzberg, Y. Liu, N. Bronn, G. Keefe, M. Brink, J. M. Chow, and B. Plourde, 2017, *Phys. Rev. Applied* **8**, 044003.

- Ikonen, J., *et al.*, 2019, *Phys. Rev. Lett.* **122**, 080503.
- İmamoğlu, A., 2009, *Phys. Rev. Lett.* **102**, 083602.
- Inomata, K., Z. Lin, K. Koshino, W. D. Oliver, J. Tsai, T. Yamamoto, and Y. Nakamura, 2016, *Nat. Commun.* **7**, 12303.
- Jeffrey, E., *et al.*, 2014, *Phys. Rev. Lett.* **112**, 190504.
- Johansson, J., S. Saito, T. Meno, H. Nakano, M. Ueda, K. Semba, and H. Takayanagi, 2006, *Phys. Rev. Lett.* **96**, 127006 (pages 4).
- Johnson, B. R., *et al.*, 2010, *Nat. Phys.* **6**, 663.
- Johnson, J. E., E. M. Hoskinson, C. Macklin, D. H. Slichter, I. Siddiqi, and J. Clarke, 2011, *Phys. Rev. B* **84**, 220503.
- Josephson, B. D., 1962, *Phys. Lett.* **1**, 251.
- Kalashnikov, K., W. T. Hsieh, W. Zhang, W.-S. Lu, P. Kamenov, A. Di Paolo, A. Blais, M. E. Gershenson, and M. Bell, 2020, *PRX Quantum* **1**, 010307.
- Kamal, A., J. Clarke, and M. H. Devoret, 2011, *Nat. Phys.* **7**, 311.
- Kandala, A., A. Mezzacapo, K. Temme, M. Takita, M. Brink, J. M. Chow, and J. M. Gambetta, 2017, *Nature (London)* **549**7671, 242.
- Kannan, B., *et al.*, 2020, *Sci. Adv.* **6**, eabb8780.
- Kapit, E., 2015, *Phys. Rev. A* **92**, 012302.
- Kerman, A. J., 2013, *New J. Phys.* **15**, 123011.
- Khaneja, N., T. Reiss, C. Kehlet, T. Schulte-Herbrüggen, and S. J. Glaser, 2005, *J. Magn. Reson.* **172**, 296.
- Kimble, H., 1994, *Advances in Atomic, Molecular, and Optical Physics, Supplement 2: Cavity Quantum Electrodynamics* (Academic Press, New York), pp. 203–267.
- Kimble, H. J., 1998, *Phys. Scr.* **T76**, 127.
- Kimble, H. J., 2008, *Nature (London)* **453**7198, 1023.
- Kirchmair, G., B. Vlastakis, Z. Leghtas, S. E. Nigg, H. Paik, E. Ginossar, M. Mirrahimi, L. Frunzio, S. M. Girvin, and R. J. Schoelkopf, 2013, *Nature (London)* **495**7440, 205.
- Kjaergaard, M., M. E. Schwartz, J. Braumüller, P. Krantz, J. I.-J. Wang, S. Gustavsson, and W. D. Oliver, 2020, *Annu. Rev. Condens. Matter Phys.* **11**, 369.
- Kjaergaard, M., *et al.*, 2020, [arXiv:2001.08838](https://arxiv.org/abs/2001.08838).
- Knill, E., and R. Laflamme, 1997, *Phys. Rev. A* **55**, 900.
- Knill, E., R. Laflamme, and G. J. Milburn, 2001, *Nature (London)* **409**, 46.
- Koch, J., T. M. Yu, J. Gambetta, A. A. Houck, D. I. Schuster, J. Majer, A. Blais, M. H. Devoret, S. M. Girvin, and R. J. Schoelkopf, 2007, *Phys. Rev. A* **76**, 042319.
- Kochetov, B. A., and A. Fedorov, 2015, *Phys. Rev. B* **92**, 224304.
- Kollár, A. J., M. Fitzpatrick, and A. A. Houck, 2019, *Nature (London)* **571**, 45.
- Kono, S., K. Koshino, Y. Tabuchi, A. Noguchi, and Y. Nakamura, 2018, *Nat. Phys.* **14**, 546.
- Kono, S., Y. Masuyama, T. Ishikawa, Y. Tabuchi, R. Yamazaki, K. Usami, K. Koshino, and Y. Nakamura, 2017, *Phys. Rev. Lett.* **119**, 023602.
- Korotkov, A. N., 2001, *Phys. Rev. B* **63**, 115403.
- Koshino, K., K. Inomata, T. Yamamoto, and Y. Nakamura, 2013, *Phys. Rev. Lett.* **111**, 153601.
- Koshino, K., Z. Lin, K. Inomata, T. Yamamoto, and Y. Nakamura, 2016, *Phys. Rev. A* **93**, 023824.
- Koshino, K., and Y. Nakamura, 2012, *New J. Phys.* **14**, 043005.
- Krantz, P., M. Kjaergaard, F. Yan, T. P. Orlando, S. Gustavsson, and W. D. Oliver, 2019, *Appl. Phys. Rev.* **6**, 021318.
- Krastanov, S., V. V. Albert, C. Shen, C.-L. Zou, R. W. Heeres, B. Vlastakis, R. J. Schoelkopf, and L. Jiang, 2015, *Phys. Rev. A* **92**, 040303.
- Krinner, S., S. Lazar, A. Remm, C. Andersen, N. Lacroix, G. Norris, C. Hellings, M. Gabureac, C. Eichler, and A. Wallraff, 2020, *Phys. Rev. Applied* **14**, 024042.
- Krinner, S., S. Storz, P. Kurpiers, P. Magnard, J. Heinsoo, R. Keller, J. Lütolf, C. Eichler, and A. Wallraff, 2019, *EPJ Quantum Technol.* **6**, 2.
- Ku, J., X. Xu, M. Brink, D. C. McKay, J. B. Hertzberg, M. H. Ansari, and B. L. T. Plourde, 2020, *Phys. Rev. Lett.* **125**, 200504.
- Kubo, Y., *et al.*, 2010, *Phys. Rev. Lett.* **105**, 140502.
- Kuhr, S., *et al.*, 2007, *Appl. Phys. Lett.* **90**, 164101.
- Kurpiers, P., T. Walter, P. Magnard, Y. Salathe, and A. Wallraff, 2017, *EPJ Quantum Technol.* **4**, 8.
- Kurpiers, P., *et al.*, 2018, *Nature (London)* **558**7709, 264.
- Kyriienko, O., and A. S. Sorensen, 2016, *Phys. Rev. Lett.* **117**, 140503.
- Lachance-Quirion, D., Y. Tabuchi, A. Gloppe, K. Usami, and Y. Nakamura, 2019, *Appl. Phys. Express* **12**, 070101.
- Lachance-Quirion, D., Y. Tabuchi, S. Ishino, A. Noguchi, T. Ishikawa, R. Yamazaki, and Y. Nakamura, 2017, *Sci. Adv.* **3**, e1603150.
- Laflamme, R., C. Miquel, J. P. Paz, and W. H. Zurek, 1996, *Phys. Rev. Lett.* **77**, 198.
- Lalumière, K., B. C. Sanders, A. F. van Loo, A. Fedorov, A. Wallraff, and A. Blais, 2013, *Phys. Rev. A* **88**, 043806.
- Lalumière, K., J. M. Gambetta, and A. Blais, 2010, *Phys. Rev. A* **81**, 040301.
- Lamb, W. E., and R. Retherford, 1947, *Phys. Rev.* **72**, 241.
- Lambert, N. J., A. Rueda, F. Sedlmeir, and H. G. Schwefel, 2020, *Adv. Quantum Technol.* **3**, 2070011.
- Lamoreaux, S. K., K. A. van Bibber, K. W. Lehnert, and G. Carosi, 2013, *Phys. Rev. D* **88**, 035020.
- Landauer, R., 1991, *Phys. Today* **44**, No. 5, 23.
- Landig, A. J., J. V. Koski, P. Scarlino, U. C. Mendes, A. Blais, C. Reichl, W. Wegscheider, A. Wallraff, K. Ensslin, and T. Ihn, 2018, *Nature (London)* **560**7717, 179.
- Lang, C., C. Eichler, L. Steffen, J. M. Fink, M. J. Woolley, A. Blais, and A. Wallraff, 2013, *Nat. Phys.* **9**, 345.
- Lang, C., *et al.*, 2011, *Phys. Rev. Lett.* **106**, 243601.
- Lauk, N., N. Sinclair, S. Barzanjeh, J. P. Covey, M. Saffman, M. Spiropulu, and C. Simon, 2020, *Quantum Sci. Technol.* **5**, 020501.
- Law, C. K., and J. H. Eberly, 1996, *Phys. Rev. Lett.* **76**, 1055.
- Lecocq, F., L. Ranzani, G. A. Peterson, K. Cicak, R. W. Simmonds, J. D. Teufel, and J. Aumentado, 2017, *Phys. Rev. Applied* **7**, 024028.
- Leek, P. J., M. Baur, J. M. Fink, R. Bianchetti, L. Steffen, S. Filipp, and A. Wallraff, 2010, *Phys. Rev. Lett.* **104**, 100504.
- Leek, P. J., S. Filipp, P. Maurer, M. Baur, R. Bianchetti, J. M. Fink, M. Göppl, L. Steffen, and A. Wallraff, 2009, *Phys. Rev. B* **79**, 180511.
- Leggett, A. J., 1980, *Prog. Theor. Phys. Suppl.* **69**, 80.
- Leggett, A. J., 1984a, in *Essays in Theoretical Physics: In Honour of Dirk ter Haar*, edited by W. E. Parry (Pergamon, Oxford), pp. 95–127.
- Leggett, A. J., 1984b, *Phys. Rev. B* **30**, 1208.
- Lehmberg, R. H., 1970, *Phys. Rev. A* **2**, 883.
- Leonhardt, U., 1997, *Measuring the Quantum State of Light* (Cambridge University Press, Cambridge, England).
- Leonhardt, U., and H. Paul, 1993, *Phys. Rev. A* **48**, 4598.
- Leppäkangas, J., M. Marthaler, D. Hazra, S. Jebari, R. Albert, F. Blanchet, G. Johansson, and M. Hofheinz, 2018, *Phys. Rev. A* **97**, 013855.
- Lescanne, R., S. Deléglise, E. Albertinale, U. Réglade, T. Capelle, E. Ivanov, T. Jacqmin, Z. Leghtas, and E. Flurin, 2020, *Phys. Rev. X* **10**, 021038.
- Lescanne, R., M. Villiers, T. Peronin, A. Sarlette, M. Delbecq, B. Huard, T. Kontos, M. Mirrahimi, and Z. Leghtas, 2020, *Nat. Phys.* **16**, 509.

- Leung, D. W., M. A. Nielsen, I. L. Chuang, and Y. Yamamoto, 1997, *Phys. Rev. A* **56**, 2567.
- Leung, N., Y. Lu, S. Chakram, R. K. Naik, N. Earnest, R. Ma, K. Jacobs, A. N. Cleland, and D. I. Schuster, 2019, *npj Quantum Inf.* **5**, 18.
- Liu, L., F.-Z. Guo, S.-J. Qin, and Q.-Y. Wen, 2017, *Sci. Rep.* **7**, 42261.
- Liu, Y., and A. A. Houck, 2017, *Nat. Phys.* **13**, 48.
- Liu, Y.-x., L. Wei, J. Johansson, J. Tsai, and F. Nori, 2007, *Phys. Rev. B* **76**, 144518.
- Lucero, E., *et al.*, 2010, *Phys. Rev. A* **82**, 042339.
- Lucero, E., *et al.*, 2012, *Nat. Phys.* **8**, 719.
- Luthi, F., *et al.*, 2018, *Phys. Rev. Lett.* **120**, 100502.
- Ma, R., B. Saxberg, C. Owens, N. Leung, Y. Lu, J. Simon, and D. I. Schuster, 2019, *Nature (London)* **566**, 51.
- Ma, W.-L., M. Zhang, Y. Wong, K. Noh, S. Rosenblum, P. Reinhold, R. J. Schoelkopf, and L. Jiang, 2020, *Phys. Rev. Lett.* **125**, 110503.
- Ma, Y., *et al.*, 2020, *Nat. Phys.* **16**, 827.
- Macklin, C., K. O'Brien, D. Hover, M. E. Schwartz, V. Bolkhovskiy, X. Zhang, W. D. Oliver, and I. Siddiqi, 2015, *Science* **350**, 307.
- Magesan, E., and J. M. Gambetta, 2020, *Phys. Rev. A* **101**, 052308.
- Magesan, E., J. M. Gambetta, A. D. Córcoles, and J. M. Chow, 2015, *Phys. Rev. Lett.* **114**, 200501.
- Magnard, P., *et al.*, 2020, *Phys. Rev. Lett.* **125**, 260502.
- Majer, J., *et al.*, 2007, *Nature (London)* **449**7161, 443.
- Makhlin, Y., G. Schön, and A. Shnirman, 1999, *Nature (London)* **398**6725, 305.
- Makhlin, Y., G. Schön, and A. Shnirman, 2001, *Rev. Mod. Phys.* **73**, 357.
- Malekakhlagh, M., A. Petrescu, and H. E. Türeci, 2017, *Phys. Rev. Lett.* **119**, 073601.
- Malekakhlagh, M., A. Petrescu, and H. E. Türeci, 2020, *Phys. Rev. B* **101**, 134509.
- Mallet, F., M. A. Castellanos-Beltran, H. S. Ku, S. Glancy, E. Knill, K. D. Irwin, G. C. Hilton, L. R. Vale, and K. W. Lehnert, 2011, *Phys. Rev. Lett.* **106**, 220502.
- Mallet, F., F. R. Ong, A. Palacios-Laloy, F. Nguyen, P. Bertet, D. Vion, and D. Esteve, 2009, *Nat. Phys.* **5**, 791.
- Malnou, M., D. A. Palken, L. R. Vale, G. C. Hilton, and K. W. Lehnert, 2018, *Phys. Rev. Applied* **9**, 044023.
- Manenti, R., A. F. Kockum, A. Patterson, T. Behrle, J. Rahamim, G. Tancredi, F. Nori, and P. J. Leek, 2017, *Nat. Commun.* **8**, 975.
- Manucharyan, V. E., E. Boaknin, M. Metcalfe, R. Vijay, I. Siddiqi, and M. Devoret, 2007, *Phys. Rev. B* **76**, 014524.
- Manucharyan, V. E., J. Koch, L. I. Glazman, and M. H. Devoret, 2009, *Science* **326**, 113.
- Mariantoni, M., E. P. Menzel, F. Deppe, M. A. Araque Caballero, A. Baust, T. Niemczyk, E. Hoffmann, E. Solano, A. Marx, and R. Gross, 2010, *Phys. Rev. Lett.* **105**, 133601.
- Mariantoni, M., *et al.*, 2011, *Science* **334**, 61.
- Marquardt, F., and C. Bruder, 2001, *Phys. Rev. B* **63**, 054514.
- Martinis, J. M., M. H. Devoret, and J. Clarke, 1985, *Phys. Rev. Lett.* **55**, 1543.
- Martinis, J. M., M. H. Devoret, and J. Clarke, 2020, *Nat. Phys.* **16**, 234.
- Martinis, J. M., and M. R. Geller, 2014, *Phys. Rev. A* **90**, 022307.
- Martinis, J. M., S. Nam, J. Aumentado, K. M. Lang, and C. Urbina, 2003, *Phys. Rev. B* **67**, 094510.
- Martinis, J. M., S. Nam, J. Aumentado, and C. Urbina, 2002, *Phys. Rev. Lett.* **89**, 117901.
- Maser, A., B. Gmeiner, T. Utikal, S. Götzinger, and V. Sandoghdar, 2016, *Nat. Photonics* **10**, 450.
- McDonald, D. G., 2001, *Phys. Today* **54**, No. 7, 46.
- McKay, D. C., S. Filipp, A. Mezzacapo, E. Magesan, J. M. Chow, and J. M. Gambetta, 2016, *Phys. Rev. Applied* **6**, 064007.
- McKay, D. C., C. J. Wood, S. Sheldon, J. M. Chow, and J. M. Gambetta, 2017, *Phys. Rev. A* **96**, 022330.
- McRae, C. R. H., H. Wang, J. Gao, M. R. Vissers, T. Brecht, A. Dunsworth, D. P. Pappas, and J. Mutus, 2020, *Rev. Sci. Instrum.* **91**, 091101.
- Megrant, A., *et al.*, 2012, *Appl. Phys. Lett.* **100**, 113510.
- Menzel, E. P., F. Deppe, M. Mariantoni, M. A. Araque Caballero, A. Baust, T. Niemczyk, E. Hoffmann, A. Marx, E. Solano, and R. Gross, 2010, *Phys. Rev. Lett.* **105**, 100401.
- Metelmann, A., and A. A. Clerk, 2015, *Phys. Rev. X* **5**, 021025.
- Mi, X., M. Benito, S. Putz, D. M. Zajac, J. M. Taylor, G. Burkard, and J. R. Petta, 2018, *Nature (London)* **555**, 599.
- Mi, X., J. V. Cady, D. M. Zajac, P. W. Deelman, and J. R. Petta, 2017, *Science* **355**, 156.
- Michael, M. H., M. Silveri, R. T. Brierley, V. V. Albert, J. Salmilehto, L. Jiang, and S. M. Girvin, 2016, *Phys. Rev. X* **6**, 031006.
- Mineev, Z. K., Z. Leghtas, S. O. Mundhada, L. Christakis, I. M. Pop, and M. H. Devoret, 2020, *arXiv:2010.00620*.
- Mineev, Z. K., S. O. Mundhada, S. Shankar, P. Reinhold, R. Gutiérrez-Jáuregui, R. J. Schoelkopf, M. Mirrahimi, H. J. Carmichael, and M. H. Devoret, 2019, *Nature (London)* **570**, 200.
- Mirhosseini, M., E. Kim, V. S. Ferreira, M. Kalae, A. Sipahigil, A. J. Keller, and O. Painter, 2018, *Nat. Commun.* **9**, 3706.
- Mirhosseini, M., E. Kim, X. Zhang, A. Sipahigil, P. B. Dieterle, A. J. Keller, A. Asenjo-Garcia, D. E. Chang, and O. Painter, 2019, *Nature (London)* **569**, 692.
- Mirrahimi, M., Z. Leghtas, V. V. Albert, S. Touzard, R. J. Schoelkopf, L. Jiang, and M. H. Devoret, 2014, *New J. Phys.* **16**, 045014.
- Mlynek, J., A. Abdumalikov, C. Eichler, and A. Wallraff, 2014, *Nat. Commun.* **5**, 5186.
- Monroe, C., R. Raussendorf, A. Ruthven, K. R. Brown, P. Maunz, L.-M. Duan, and J. Kim, 2014, *Phys. Rev. A* **89**, 022317.
- Mooji, J. E., T. Orlando, L. Levitov, L. Tian, C. H. van der Wal, and S. Lloyd, 1999, *Science* **285**, 1036.
- Motzoi, F., J. M. Gambetta, P. Rebentrost, and F. K. Wilhelm, 2009, *Phys. Rev. Lett.* **103**, 110501.
- Movshovich, R., B. Yurke, P. G. Kaminsky, A. D. Smith, A. H. Silver, R. W. Simon, and M. V. Schneider, 1990, *Phys. Rev. Lett.* **65**, 1419.
- Müller, C., 2020, *Phys. Rev. Research* **2**, 033046.
- Müller, C., J. H. Cole, and J. Lisenfeld, 2019, *Rep. Prog. Phys.* **82**, 124501.
- Murch, K. W., S. J. Weber, K. M. Beck, E. Ginossar, and I. Siddiqi, 2013, *Nature (London)* **499**, 62.
- Murch, K. W., S. J. Weber, C. Macklin, and I. Siddiqi, 2013, *Nature (London)* **502**7470, 211.
- Naik, R. K., N. Leung, S. Chakram, P. Groszkowski, Y. Lu, N. Earnest, D. C. McKay, J. Koch, and D. I. Schuster, 2017, *Nat. Commun.* **8**, 1904.
- Nakamura, Y., Y. A. Pashkin, and J. S. Tsai, 1999, *Nature (London)* **398**6730, 786.
- Narla, A., *et al.*, 2016, *Phys. Rev. X* **6**, 031036.
- Negirneac, V., *et al.*, 2020, *arXiv:2008.07411*.
- Nersisyan, A., *et al.*, 2019, in *Proceedings of the 65th IEEE International Electron Devices Meeting (IEDM), San Francisco, 2019* (IEEE, New York), pp. 31.1.1–31.1.4, <https://ieeexplore.ieee.org/document/8993458>.
- Nielsen, M. A., and I. L. Chuang, 2000, *Quantum Computation and Quantum Information* (Cambridge University Press, Cambridge, England).

- Niemczyk, T., *et al.*, 2010, *Nat. Phys.* **6**, 772.
- Nigg, S. E., H. Paik, B. Vlastakis, G. Kirchmair, S. Shankar, L. Frunzio, M. H. Devoret, R. J. Schoelkopf, and S. M. Girvin, 2012, *Phys. Rev. Lett.* **108**, 240502.
- Niskanen, A. O., K. Harrabi, F. Yoshihara, Y. Nakamura, S. Lloyd, and J. S. Tsai, 2007, *Science* **316**, 723.
- Niskanen, A. O., Y. Nakamura, and J.-S. Tsai, 2006, *Phys. Rev. B* **73**, 094506.
- O'Brien, K., C. Macklin, I. Siddiqi, and X. Zhang, 2014, *Phys. Rev. Lett.* **113**, 157001.
- Oelsner, G., C. K. Andersen, M. Reháč, M. Schmelz, S. Anders, M. Grajcar, U. Hübner, K. Mølmer, and E. Il'ichev, 2017, *Phys. Rev. Applied* **7**, 014012.
- Ofek, N., *et al.*, 2016, *Nature (London)* **536**, 441.
- Oliver, W. D., and P. B. Welander, 2013, *MRS Bull.* **38**, 816.
- O'Malley, P. J. J., *et al.*, 2016, *Phys. Rev. X* **6**, 031007.
- Ong, F. R., M. Boissonneault, F. Mallet, A. C. Doherty, A. Blais, D. Vion, D. Esteve, and P. Bertet, 2013, *Phys. Rev. Lett.* **110**, 047001.
- Opremcak, A., *et al.*, 2018, *Science* **361**, 1239.
- Orlando, T. P., J. E. Mooij, L. Tian, C. H. van der Wal, L. S. Levitov, S. Lloyd, and J. J. Mazo, 1999, *Phys. Rev. B* **60**, 15398.
- Paik, H., *et al.*, 2011, *Phys. Rev. Lett.* **107**, 240501.
- Paik, H., *et al.*, 2016, *Phys. Rev. Lett.* **117**, 250502.
- Palomaki, T. A., J. W. Harlow, J. D. Teufel, R. W. Simmonds, and K. W. Lehnert, 2013, *Nature (London)* **495**, 210.
- Palomaki, T. A., J. D. Teufel, R. W. Simmonds, and K. W. Lehnert, 2013, *Science* **342**, 710.
- Parra-Rodriguez, A., E. Rico, E. Solano, and I. L. Egusquiza, 2018, *Quantum Sci. Technol.* **3**, 024012.
- Pashkin, Y. A., T. Yamamoto, O. Astafiev, Y. Nakamura, D. V. Averin, and J. S. Tsai, 2003, *Nature (London)* **421**, 823.
- Pechal, M., L. Huthmacher, C. Eichler, S. Zeytinoglu, A. A. Abdumalikov Jr., S. Berger, A. Wallraff, and S. Filipp, 2014, *Phys. Rev. X* **4**, 041010.
- Pechenezhskiy, I. V., R. A. Mencia, L. B. Nguyen, Y.-H. Lin, and V. E. Manucharyan, 2020, *Nature (London)* **585**, 368.
- Petersson, K. D., L. W. McFaul, M. D. Schroer, M. Jung, J. M. Taylor, A. A. Houck, and J. R. Petta, 2012, *Nature (London)* **490**, 380.
- Petrescu, A., M. Malekakhlagh, and H. E. Türeci, 2020, *Phys. Rev. B* **101**, 134510.
- Pfaff, W., C. J. Axline, L. D. Burkhardt, U. Vool, P. Reinhold, L. Frunzio, L. Jiang, M. H. Devoret, and R. J. Schoelkopf, 2017, *Nat. Phys.* **13**, 882.
- Pietikäinen, I., S. Danilin, K. S. Kumar, A. Vepsäläinen, D. S. Golubev, J. Tuorila, and G. S. Paraoanu, 2017, *Phys. Rev. B* **96**, 020501.
- Pioro-Ladrière, M., T. Obata, Y. Tokura, Y. S. Shin, T. Kubo, K. Yoshida, T. Taniyama, and S. Tarucha, 2008, *Nat. Phys.* **4**, 776.
- Place, A. P., *et al.*, 2020, *arXiv:2003.00024*.
- Planat, L., R. Dassonneville, J. P. Martínez, F. Foughi, O. Buisson, W. Hasch-Guichard, C. Naud, R. Vijay, K. Murch, and N. Roch, 2019, *Phys. Rev. Applied* **11**, 034014.
- Planat, L., A. Ranadive, R. Dassonneville, J. Puertas Martínez, S. Léger, C. Naud, O. Buisson, W. Hasch-Guichard, D. M. Basko, and N. Roch, 2020, *Phys. Rev. X* **10**, 021021.
- Plastina, F., and G. Falci, 2003, *Phys. Rev. B* **67**, 224514.
- Poletto, S., *et al.*, 2012, *Phys. Rev. Lett.* **109**, 240505.
- Potočnik, A., *et al.*, 2018, *Nat. Commun.* **9**, 904.
- Pozar, D. M., 2011, *Microwave Engineering*, 4th ed. (John Wiley & Sons, New York).
- Preskill, J., 2018, *Quantum* **2**, 79.
- Purcell, E. M., 1946, *Phys. Rev.* **69**, 681.
- Puri, S., and A. Blais, 2016, *Phys. Rev. Lett.* **116**, 180501.
- Puri, S., S. Boutin, and A. Blais, 2017, *npj Quantum Inf.* **3**, 18.
- Puri, S., *et al.*, 2020, *Sci. Adv.* **6**, eaay5901.
- Ralph, T. C., A. Gilchrist, G. J. Milburn, W. J. Munro, and S. Glancy, 2003, *Phys. Rev. A* **68**, 042319.
- Rau, I., G. Johansson, and A. Shnirman, 2004, *Phys. Rev. B* **70**, 054521.
- Reagor, M., *et al.*, 2016, *Phys. Rev. B* **94**, 014506.
- Reagor, M., *et al.*, 2018, *Sci. Adv.* **4**, eaao3603.
- Reagor, M. J., 2015, Ph.D. thesis (Yale University).
- Reed, M. D., L. DiCarlo, B. R. Johnson, L. Sun, D. I. Schuster, L. Frunzio, and R. J. Schoelkopf, 2010, *Phys. Rev. Lett.* **105**, 173601.
- Reed, M. D., B. R. Johnson, A. A. Houck, L. DiCarlo, J. M. Chow, D. I. Schuster, L. Frunzio, and R. J. Schoelkopf, 2010, *Appl. Phys. Lett.* **96**, 203110.
- Reinhold, P., S. Rosenblum, W.-L. Ma, L. Frunzio, L. Jiang, and R. J. Schoelkopf, 2020, *Nat. Phys.*, **16** 822.
- Rempe, G., H. Walther, and N. Klein, 1987, *Phys. Rev. Lett.* **58**, 353.
- Rice, P., and R. Brecha, 1996, *Opt. Commun.* **126**, 230.
- Richer, S., and D. DiVincenzo, 2016, *Phys. Rev. B* **93**, 134501.
- Richer, S., N. Maleeva, S. T. Skacel, I. M. Pop, and D. DiVincenzo, 2017, *Phys. Rev. B* **96**, 174520.
- Rigetti, C., and M. Devoret, 2010, *Phys. Rev. B* **81**, 134507.
- Rigetti, C., *et al.*, 2012, *Phys. Rev. B* **86**, 100506.
- Ristè, D., M. Dukalski, C. A. Watson, G. de Lange, M. J. Tiggelman, Y. M. Blanter, K. W. Lehnert, R. N. Schouten, and L. DiCarlo, 2013, *Nature (London)* **502**, 350.
- Ristè, D., S. Poletto, M.-Z. Huang, A. Bruno, V. Vesterinen, O.-P. Saira, and L. DiCarlo, 2015, *Nat. Commun.* **6**, 6983.
- Roch, N., M. E. Schwartz, F. Motzoi, C. Macklin, R. Vijay, A. W. Eddins, A. N. Korotkov, K. B. Whaley, M. Sarovar, and I. Siddiqi, 2014, *Phys. Rev. Lett.* **112**, 170501.
- Rol, M. A., L. Ciorciaro, F. K. Malinowski, B. M. Tarasinski, R. E. Sagastizabal, C. C. Bultink, Y. Salathe, N. Haandbaek, J. Sedivy, and L. DiCarlo, 2020, *Appl. Phys. Lett.* **116**, 054001.
- Rol, M. A., *et al.*, 2019, *Phys. Rev. Lett.* **123**, 120502.
- Romanenko, A., R. Pilipenko, S. Zorzetti, D. Frolov, M. Awida, S. Belomestnykh, S. Posen, and A. Grassellino, 2020, *Phys. Rev. Applied* **13**, 034032.
- Romero, G., J. J. García-Ripoll, and E. Solano, 2009, *Phys. Rev. Lett.* **102**, 173602.
- Rosenberg, D., *et al.*, 2017, *npj Quantum Inf.* **3**, 42.
- Rosenblum, S., P. Reinhold, M. Mirrahimi, L. Jiang, L. Frunzio, and R. J. Schoelkopf, 2018, *Science* **361**, 266.
- Roushan, P., *et al.*, 2017, *Science* **358**, 1175.
- Roy, A., and M. Devoret, 2016, *C.R. Phys.* **17**, 740.
- Roy, D., C. M. Wilson, and O. Firstenberg, 2017, *Rev. Mod. Phys.* **89**, 021001.
- Roy, T., S. Kundu, M. Chand, A. M. Vadiraj, A. Ranadive, N. Nehra, M. P. Patankar, J. Aumentado, A. A. Clerk, and R. Vijay, 2015, *Appl. Phys. Lett.* **107**, 262601.
- Royer, B., A. L. Grimsmo, A. Choquette-Poitevin, and A. Blais, 2018, *Phys. Rev. Lett.* **120**, 203602.
- Royer, B., A. L. Grimsmo, N. Didier, and A. Blais, 2017, *Quantum Opt.* **1**, 11.
- Ryan, C. A., B. R. Johnson, J. M. Gambetta, J. M. Chow, M. P. da Silva, O. E. Dial, and T. A. Ohki, 2015, *Phys. Rev. A* **91**, 022118.
- Sage, J. M., V. Bolkhovskiy, W. D. Oliver, B. Turek, and P. B. Welander, 2011, *J. Appl. Phys.* **109**, 063915.
- Salathé, Y., P. Kurpiers, T. Karg, C. Lang, C. K. Andersen, A. Akin, S. Krinmer, C. Eichler, and A. Wallraff, 2018, *Phys. Rev. Applied* **9**, 034011.

- Salathé, Y., *et al.*, 2015, *Phys. Rev. X* **5**, 021027.
- Samkharadze, N., G. Zheng, N. Kalhor, D. Brousse, A. Sammak, U. C. Mendes, A. Blais, G. Scappucci, and L. M. K. Vandersypen, 2018, *Science* **359**6380, 1123.
- Sandberg, M., C. M. Wilson, F. Persson, T. Bauch, G. Johansson, V. Shumeiko, T. Duty, and P. Delsing, 2008, *Appl. Phys. Lett.* **92**, 203501.
- Sank, D., *et al.*, 2016, *Phys. Rev. Lett.* **117**, 190503.
- Sathyamoorthy, S. R., L. Tornberg, A. F. Kockum, B. Q. Baragiola, J. Combes, C. M. Wilson, T. M. Stace, and G. Johansson, 2014, *Phys. Rev. Lett.* **112**, 093601.
- Schleich, W., and J. A. Wheeler, 1987, *Nature (London)* **326**, 574.
- Schmidt, S., and J. Koch, 2013, *Ann. Phys. (Berlin)* **525**, 395.
- Schneider, A., J. Braumüller, L. Guo, P. Stehle, H. Rotzinger, M. Marthaler, A. V. Ustinov, and M. Weides, 2018, *Phys. Rev. A* **97**, 062334.
- Schoelkopf, R., A. Clerk, S. Girvin, K. Lehnert, and M. Devoret, 2003, *Quantum Noise in Mesoscopic Physics* (Kluwer Academic Publishers, Amsterdam), pp. 175–203.
- Schoelkopf, R. J., and S. M. Girvin, 2008, *Nature (London)* **451**, 664.
- Schreier, J. A., *et al.*, 2008, *Phys. Rev. B* **77**, 180502.
- Schrieffer, J. R., and P. A. Wolff, 1966, *Phys. Rev.* **149**, 491.
- Schuller, J. A., E. S. Barnard, W. Cai, Y. C. Jun, J. S. White, and M. L. Brongersma, 2010, *Nat. Mater.* **9**, 193.
- Schuster, D. I., 2007, Ph.D. thesis (Yale University).
- Schuster, D. I., A. Wallraff, A. Blais, L. Frunzio, R.-S. Huang, J. Majer, S. M. Girvin, and R. J. Schoelkopf, 2005, *Phys. Rev. Lett.* **94**, 123602.
- Schuster, D. I., *et al.*, 2007, *Nature (London)* **445**, 515.
- Schuster, D. I., *et al.*, 2010, *Phys. Rev. Lett.* **105**, 140501.
- Sete, E. A., A. Galiatdinov, E. Mlinar, J. M. Martinis, and A. N. Korotkov, 2013, *Phys. Rev. Lett.* **110**, 210501.
- Sete, E. A., J. M. Gambetta, and A. N. Korotkov, 2014, *Phys. Rev. B* **89**, 104516.
- Shalm, L. K., *et al.*, 2015, *Phys. Rev. Lett.* **115**, 250402.
- Sheldon, S., E. Magesan, J. M. Chow, and J. M. Gambetta, 2016, *Phys. Rev. A* **93**, 060302.
- Shen, J.-T., and S. Fan, 2005, *Phys. Rev. Lett.* **95**, 213001.
- Shnirman, A., G. Schön, and Z. Hermon, 1997, *Phys. Rev. Lett.* **79**, 2371.
- Sillanpää, M. A., J. I. Park, and R. W. Simmonds, 2007, *Nature (London)* **449**, 438.
- Simons, R. N., 2001, *Coplanar Waveguide Circuits, Components and Systems*, Wiley Series in Microwave and Optical Engineering (Wiley InterScience, New York).
- Sirois, A. J., M. A. Castellanos-Beltran, M. P. DeFeo, L. Ranzani, F. Lecocq, R. W. Simmonds, J. D. Teufel, and J. Aumentado, 2015, *Appl. Phys. Lett.* **106**, 172603.
- Sivak, V., N. Frattini, V. Joshi, A. Lingenfelter, S. Shankar, and M. Devoret, 2019, *Phys. Rev. Applied* **11**, 054060.
- Sivak, V. V., S. Shankar, G. Liu, J. Aumentado, and M. H. Devoret, 2020, *Phys. Rev. Applied* **13**, 024014.
- Sletten, L. R., B. A. Moores, J. J. Viennot, and K. W. Lehnert, 2019, *Phys. Rev. X* **9**, 021056.
- Slichter, C. P., 1990, *Principles of Magnetic Resonance*, 3rd ed. (Springer-Verlag, Berlin).
- Slichter, D. H., R. Vijay, S. J. Weber, S. Boutin, M. Boissonneault, J. M. Gambetta, A. Blais, and I. Siddiqi, 2012, *Phys. Rev. Lett.* **109**, 153601.
- Solgun, F., D. W. Abraham, and D. P. DiVincenzo, 2014, *Phys. Rev. B* **90**, 134504.
- Solgun, F., D. P. DiVincenzo, and J. M. Gambetta, 2019, *IEEE Trans. Microwave Theory Tech.* **67**, 928.
- Srinivasan, S. J., A. J. Hoffman, J. M. Gambetta, and A. A. Houck, 2011, *Phys. Rev. Lett.* **106**, 083601.
- Srinivasan, S. J., N. M. Sundaresan, D. Sadri, Y. Liu, J. M. Gambetta, T. Yu, S. M. Girvin, and A. A. Houck, 2014, *Phys. Rev. A* **89**, 033857.
- Stockklauser, A., P. Scarlino, J. V. Koski, S. Gasparinetti, C. K. Andersen, C. Reichl, W. Wegscheider, T. Ihn, K. Ensslin, and A. Wallraff, 2017, *Phys. Rev. X* **7**, 011030.
- Strand, J. D., M. Ware, F. Beaudoin, T. A. Ohki, B. R. Johnson, A. Blais, and B. L. T. Plourde, 2013, *Phys. Rev. B* **87**, 220505.
- Strauch, F. W., P. R. Johnson, A. J. Dragt, C. J. Lobb, J. R. Anderson, and F. C. Wellstood, 2003, *Phys. Rev. Lett.* **91**, 167005.
- Sun, L., *et al.*, 2014, *Nature (London)* **511**, 444.
- Sundaresan, N. M., Y. Liu, D. Sadri, and L. J. Szócs, D. L. Underwood, M. Malekakhlagh, H. E. Türeci, and A. A. Houck, 2015, *Phys. Rev. X* **5**, 021035.
- Takita, M., A. Córcoles, E. Magesan, B. Abdo, M. Brink, A. Cross, J. M. Chow, and J. M. Gambetta, 2016, *Phys. Rev. Lett.* **117**, 210505.
- Tavis, M., and F. W. Cummings, 1968, *Phys. Rev.* **170**, 379.
- Terhal, B. M., J. Conrad, and C. Vuillot, 2020, *Quantum Sci. Technol.* **5**, 043001.
- Tesche, C. D., 1987, *Jpn. J. Appl. Phys.* **26**, 1409.
- Teufel, J. D., T. Donner, D. Li, J. W. Harlow, M. S. Allman, K. Cicak, A. J. Sirois, J. D. Whittaker, K. W. Lehnert, and R. W. Simmonds, 2011, *Nature (London)* **475**, 359.
- Teufel, J. D., D. Li, M. S. Allman, K. Cicak, A. J. Sirois, J. D. Whittaker, and R. W. Simmonds, 2011, *Nature (London)* **471**, 204.
- Tey, M. K., Z. Chen, S. A. Aljunid, B. Chng, F. Huber, G. Maslennikov, and C. Kurtsiefer, 2008, *Nat. Phys.* **4**, 924.
- Thompson, R. J., G. Rempe, and H. J. Kimble, 1992, *Phys. Rev. Lett.* **68**, 1132.
- Tinkham, M., 2004, *Introduction to Superconductivity*, 2nd ed. (Dover Publications, Mineola, NY).
- Toida, H., T. Nakajima, and S. Komiyama, 2013, *Phys. Rev. Lett.* **110**, 066802.
- Touzard, S., A. Kou, N. E. Frattini, V. V. Sivak, S. Puri, A. Grimm, L. Frunzio, S. Shankar, and M. H. Devoret, 2019, *Phys. Rev. Lett.* **122**, 080502.
- Toyli, D. M., A. W. Eddins, S. Boutin, S. Puri, D. Hover, V. Bolkhovskiy, W. D. Oliver, A. Blais, and I. Siddiqi, 2016, *Phys. Rev. X* **6**, 031004.
- Tripathi, V., M. Khezri, and A. N. Korotkov, 2019, *Phys. Rev. A* **100**, 012301.
- Tsang, M., and C. M. Caves, 2012, *Phys. Rev. X* **2**, 031016.
- Tuckett, D. K., S. D. Bartlett, and S. T. Flammia, 2018, *Phys. Rev. Lett.* **120**, 050505.
- Tuckett, D. K., S. D. Bartlett, S. T. Flammia, and B. J. Brown, 2020, *Phys. Rev. Lett.* **124**, 130501.
- Tuckett, D. K., A. S. Darmawan, C. T. Chubb, S. Bravyi, S. D. Bartlett, and S. T. Flammia, 2019, *Phys. Rev. X* **9**, 041031.
- Turchette, Q. A., N. P. Georgiades, C. J. Hood, H. J. Kimble, and A. S. Parkins, 1998, *Phys. Rev. A* **58**, 4056.
- Vandersypen, L. M. K., H. Bluhm, J. S. Clarke, A. S. Dzurak, R. Ishihara, A. Morello, D. J. Reilly, L. R. Schreiber, and M. Veldhorst, 2017, *npj Quantum Inf.* **3**, 34.
- van Loo, A., A. Fedorov, K. Lalumière, B. Sanders, A. Blais, and A. Wallraff, 2013, *Science* **342**, 1494.
- Varcoe, B. T. H., S. Brattke, M. Weidinger, and H. Walther, 2000, *Nature (London)* **403**, 743.
- Vepsäläinen, A. P., *et al.*, 2020, *Nature (London)* **584**, 551.
- Verney, L., R. Lescanne, M. H. Devoret, Z. Leghtas, and M. Mirrahimi, 2019, *Phys. Rev. Applied* **11**, 024003.

- Viennot, J. J., M. R. Delbecq, M. C. Dartiailh, A. Cottet, and T. Kontos, 2014, *Phys. Rev. B* **89**, 165404.
- Vijay, R., M. H. Devoret, and I. Siddiqi, 2009, *Rev. Sci. Instrum.* **80**, 111101.
- Vijay, R., D. H. Slichter, and I. Siddiqi, 2011, *Phys. Rev. Lett.* **106**, 110502.
- Vion, D., A. Aassime, A. Cottet, P. Joyez, H. Pothier, C. Urbina, D. Esteve, and M. H. Devoret, 2002, *Science* **296**, 886.
- Vissers, M. R., J. Gao, D. S. Wisbey, D. A. Hite, C. C. Tsuei, A. D. Corcoles, M. Steffen, and D. P. Pappas, 2010, *Appl. Phys. Lett.* **97**, 232509.
- Vlastakis, B., G. Kirchmair, Z. Leghtas, S. E. Nigg, L. Frunzio, S. M. Girvin, M. Mirrahimi, M. H. Devoret, and R. J. Schoelkopf, 2013, *Science* **342**, 607.
- Vollmer, M., 2004, *Phys. Educ.* **39**, 74.
- Vool, U., and M. Devoret, 2017, *Int. J. Circuit Theory Appl.* **45**, 897.
- Vool, U., *et al.*, 2016, *Phys. Rev. Lett.* **117**, 133601.
- Wallraff, A., D. I. Schuster, A. Blais, L. Frunzio, R.-S. Huang, J. Majer, S. Kumar, S. M. Girvin, and R. J. Schoelkopf, 2004, *Nature (London)* **431**, 162.
- Wallraff, A., D. I. Schuster, A. Blais, L. Frunzio, J. Majer, M. H. Devoret, S. M. Girvin, and R. J. Schoelkopf, 2005, *Phys. Rev. Lett.* **95**, 060501.
- Wallraff, A., A. Stockklauser, T. Ihn, J. R. Petta, and A. Blais, 2013, *Phys. Rev. Lett.* **111**, 249701.
- Walls, D. F., and G. J. Milburn, 2008, *Quantum Optics*, 2nd ed. (Springer-Verlag, Berlin).
- Walter, T., *et al.*, 2017, *Phys. Rev. Applied* **7**, 054020.
- Wang, C., C. Axline, Y. Y. Gao, T. Brecht, Y. Chu, L. Frunzio, M. H. Devoret, and R. J. Schoelkopf, 2015, *Appl. Phys. Lett.* **107**, 162601.
- Wang, C. S., *et al.*, 2020, *Phys. Rev. X* **10**, 021060.
- Wang, H., *et al.*, 2008, *Phys. Rev. Lett.* **101**, 240401.
- Wang, H., *et al.*, 2011, *Phys. Rev. Lett.* **106**, 060401.
- Wang, Z., S. Shankar, Z. Mineev, P. Campagne-Ibarcq, A. Narla, and M. Devoret, 2019, *Phys. Rev. Applied* **11**, 014031.
- Ware, M., B. R. Johnson, J. M. Gambetta, T. A. Ohki, J. M. Chow, and B. L. T. Plourde, 2019, [arXiv:1905.11480](https://arxiv.org/abs/1905.11480).
- Wehner, S., D. Elkouss, and R. Hanson, 2018, *Science* **362**, eaam9288.
- Wei, K. X., I. Lauer, S. Srinivasan, N. Sundaresan, D. T. McClure, D. Toyli, D. C. McKay, J. M. Gambetta, and S. Sheldon, 2020, *Phys. Rev. A* **101**, 032343.
- Wen, C., 1969, *IEEE Trans. Microwave Theory Tech.* **17**, 1087.
- Wen, P. Y., *et al.*, 2019, *Phys. Rev. Lett.* **123**, 233602.
- Wendin, G., 2017, *Rep. Prog. Phys.* **80**, 106001.
- Wenner, J., *et al.*, 2014, *Phys. Rev. Lett.* **112**, 210501.
- White, T. C., *et al.*, 2015, *Appl. Phys. Lett.* **106**, 242601.
- Winkler, R., 2003, *Spin-Orbit Coupling Effects in Two-Dimensional Electron and Hole Systems*, Springer Tracts in Modern Physics Vol. 191 (Springer, Berlin).
- Wiseman, H., and G. Milburn, 2010, *Quantum Measurement and Control* (Cambridge University Press, Cambridge, England).
- Wustmann, W., and V. Shumeiko, 2013, *Phys. Rev. B* **87**, 184501.
- Xiang, Z.-L., S. Ashhab, J. Q. You, and F. Nori, 2013, *Rev. Mod. Phys.* **85**, 623.
- Xu, K., *et al.*, 2018, *Phys. Rev. Lett.* **120**, 050507.
- Yamamoto, T., K. Inomata, M. Watanabe, K. Matsuba, T. Miyazaki, W. D. Oliver, Y. Nakamura, and J. S. Tsai, 2008, *Appl. Phys. Lett.* **93**, 042510.
- Yamamoto, T., Y. A. Pashkin, O. Astafiev, Y. Nakamura, and J. S. Tsai, 2003, *Nature (London)* **425**, 961, 941.
- Yamamoto, T., *et al.*, 2010, *Phys. Rev. B* **82**, 184515.
- Yan, F., P. Krantz, Y. Sung, M. Kjaergaard, D. L. Campbell, T. P. Orlando, S. Gustavsson, and W. D. Oliver, 2018, *Phys. Rev. Applied* **10**, 054062.
- Yan, F., *et al.*, 2016, *Nat. Commun.* **7**, 12964.
- Yang, C.-P., S.-I. Chu, and S. Han, 2003, *Phys. Rev. A* **67**, 042311.
- Yin, Y., *et al.*, 2013, *Phys. Rev. Lett.* **110**, 107001.
- Yoshihara, F., T. Fuse, S. Ashhab, K. Kakuyanagi, S. Saito, and K. Semba, 2017, *Nat. Phys.* **13**, 44.
- You, J. Q., X. Hu, S. Ashhab, and F. Nori, 2007, *Phys. Rev. B* **75**, 140515.
- You, J. Q., and F. Nori, 2003, *Phys. Rev. B* **68**, 064509.
- Yurke, B., 1987, *J. Opt. Soc. Am. B* **4**, 1551.
- Yurke, B., 2004, *Input-Output Theory* (Springer, New York), Chap. 3, pp. 53–96.
- Yurke, B., L. R. Corruccini, P. G. Kaminsky, L. W. Rupp, A. D. Smith, A. H. Silver, R. W. Simon, and E. A. Whittaker, 1989, *Phys. Rev. A* **39**, 2519.
- Yurke, B., and J. S. Denker, 1984, *Phys. Rev. A* **29**, 1419.
- Yurke, B., P. G. Kaminsky, R. E. Miller, E. A. Whittaker, A. D. Smith, A. H. Silver, and R. W. Simon, 1988, *Phys. Rev. Lett.* **60**, 764.
- Zagoskin, A., and A. Blais, 2007, *Phys. Can.* **63**, 215, <https://pic-pac.ca/static/downloads/7431c64c8e42dfeddae5e4768467a125f938ad2f.pdf>.
- Zeytinoglu, S., M. Pechal, S. Berger, A. A. Abdumalikov, Jr., A. Wallraff, and S. Filipp, 2015, *Phys. Rev. A* **91**, 043846.
- Zhang, H., S. Chakram, T. Roy, N. Earnest, Y. Lu, Z. Huang, D. Weiss, J. Koch, and D. I. Schuster, 2021, *Phys. Rev. X* **11**, 011010.
- Zhang, J., J. Vala, S. Sastry, and K. B. Whaley, 2003, *Phys. Rev. A* **67**, 042313.
- Zheng, H., and H. U. Baranger, 2013, *Phys. Rev. Lett.* **110**, 113601.
- Zheng, H., M. Silveri, R. T. Brierley, S. M. Girvin, and K. W. Lehnert, 2016, [arXiv:1607.02529](https://arxiv.org/abs/1607.02529).
- Zheng, Y., *et al.*, 2017, *Phys. Rev. Lett.* **118**, 210504.
- Zhong, L., *et al.*, 2013, *New J. Phys.* **15**, 125013.
- Zhu, G., D. G. Ferguson, V. E. Manucharyan, and J. Koch, 2013, *Phys. Rev. B* **87**, 024510.
- Zhu, N., X. Zhang, X. Han, C.-L. Zou, C. Zhong, C.-H. Wang, L. Jiang, and H. X. Tang, 2020, *Optica* **7**, 1291.
- Zurek, W. H., 1981, *Phys. Rev. D* **24**, 1516.